



PIERCE1: a determinant of left-right asymmetry in mammals

A thesis presented for the degree of Doctor of Philosophy (DPhil)

University College, University of Oxford

Hannah Jane Farley

Mammalian Genetics Unit, MRC Harwell

Department of Physiology, Anatomy and Genetics, University of Oxford

Supervisors: Dr Dominic Norris (MGU, MRC Harwell)

Professor Shankar Srinivas (DPAG, Oxford)

Hilary Term 2019

Word count: 46, 762

Abstract

PIERCE1: a determinant of left-right asymmetry in mammals

Hannah Jane Farley, University College

Doctor of Philosophy (DPhil)

Hilary Term 2019

The study of mice with heart and situs defects can provide useful models for improving our understanding of congenital heart defects in humans. This project characterised the involvement of *1700007K13Rik* (PIERCE1) in left-right patterning. A proportion of homozygotes with a mutation in this gene were identified by the International Mouse Phenotyping Consortium as exhibiting situs inversus totalis and heart defects, which are indicative of faulty left-right patterning. We hypothesised that this gene is involved in the establishment of ciliary motility at the embryonic node. Motile cilia are also found in the trachea, and if the tracheal cilia of knock-out mice also have motility defects, *C9orf116* (the human orthologue of *1700007K13Rik*) may be a new candidate gene for primary ciliary dyskinesia, a heterogeneous recessive condition.

The evaluation of nodal ciliary motility and nodal flow in mice homozygous for a *Pierce1*-null allele demonstrated that aberrant motility, leading to a lack of effective leftwards nodal flow, underlies the left-right patterning defects in these mice. In addition to this, studies of tracheal ciliary and sperm flagellar motility showed that PIERCE1 is required for correct motility in all classes of motile cilia and flagellar evaluated. Transmission electron microscopy studies point towards a role for PIERCE1 in the assembly or trafficking of dynein arms and their components; however, protein interaction studies have proved inconclusive thus far at placing PIERCE1 within the network of known dynein arm assembly factors.

Acknowledgements

I would like to thank my supervisor, Dr Dominic Norris, for his support throughout the course of this project. Thanks also go to the rest of the PIERCE1 group – Priyanka Anujan, Colin Bingle and Sudipto Roy, for many enlightening discussions.

The research community at MRC Harwell has been invaluable and this project would not have been possible without the team at the Mary Lyon Centre, who have taken great care of my mouse lines over the years. I am particularly grateful to Chris Esapa, Michelle Simon, Jeremy Sanderson, Debbie Ashworth and Henrik Westburg for their advice and support with experimental techniques and data analysis. The Norris lab, particularly Jenny Keynton, David Asante and Becca Walker, taught me the majority of what I know about molecular biology and good coffee, and I am grateful for their guidance. Outside of the lab, the student community at Harwell provides a supportive environment in which to complete a DPhil; I wish each of you the best of luck in completing your own theses.

I would have been unlikely to complete this thesis without the support of the University College community. Special thanks go to my undergraduate tutors, particularly Dr Keith Dorrington, Professor Trevor Sharp, and Dr Najib Rahman, for their encouragement and support during the transition to and from medical school. University College Boat Club has given me an escape from academia when it has been much needed. Thanks go to captains who have wrangled training sessions around lab hours made more complex by the mating habits of mice – especially Lara Drew, for her steadfast support and encouragement.

I have been fortunate enough to live with some brilliant housemates during this DPhil, who have learnt more about cilia than they ever thought they would. Thanks to Hannah Jeffries, Jess Macready, Shahana

Sengupta, Ann Laube and Sarah Robinson for the chats, cake and occasional car-pools.

The women I have met through Girlguiding in Oxfordshire have supported me no end throughout my studies. From providing a place to live to being a listening ear, they have all enabled the work that went into this project. I am particularly grateful to the girls and women of GOLD Rwanda, 1st Wolvercote Guides and Isis Rangers for providing endless entertainment and fire-building opportunities.

Lastly, thanks to my family, particularly my parents and siblings, to whom this thesis is dedicated.

Abbreviations

B6N	C57BL/6N mouse strain
BBS	Bardet-Biedl syndrome
BSA	Bovine serum albumin
CASA	Computer-assisted sperm analysis
CBF	Ciliary beat frequency
CBP	Ciliary beat pattern
CCDC	Coiled coil domain containing
cDNA	Complementary DNA
CF	Cystic fibrosis
CPC	Central pair complex
CSF	Cerebrospinal fluid
CST	Cell Signalling Technology
CT	Cycle threshold
D	Donkey
DAB	3, 3′-diaminobenzidine
DAPI	4', 6-diamidino-2-phenylindole
DIC	Differential interference contrast
DIG	Digoxigenin
DMEM	Dulbecco's modified eagle medium
DNAAF	Dynein arm assembly factor
dpc	Days post coitum
dpp	Days post-partum

DTT	Dithiothreitol
DUF	Domain of unknown function
DynAP	Dynein assembly particle
EDTA	Ethylenediaminetetraacetic acid
(E)GFP	(Enhanced) green fluorescent protein
FAM	Fluorescein amidite
FBS	Fetal bovine serum
FGF	Fibroblast growth factor
GliA	Gli activator
GliR	Gli repressor
GO	Gene ontology
HA	Hemagglutinin
Hh	Hedgehog
HISS	Heat-inactivated sheep serum
ICSI	Intra-cytoplasmic sperm injection
IDA	Inner dynein arm
IFT	Intraflagellar transport
IgG	Immunoglobulin G
IMPC	International Mouse Phenotyping Consortium
IP	Immunoprecipitation
IPTG	Isopropyl-β-D-thiogalactoside
LB	Luria broth
LDS	Lithium dodecyl sulphate

LPM	Lateral plate mesoderm
LR	Left-right
MCCs	Multiciliated cells
MEF	Mouse embryonic fibroblast
mRNA	Messenger RNA
Ms	Mouse
µCT	Micro computed tomography
NBT/BCIP	Nitro-blue tetrazolium/5-bromo-4-chloro-3'-indolyphosphate
NP-40	Nonidet P-40
NPC	Nuclear pore complex
NTMT	Alkaline phosphatase buffer (NaCl, Tris-Cl, $MgCl_2$, Tween)
OCT	Optimum cutting temperature compound
ODA	Outer dynein arm
PBS	Phosphate-buffered saline
PBT	PBS + 0.1% Tween 20
PCD	Primary ciliary dyskinesia
PCL	Periciliary layer
PCP	Planar cell polarity
PFA	Paraformaldehyde
PIERCE1	*p53*-induced expression in $Rb^{-/-}$ cells 1
PIV	Particle image velocimetry
ppm	Parts per million
PTM	Post-translational modification

qPCR	Quantitative polymerase chain reaction
RA	Retinoic acid
Rb	Rabbit
RIPA	Radioimmunoprecipitation assay
RPM	Revolutions per minute
RT	Room temperature
SA	Situs ambiguus
SDS	Sodium dodecyl sulphate
SEM	Scanning electron microscopy
SHH	Sonic hedgehog
SIT	Situs inversus totalis
SS	Situs solitus
SSC	Saline sodium citrate
TAE	Tris-acetate-EDTA
TBE	Tris-borate-EDTA
TBST	Tris-buffered saline + 0.1% Tween 20
TE	Tris-EDTA
TEM	Transmission electron microscopy
TGF	Transforming growth factor
TX-100	Triton-X-100
Y2H	Yeast two-hybrid
X-gal	5-bromo-4-chloro-3-indolyl-β-D-galactopyranoside

Contents

Abstract i

Acknowledgements iii

Abbreviations v

1: Introduction 1

1.1: *Pierce1*: an orphan gene 1

1.2: Cilia 4

1.2.1: Immotile cilia: ultrastructure 5

1.2.2: Ciliary assembly 9

1.2.3: Access to the cilium 12

1.2.4: Regulatory inputs to primary ciliogenesis and links to the cell cycle 13

1.2.5: Immotile cilia: function 15

1.2.6: Phenotypes resulting from defects in immotile cilia 19

1.2.7: *Pierce1* and immotile cilia 20

1.3: Motile cilia 21

1.3.1: Motile cilia: ultrastructure 21

1.3.2: Transcriptional regulation of ciliogenesis 26

1.3.3: Motile cilia: function 32

1.4: Primary ciliary dyskinesia: a genetic disorder 33

1.4.1: Kartagener's syndrome 33

1.4.2: Incidence and pathology 33

1.4.3: Causative mutations 35

1.5: Mouse models of primary ciliary dyskinesia 36

1.5.1: Strain differences: an important consideration 36

1.6: Aims of project 38

2: The role of PIERCE1 in embryonic ciliary motility 40

2.1: Introduction 41

2.1.1: Fluid flow at the embryonic node 41

2.1.2: How is fluid flow translated into a downstream genetic signal? 42

2.1.3: *Pierce1* and left-right patterning 47

2.2: Results 48

2.2.1: *Pierce1*$^{-/-}$ embryos show a lack of organised leftwards nodal flow. 48

2.2.2: *Pierce1*$^{-/-}$ embryos show a significant reduction in nodal ciliary beat frequency. 57

2.2.3: *Pierce1*$^{-/-}$ nodal cilia show a significant increase in "disrupted rotation" and "waving" beat patterns. 61

2.2.4: Our *Pierce1*-null allele shows similar left-right patterning defects to the *Pierce1*-null line characterised by Sung et al (Sung et al. 2016). 65

2.2.5: Defects in expression of left-right asymmetric genes at 8.0 dpc in *Pierce1*$^{-/-}$ embryos are concordant with later defective visceral organ situs. 70

2.2.6: Node morphology is grossly normal in *Pierce1*$^{-/-}$ embryos 76

2.3: Discussion 79

2.3.1: Flow at the embryonic node 79

2.3.2: Caveats and limitations of particle image velocimetry ..79

2.3.3: Our allele shows similar phenotypes to those observed by Sung et al. 81

2.3.4: Left-right asymmetric gene expression 83

2.3.5: Node morphology 86

2.4: Conclusions 87

2.4.1: Areas for future study 88

3: *Pierce1*$^{-/-}$ mice show ciliary motility defects in adult tissues. 90

3.1: Motile cilia in the adult: an introduction 91

3.1.1: The ventricular system 91

3.1.2: The reproductive systems 92

3.1.3: The respiratory system: the mucociliary escalator 93

3.1.4: Rationale for experimental work 96

3.2: Results of investigations into adult tracheal ciliary motility .. 98

3.2.1: Ciliary beat frequency is significantly reduced in *Pierce1*$^{-/-}$ mice. 98

3.2.2: *Pierce1*$^{-/-}$ mice show an increase in stiff ciliary beat pattern. 102

3.2.3: No significant differences in airway pathology are observed between *Pierce1*$^{+/+}$ and *Pierce1*$^{-/-}$ animals. 107

3.2.4: *Pierce1*$^{-/-}$ mice show a significant increase in dynein arm defects in the motile cilia of the respiratory epithelium. 109

3.3: Discussion of tracheal ciliary motility 115

3.4: Sperm flagellar motility 121

3.4.1: Introduction 121

3.5: Results of investigations into adult sperm flagellar motility. 126

3.5.1: Computer-assisted sperm analysis demonstrates significant differences in some motility attributes between *Pierce1*$^{+/+}$ *and Pierce1*$^{-/-}$ sperm. 126

3.5.2: *Pierce1*$^{-/-}$ sperm show no significant difference in morphology attributes, compared to *Pierce1*$^{+/+}$ sperm..... 131

3.5.3: *Pierce1*$^{-/-}$ sperm samples show a decrease in “rapid” swimming and an increase in “static” sperm..... 131

3.5.4: *Pierce1*$^{-/-}$ sperm samples show a significant decrease in total sperm count. 132

3.5.5: *Pierce1* expression initiates in concordance with a wave of flagellar motility-related genes. 134

3.5.6: Transmission electron microscopy of sperm flagellar axonemes does not demonstrate ultrastructural defects in *Pierce1*$^{-/-}$ sperm flagella. 141

3.6: Discussion of sperm motility defects in the mouse 144

3.7: Conclusions 148

4: Functional studies of PIERCE1 149

4.1: Introduction 149

4.2: Results 150

4.2.1: Analysis of the expression of *Pierce1* genetic product 150

4.2.2: In silico analysis of PIERCE1 structure 165

4.2.3: Phylogenetic analyses of *Pierce1* 173

4.2.5: Evaluation of *Pierce1* orthologue expression 176

4.2.6: Regulation of *Pierce1* expression 182

4.2.7: Yeast two-hybrid screen and investigation of putative interactors 185

4.3: Discussion 193

4.3.1: *Pierce1* expression is restricted to tissues with motile cilia. 193

4.3.2: Immunohistochemistry using an anti-PIERCE antibody is inconclusive. 194

4.3.3: Subcellular localisation of PIERCE1 in cell culture 195

4.3.4: In silico analysis of PIERCE1 196

4.3.5: *Ccpg1os*, the *Pierce1* orthologue 197

4.3.6: Regulation of *Pierce1* expression 199

4.3.7: Yeast two-hybrid studies 200

4.4: Conclusions 202

4.4.1: Future work 202

5: *Ccdc103* and ciliary motility in the mouse 204

5.1: Introduction 204

5.2: Results 209

5.2.1: *Ccdc103* shows restricted expression to the mouse node. 209

5.2.2: *Ccdc103*$^{H154P/H154P}$ mice show leftwards nodal flow. 209

5.2.3: *Ccdc103*$^{H154P/H154P}$ mice show normal ciliary beat frequency and motility. 215

5.2.4: *Ccdc103*$^{H154P/H154P}$ mice show no evidence of gross situs defects. 217

5.2.5*: Ccdc103*$^{del13/del13}$ mice show abnormal nodal flow. 218

5.2.6: *Ccdc103*$^{del13/del13}$ mice have largely immotile nodal cilia. 222

5.2.7: *Ccdc103*$^{del13/del13}$ mice exhibit a high incidence of situs defects. 224

5.3: Discussion 226

6: Overall discussion and conclusions 230

6.1: Ciliary motility is disrupted in the *Pierce1*$^{-/-}$ node, causing aberrant nodal flow and downstream left-right patterning defects..... 230

6.2: Ciliary motility is disrupted in *Pierce1*$^{-/-}$ adult tissues, but this disruption is not sufficient to cause associated pathology..... 230

6.3: PIERCE1: a putative DynAP component?..... 232

6.4: *Ccdc103* p.His154Pro does not associate with a phenotype in the C57BL/6N mouse, but a 13 nucleotide deletion in the same gene causes a severe ciliary immotility phenotype. 235

6.5: *C9ORF116*: a candidate gene for human heterotaxy..... 239

Appendix 1: Presentations associated with primary ciliopathies. . 241

Appendix 2: Causative PCD genes..... 242

Appendix 3: Genes known to cause PCD in humans, and their phenotype when knocked-out in the mouse. 246

Appendix 4: Mouse knock-outs associated with ciliary motility phenotypes. 250

Appendix 5: Experimental Methods 253

EM1: Genotyping *1700007K13Rik*^{tm2b} 254

EM1.1: Tissue preparation:..... 254

EM2: Genotyping CCDC103^{H154P} 255

EM2.1: Tissue preparation:..... 255

EM3: Molecular biology 256

EM3.1: Agarose gel electrophoresis 256

EM3.2: Purification of PCR products 256

EM3.3: DNA sequencing..... 257

EM3.4: cDNA synthesis 257
EM3.5: Restriction enzyme digestion 257
EM3.6: RNA isolation from tissues 257
EM3.7: RT-qPCR 257
EM3.8: Western blotting 258
EM3.9: Co-immunoprecipitation 260
EM4: X-Galactosidase staining 261
EM4.1: Whole embryos (7.5-8.5 dpc) 261
EM4.2: Cryosectioned tissue 261
EM5: Cell culture 262
EM5.1: Thawing cells 262
EM5.2: Splitting cells 262
EM5.3: Counting cells 262
EM5.4: Transfection of constructs 263
EM5.5: Immunocytochemistry 263
EM6: Dissection of embryos 264
EM6.1: Situs phenotyping of 13.5 dpc embryos 264
EM6.2: Whole mount immunofluorescence (7.5-8.5 dpc): 264
EM6.3: Whole mount in situ hybridisation 265
EM6.4: Scanning electron microscopy 270
EM6.5: Differential interference contrast imaging of embryonic nodal cilia 271
EM6.6: Particle image velocimetry of embryonic nodal cilia 271
EM7: Histological techniques 272
EM7.1: Immunofluorescence of cryosectioned tracheae 272

EM7.2: DAB Staining 272
EM8: Live imaging of adult tissues 273
EM8.1: Trachea preparation 273
EM8.2: High-speed video microscopy of tracheal motile cilia 273
EM8.3: Computer-assisted sperm analysis 274
EM9: Transmission electron microscopy 274
EM9.1: Sperm flagella: 274
EM9.2: Tracheal motile cilia: 274
Table EM1: primers and oligonucleotides 276
Table EM2: antibodies 279

1: Introduction

This thesis aims to contribute to our understanding of a class of defects termed ciliopathies, or diseases of the cilium, in humans, through the use of a mouse model. Ciliopathies are known to have genetic aetiology, and several of the implicated genes have been identified. However, multiple causative genes remain to be discovered.

Genetic variation has long been understood as a major contributor to disease itself, as well as predisposition to disease. Studying the precise relationship between causal genetic defects and the resulting pathological phenotype in humans is ethically challenging, and as such, science has made great use of model organisms to further our understanding of disease-linked genes. Model organisms, such as the mouse, enable genetic manipulation in a controlled environment, permitting experimental analysis of the contribution of specific genetic components to disease phenotypes.

1.1: *Pierce1*: an orphan gene

At the start of this project in 2015, *1700007K13Rik* was largely uncharacterised. The sole publication on this gene described it as being upregulated in *Rb* (retinoblastoma)-null mouse embryonic fibroblasts (MEFs) following exposure to ultraviolet radiation, hence the name (p53 induced expression in $Rb^{-/-}$ cells 1; *Pierce1;* Sung et al. 2010).

The Rb/E2F transcription factors and p53 are central to a regulatory network that is critical for cell cycle control in the context of tumour suppression. These transcription factors are often mutated in cancerous cells. In $Rb/E2F^{-/-}$ MEFs, *Pierce1* is upregulated in the S and G_2 phases of the cell cycle, but downregulated in the case of spontaneous immortalisation. Analyses demonstrated that *Pierce1* did not appear to be directly regulated by Rb/E2F, but instead by p53. When *Pierce1* itself is knocked down in MEFs, the expression of DNA damage response genes

after exposure to ultraviolet C light is downregulated. This was believed to point to a regulatory role for PIERCE1 in the cell cycle, and potentially in tumorigenesis.

As part of the International Mouse Phenotyping Consortium (IMPC; IMPC 2018; Meehan et al. 2017) project, a mouse knock-out of *1700007K13Rik* was analysed (allele design displayed in **Experimental Methods, Fig. EM1**). The IMPC was established to systematically phenotype mice homozygous for a null allele of each gene in the mouse genome, with the animals examined according to standardised methods to reduce variability (Brown, Hancock and Gates, 2006). The resulting data and mouse lines are then made available worldwide, providing insight and resources to support research into both more and less well characterised genes. To date, the project has phenotyped over 3000 lines. Initial data from the IMPC-derived *Pierce1*$^{-/-}$ mouse colony led to the commencement of this DPhil project in late 2015.

In 2016, an initial phenotyping paper of a *Pierce1*$^{-/-}$ mouse was published (Sung *et al.*, 2016) by a group external to the IMPC. Contrary to the expectations of the authors, who had published the initial paper linking PIERCE1 to cell cycle regulation, the mouse had no cell cycle related or cancer phenotype. Instead, approximately 40% of homozygous null mice exhibited situs inversus totalis (SIT; **Chapter 2**). A spectrum of other heterotaxy-associated, particularly cardiac, defects was observed, as was aberrant expression of genes immediately downstream of the break in left-right (LR) symmetry in the early embryo. This phenotype mirrored that detected in the IMPC-derived *Pierce1*-null line.

The LR patterning defects observed in this mouse line led us to suspect ciliary dysfunction as a causative mechanism. Understanding the physiological function of the cilium helps us to more accurately classify defects observed both in patients and animal models. In this chapter, I will

review what is known about the ultrastructure and function of immotile and motile cilia and the resulting phenotypes when these organelles are disrupted in model organisms, paying particular attention to the phenotypic effects that made us hypothesise a ciliary origin for the defects in *Pierce1*$^{-/-}$ mice. Tissue-specific roles of motile cilia are discussed in further depth in **Chapter 2** and **Chapter 3**.

I will also include a brief review of the links of ciliogenesis to the cell cycle, to enable a thorough evaluation of any implications from the existing literature surrounding PIERCE1. I will examine regulatory genes upstream of motile ciliogenesis, and evidence for *Pierce1* lying downstream of these genes. After reviewing a recessive genetic condition resulting from ciliary immotility in humans (primary ciliary dyskinesia, PCD), I will give an overview of the principal aims of this thesis.

1.2: Cilia

Cilia are membrane-bounded, microtubule-based organelles that protrude from the apical surface of the cell. They are present across diverse species, from *C. elegans* to humans, hinting at broad, evolutionarily conserved roles. Over the past few decades, the wide importance of these organelles in cellular and whole-organism function has been uncovered (Malicki and Johnson, 2017; Wheway, Nazlamova and Hancock, 2018). Cilia are found in both motile and immotile forms, and are required for vast swathes of embryonic development, from LR axis to neural patterning. In adults, ciliary dysfunction can lead to clinical presentations as wide-ranging as male infertility and polycystic kidney disease. Motile and immotile cilia play different roles in biology, and thus are associated with distinct pathologies when they do not function correctly (Fliegauf, Benzing and Omran, 2007).

In the 1990s and early 2000s, pioneering studies in model organisms such as *C. elegans* and the mouse paved the way to a greater understanding of ciliary function (Goetz and Anderson, 2010; Wheway, Nazlamova and Hancock, 2018). These studies identified a link between ciliary dysfunction and phenotypes affecting neural patterning (Goetz and Anderson, 2010) and the formation of cystic kidneys (Pazour *et al.*, 2000). As the identification of candidate genes for complex syndromes became more effective in the 2000s, it soon became apparent that the protein products of a number of genes associated with complex syndromic phenotypes localised to the cilium or basal body (Badano *et al.*, 2006) in their native state. A combination of fundamental and clinical research allowed the clustering of specific disease phenotypes resulting from aberrant ciliary function, leading to identification of syndromic disorders characteristic of ciliary dysfunction - the ciliopathies (Fliegauf, Benzing and Omran, 2007; Wheway, Nazlamova and Hancock, 2018).

1.2.1: Immotile cilia: ultrastructure

Primary, or immotile, cilia have a so-called 9+0 arrangement of microtubule doublets (Satir and Christensen, 2007). This is due to the presence of nine of these doublets, with nine-fold rotational symmetry. The "+0" refers to the lack of a central pair of microtubules in the centre of the cilium (c.f. 9+2, **Fig. 1.1**). The 9-fold symmetry of the microtubule doublets is templated from the basal body, a derivative of the centriole (Fu, Hagan and Glover, 2015).

Centrioles are barrel-shaped microtubule organising centres formed from a 9+0 microtubule triplet core with associated proteins (Farina *et al.*, 2016). Centrioles have important roles in both the cell cycle and ciliogenesis, meaning that cilia must be destroyed for correctly regulated cell division to occur (**Fig. 1.2**; Sánchez & Dynlacht 2016). In its ciliary capacity, the centriole becomes the basal body and acts as a template for ciliogenesis (Ishikawa and Marshall, 2011), with axonemal microtubule doublets extending from the triplets present in the basal body.

The microtubule axoneme is bounded by the ciliary membrane. Both cell and ciliary membranes are contiguous, but differences are observed in their protein and lipid composition. This is due to the active separation of the two membrane domains by the ciliary gate, a specialised area immediately apical to the basal body (Gonçalves and Pelletier, 2017).

The ciliary gate is composed of two subregions: the transition zone and transition fibres (**Fig. 1.3**). The transition fibres are formed from the distal appendages of the mother centriole, and have been proposed to form a ciliary pore complex (Kee *et al.*, 2012; Takao *et al.*, 2014), which has been argued to be analogous to the nuclear pore complex (NPC), which regulates protein trafficking into the nucleus. The NPC carries out this function in two main ways (Görlich and Kutay, 1999; Fahrenkrog and Aebi, 2003; Stewart, 2007). Firstly, it provides a size barrier that prevents

the diffusion into the nucleus of proteins over 30 kDa. For proteins over this size limit, a specific nuclear transport system utilises nuclear localisation signals, nuclear transport receptors and a small GTPase to cross the NPC and nuclear membrane (Stewart, 2007). The primary cilium has been shown to have a size-restricted diffusion barrier too, and blocking the function of nucleoporins (constituents of the NPC) also blocks the ciliary entry of KIF2, a key component of the cilium (Kee *et al.*, 2012). This adds weight to a putative ciliary pore complex, similar in function to the NPC, regulating ciliary protein entry.

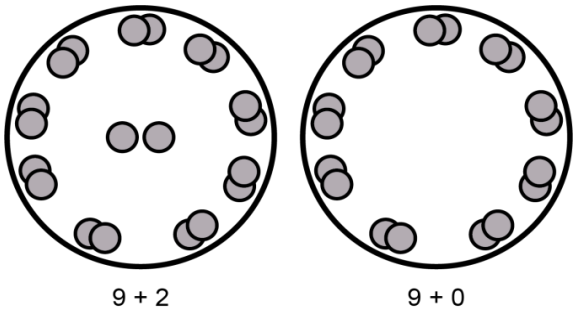
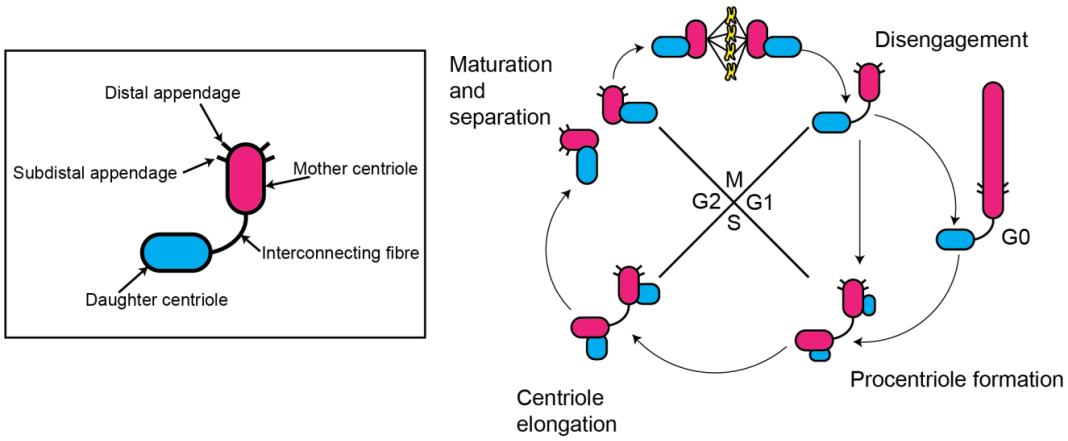


Figure 1.1 (top): Diagrammatic comparison of microtubule doublet arrangement of 9+2 and 9+0 cilia in cross-section.
Figure 1.2 (bottom): The centrosome cycle. Before cell division (M), the centrioles must duplicate, elongate, mature and separate. After cell division, the centrioles disengage and a cilium may be templated from the mother centriole (Fu, Hagan and Glover, 2015).



The transition zone is distal to the transition fibres and contains Y-shaped linkers that were initially identified in transmission electron microscopy (TEM) studies in *C. elegans* (Williams *et al.*, 2011). The transition zone has a sophisticated modular organisation, and is proposed to regulate trafficking into and out of the cilium (Gonçalves and Pelletier, 2017). The key role of the transition zone and transition fibres in regulating and maintaining ciliary composition is underlined by the fact that many of the proteins that are known to localise here cause ciliopathies when mutated (Fliegauf, Benzing and Omran, 2007).

Immediately adjacent to the ciliary membrane at the base of the cilium lies the ciliary pocket (**Fig. 1.3**). Recent studies have demonstrated the presence of clathrin-coated pits in the pocket, suggestive of a role for the pocket as an endocytic membrane domain involved in ciliary signalling (Molla-Herman *et al.*, 2010; Rattner *et al.*, 2010). The equivalent flagellar pocket of trypanosomatids is the exclusive point of origin of vesicles trafficking to the membrane in these organisms (Field and Carrington, 2009). Clathrin-coated pits bud from the flagellar pocket to form endocytic vesicles; the structural similarity between the flagellar pocket and ciliary pit raises the question of possible functional similarity. The full range of functions of the ciliary pocket is almost certainly yet to be elucidated (Rohatgi and Snell, 2010; Benmerah, 2013).

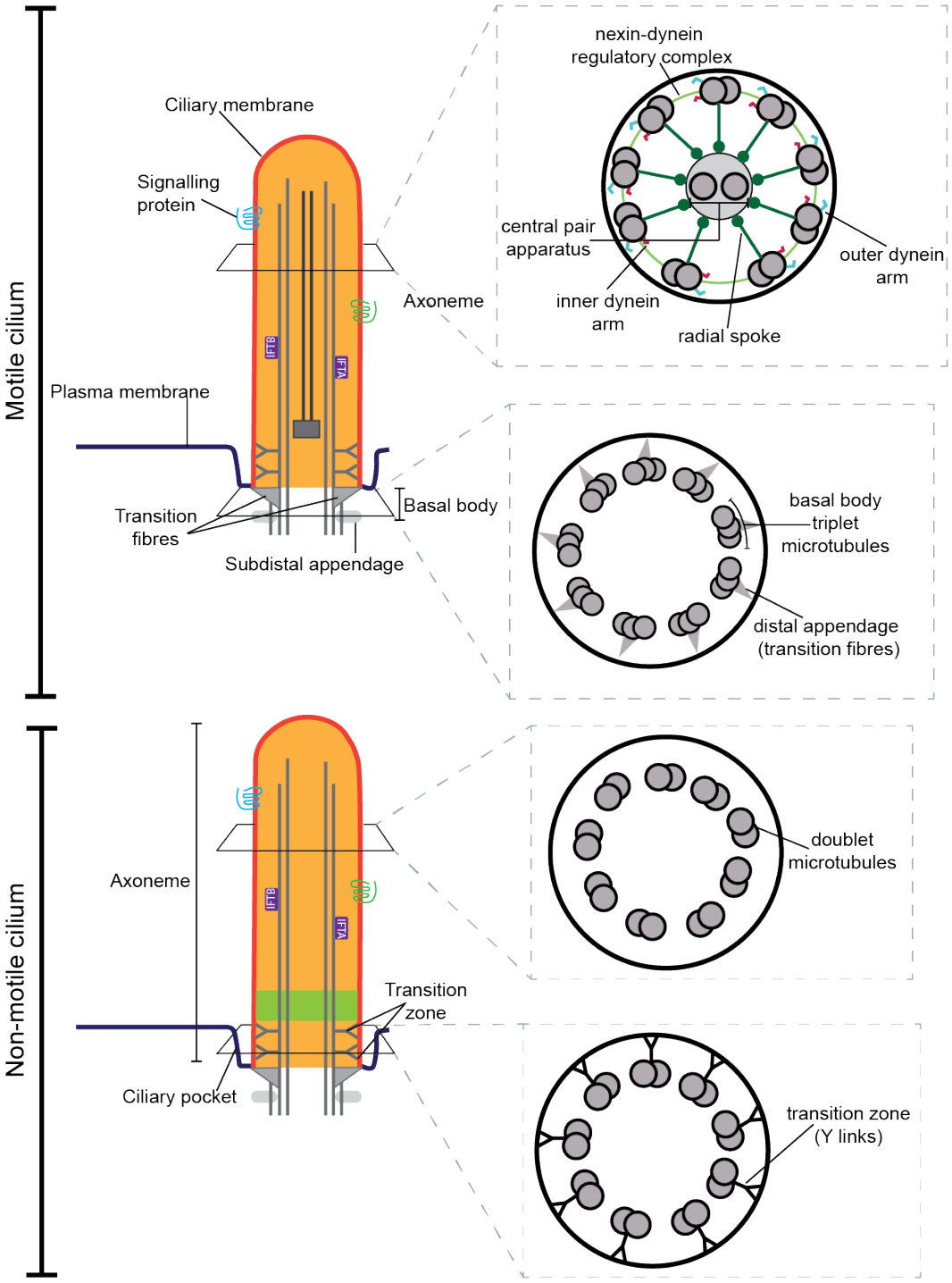


Figure 1.3: Diagrammatic representation of the ultrastructure of a motile (top) and immotile (bottom) cilium.

1.2.2: Ciliary assembly

Growth and replication of the cell is tightly controlled, and the distinct phases of this process are well understood (Harashima, Dissmeyer and Schnittger, 2013). To enable successful division, the cell must regulate the replication and trafficking of cellular components and organelles. This is particularly notable in the context of ciliary biology; in the majority of organisms, the centrioles are required both for effective segregation of packaged DNA in the form of chromosomes and as a template for the outgrowth of the ciliary axoneme. Thus, ciliogenesis and ciliary assembly are linked to the cell's growth and division, with the position and status of the centrioles showing cyclical behaviour in tandem with that of the whole cell (**Fig. 1.2**).

After entry into the G_0 phase of the cell cycle, one of the earliest steps in ciliogenesis is believed to be the transport of pre-ciliary vesicles to the distal appendages of the mother centriole (Sánchez and Dynlacht, 2016). The transport of the earliest vesicles has recently been shown to be mediated by the Myosin-Va motor complex (Wu, Chen and Tang, 2018). The formation of larger vesicles containing membrane-remodelling proteins, such as EHD1/EHD3 (Lu *et al.*, 2015), follows, and the mother centriole migrates to the actin-rich cortex at the apical membrane of the cell (Reiter, Blacque and Leroux, 2012). The distal appendages of the mother centriole are required to anchor the basal body to the plasma membrane (Tanos *et al.*, 2013) through proteins including CEP164 (Graser *et al.*, 2007) and ODF2 (Ishikawa *et al.*, 2005). After docking with the plasma membrane, the basal body templates the outgrowth of axonemal microtubule doublets in the cilium.

1.2.2.1: Intraflagellar transport

Protein synthesis is restricted to the cytoplasm. As such, ciliary outgrowth requires the selective import of protein cargoes, and their trafficking to the tip of the cilium, the site of microtubule assembly (Ishikawa and Marshall, 2011). This process is carried out by intraflagellar transport (IFT; Prevo et al. 2017; Lechtreck 2015a; Stepanek et al. 2016), a process first identified by Kozminski and Rosenbaum in the 1990s (Kozminski *et al.*, 1993). Through the use of differential interference microscopy, they visualised particles moving along the flagellar axoneme in *C. reinhardtii* (Lechtreck, 2015a) in both the anterograde and retrograde directions, that is to say, both away from and towards the cell body respectively.

The KIF3 motor complex is primarily associated with the anterograde transport of IFT cargo complexes and cytoplasmic dynein 2, which must undergo anterograde transport to enable its facilitation of retrograde transport. The KIF3 motor complex is comprised of two kinesin-2 family proteins, KIF3A and KIF3B, and the KIF-associated protein, KAP3 (Cole *et al.*, 1993). Cytoplasmic dynein-2 mediates retrograde IFT, or transport towards the cell. Its composition is more complex, and is detailed in **Table 1.1** (Witman and Hou, 2017). A loss of the KIF3 motor complex components leads to very short or absent cilia (Morris and Scholey, 1997; Nonaka *et al.*, 1998b; Huangfu and Anderson, 2005; Mueller, 2005; Hirokawa, Tanaka and Okada, 2012), whilst a loss of the cytoplasmic dynein 2 complex leads to shortened cilia with bulges at the tip and base (Pazour, Wilkerson and Witman, 1998; G J Pazour, Dickert and Witman, 1999; Gregory J. Pazour, Dickert and Witman, 1999; Porter *et al.*, 1999; Signor *et al.*, 1999; Hou, 2004).

IFT particles are constructed from a large number of proteins (Piperno and Mead, 1997; Cole *et al.*, 1998), most of which are highly

conserved across ciliated organisms. They have traditionally been divided into A and B complexes due to their initial identification in two clusters of biochemically interacting proteins; it is unclear whether these complexes carry distinct cargo, and the function of many of the component proteins remains to be elucidated. Losing IFTB or IFTA complex proteins has a similar effect on ciliogenesis as to losing kinesin-2 or cytoplasmic dynein 2 respectively – IFTB disruption leads to shortened or absent cilia (Fujiwara, Ishihara and Katsura, 1999; Pazour *et al.*, 2000; Brazelton *et al.*, 2001; Deane *et al.*, 2001; Haycraft *et al.*, 2003; Huangfu *et al.*, 2003; Sun, 2004; Follit, 2006; Qin *et al.*, 2007), whilst IFTA disruption leads to bulging cilia with accumulation of IFTA complexes at the tip (Iomini *et al.*, 2001, 2009; Efimenko *et al.*, 2006; Absalon *et al.*, 2008; Tran *et al.*, 2008; Tsao and Gorovsky, 2008).

Cytoplasmic dynein 2 component		***Human gene***
Heavy chain		*DYNC2H1*
Light intermediate chain		*DYNC2LI1*
Intermediate chain		*WDR34; WDR60*
Light chains	*DYNLL/LC8 group*	*DYNLL1; DYNLL2*
	DYNLT/Tctex group	*DYNLT1; DYNLT3; TCTEX1D3*
	DYNLRB/LC7 group	*DYNLRB1; DYNLRB2*

Table 1.1: Components of cytoplasmic dynein two and their human gene counterparts.

1.2.3: Access to the cilium

Ciliary proteins and membrane must be transported across the cell, or trafficked, to the cilium. Membrane proteins are synthesised at the endoplasmic reticulum and are packaged into vesicles both there and at the Golgi, before transport towards their ciliary destination. In *C. reinhardtii*, IFT20 and IFT54 have been implicated in transport of vesicles from the Golgi to cilia (Follit, 2006; Omori *et al.*, 2008; Follit *et al.*, 2009).

Proteins that result in Bardet-Biedl syndrome (BBS) when mutated have been implicated in vesicle transport to the cilium (Nachury *et al.*, 2007) – at least seven have been shown to form a complex, termed the BBSome, which interacts with RABIN8. RABIN8 is a guanine nucleotide exchange factor for RAB8, a small GTPase that promotes vesicle trafficking (Yoshimura *et al.*, 2007). The BBSome has also been shown to form a coat complex (Jin *et al.*, 2010) that sorts membrane proteins through its interaction with ARF6, a GTPase. Clathrin-adaptin and COP1 (coat protein 1) form scaffolds to drive vesicle transport elsewhere in the cell (Arakel and Schwappach, 2018); several BBSome and IFT proteins have been shown to share structural components with these (Avidor-Reiss *et al.*, 2004; Jékely and Arendt, 2006; Jin *et al.*, 2010), indicating that these groups of proteins may share a similar evolutionary lineage, and perform similar functions in the cell.

As the protein make-up of the cilium is so distinct from that of the cell, there may be a protein-encoded ciliary localisation signal (Lechtreck, 2015b), analogous to that required for nuclear localisation. However, although a variety of targeting signals in different proteins have been identified (Geng, 2006; Jenkins *et al.*, 2006; Berbari *et al.*, 2008; Mazelova *et al.*, 2009; Tao *et al.*, 2009; Follit *et al.*, 2010; Nagata *et al.*, 2012; Geneva, Tan and Calvert, 2016), a universal consensus sequence has not been elucidated (Hsiao, Tuz and Ferland, 2012). Multiple targeting

sequences could be involved, potentially sharing homology in a form that we have not yet understood. The molecular machinery required to interpret these targeting signals is also unclear.

1.2.4: Regulatory inputs to primary ciliogenesis and links to the cell cycle

1.2.4.1: Cell cycle

Suppression of ciliogenesis is essential for proper cell proliferation due to the requirement for the centriole in the mitotic spindle. It is unsurprising, therefore, that key regulators of mitosis have been shown to play crucial roles in the regulation of ciliogenesis (Malicki and Johnson, 2017), and interact with components of the transition zone and other ciliary locations. For example, AURKA (aurora kinase A) and PLK1 (polo-like kinase 1) are regulatory kinases, functioning to control both passage through the cell cycle and ciliogenesis.

PLK1 has been shown to play a role in regulating daughter centriole maturation across multiple cell cycles (Godinho *et al.*, 2012; Kong *et al.*, 2014; Shukla *et al.*, 2015). PLK1 regulates the distance of the daughter from the mother centriole. It promotes the association of appendage proteins with the daughter centriole, as well as the formation of the appendages themselves. This is a prime example of a regulatory kinase with dual roles in ciliogenesis and the cell cycle – PLK1 also localises to the basal body of the cilium during G_0 where it phosphorylates NPHP1 (nephrocystin 1; Seeger-Nukpezah et al. 2012). NPHP1 is a ciliary protein whose loss in humans is a key cause of nephronophthisis, an autosomal-recessive form of polycystic kidney disease. AURKA is a component of the spindle assembly checkpoint (Yu *et al.*, 2017; Courtheoux *et al.*, 2018) in mitosis, and its activation has been shown to induce ciliary disassembly (Pugacheva *et al.*, 2007).

Cell cycle kinases also regulate ciliogenesis via their effect on HDAC6 (histone deacetylase 6), an enzyme that de-acetylates tubulins. Axonemal tubulins have a wide range of post-translational modifications (PTMs), including acetylation (Satir and Christensen, 2007). These modifications are thought to coordinate the many functions of tubulin within the cell (Janke, 2014). Increased catalytic activity in AURKA has been reported to promote the de-acetylating activities of HDAC6 (Pugacheva *et al.*, 2007), and HDAC6 has been associated with the ciliary resorption process in several studies (Pugacheva *et al.*, 2007; De Diego *et al.*, 2014; Kim *et al.*, 2014). However, mice lacking HDAC6 have no overt ciliary phenotype (Zhang *et al.*, 2008). As axonemal tubulins are subject to a wide variety of modifications, it is quite possible that there may be redundancy in the function of these alterations.

1.2.4.2: The actin cytoskeleton

Actin is a central component of the cytoskeleton, and control of the synthesis and branching of this protein is crucial for effective cell growth and division (Blanchoin *et al.*, 2014). An actin mesh at the apical cortex of the cell is required for basal body docking at the cell surface in ciliogenesis (Pitaval *et al.*, 2010), and actin branching appears to play a role in the inhibition of ciliogenesis (Bershteyn *et al.*, 2010; Kim *et al.*, 2010; Cao *et al.*, 2012). Indeed, actin is proposed to modulate ciliogenesis through a combination of three distinct mechanisms. Actin is proposed as a modulator of the transport of vesicles required for ciliogenesis to the prospective ciliary base (Kim *et al.*, 2010, 2015; Cao *et al.*, 2012). Actin filaments are also implicated in localising ciliary disassembly factors, such as HDAC6, to the base of the cilium (De Diego *et al.*, 2014). Thirdly, F-actin polymerisation upregulates the YAP/TAZ pathway, which itself goes on to activate AURKA. This in turn activates HDAC6, which is thought to

induce ciliary disassembly through deacetylation of axonemal microtubules (Kim *et al.*, 2014, 2015; Zanconato *et al.*, 2015).

1.2.4.3: Length

Correct ciliary length is of importance to the function of both immotile and motile cilia. Disruption of ciliary length has been proposed to affect the cilium's efficacy in transducing signalling pathways, via alterations in IFT (Canterini *et al.*, 2017; Thorpe *et al.*, 2017; Wheway, Nazlamova and Hancock, 2018), and the fluid dynamics associated with motile cilia have also been shown to be affected by alterations in ciliary length (Lopes *et al.*, 2010; Pintado *et al.*, 2017). Pathways that regulate the presence or absence of a primary cilium can be more subtly involved in adjusting ciliary length - multiple mutations have been shown to affect ciliary length, including those identified via screens in *C. reinhardtii* (Wemmer and Marshall, 2007) and in mammalian cell culture (Kim *et al.*, 2010). Several studies have implicated a variety of regulatory kinases (Berman *et al.*, 2003; Wiese, Kuhn and Grünfelder, 2003; Wilson and Lefebvre, 2004; Tam, Wilson and Lefebvre, 2007; Besschetnova *et al.*, 2010; Ko *et al.*, 2010; Omori *et al.*, 2010; Pitaval *et al.*, 2010), however the underlying mechanisms remain unclear.

1.2.5: Immotile cilia: function

The primary cilium has been called a sensory antenna for the cell (Singla and Reiter, 2006). It acts as a central location for the reception of diverse signals from the extracellular environs, including mechanical, light and molecular cues (Pazour and Witman, 2003; Goetz and Anderson, 2010). When functioning correctly, the cilium receives these cues and translates them into a cellular response.

1.2.5.1: Hedgehog signalling

The link between cilia and Hedgehog (Hh) signalling in vertebrates was revealed by a large-scale genetic screen which aimed to identify mutations that altered the patterning of the mouse embryo. Phenotypes typically associated with a loss of Hh signalling, such as a loss of ventral cell types in the neural tube, were found to be associated with mutations in components of the IFT system, such as *Dync2h1* (May *et al.*, 2005), *Ift72* and *Ift88* (Huangfu *et al.*, 2003; Huangfu and Anderson, 2005). Disrupting the kinesin-2 motor system in embryos lacking KIF3A resulted in a similar phenotype (Zhou, 2009). Genetic studies showed that these IFT proteins were central to Hh signalling, lying downstream of Smoothened and Patched1, but upstream of the Gli family of transcription factors that implement the pathway by binding to target gene DNA in cells (Huangfu *et al.*, 2003; Huangfu and Anderson, 2005). It has since been established that the tip of the cilium is a key regulatory compartment for activity of the effectors of Hh signalling (Bangs and Anderson, 2017). Strikingly, it should be noted that *Drosophila* appear to have uncoupled Hh signalling from the primary cilium (Lee, Zhao and Ingham, 2016).

The role of Hh signalling in embryonic patterning is complex. In the absence of Hh ligand, Gli proteins are cleaved to form Gli repressors (GliR), which repress transcription of target genes. When a ligand is present, however, this proteolytic processing is inhibited. This leaves activated Gli factors (GliA) to promote target gene expression. Importantly, IFT is required both for the production of GliAs and GliRs (Huangfu and Anderson, 2005; Liu, 2005; May *et al.*, 2005; Ocbina and Anderson, 2008). This leads to the confusing situation whereby mutations disrupting IFT lead to both loss and gain of function Hh phenotypes. For example, GliAs are central to neural patterning, whilst GliRs are required for limb patterning. IFT mutants show a loss of Hh signaling in the neural tube,

whilst those that survive to later embryogenesis show pre-axial polydactyly; a loss of GliR phenotype (i.e., a gain of Hh signalling).

1.2.5.2: Other signaling pathways

The primary cilium is also associated with other signaling pathways. Though mice and zebrafish lacking primary cilia show no defect in canonical Wnt signaling (Huang and Schier, 2009; Ocbina, Tuson and Anderson, 2009), evidence from pre-clinical studies shows that ciliary defects can lead to a massive overactivation of Wnt signaling (Wheway *et al.*, 2013). Primary cilia are thus potentially implicated in the attenuation of canonical Wnt signaling.

Primary cilia are closely associated with the non-canonical Wnt planar cell polarity (PCP) signaling pathway; migration of the centriole to the apical cell membrane is a major downstream effect of this cascade (Gó Mez-Orte *et al.*, 2013), and mutations that affect PCP proteins often lead to mislocalisation of the centriole or basal body.

Notch has been shown to act through the primary cilium in specific cell types during development, in a highly context-dependent manner (Wheway, Nazlamova and Hancock, 2018). The Hippo signaling pathway acts through proteins that have been shown to localize to the base of the cilium, and proteins required for ciliogenesis have been shown to disrupt Hippo signaling in the cell when mutated. Several receptor tyrosine kinase signaling cascades, such as PDGFRα, FGFR, EGFR and IGFR, have also been linked to the primary cilium (Christensen *et al.*, 2012; Wheway, Nazlamova and Hancock, 2018).

1.2.5.3: Primary cilia and fluid flow

The requirement for primary cilia for preventing cyst formation in the kidney was first identified by Pazour and colleagues, while studying the *Orpk* (Oak Ridge Polycystic Kidney/*Tg737)* mouse (Pazour *et al.*, 2000).

This mouse carries a mutation in *Ift88*, and has shortened, malfunctioning primary cilia. It has since been shown that cilia in the kidney tubules are required for interpretation of fluid flow (Yoder, Hou and Guay-Woodford, 2002; Nauli *et al.*, 2003). Defective cilia in this tissue are proposed to cause kidney cysts to form which eventually lead to kidney failure, a condition known as polycystic kidney disease (Harris and Torres, 2009).

There are two major proposed mechanisms behind this pathology, which is known to occur in association with mutations in PKD1 (polycystin 1) and PKD2 (Wu *et al.*, 2000; Lantinga-van Leeuwen *et al.*, 2004). Proposals for their function include the formation of a mechanosensitive complex in the renal tubule primary cilia, or alternately, involvement in PCP signalling in the kidney (Goggolidou, 2014). However, recent studies have shown that whilst PCP is required for correct tubule patterning, defects in PCP are not themselves cystogenic, and mutations in the PKD proteins do not disrupt PCP Wnt signalling (Kunimoto *et al.*, 2017).

The initial break in LR symmetry in human, and mouse, embryos occurs through a leftwards fluid flow over a thumbprint-like depression in the surface of the embryo, a structure called the embryonic node (**Chapter 2**). Disrupting PKD2, but not PKD1 (Karcher *et al.*, 2005), also results in LR patterning defects (Pennekamp *et al.*, 2002). PKD1 is not expressed in the embryonic node, though a homologue, PKD1L1, is (Kamura *et al.*, 2011). Indeed, mutating PKD1L1 causes LR patterning defects in the mouse, fish and human (Vogel et al. 2010; Vetrini et al. 2016; Field et al. 2011; Grimes et al. 2016). Ciliary localisation of PKD1L1 and PKD2 is argued to be required for correct interpretation of nodal fluid flow, and thus is essential for correct LR patterning (Field et al. 2011; Grimes et al. 2016), although the molecular mechanism remains unclear (Shinohara *et al.*, 2012; Yoshiba *et al.*, 2012; Delling *et al.*, 2016).

1.2.6: Phenotypes resulting from defects in immotile cilia

Sensory ciliopathies result from defects in the sensory and signalling functions of primary cilia (Waters and Beales, 2011; Reiter and Leroux, 2017). They mostly appear to occur due to defects in the function of immotile cilia, though concurrent defects in motile cilia have been observed (Budny *et al.*, 2006; Moore *et al.*, 2006; Driscoll *et al.*, 2008). These ciliopathies are complex - there isn't a simple one gene: one phenotype Mendelian relationship. A gene can be implicated in multiple ciliopathies with no or very limited phenotypic overlap, whilst differing strength alleles of the same gene can cause distinct ciliopathies. Genetic modifiers, and mutations in different coding isoforms of the same gene, further complicate the picture (Fliegauf, Benzing and Omran, 2007).

The ciliopathies first began to be grouped together, with putative shared causal defects, in the early 2000s. This followed the identification of causative genes for a number of these phenotypically overlapping syndromes, such as nephronophthisis (Hildebrandt *et al.*, 1997; Saunier *et al.*, 1997; Mollet *et al.*, 2002; Otto *et al.*, 2002, 2003; Olbrich *et al.*, 2003) and Bardet-Biedl syndrome (Ansley *et al.*, 2003; Li *et al.*, 2004). The downstream protein products of these genes were found to localise to the cilium or the basal body in physiological conditions. Some of these ciliopathies have particular signs and symptoms (**Appendix 1**), such as the molar tooth sign associated with Joubert syndrome. However, the ciliopathies broadly show variable penetrance and expressivity, which may partly be a result of the varying expression of, and requirement for, ciliopathy proteins in different tissues and organ systems throughout the body.

Many of the pathological features of these syndromes have developmental origins. For example, many neurological defects are attributed to a failure in Hh signalling (Badano *et al.*, 2006), whilst

polycystin protein complexes are required in the cilia of the developing kidney to prevent the formation of fluid-filled cysts. Conditional knock-out animal models for these genes only serve to further highlight the diversity of roles the cilium is required to play. The *orpk* mouse was central to the discovery of the role for cilia in the developing kidney, but a conditional knock out of the same gene shows adult-onset kidney disease in combination with hyperphagia-induced obesity (Davenport *et al.*, 2007). All in all, the ciliopathies encompass a range of conditions which severely impact the lives of patients and their families.

1.2.7: *Pierce1* and immotile cilia

We suspected ciliary involvement in the *Pierce1*$^{-/-}$ mouse phenotype due to the LR patterning defects. The 2016 Sung et al paper (Sung *et al.*, 2016) reported scanning electron microscopy (SEM) images of the embryonic nodes of *Pierce1*$^{-/-}$ mice to appear grossly normal, with cilia of the correct length and physical appearance. This means that PIERCE1 is unlikely to be playing a significant role in the assembly and function of immotile cilia. However, as previously discussed, the initial break in LR symmetry in the mouse and human embryo occurs through leftwards fluid flow across the surface of the node, which is created by the rotation of posteriorly orientated motile cilia. The authors did not conduct live imaging experiments of motile cilia, limiting the conclusions that they could draw. In the next section of this introduction, I will discuss the ultrastructure and function of the motile cilium, before discussing the regulation of motile ciliogenesis and further evidence for a role for PIERCE1 in the motile cilium.

1.3: Motile cilia

1.3.1: Motile cilia: ultrastructure

Motile cilia are found in a variety of tissues in the body (**Fig. 1.4**), where they perform distinct functions. They share much of the overarching structure and assembly of immotile cilia with several key differences. As opposed to a 9+0 axonemal microtubule arrangement, motile cilia usually show a 9+2 arrangement, with the "+2" referring to a central pair of microtubules. Organisms with 9+2 motile cilia are present in all the eukaryotic phyla. Thus, it follows that the last eukaryotic common ancestor possessed a motile 9+2 cilium, and the variety of microtubular arrangements observed today have all arisen from this (Cavalier-Smith, 2002; Cavalier-Smith and Chao, 2003). The "+2" central pair of microtubules acts to regulate the planar beating of the motile cilium in the adult. In the mammalian embryonic node, beat pattern is rotational; the central pair apparatus would interfere with ciliary motility, and a 9+0 arrangement is observed.

The molecular mechanism of motion is conserved from humans to unicellular flagellates such as *C. reinhardtii*. Indeed, many key proteins for ciliary motility were identified first as modifiers of flagellar motility through

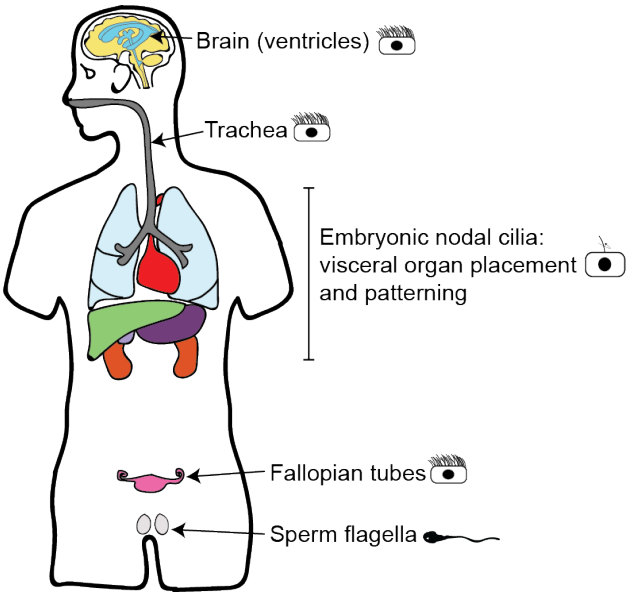


Figure 1.4: Diagram showing the location of tissues associated with motile cilia in the human.

screens in unicellular flagellates.

1.3.1.1: Outer and inner dynein arms

Motile cilia show inner and outer dynein arms anchored in an ATP-independent fashion on the outermost (A) microtubule of each pair. They effectively walk, in an ATP-dependent manner, along the B microtubule of the neighbouring doublet (**Fig. 1.5**). Dynein arms are minus-end directed motors (Sale and Satir, 1977), and all outer dynein arms (ODAs), as well as almost certainly all inner dynein arms (IDAs), can be seen as producers of unidirectional vectorial force. This means that for the cilium to beat effectively, one side of the axoneme contracts to produce the force behind the effective stroke. The other half then contracts, producing the force behind the recovery stroke (Satir and Christensen, 2007). The activation of the dynein arms must therefore be coordinated for effective beating and waveform production – if all arms were active at once, no net propulsion would occur (Satir and Christensen, 2007).

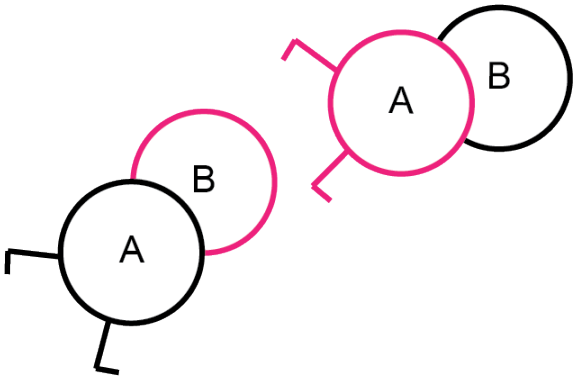


Figure 1.5: Diagram showing the relation between the inner and outer microtubules in each doublet. Microtubules highlighted in pink form an interacting pair, with the outer (A) microtubule walking along the neighbouring inner (B) microtubule.

Along the vast majority of the axoneme, each ODA is structurally, and usually biochemically, indistinguishable from its neighbours. These motors are biochemically complex - in vertebrates, each is composed of two distinct dynein ATPases, and a minimum of 16 different subunits (Goodenough and Heuser, 1982). Studies disrupting or biochemically removing the ODA lead to reduced ciliary beat frequency (CBF; Gibbons & Gibbons 1973; Brokaw & Kamiya 1987; Brokaw 1994), and beat frequency itself can be regulated by cAMP-dependent phosphorylation of axonemal

proteins, such as the dynein motors (Salathe, 2007; Wirschell *et al.*, 2011). This may hint at phosphorylation as a mechanism through which ODA activity, and thus CBF, can be regulated.

Understanding the role of IDA has presented a greater challenge to the field. Each IDA is composed of at least seven distinct dynein subunits, with their own individual composition and localisation (Bui *et al.*, 2012). Indeed, the IDAs were only truly characterised following biochemical fractionation of dynein components, in combination with electron microscopy analysis of defective axonemes (Satir, Heuser and Sale, 2014). Mutants lacking any of the IDAs show altered flagellar waveform (Brokaw and Kamiya, 1987), as opposed to the reduced beat frequency observed in ODA mutants.

The individual purpose of each IDA component is not yet fully understood, but there are aspects that are becoming clearer. For example, dynein I1 is one of the seven dyneins that make up the IDA and appears to play a regulatory role in axonemal bending in unicellular flagellates. Dynein I1 activity correlates with changes in microtubule sliding velocity (Kotani *et al.*, 2007), and as such it could alter axonemal bend amplitude during the recovery and effective strokes. Dynein I1 has been shown to be regulated by kinases and phosphatases in the axoneme (Wirschell *et al.*, 2011) that act on radial spoke proteins (Habermacher and Sale, 1997), which could provide a link between intracellular signalling and ciliary beat waveform (Salathe, 2007; Wirschell *et al.*, 2011).

Patients with abnormally moving or static motile cilia have also provided insight into the effects of dynein motors on ciliary motility. For example, it is known that patients with reduced numbers of ODAs in their motile cilia have a reduced CBF (De Iongh and Rutland, 1995). In contrast, a loss of IDAs is associated with defective wave form as opposed

to beat frequency, mirroring the results in unicellular model organisms described above.

1.3.1.2: Radial spokehead proteins and the central pair complex

The importance of radial spokehead proteins to flagellar and ciliary motility was discovered through high-throughput genetic screens using *C. reinhardtii* in the 1970s (Witman, Plummer and Sander, 1978). The radial spokehead complex (**Fig. 1.3**) is a highly conserved component of the 9+2 motile cilium or flagellum. It repeats every 96 nm along each outer microtubule doublet, either in pairs or triplets, depending on the organism. A stalk-like structure is anchored to the microtubule doublet itself, adjacent to the IDAs. The stalk projects towards the central pair, and interacts with the central pair complex (CPC) via its bulbous head (Warner and Satir, 1974; Goodenough and Heuser, 1985). This puts the radial spokehead complex in an ideal position to relay signals from the central pair to the outer microtubules and their associated dynein arm complexes.

The CPC refers to both the central pair of microtubules, and the assortment of interacting proteins surrounding them. The CPC is required for effective ciliary motility through regulation of dynein activation (Ruiz-Binder, Geimer and Melkonian, 2002) - many CPC proteins were initially identified through flagellar motility screens in *C. reinhardtii*. Although these proteins are well conserved in mammals, key differences exist. Whilst only one protein isoform has been identified for each CPC protein in *C. reinhardtii*, multiple isoforms are present in mammalian species and result from duplication events, differential splicing, alternative promoters and PTMs (Zhang *et al.*, 2002, 2004; Z. Zhang *et al.*, 2006). Moreover, recent discoveries point to tissue-specific roles for various CPC proteins in mammals, as well as potential extra-ciliary CPC protein functions

(Nagarkatti-Gude *et al.*, 2011). The importance of these is not yet fully understood.

The radial spokehead proteins interact with the CPC to harmonize doublet sliding with beat direction and propagation. Radial spoke defects lead to lack of coordination between the IDAs and radial spokeheads. Ciliary beating lacks planar directionality, and tracheal motile multicilia exhibit rotational beat forms (Daniels *et al.*, 2013; Kott *et al.*, 2013; Knowles *et al.*, 2014; Onoufriadis, Shoemark, Schmidts, *et al.*, 2014; Raidt *et al.*, 2014; Jeanson, Copin, Papon, Dastot-Le Moal, *et al.*, 2015).

1.3.1.3: Nexin-dynein regulatory complex

Neighbouring microtubule doublets are connected by nexin links. These were initially identified through electron microscopy of axonemal cross-sections in the 1960s (Gibbons, 1963). These links were proposed to restrict the sliding of the A microtubule relative to the neighbouring B microtubule (**Fig. 1.5**), and as such, convert microtubule sliding into axonemal bending (Satir, 1968).

Flagellar motility screens in the 1990s uncovered a class of genes that, when mutated, relieved the paralysis observed in unicellular flagellates associated with central pair and radial spokehead defects (Piperno *et al.*, 1994). These genes were initially said to code for “dynein regulatory complexes” due to the effects on motility observed in mutated organisms. High resolution cryo-electron tomography demonstrated that dynein regulatory complex mutants showed a lack of nexin links - dynein regulatory complex genes are those that encode the nexin link elements (Heuser *et al.*, 2009). Since this discovery, individual components of the nexin-dynein regulatory complex, such as DRC1, have been shown to play a role in human ciliary motility (Wirschell *et al.*, 2013).

1.3.2: Transcriptional regulation of ciliogenesis

1.3.2.1: RFX factors

Some of the first transcription factors to be associated with defects in ciliogenesis were members of the RFX transcription factor family. These transcription factors all encompass a highly conserved winged helix DNA binding domain (Gajiwala *et al.*, 2000), which recognises target sequences when the minor groove of the DNA contacts the wing subdomain. RFX factors bind to X-box DNA sequences - symmetrical promoter motifs, composed of an imperfect inverted repeat, with two half sites joined by a 1-3 nucleotide linker. RFX transcription factors contact this DNA sequence as dimers, with a wide variety of homo- and heterodimers identified for RFX factors 1-4.

Eight RFX factors are present or predicted in all vertebrates save fish, which have 9 RFX factors due to an early genome duplication event (Chu, Baillie and Chen, 2010). RFX factors are also present in *D. melanogaster*, yeast and *C. elegans*. Indeed, the *C. elegans* RFX factor homologue *daf-19* is exclusively expressed in the 60 immotile ciliated sensory neurons in the worm, and *daf-19* knock-out worms have sensory neurons with no cilia (Swoboda, Adler and Thomas, 2000). *daf-19* has also been shown to be required for the transcription of many ciliary genes, such as IFT subunits (Burghoorn *et al.*, 2012).

RFX factors can be subdivided into two main groups: those with conservation only in the DNA binding domain (RFX5-8), and those with additional conserved protein domains which show homology to *daf-19* (RFX1-4). Studies in knock-out animals have provided insight into the function of these more homologous proteins.

Mice lacking RFX1 die before 2.5 days post coitum (dpc) (Feng, Xu and Zuo, 2009), and RFX1 itself appears to have a range of ciliary and non-ciliary targets (Steimle *et al.*, 1995; Iwama *et al.*, 1999). *Rfx2* exhibits

preferential expression in ciliated tissues, including the kidney, the LR organiser and the testis, from early in development (Thisse *et al.*, 2001; Horvath, Kistler and Kistler, 2004; Wolfe *et al.*, 2004; Liu *et al.*, 2007; Ma and Jiang, 2007; Bisgrove *et al.*, 2012; Chung *et al.*, 2012). Knocking down *rfx2* in zebrafish (Yu *et al.*, 2008) leads to reduced numbers of primary cilia in the neural tube, with truncated cilia in Kupffer's vesicle (zebrafish LR organiser) that exhibit aberrant motility.

Rfx3 again shows preferential expression in tissues enriched for both motile and immotile cilia, such as the kidney and testis respectively (Bonnafe *et al.*, 2004; Baas *et al.*, 2006; El Zein *et al.*, 2009; Benadiba *et al.*, 2012). Cilia in knock-out mice show a variety of abnormalities - in some tissues, such as the embryonic node, they are shortened, in a similar fashion to *Rfx2*$^{-/-}$ mice. Cilia in the pancreas show a decrease both in ciliary number and length, and significant change is observed in the cellular composition of the islets of Langerhans (Ait-Lounis *et al.*, 2007). Mice lacking RFX3 show notable neuroanatomical defects – cilia in the subcommisural organ of the brain are overproduced, and the subcommisural organ itself is severely disorganised (Baas *et al.*, 2006).

Rfx4 is expressed in the testis and brain in mammals (Morotomi-Yano *et al.*, 2002; Blackshear *et al.*, 2003; Ait-Lounis *et al.*, 2007; Ashique *et al.*, 2009). Homozygous mutant mice die perinatally with severe neuroanatomical defects, including severe hydrocephalus and reduction or absence of the subcommisural organ. This is due to a failure to pattern the dorsal signalling centres of the brain (Blackshear *et al.*, 2003; D. Zhang *et al.*, 2006), which itself is thought to be a result of a loss of ciliary integrity and the ensuing effects on Hh signalling (Ashique *et al.*, 2009). RFX4 has also been shown to directly regulate the transcription of genes implicated in Joubert syndrome, such as *TMEM138* and *TMEM216* (Lee *et al.*, 2012). These proteins are known to be required for ciliogenesis.

Overall, the RFX factors play key yet overlapping roles in the transcriptional control of ciliogenesis. The factors act together in a tightly controlled manner to stimulate the upregulation of both core ciliary component proteins, such as the IFT complexes, and cilia-specific X-box-containing transcription factors. These transcription factors then amplify the ciliogenic transcription programme.

1.3.2.2: Foxj1: a master regulator of motile ciliogenesis

Foxj1 was first identified in 1993 through degenerate amplification of rat cDNA using PCR primers for the forkhead domain (Clevidence *et al.*, 1993). Its expression was found to be restricted to motile ciliated cells (Clevidence *et al.*, 1994; Hackett *et al.*, 1995; Murphy *et al.*, 1997) and FOXJ1 protein showed nuclear localisation with its mRNA levels peaking prior to the onset of ciliogenesis (Blatt *et al.*, 1999; Tichelaar *et al.*, 1999). These findings all led to the suggestion that FOXJ1 plays a transcriptional, regulatory role in motile ciliogenesis (Murphy *et al.*, 1997).

This was confirmed with the publication of two reports describing *Foxj1*$^{-/-}$ mice, which completely lack motile cilia. These mice show axonemal loss of motile cilia and die at birth or shortly after (Hackett *et al.*, 1995; Chen *et al.*, 1998). Isolated and cultured airway cells from these mice show multiple basal bodies present at the apical surface of the cell that had failed to dock and initiate axonemal extension at the apical membrane. This discovery helped to identify the stages of motile ciliogenesis that FOXJ1 impacts – it is not acting upstream of basal body replication or trafficking towards the apical cell membrane as these processes are unaffected, but is upstream of basal body docking and subsequent axonemal extension.

The role of FOXJ1 in regulating motile ciliogenesis transcriptional networks has since been shown to be conserved across vertebrates, and

further research has investigated the downstream components of those transcriptional networks (Choksi *et al.*, 2014).

1.3.2.3: Cell-type specific regulatory programmes

Cell-type specific motile cilia, for example nodal monocilia, appear to be controlled by a network of pro-ciliary transcription factors that then initiate the *Foxj1*/*Rfx* ciliary transcriptional programme (Choksi *et al.*, 2014).

1.3.2.3.1: Motile multicilia

The initial transcriptional change in future motile multiciliated cells (MCCs) in the respiratory epithelium occurs due to Notch signalling. Inhibition of Notch signalling promotes ciliation through the upregulation of a transcriptional programme that includes *GMNC* (Geminin Coiled-Coiled Containing) (Zhou *et al.*, 2015; Terré *et al.*, 2016). GMNC activates gene expression of the *MCIDAS* locus, which encodes MULTICILIN (Stubbs et al. 2012; Boon et al. 2014), a transcriptional cofactor. MULTICILIN upregulates the transcription of various ciliary regulatory genes, including *TAp73*, which was recently discovered to lie upstream of the *Rfx*/*Foxj1* regulatory cassette in MCCs (Marshall *et al.*, 2016; Nemajerova *et al.*, 2016).

Murine tracheal epithelial cells lacking TAp73 show basal body amplification, but lack the apical localisation observed in *Foxj1*$^{-/-}$ mice. TAp73 binds directly to the enhancers of many genes known to be associated with motile ciliary components and knocking out *TAp73* leads to a downregulation in the expression of these genes during differentiation of airway epithelial cells (Marshall *et al.*, 2016; Nemajerova *et al.*, 2016). The discovery of this regulatory role for TAp73 in 2016 (Marshall *et al.*, 2016; Nemajerova *et al.*, 2016) provided an important, if surprising, piece in the puzzle of the regulation of motile multiciliogenesis.

1.3.2.3.2: Motile monocilia

Several candidate genes upstream of the *Foxj1*/*Rfx* transcriptional cassette in the node have been identified, largely through genetic screens in the mouse and zebrafish. FGF (fibroblast growth factor) and Wnt signalling have been implicated in the upregulation of FOXJ1 signalling in the zebrafish (Neugebauer *et al.*, 2009; Caron, Xu and Lin, 2012) and *Xenopus* (Walentek *et al.*, 2012) LR organiser, though it is unclear how these signalling cascades interact with individual genes that have already been identified as key players in this process.

NOTO, a transcription factor, has been shown to regulate nodal motile cilia formation through its effects on posterior basal body localisation (along the antero-posterior axis). *Noto*$^{-/-}$ mice have abnormal cilia (shortened; basal bodies detached) in the node, but the node itself is also highly disorganised, and it has been difficult to ascertain whether NOTO is acting on ciliogenesis itself, or affecting ciliogenesis through its role in node morphogenesis (Beckers *et al.*, 2007; Alten *et al.*, 2012).

Noto is believed to lie upstream of *Foxj1*, and *Foxj1*, along with other downstream members of the motile ciliogenic cascade, is downregulated in embryos lacking NOTO. Replacing *Noto* with *Foxj1* restores the expression of motile ciliary components at the node, and indeed nodal ciliary motility itself (Alten *et al.*, 2012). Thus, *Noto*-dependent regulation of motile monociliogenesis is believed to be enacted through the direct effects on of NOTO on node morphology and ciliary antero-posterior patterning, as well as through NOTO-dependent activation of *Foxj1*.

Zic2 has been argued to cause shortened, aberrant nodal motile cilia when knocked out in the mouse, in combination with a downregulation in *Noto*, *Foxj1* and *Rfx2*/*Rfx3* expression (Barratt, Glanville-Jones and Arkell, 2014). In addition to this, *Zic2* has recently been associated with a

direct regulatory role in *Nodal* expression at the node, perhaps pointing to a broader role for *Zic2* in laterality determination (Dykes *et al.*, 2018).

TAp73$^{-/-}$ mice do not display situs defects (Marshall *et al.*, 2016; Nemajerova *et al.*, 2016), and *TAp73* itself is not specifically expressed at the node. Although the full picture remains unclear, there is sufficient evidence to point to a node-specific motile cilia transcriptional programme upstream of the *Foxj1*/*Rfx* cassette, with NOTO as a central regulatory factor.

1.3.2.4: Identification of Pierce1 in TAp73 and Foxj1 regulatory network

Isolated tracheal epithelial cells grown in air-liquid interface culture differentiate into a multiciliated tracheal epithelium (Gruenert, Finkbeiner and Widdicombe, 1995); *Pierce1* is upregulated during this differentiation process. When *TAp73* is knocked out in these cells, they fail to differentiate; *Pierce1* expression equally does not increase (Marshall *et al.*, 2016; Nemajerova *et al.*, 2016), implying that *Pierce1* lies downstream of *TAp73* in the motile multiciliogenesis regulatory network. *Pierce1* was also shown to be a downstream target of FOXJ1, another key regulator of motile ciliogenesis (Yu *et al.*, 2008) in both multi- and monociliated cells.

1.3.3: Motile cilia: function

Motile cilia play key roles in several tissues in the embryo and adult, either moving fluid over cells or moving cells through fluid. Motile monocilia create a leftwards fluid flow in the early embryo that is required for the initial break in LR symmetry (Norris, 2012). Multiciliated epithelia enable the transport of mucus in the respiratory system (Brooks and Wallingford, 2014) and cerebrospinal fluid (CSF) in the brain ependyma (Sakka, Coll and Chazal, 2011), whilst both the male and female reproductive systems make use of ciliary motility. The oviduct exhibits a motile multiciliated epithelium that assists the passage of the fertilised ovum towards the uterus (Ezzati *et al.*, 2014), whilst the sperm flagellum is in essence a modified motile cilium (Kumar and Singh, 2015). Many insights into the function of motile cilia in humans and other mammals can be gained from the distinct set of symptoms that form the hallmarks of PCD (Zariwala, Knowles and Omran, 2007; Lucas *et al.*, 2014; Raidt *et al.*, 2014), a recessive genetic disease of defective ciliary motility.

1.4: Primary ciliary dyskinesia: a genetic disorder

1.4.1: Kartagener's syndrome

Kartagener's syndrome refers to the clustering of chronic respiratory infections, male infertility and SIT, and was first described in 1933 by Manes Kartagener (Kartagener, 1933). The recognition that Kartagener's syndrome was caused by motile cilia dysfunction, and a broader understanding of how this linked to the occurrence of SIT in patients, led to a change in nomenclature – first to immotile cilia syndrome, and later to PCD (Lucas *et al.*, 2014). PCD refers to ciliary dyskinesia as the primary cause of pathology in patients. Not only that, but with greater understanding of the pathogenesis of the condition, it was recognised that only an estimated 40% of patients with PCD also exhibit SIT, as opposed to SIT being a pre-requisite for diagnosis. This is because immotile cilia at the node, and a lack of nodal fluid flow, leads to randomisation of visceral organ situs (Okada *et al.*, 1999).

1.4.2: Incidence and pathology

PCD is an autosomal recessive condition with an incidence of approximately 1:10,000 live births, although this varies between populations (Lucas *et al.*, 2017). As with all recessive genetic disorders, incidence increases in populations with a greater degree of consanguinity. Patients with PCD have aberrant ciliary motility, including a complete absence of ciliary motility.

If the embryonic nodal motile cilia are affected, LR patterning can be disrupted. Some PCD-causative genes do not affect the nodal cilia, as they encode structures that are only required for effective function of motile multicilia as opposed to monocilia. PCD caused by defects in radial spokehead proteins or the CPC is not associated with situs defects(Prevost *et al.*, 2014), as these aspects of ciliary ultrastructure are not typically present in the mammalian node. Current estimates state that

50% of patients with PCD exhibit physiological situs solitus (SS; **Chapter 2**), whilst approximately 40% exhibit SIT. The remaining patients show heterotaxy. Defects in LR patterning means that patients with PCD have an increased incidence of congenital heart disease compared to the general population (12% c.f. 1% (Shapiro *et al.*, 2014)).

The largest clinical burden for most patients results from repeated respiratory infections due to failure of mucociliary clearance. This can lead to chronic bronchiectasis, declining lung function, and can eventually require lung transplantation (Rubbo and Lucas, 2017). Management of PCD lung pathology is largely based on that of cystic fibrosis (CF; Schofield et al. 2018), although the two conditions have distinct aetiologies; clinical trials specifically evaluating treatment options in patients with PCD are beginning to occur, but none have concluded as of yet (Farley *et al.*, 2018).

Many male patients with PCD have asthenozoospermia, or immotile sperm, leading to infertility (Lucas *et al.*, 2014). With modern fertility interventions, this is often readily treated (Ortega *et al.*, 2011). It is important to note that not all patients with asthenozoospermia also have PCD, and vice versa. The structure of the sperm flagellum is not identical to that of the motile multicilia in the respiratory tract, thus some proteins are required in one structure and not the other. Equally, there are other causes of sperm immotility than solely flagellar dysfunction, for example metabolic deficiencies (Kumar and Singh, 2015). There is conflicting literature regarding the effect of PCD on female fertility (Blyth and Wellesley, 2008; Sivaramakrishnan, Cottee and Coon, 2015), and it is difficult to conclude a general effect or lack thereof without a larger, more powerful study.

1.4.3: Causative mutations

PCD is a heterogeneous genetic disorder. Unlike CF, which is caused by mutations in one particular gene (Cutting, 2015), PCD can be caused by mutations in many different genes, not all of which are known (Horani and Ferkol, 2018). At present, nearly 40 genes have been confirmed to cause PCD in patients, covering an estimated 70% of known patient population (Horani *et al.*, 2016). Known PCD-causative genes are summarised in **Appendix 2**.

If *Pierce1*$^{-/-}$ mice exhibit ciliary motility defects, it would be necessary to evaluate whether the human *Pierce1* orthologue (*C9ORF116*) is a likely PCD candidate gene. To aid in this evaluation, I will briefly discuss the phenotypes observed in mouse models of PCD.

1.5: Mouse models of primary ciliary dyskinesia

Mice are a long-studied mammalian model organism with a similar respiratory system to that of humans. In addition to this, mouse and human genetics have a large overlap in both genetic sequence and gene product function (Nguyen and Xu, 2008). The advantages of using the mouse as a model system include the existence of inbred strains that provide a solid foundation for targeted genetic manipulation due to the lack of genetic variation between individual mice of a particular strain.

However, the genetic alteration of many genes that cause PCD in humans lead to high pre-wean lethality in the mouse (**Appendix 3**). This is thought to be due to genetic modifiers in particular inbred strains that alter ventricular anatomy, leading to a high incidence of hydrocephalus (Lee, 2013). As well as this, a significant proportion of embryonic and pre-wean lethality results from heterotaxy, particularly severe congenital heart defects that are non-viable.

The nearest that we have come to a mouse model of PCD is an adult inducible *Dnaic2*$^{-/-}$ mouse. Although obviously lacking any embryonic phenotype, this mouse exhibits sinusitis and male infertility (Ostrowski *et al.*, 2010). The *iv* mouse also provides a model of PCD, though is associated with a significant embryonic lethality rate due to heterotaxy (Lucas *et al.*, 2012). Multiple lines have been created that show some features of PCD, but thorough and consistent phenotyping of ciliary motility is lacking (**Appendices 3 & 4**).

1.5.1: Strain differences: an important consideration

There has been no overarching analysis of the effect of mouse inbred strains on ciliary motility. A study by Goodson et al (Goodson *et al.*, 2011) used computer-assisted sperm analysis to assess the motility of sperm from different strains of mice, and found significant differences in flagellar beat frequency. This is worth noting when evaluating CBF data

across mouse strains. The effect of strain differences on hydrocephalus-associated lethality should also be considered (Lee, 2013). Lee et al provided substantial evidence for genetic modifiers altering the penetrance of hydrocephalus in mouse. The increase in susceptibility to hydrocephalus is thought to be due to anatomical changes in the ventricles of particular inbred strains, notably C57BL/6 (Lee, 2013; Finn, Evans and Lee, 2014), as opposed to a reduction in CBF of the ependymal motile cilia. The B6 strain is the most commonly used inbred strain in research due to its physical activity levels, intelligence, and frequent breeding (Bryant, 2011).

1.6: Aims of project

The initial aims of this project focused on the causative mechanism underlying LR patterning defects in *Pierce1*$^{-/-}$ mice, through an examination of flow and ciliary motility in the early embryo. An overall investigation of ciliary motility in the *Pierce1*$^{-/-}$ mouse was also an aim of this thesis, through studies of the motile cilia in the tracheal epithelium, and the motility of the sperm flagellum.

I hypothesised that dysfunction of the embryonic nodal motile cilia caused the left-right patterning defects present in Pierce1-/- mice. To investigate this further, I aimed to analyse flow at the embryonic node with particle image velocimetry. I also aimed to evaluate the motility of nodal cilia through live imaging studies, to determine whether any difference in motility could account for the hypothesised difference in or absence of flow. The results from this work are presented in Chapter 2.

To investigate the motility of cilia in other tissues, two major areas of research were planned. I aimed to first evaluate motility of cilia in the respiratory epithelium, again through live imaging. I also aimed to look for ultrastructural defects in the motile cilium that may be underlying motility defects using transmission electron microscopy. I designed experiments to enable analysis of sperm flagellar motility, as well as a repetition of the transmission electron microscopy study investigating ultrastructural defects in the sperm flagellum. The results from these avenues of enquiry are presented in Chapter 3.

In order to more thoroughly evaluate potential subcellular functions of PIERCE1, I planned to investigate the expression of this gene, with the aim of investigating whether its expression tallied with a role in ciliary motility. I also aimed to carry out in silico analyses of the PIERCE1 coding sequence to determine whether any reliable prediction of protein structure or function could be made. A yeast 2-hybrid study was also planned, with

the aim of identifying putative interaction partners of PIERCE1. Results from studies into the function of the PIERCE1 protein are presented in Chapter 4.

On the whole, this body of work should serve to further our understanding first of all, of the causative defect underlying the LR patterning defect observed in this mouse line, and may broaden our understanding of genes implicated in the occurrence of LR patterning defects in humans. A deeper analysis of the impact of *Pierce1* loss on ciliary motility will aid us in our understanding the protein network required for ciliary motility in different tissues. Of particular note is the potential for this work to identify a candidate gene for PCD.

2: The role of PIERCE1 in embryonic ciliary motility

The initial defects present in the *Pierce1*$^{-/-}$ mice, combined with the LR patterning defects including SIT and cardiac abnormalities described by Sung et al (Sung *et al.*, 2016), led me to hypothesise that ciliary motility in the node was defective in *Pierce1*$^{-/-}$ embryos. Therefore, an investigation of nodal ciliary motility was a key aim of this thesis. Motile monocilia are found at the embryonic node, and drive a leftwards fluid flow that breaks LR symmetry in the early embryo. This occurs at 8.0-8.5 dpc in the mouse, and between 21 and 28 days of gestation in the human. As such, I aimed to not only investigate the motility of the nodal cilia through live imaging, but also to examine the resultant flow for any defects that may cause later abnormalities of LR organ patterning.

In this chapter I will first review our understanding of LR patterning, before discussing the rationale behind experimental analysis of *Pierce1*$^{-/-}$ nodal ciliary motility and then presenting the results of my investigations.

2.1: Introduction

2.1.1: Fluid flow at the embryonic node

Manes Kartagener first noted the clustering of SIT (**Fig. 2.1**), male infertility and chronic bronchiectasis in several patients in the 1930s (Kartagener, 1933). This syndrome went on to bear his name, but was poorly understood until the 1970s, when Afzelius discovered that the respiratory pathology and male infertility in Kartagener's syndrome are the result of ciliary and flagellar immotility in the respiratory tract and sperm flagellum respectively (Afzelius, 1976). It followed that a ciliary motility defect during embryogenesis was likely underlying the LR patterning defect.

The mechanism underlying the initial break in LR symmetry was revealed in a seminal paper by Nonaka et al (Nonaka *et al.*, 1998b) that first described the role of motile cilia in LR patterning. Using live imaging of the embryonic mouse node, they clearly showed the presence of rotating monocilia in the embryo, which could drive ectopically applied fluorescent particles towards the left hand side of the node. Crucially, they showed a lack of nodal monocilia, and an absence of leftwards fluid flow in the node of the *Kif3b*$^{-/-}$ mouse (Nonaka *et al.*, 1998a). Similar results were collected for *Kif3a*$^{-/-}$ mice (Takeda *et al.*, 1999).

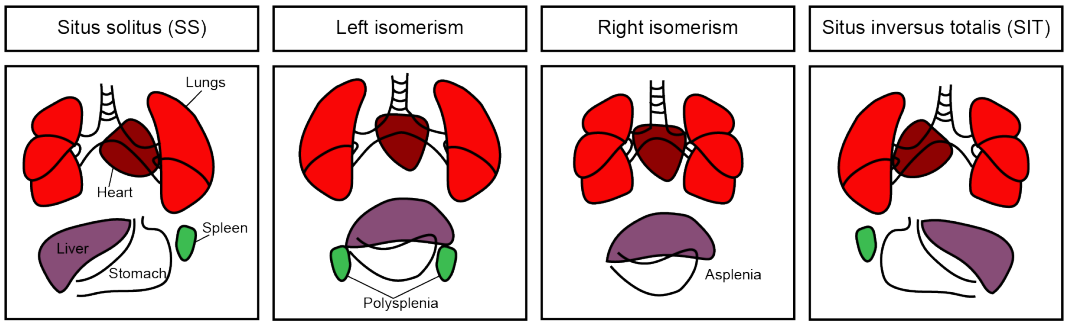


Figure 2.1: Diagrammatic representation of situs presentations.

The *iv/iv* mouse, a seminal model of defective LR patterning, was first described by Hummel and Chapman in the 1950s (Layton and Hummel, 1976). The *iv* allele encodes a missense mutation in the conserved AAA2 domain of *Dnahc11* (Supp *et al.*, 1997). Approximately 50% of live offspring showed SIT and the line is associated with a noted pre-wean lethality due to an increased incidence of congenital heart defects (Layton and Hummel, 1976). *Inv* mice were created in the early 1990s through a transgenic insertion event in the *inversin* gene, resulting in a 47kb deletion that removed exons 3 to 11 (Morgan *et al.*, 1998). Homozygous embryos demonstrated 90% penetrant SIT along with a range of other phenotypes (Yokoyama *et al.*, 1993). Okada et al (Okada *et al.*, 1999) demonstrated that abnormal nodal fluid flow precedes LR patterning in both *iv* and *inv* mice, causing their respective characteristic LR patterning defects. Finally, Nonaka et al (Nonaka *et al.*, 2002) demonstrated that artificially applying flow to wild-type and *iv/iv* embryos could reverse LR patterning. Motile cilia, and the fluid flow that they produce, were thereby established to be central to physiological LR embryonic patterning.

2.1.2: How is fluid flow translated into a downstream genetic signal?

Initial discussion concerning the mechanism behind fluid sensation in the node eventually settled on two main possibilities: chemosensation of a morphogen gradient, or mechanosensation. Immotile primary cilia on the crown cells around the embryonic node were recognised as central to flow sensation (McGrath *et al.*, 2003), and all resulting hypotheses have converged on models requiring both motile monocilia and immotile sensory monocilia. Motile cilia in the pit of the node produce flow, whilst immotile cilia surrounding the node are necessary to respond to this flow, and translate it into a genetic signal that differentiates left from right.

Tanaka et al (Tanaka, Okada and Hirokawa, 2005) proposed a modified form of the morphogen gradient hypothesis in which FGF-induced vesicles in the node carry SHH and retinoic acid (RA). They proposed that these vesicles would burst on the far side of the node in a cilia-dependent manner, leading to asymmetric signalling. Fluid dynamic calculations demonstrate that the surface tension that would be needed to form and maintain a vesicle in the low Reynolds' number environment of the node, where viscosity is an overriding force, would make this hypothesis unlikely. This is because the tension required would be so high that the vesicle would not be able to burst upon impact when travelling at the described velocities, unless specific docking mechanisms for vesicles that enable bursting exist (Cartwright, Piro and Tuval, 2004; Cartwright *et al.*, 2008).

The mechanosensation hypothesis posits that immotile cilia around the node sense the force of the fluid flow itself (Norris, 2012). Two polycystin proteins suggested to act as mechanosensors elsewhere in the body have been implicated. In the kidney, PKD2 (polycystin 2) is argued to form a mechanosensitive complex with PKD1 to ensure correctly regulated cell growth and prevent the formation of kidney cysts (Nauli *et al.*, 2003). Failure of this complex leads to polycystic kidney disease. *PKD2* mutations account for approximately 15% of autosomal dominant polycystic kidney disease cases. A requirement for PKD2 has also been demonstrated for correct LR patterning in the mouse (Pennekamp *et al.*, 2002). Indeed, it localises to primary cilia on the crown cells around the node, adding further weight to a putative role in fluid-flow sensation (Kamura *et al.*, 2011; Nakamura, Hamada, *et al.*, 2012; Yoshiba *et al.*, 2012).

Pkd1 mutations do not lead to situs abnormalities in the mouse (Karcher *et al.*, 2005), and PKD1 does not localise to the nodal cilium (Karcher *et al.*, 2005). PKD2 and PKD1 are both required in the putative

mechanosensitive complex in the kidney; if PKD1 is not present in the node and not essential for correct LR patterning, it follows that PKD2 may be operating with another partner protein. Another polycystin protein, PKD1L1, was discovered to cause LR patterning defects when mutated in mouse (Vogel *et al.*, 2010; Field *et al.*, 2011) and medaka fish (Kamura *et al.*, 2011) models, and was also shown to physically interact with PKD2; the presence of functional PKD1L1-PKD2 complex in the cilium has been argued to be a requirement for LR patterning (Grimes et al. 2016).

Cellular calcium signalling has been associated with the immediate downstream translation of nodal flow sensation. Intraciliary calcium oscillations were described at the LRO in zebrafish (Yuan *et al.*, 2015). These oscillations were dependent on fluid flow and the presence of PKD2 in the primary cilium. In this model, the PKD1L1-PKD2 complex would act as a mechanosensitive calcium channel. The initial influx of calcium into the cilium would induce Ca^{2+} signalling in the cytosol, leading to changes in genetic regulation.

This work was supported by publications from distinct groups arguing that PKD2 (Yoshiba *et al.*, 2012) and PKD1L1 (Grimes et al. 2016) are required for the formation of a mechanosensitive calcium channel complex in nodal crown cilia. However, recent data from the Clapham group challenged this, failing to show mechanically-induced calcium signalling in the primary cilia of cultured and primary tissues (Delling *et al.*, 2016). Evidence in this field is contradictory and difficult to interpret; the exact mechanism of translation of fluid flow into downstream genetic signalling is yet to be fully elucidated.

Lefty2, *Nodal* and *Pitx2* comprise a core, highly conserved, genetic motif (**Fig. 2.2**), the expression of which results from the initial break in LR symmetry provided by fluid flow at the node (Nakamura, Hamada, *et al.*, 2012). Predating the discovery of motile cilia at the embryonic node, the

1990s saw the identification of highly evolutionarily conserved genes with differential expression patterns on the left and right hand sides of the early embryo. *Dand5*/*Cerl2* is the earliest asymmetric genetic product (Marques *et al.*, 2004) - initial symmetric expression of *Cerl2* mRNA on both sides of the node is followed by flow-induced decay on the left-hand side of the node, such that there is a greater concentration of mRNA on the right than the left hand side of the node.

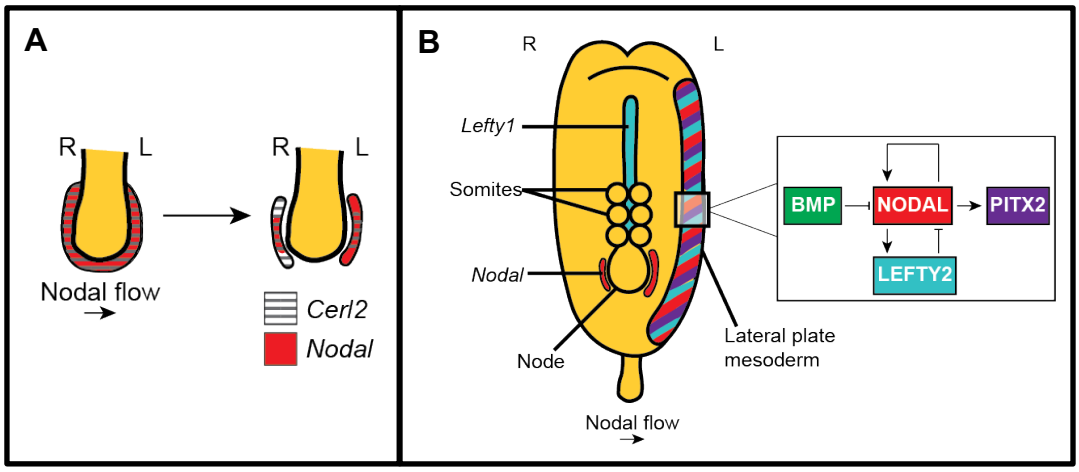


Figure 2.2: A (left): Diagram representing initial changes in gene expression following onset of nodal flow. B (right): diagram showing expression pattern of *Nodal*/*Pitx2*/*Lefty* cascade in the mouse embryo.

Cerl2 mRNA decay is a post-transcriptional event, dependent on 3' untranslated region sequence (Nakamura, Saito, *et al.*, 2012). Fluid flow initiates *Cerl2* degradation. This relieves CERL2-inhibition of a WNT3-dependent positive feedback loop, and increases the amount of WNT3 on the left-hand side of the node. WNT3 in turn promotes CERL2 degradation, and thus a small initial change in *Cerl2* mRNA levels is converted to a robust and stable asymmetry (Nakamura, Saito, *et al.*, 2012). This means that fluid flow at the node is only required to be directional and present for a small period of time. Indeed, studies using methyl cellulose to slow flow demonstrate that flow can in fact be very weak and/or short-lived, whilst still leading to correct LR patterning (Shinohara *et al.*, 2012). Mathematical modelling has shown that this

system should be resistant to noise, and able to robustly amplify small changes in degradation rates (Nakamura, Saito, *et al.*, 2012).

CERL2 represses NODAL, a TGF-β superfamily member. *Cerl2* mRNA degradation thus leads to upregulation of NODAL activity on the left-hand side of the node, as evidenced by an asymmetry of phosphorylated SMAD2 (Brennan, Norris and Robertson, 2002; Kawasumi *et al.*, 2011). GDF-1 (another TGF-β family member) is thought to heterodimerise with NODAL, and this heterodimer signals to cells in the LPM, where it activates *Nodal* expression in that location (Tanaka *et al.*, 2007; Viotti *et al.*, 2012). A role has also been proposed for an endodermal calcium signal in this process (Saund *et al.*, 2012).

Once activated in the left LPM, NODAL stimulates its own expression via an NODAL-responsive enhancer element, termed an asymmetric enhancer due to the necessity of this enhancer for asymmetric *Nodal* expression (Adachi *et al.*, 1999; Norris and Robertson, 1999). NODAL also activates *Lefty2* expression via a similar enhancer. LEFTY2 is a Nodal antagonist with a high diffusion velocity; it acts to restrict *Nodal* expression to the left LPM, whilst the NODAL positive feedback loop strengthens the expression of NODAL itself. This ensures robust isolation of *Nodal* in the left LPM (Nakamura *et al.*, 2006).

Lefty1 is induced by NODAL protein that has diffused from its expression domain at the left LPM. *Lefty1* is expressed in the midline of the embryo, as opposed to the left LPM, and prevents expression of *Lefty2* and *Nodal* on the right hand side of the midline (Meno *et al.*, 1998). NODAL is a potent activator of its own transcription; LEFTY2 to the anterior and BMP1 to the posterior provide reinforcement to the LEFTY1 midline barrier and restrict *Nodal* expression to the left-hand lateral plate mesoderm (LPM; Shiratori & Hamada 2014).

PITX2 is a transcription factor that acts in a cell-autonomous fashion as the key downstream effector of NODAL, and is required for correct LR patterning. Distinct isoforms of PITX2 play different roles at distinct points in development, and in different organ systems (Schweickert *et al.*, 2000; Yu *et al.*, 2001). Overall, PITX2 coordinates the expression of genes driving cell proliferation and migration, leading to the LR asymmetric organ position and patterning that is central to the formation of functioning visceral organ systems (Grimes and Burdine, 2017).

2.1.3: *Pierce1* and left-right patterning

A key question remaining after the publication by Sung et al (Sung *et al.*, 2016) was the cause of the LR patterning defects present in *Pierce1*$^{-/-}$ mice. As nodal flow is a key step in LR symmetry breaking in the mouse, I wanted to investigate whether *Pierce1*$^{-/-}$ mice demonstrated effective leftwards nodal flow; a lack thereof could explain their situs defects. I also aimed to conduct live imaging of the nodal cilia themselves, in order to evaluate their motility.

In addition to the ciliary motility analysis, I planned further studies into the embryonic phenotype in this line. These would serve to test the similarities between our *Pierce1*-null line and that developed by Sung et al (Sung *et al.*, 2016). These studies included SEM analysis of the embryonic nodal cilia; in situ hybridization staining for LR asymmetrically expressed genes; and gross phenotyping of visceral organ situs.

2.2: Results

2.2.1: *Pierce1*$^{-/-}$ embryos show a lack of organised leftwards nodal flow.

To investigate the presence of nodal flow in *Pierce1*$^{-/-}$ embryos, I used particle image velocimetry (PIV; Shinohara et al. 2012; Nonaka et al. 1998a). This technique assesses the movement of fluorescent beads between frames of a video. By calculating speed of the beads by analysing distance of bead movement between frames, and the time interval between frames, I could create a 2D vector map summarising average speed and directionality of flow across the imaging plane.

I mounted individual embryos with their nodes facing upwards in a mixture of fluorescent beads and media. I used a VivaTome imaging system, which is pseudo-confocal, to video flow of these fluorescent beads at the node, as this enabled me to subtract out-of-focus fluorescent signal. I processed the resulting data sequences in ImageJ and used the PIVlab (Thielicke and Stamhuis, 2014) plugin in MatLab to track the movement of each fluorescent bead frame-to-frame. This enabled the assessment of flow velocity across the embryonic node. Heat maps of mean velocity magnitude were created and scaled appropriately to the flow velocities observed.

In wild-type embryos, the beads moved across the surface of the node due to leftwards flow created by the rotation of posteriorly oriented cilia. Velocity magnitude heat maps for nodal flow in *Pierce1*$^{+/+}$ (n=2) and *Pierce1*$^{+/-}$ (n=2) embryos are presented in **Fig. 2.3**. Brightfield images of each videoed node taken at 40X magnification are shown in panels labelled (**i**), demonstrating that nodes were not damaged. Panels showing unprocessed images (**ii**) show fluorescent signal present in the node in the first frame of the video for that embryo. In processed panels (**iii**), the fluorescence has been binarised, with an erosion filter applied to reduce

artefactual noise and highlight bead signal. Velocity magnitude heat maps themselves are presented in panels labelled (**iv**).

As expected, in wild-type (**Fig. 2.3: A, B**) and heterozyote embryos (**Fig. 2.3: C, D**) strong and organized leftwards nodal flow was consistently observed. Velocity magnitude heat maps for nodal flow in *Pierce1*$^{-/-}$ embryos (n=8) are presented in **Fig. 2.5**. Results from all *Pierce1*$^{-/-}$ nodes that passed quality control parameters (**Chapter 2.3.1, 2.3.2**) have been included to accurately represent the data. Brightfield, processed and unprocessed image panels (**Fig. 2.2 A-H, i-iii**) show no distinction from wild-type and heterozygous embryos. The nodes are not damaged and fluorescent signal is detected and processed in the same manner as their wild-type and heterozygous counterparts.

However, when particle velocity tracking is applied, a range of nodal flow phenotypes were detected. In two embryos (**Fig. 2.5; A: iv, B:iv; Fig. 2.6**), some leftwards flow was detected, although this is not as strong as that observed in wild-type (**Fig. 2.3; A: iv, B:iv**) and heterozygous (**Fig. 2.3; C: iv, D:iv**) nodes. In all other *Pierce1*$^{-/-}$ videos analysed, flow was not leftwards. Patches of high velocity flow were observed in some nodes (**Fig. 2.5; D: iv, E: iv; Fig. 2.6**), but did not show leftwards directionality. Other nodes showed no net directionality (**Fig. 2.5; G: iv, H: iv; Fig. 2.7**). Again, enlarged PIV plots are presented to aid visualisation of the change in flow directionality as shown by black arrows on the plot (**Fig. 2.6, Fig. 2.7**). Overall, nodal flow was significantly disrupted in the *Pierce1*$^{-/-}$ embryo population. I hypothesised that this could explain the LR patterning defects observed in this line.

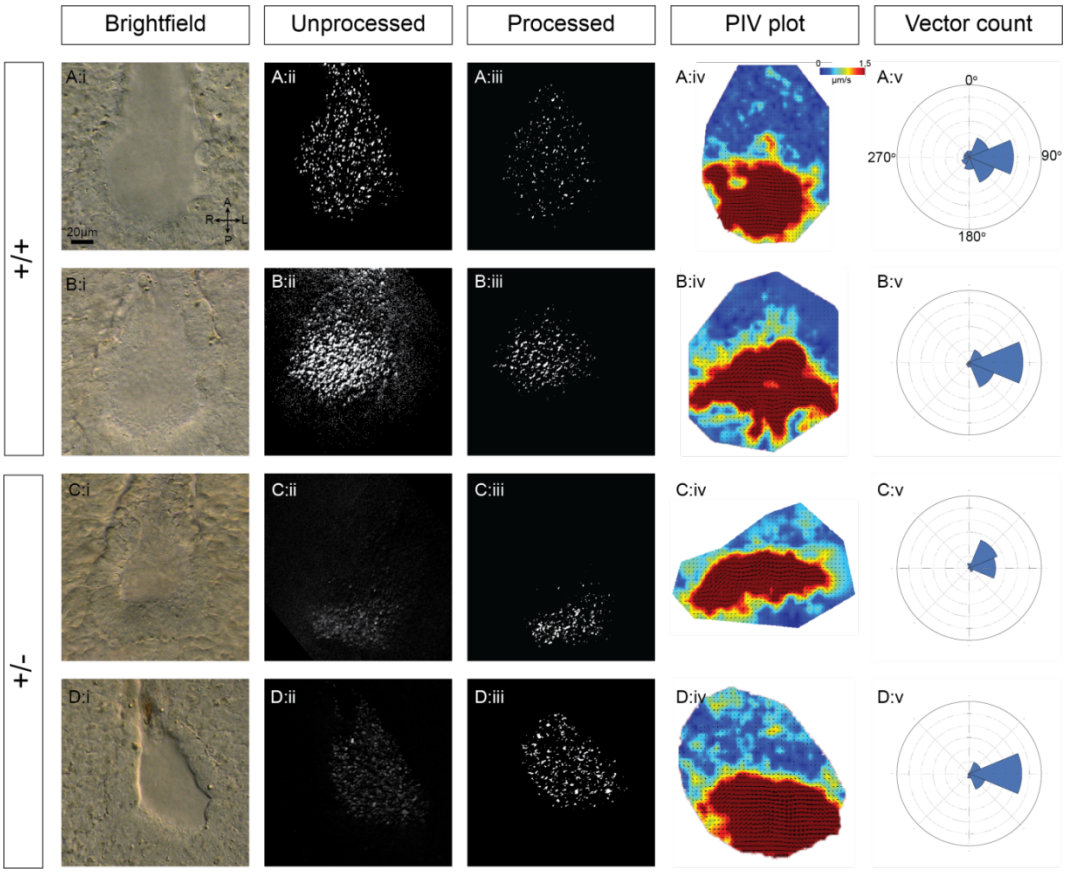


Figure 2.3: Wild-type and heterozygous embryonic nodes exhibit leftwards fluid flow.
Particle image velocimetry (PIV) plots of *Pierce1*$^{+/+}$ (A, B) and *Pierce1*$^{+/-}$ (C, D) embryonic nodes at 8.0 dpc. Panels show (i) a brightfield image of the node (scale bar shows 20 μm), (ii) an unprocessed image showing fluorescent beads in the node, (iii) a processed image with beads binarised and dilated, (iv) a mean velocity magnitude plot, and (v) a rose plot showing vector counts in direction segments. All embryos show leftwards flow. Velocity is colour coded; dark red refers to high velocity (1.5 μm/s), whilst dark blue refers to low velocity (0 μm/s); a scale bar is shown in A:iv. Data collected over 33 experimental data collection sessions. n= 8+/+ embryos (two shown); n=16 +/- embryos (two shown).

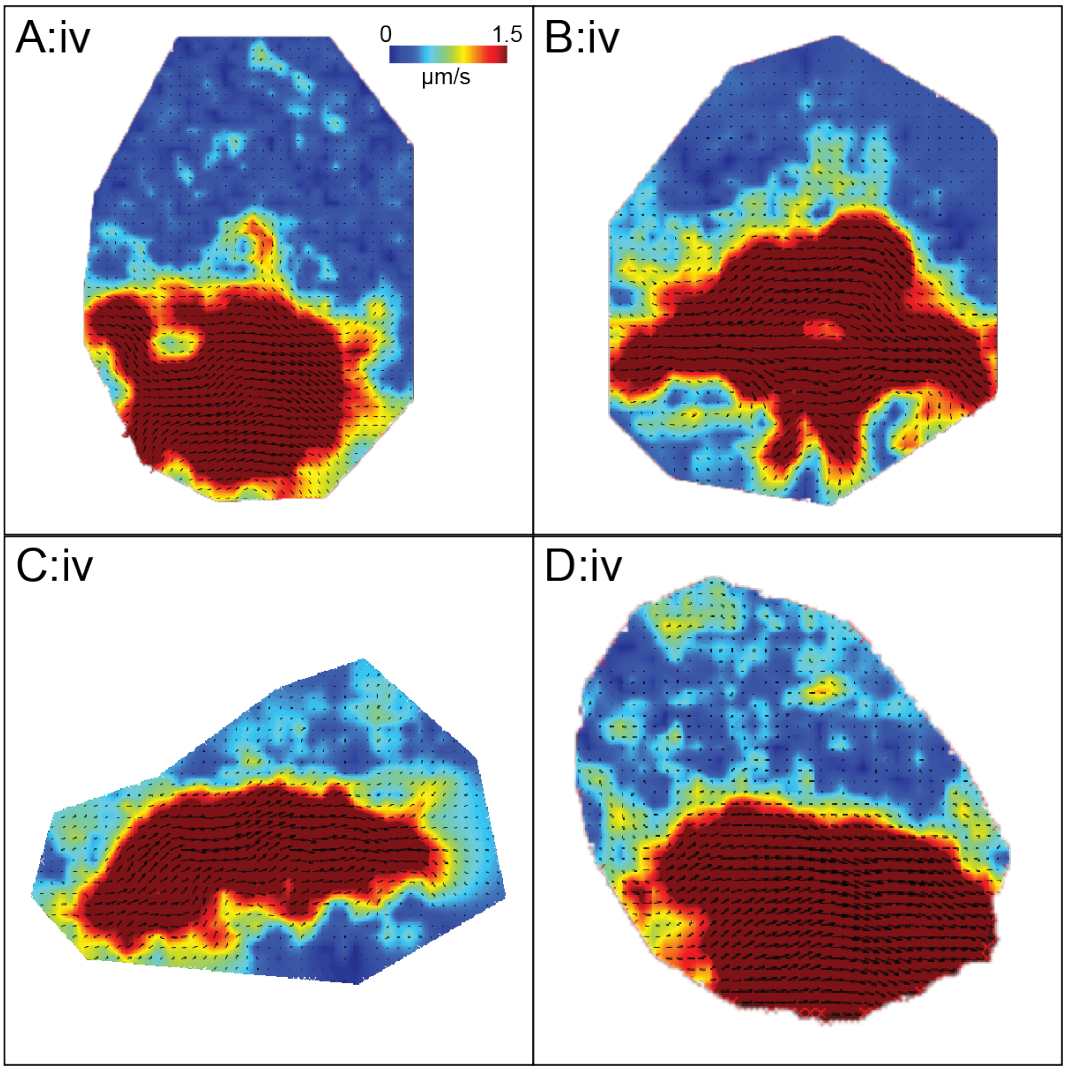


Figure 2.4: Wild-type and heterozygous embryonic nodes exhibit leftwards fluid flow.
Enlarged particle image velocimetry (PIV) plots of *Pierce1*$^{+/+}$ (A:iv, B:iv) and *Pierce1*$^{+/-}$ (C:iv, D:iv) embryonic nodes at 8.0 dpc. All embryos show leftwards flow. Velocity is colour coded; dark red refers to high velocity (1.5 µm/s), whilst dark blue refers to low velocity (0 µm/s); a scale bar is shown in A:iv. Directionality of vectors is shown by black arrows. Data collected over 33 experimental data collection sessions.

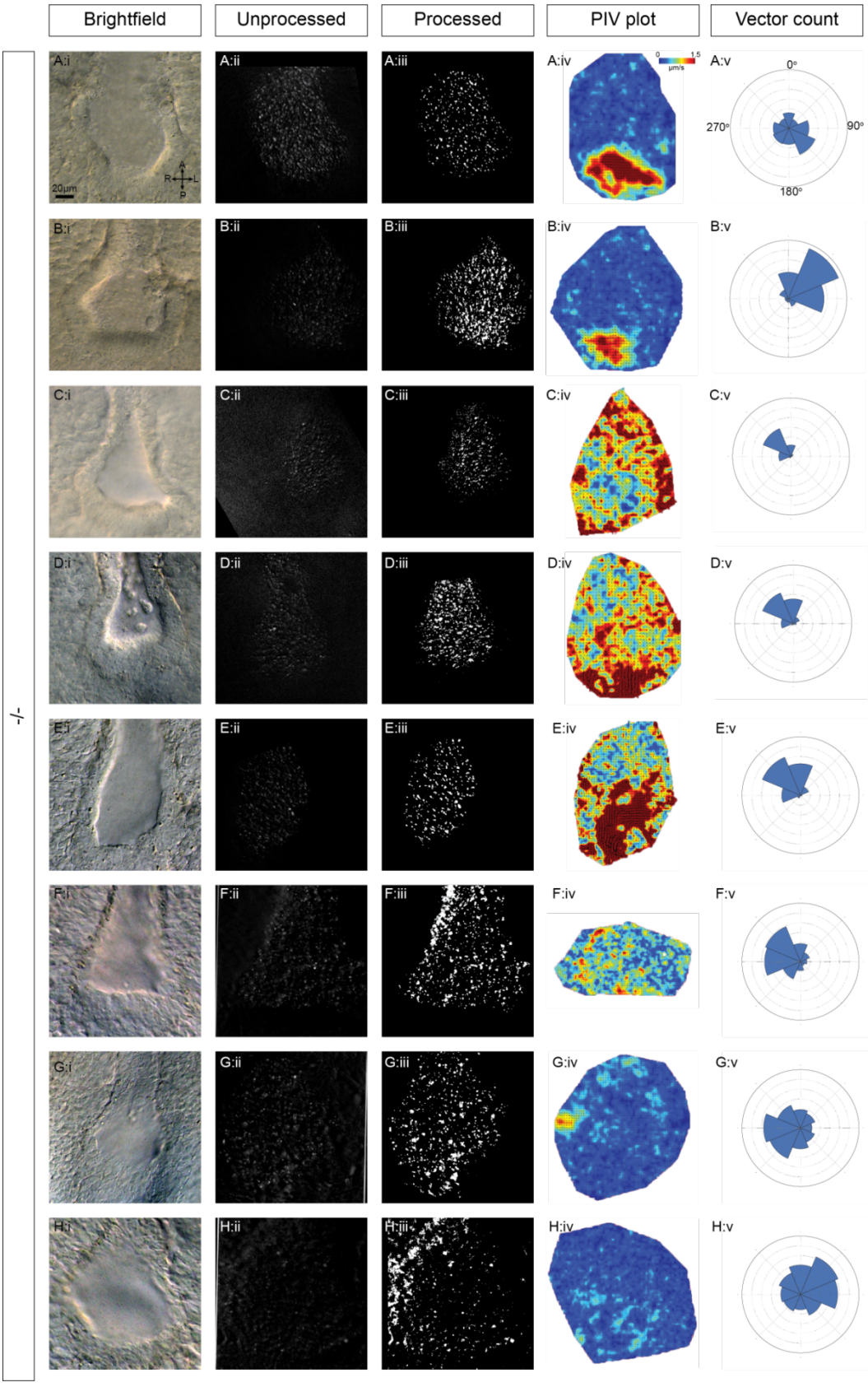

Brightfield
Unprocessed
Processed
PIV plot
Vector count
-/-
A:i
A:ii
A:iii
A:iv
A:v
20µm
A
R
L
P
0
1.5
µm/s
0°
90°
180°
270°
B:i
B:ii
B:iii
B:iv
B:v
C:i
C:ii
C:iii
C:iv
C:v
D:i
D:ii
D:iii
D:iv
D:v
E:i
E:ii
E:iii
E:iv
E:v
F:i
F:ii
F:iii
F:iv
F:v
G:i
G:ii
G:iii
G:iv
G:v
H:i
H:ii
H:iii
H:iv
H:v

Figure 2.5 (p52): *Pierce1*$^{-/-}$ embryonic nodes showed disrupted nodal flow.
Particle image velocimetry plots of *Pierce1*$^{-/-}$ embryonic nodes (n=8) at 8.0 dpc. Images are shown as described in **Fig. 2.3**. Nodes A-B show leftwards flow, nodes C-F show disordered flow and nodes G-H show no overall directionality of flow. Data collected over 33 experimental data collection sessions.

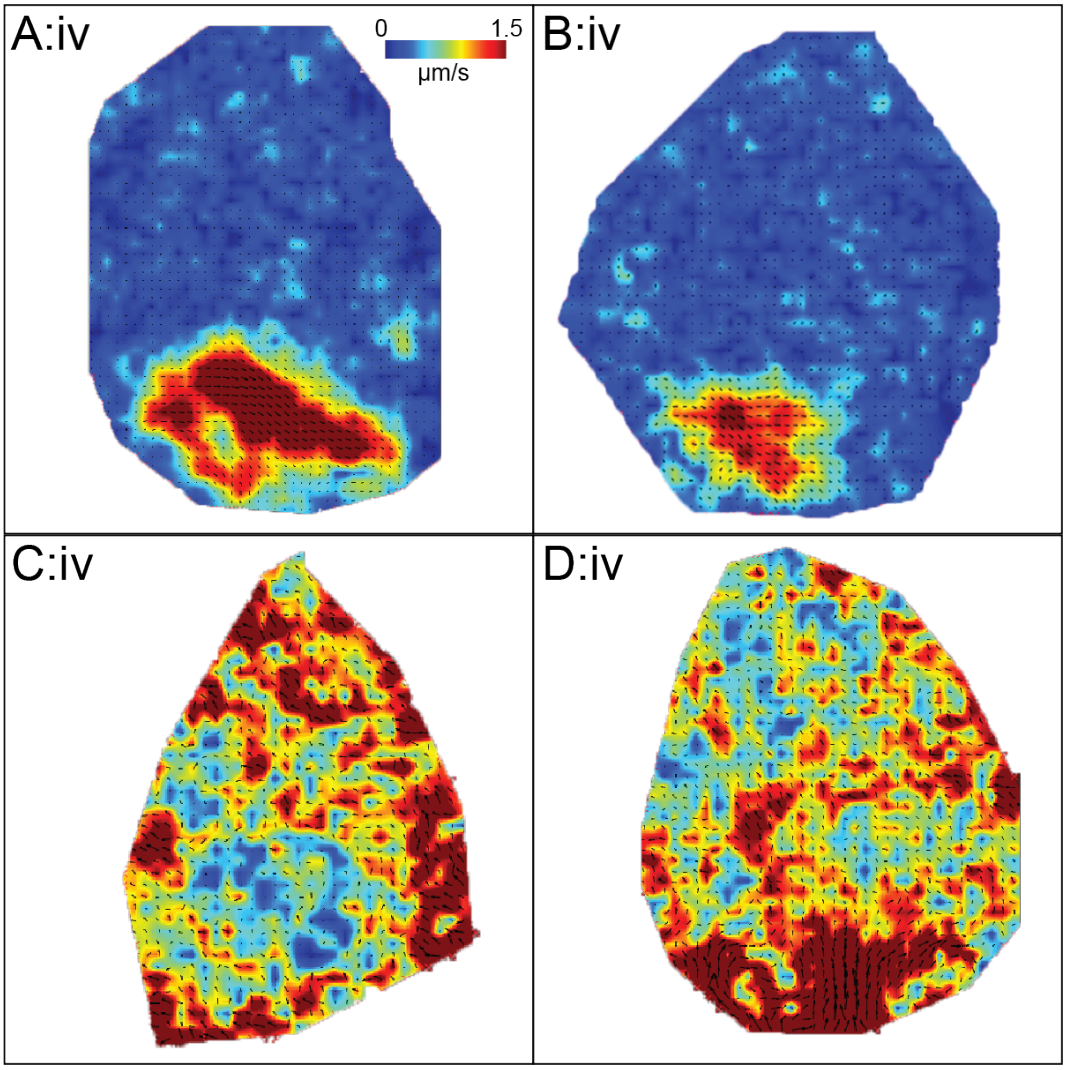


Figure 2.6: *Pierce1*$^{-/-}$ embryonic nodes showed disrupted nodal flow.
Enlarged particle image velocimetry (PIV) plots of *Pierce1*$^{-/-}$ embryonic nodes at 8.0 dpc. Nodes A:iv-B:iv show leftwards flow, nodes C:iv-D:iv show disordered flow. Velocity is colour coded; dark red refers to high velocity (1.5 μm/s), whilst dark blue refers to low velocity (0 μm/s); a scale bar is shown in A:iv. Directionality of vectors is shown by black arrows. Data collected over 33 experimental data collection sessions.

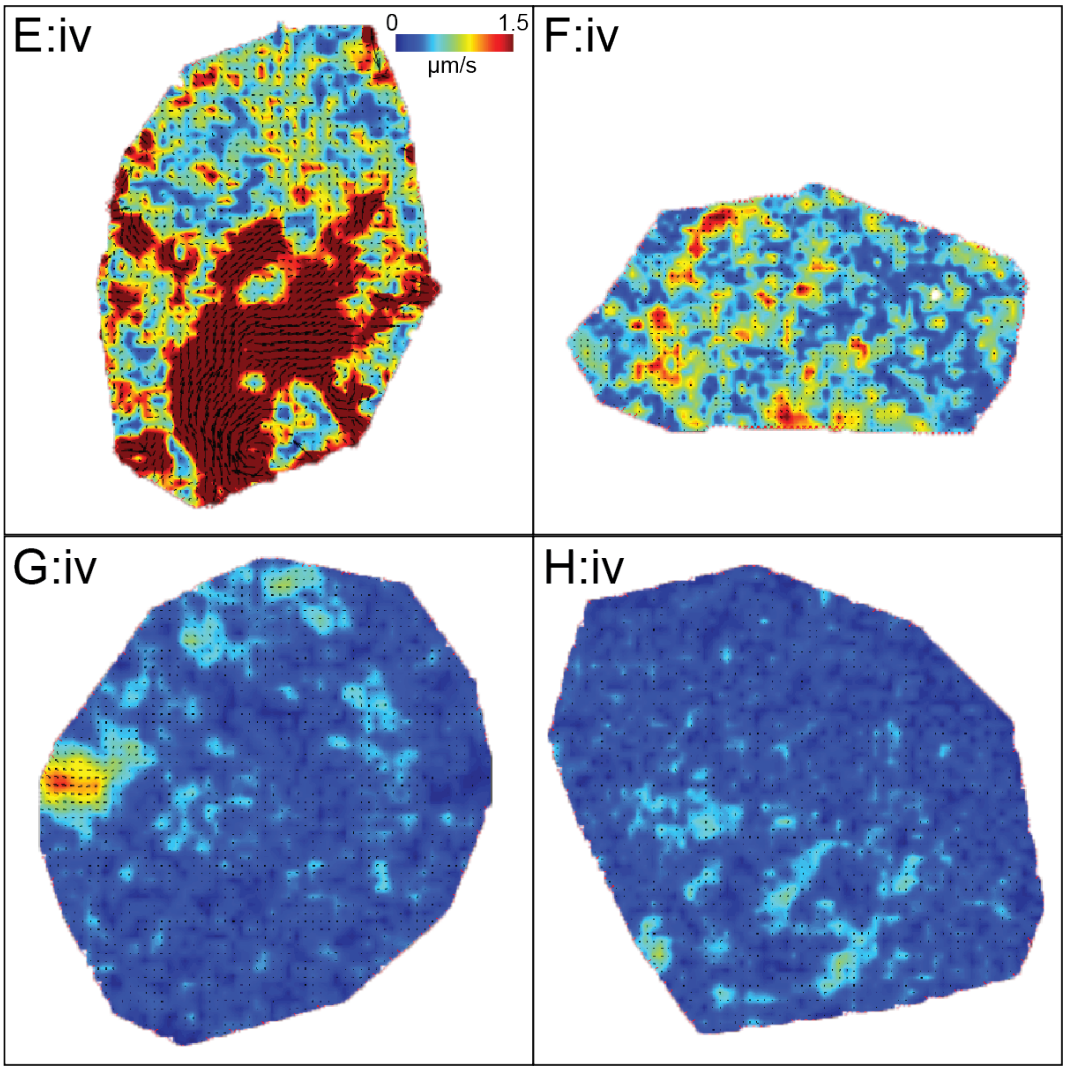


Figure 2.7: *Pierce1*$^{-/-}$ embryonic nodes showed disrupted nodal flow. Enlarged particle image velocimetry (PIV) plots of *Pierce1*$^{-/-}$ embryonic nodes at 8.0 dpc. Nodes E: iv-F: iv show disordered flow, nodes G: iv-H: iv show no overall flow. Velocity is colour coded; dark red refers to high velocity (1.5 µm/s), whilst dark blue refers to low velocity (0 µm/s); a scale bar is shown in E: iv. Directionality of vectors is shown by black arrows. Data collected over 33 experimental data collection sessions.

2.2.1.1: Pierce1$^{-/-}$ embryos show a significant alteration in mean nodal flow vector directionality, compared to wild-type and heterozygous litter-mates.

After evaluating overall flow directionality at the node, I utilised counts of the vectors in different directions present at each node to re-analyse the data (**Fig. 2.8**). Vector counts were binned by directionality in 45º sectors, where 0º is the anterior pole of the node, 90º is the left hand side of the embryo, and 180º is the posterior pole. Using a mean average of vector counts in each sector gave a side-by-side comparison of the differences between mean *Pierce1*$^{+/+}$ (n=2) and *Pierce1*$^{+/-}$ (n=2) directionality when compared to *Pierce1*$^{-/-}$ (n=8) directionality. Mean vector counts across the analysed samples showed a more even spread in *Pierce1*$^{-/-}$ embryos compared to a strong bias for leftwards directionality in *Pierce1*$^{+/+}$ and $^{+/-}$ embryos. I concluded that overall, nodal flow in the *Pierce1*$^{-/-}$ embryo population shows a lack of directionality, and I propose that this lack of leftwards flow underpins the LR patterning defects observed later in the gestational development of this line.

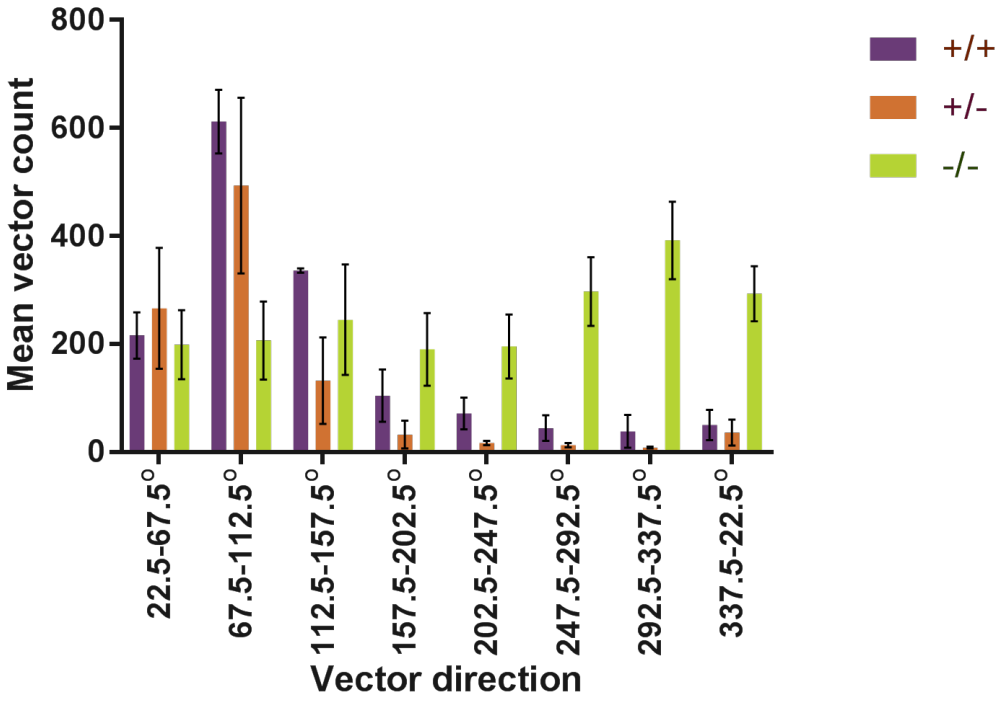


Figure 2.8: Mean vector directionality was disrupted in *Pierce1*$^{-/-}$ nodes. Vector directionality by genotype. Mean counts per segment are shown. Wild-type: n=2; heterozygous: n=2; *Pierce1*$^{-/-}$: n=8. Error bars indicate range. Data collected over 33 experimental data collection sessions.

2.2.2: *Pierce1*$^{-/-}$ embryos show a significant reduction in nodal ciliary beat frequency.

Although I have demonstrated absence of leftwards nodal flow in the *Pierce1*$^{-/-}$ embryos, the question remained of why nodal flow is not being effectively and reliably produced. As ciliary motility causes flow, I next imaged the nodal cilia of *Pierce1*$^{-/-}$ embryos at 8.0 dpc.

I dissected and mounted embryos in warmed DMEM with 10% FBS. I took videos of differential interference contrast (DIC) images of nodal cilia at 90-100 f/s, 100X magnification on an upright compound microscope. 300 frames of data were collected and played back at 7 f/s. This enabled me to count ciliary rotations and calculate rotational beat frequency of nodal cilia. Videos were scanned to ensure that cilia were clearly identifiable for all frames before being used for analysis; only motile cilia were used for CBF analysis.

Pierce1$^{+/+}$ and *Pierce1*$^{+/-}$ exhibited mean CBF values of 7.381 Hz and 7.292 Hz respectively. In contrast, analysis revealed a significant reduction in nodal CBF in *Pierce1*$^{-/-}$ embryos (4.712 Hz, **Fig. 2.9**). This reduction in beat frequency could be partially causative for the lack of effective nodal flow observed in the majority of *Pierce1*$^{-/-}$ embryos.

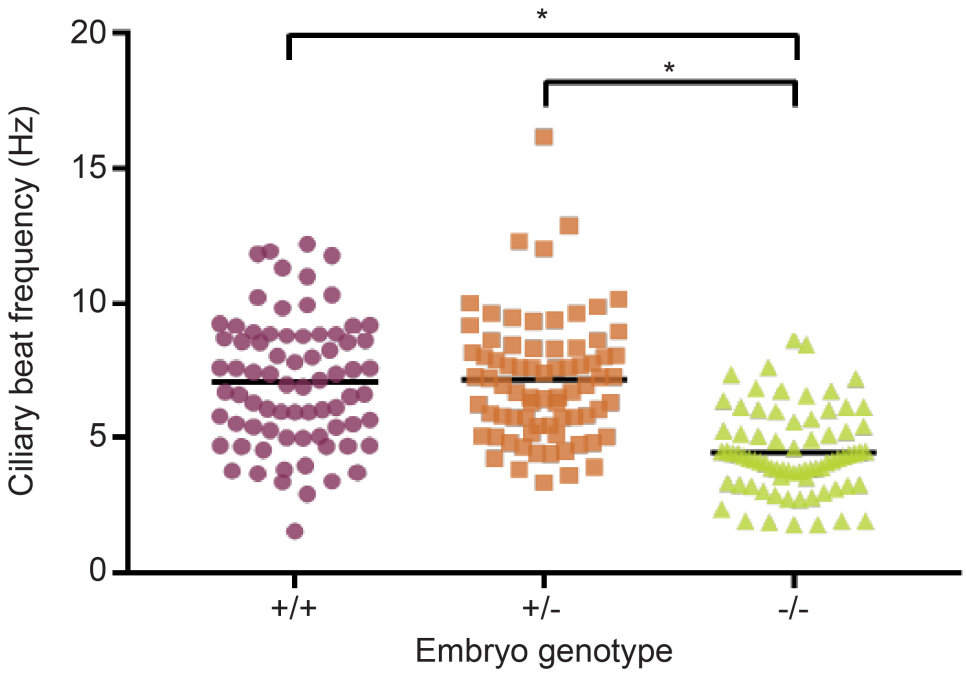


Figure 2.9: Ciliary beat frequency is significantly reduced in *Pierce1*$^{-/-}$ nodal motile cilia.
Ciliary beat frequency (Hz) counts from embryonic nodal cilia. n=18 embryos per genotype, n=5 cilia evaluated per node. *p<0.005 (mixed model analysis, pairwise comparison). Mean ciliary beat frequency: 7.381 Hz (+/+); 7.292 Hz (+/-); 4.712 Hz (-/-).Data collected over 38 experimental data collection sessions.

2.2.2.1: The reduction in mean ciliary beat frequency is not driven by a small sub-population of embryos.

From the data plotted in **Fig. 2.5** and **Fig. 2.9**, it seemed possible that a small population of more severely affected embryos could be driving the significant decrease in CBF observed in *Pierce1*$^{-/-}$ nodal cilia. I accounted for any bias arising from litter of origin of each embryo by including litter of origin as a variable in a generalised linear mixed model analysis of this data (**EM6.5**). To further test whether there is a significant litter-dependent influence, nodal CBF (Hz) was plotted by embryo (**Fig. 2.10**). This reveals that although there were slight variations between each embryo, there was a general trend for reduced beat frequency among all *Pierce*$^{-/-}$ embryos.

Although there are three embryos from one litter (290317B2, C2, E2, **Fig. 2.10**) that appear by eye to have an elevated CBF in the range of wild-type and heterozygous cilia, this is not a statistically significant occurrence. I hypothesised that this trend, as opposed to a smaller group of more significantly affected embryos, was driving the reduction in nodal CBF as calculated by mixed model analysis. There was no evidence for a dual population of *Pierce1*$^{-/-}$ embryos with stark differences in nodal CBF.

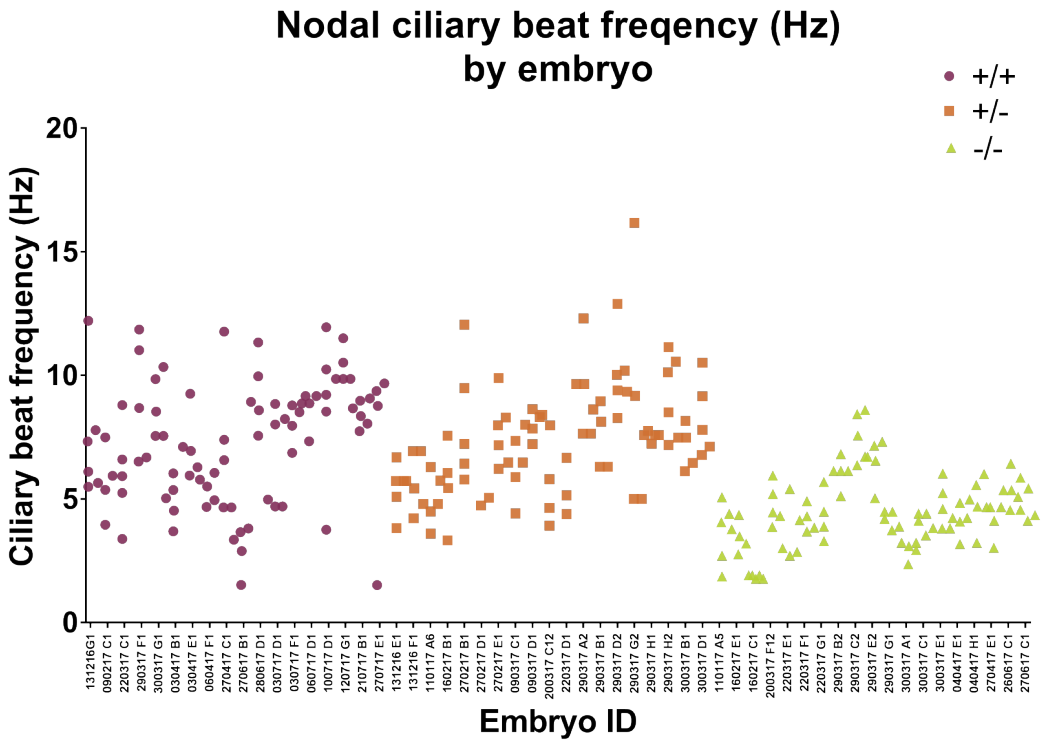


Figure 2.10: The reduction in ciliary beat frequency in *Pierce1*$^{-/-}$ embryos is not due to a small population of more severely affected embryos.
Ciliary beat frequency (Hz) counts from embryonic nodal cilia in *Pierce1*$^{+/+}$, *Pierce1*$^{+/-}$ and *Pierce1*$^{-/-}$ embryos, shown by individual embryo (ID in X axis). n=18 embryos each genotype, n=5 cilia evaluated in each node. Data collected over 38 experimental data collection sessions.

2.2.3: *Pierce1*$^{-/-}$ nodal cilia show a significant increase in "disrupted rotation" and "waving" beat patterns.

Although a significant drop in nodal CBF had been detected, this was unlikely to be the cause of disrupted flow alone. There was substantial overlap in CBF values calculated for +/+, +/- and -/- cilia. Moreover, published data has shown that only two rotating cilia are required to break LR symmetry in the mouse node (Shinohara *et al.*, 2012). Nasal brushing samples from patients with PCD are evaluated for ciliary beat pattern (CBP) in addition to CBF. I hypothesised that alterations in CBP could be an additional factor underlying aberrant nodal flow, leading to defective LR patterning in *Pierce1*$^{-/-}$ embryos.

I evaluated the nodal cilia videos to assess CBP. I defined classes of ciliary beating as continuous (**Fig. 2.11**), waving (**Fig. 2.12**), discontinuous (**Fig. 2.13**), twitching and immotile. Discontinuously rotating cilia showed obvious pausing in their rotation cycle, and took a noticeably larger number of frames to complete a full rotation compared to continuously rotating (**Fig. 2.11**) cilia. "Waving" cilia showed no rotational pattern and instead showed only planar waving movement. After defining these classes, I scored all videos blind to genotype.

The proportions of continuously beating cilia in wild-type (59.7%) and heterozygous (64.0%) were markedly higher than that observed in *Pierce1*$^{-/-}$ embryos (23.0% continuously rotating cilia). On the other hand, *Pierce1*$^{-/-}$ embryos showed a predominant incidence of discontinuously rotating, waving and twitching cilia (**Table 2.1**). I statistically analysed the proportions observed in each genotype using a generalised linear mixed model. A significant difference was detected between the proportions of cilia allocated to the different classes when comparing *Pierce1*$^{-/-}$ to wild-type and heterozygous cilia (**Fig. 2.14**).

My conclusion from this work was that aberrant motility patterns, in combination with a reduced CBF, underlie the lack of effective leftwards nodal flow in *Pierce1*$^{-/-}$ embryos.

	Ciliary beat pattern (%)				
Genotype	Continuous % (n)	Disrupted % (n)	Waving % (n)	Twitching % (n)	Other % (n)
***Pierce1*$^{+/+}$**	59.7 (166)	19.4 (54)	12.2 (34)	7.2 (20)	1.4 (4)
***Pierce1*$^{+/-}$**	64.0 (695)	15.6 (169)	11.0 (120)	9.4 (102)	0.1 (1)
***Pierce1*$^{-/-}$**	23.0 (107)	35.0 (163)	26.2 (122)	15.9 (74)	0.0

Table 2.1: Proportions of ciliary beat pattern observed in *Pierce1*$^{+/+}$, *Pierce1*$^{+/-}$ and *Pierce1*$^{-/-}$ embryos. *Pierce1*$^{+/+}$: n=278 cilia; 19 embryos. *Pierce1*$^{+/-}$: n=1087 cilia; 62 embryos. *Pierce1*$^{-/-}$: n=466 cilia; 36 embryos. Data collected over 38 experimental data collection sessions.

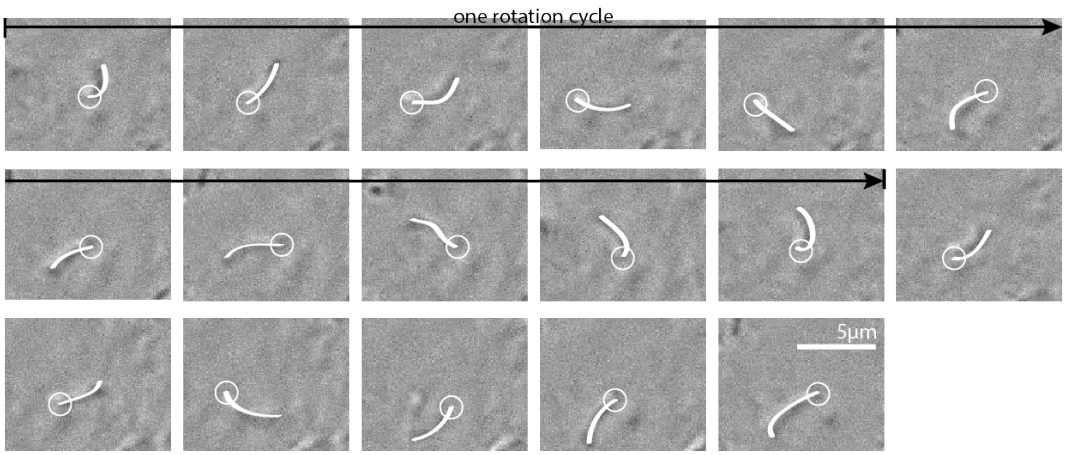
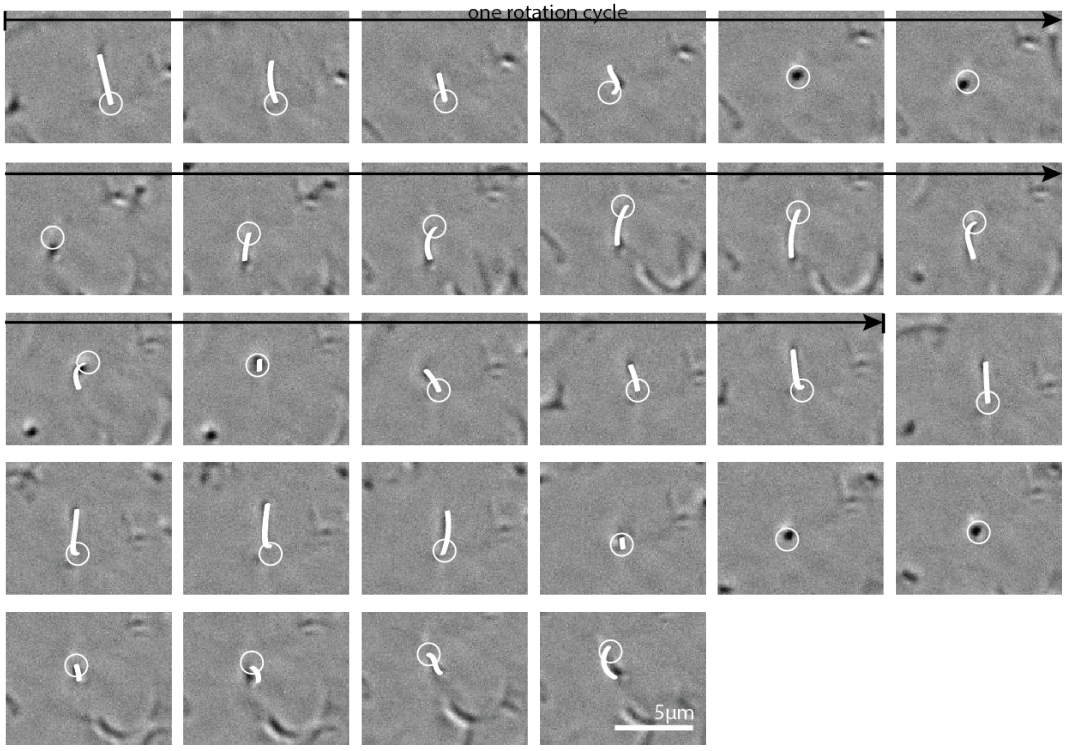


Figure 2.11 (top): Image sequence showing a continuously rotating cilium. The length of the cilium is outlined in white, and the base is ringed in white. One rotation cycle is denoted by a black bar. Scale bar shows 5 µm.
Figure 2.12 (bottom): Image sequence showing a waving cilium. The length of the cilium is outlined in white, and the base is ringed in white. One rotation cycle is denoted by a black bar. Scale bar shows 5 µm.



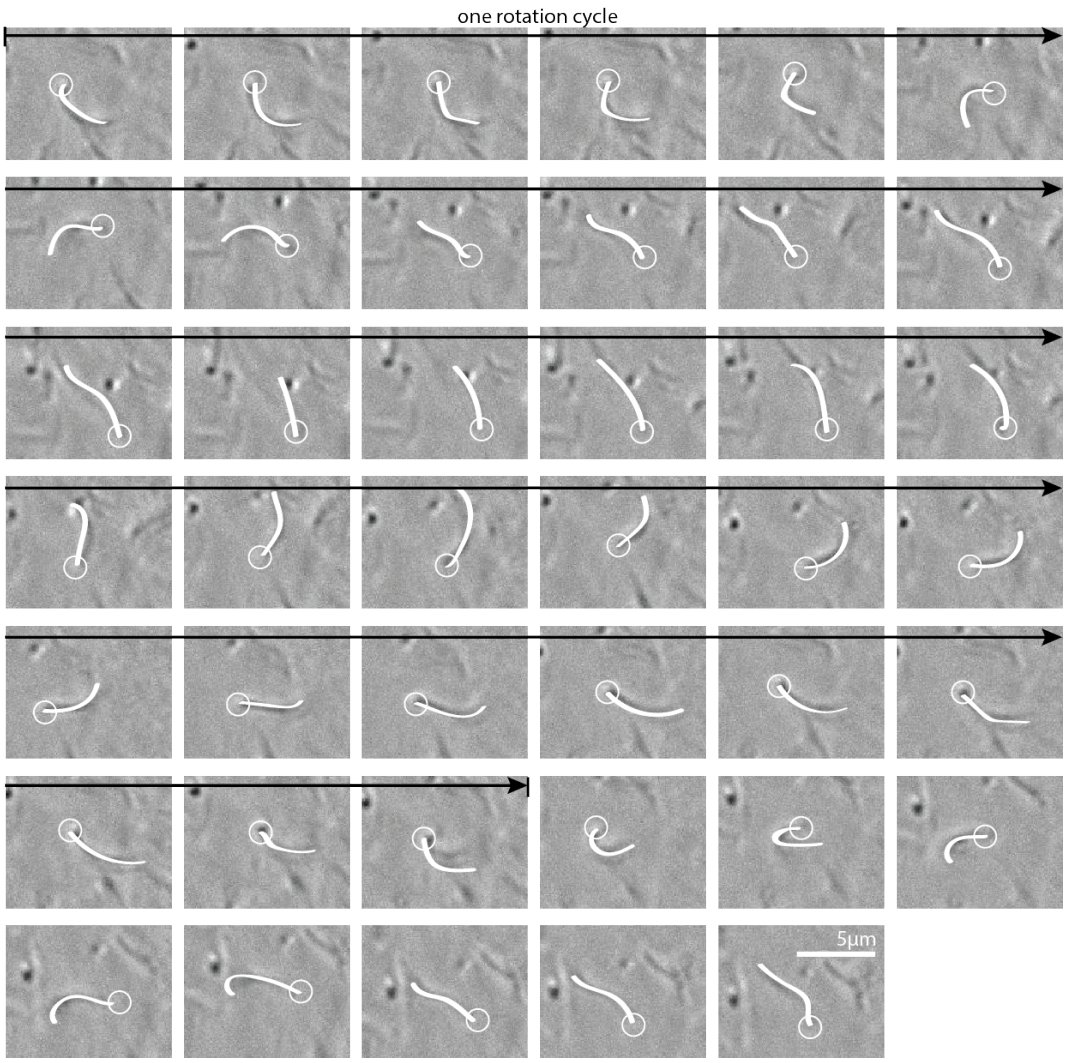


Figure 2.13: Image sequence showing a disrupted rotating cilium. The length of the cilium is outlined in white, and the base is ringed in white. One rotation cycle is denoted by a black bar. Scale bar shows 5 µm.

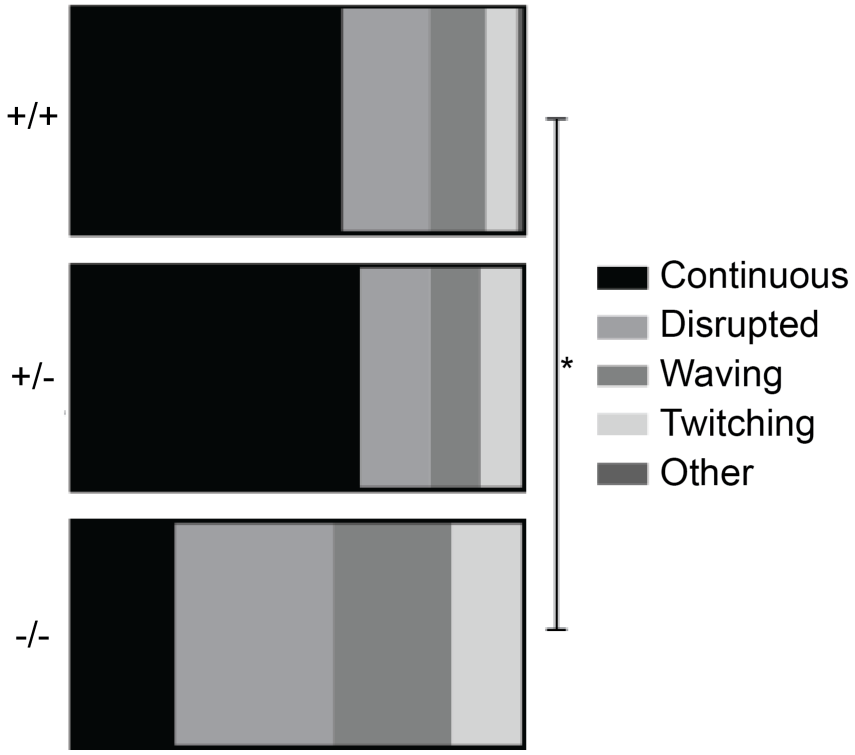


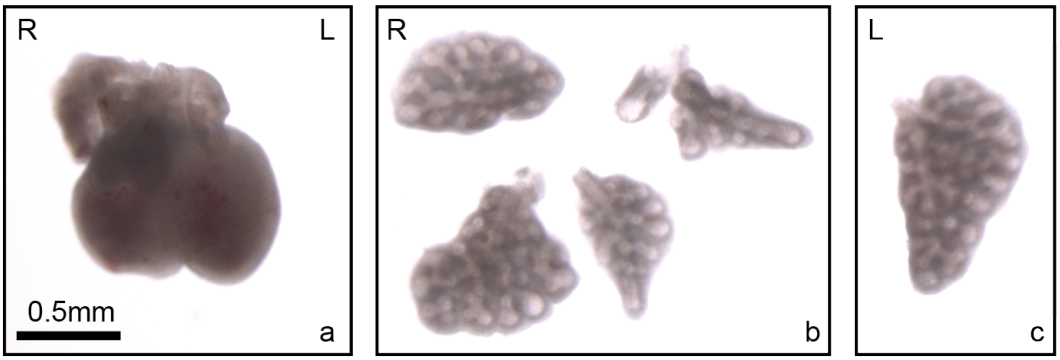
Figure 2.14: A decrease in the proportion of continuously rotating cilia, and an increase in the proportion of disrupted and waving cilia, was observed in *Pierce1*$^{-/-}$ nodes.
Ciliary beat pattern categorisation distribution for *Pierce1*$^{+/+}$, *Pierce1*$^{+/-}$ and *Pierce1*$^{-/-}$ embryos. *Pierce1*$^{+/+}$: n=278 cilia; 19 embryos. *Pierce1*$^{+/-}$: n=1087 cilia; 62 embryos. *Pierce1*$^{-/-}$: n=466 cilia; 36 embryos. *p<0.005 (Fisher's). Data collected over 38 experimental data collection sessions.

2.2.4: Our *Pierce1*-null allele shows similar left-right patterning defects to the *Pierce1*-null line characterised by Sung et al (Sung *et al.*, 2016).

The *Pierce1*-null line developed by Sung et al (Sung *et al.*, 2016) shows a range of situs defects. In contrast, IMPC analysis had revealed 2-3 embryos with incompletely characterised situs defects. However, I wanted to evaluate whether we see the same proportion of affected embryos in our line as in the Sung et al (Sung *et al.*, 2016) situs analysis. We know that some cilia remain motile in our *Pierce1*$^{-/-}$ embryonic nodes, and that a small proportion of nodes examined show leftwards flow. I aimed to test whether the *Pierce1-tm2b* allele exhibited a less penetrant situs phenotypes than the Sung et al null (Sung *et al.*, 2016) allele, and extrapolate from that whether or not it would be reasonable to assume a similar level of ciliary motility defect in both lines. Potentially, we would see a smaller proportion of situs defects in the *Pierce1-tm2b* line if ciliary motility in these embryos was better preserved than that of those examined by Sung et al.

In the mouse, visceral organ situs is readily scored at 13.5 dpc, with the visceral organs demonstrating asymmetry in their patterning and position within the thoracic and abdominal cavities. In this analysis, I focused on the heart, lungs and stomach, due to readily identifiable aspects of their situs. The heart apex points to the left (**Fig. 2.15: a**), whilst the left lung has one lobe and the right lung has four lobes, giving a 4:1 (R: L) lung lobation pattern (**Fig. 2.15: b & c**). The stomach is situated on the left hand side of the abdomen. This normal exhibition of situs is referred to as “situs solitus (SS)”. A complete inversion of this is referred to as “situs inversus totalis (SIT)”, while disconcordant situs referred to as “situs ambiguus (SA)” (**Fig. 2.1**).

I dissected embryos at 13.5 dpc and observed SS in all wild-type (n=16) and heterozygous (n=47) embryos examined. In *Pierce1*$^{-/-}$ embryos (n=16), although some embryos displayed SS (n=7), a variety of situs abnormalities were present in other embryos. These included left pulmonary isomerism (n=4), SIT (n=3) and SA (n=2) (**Table 2.2**). I statistically analysed proportions of situs presentations present in each genotype (**Fig. 2.16**) using Fisher's exact t-test and found a significant difference when comparing *Pierce1*$^{-/-}$ embryos with wild-type and heterozygous embryos.



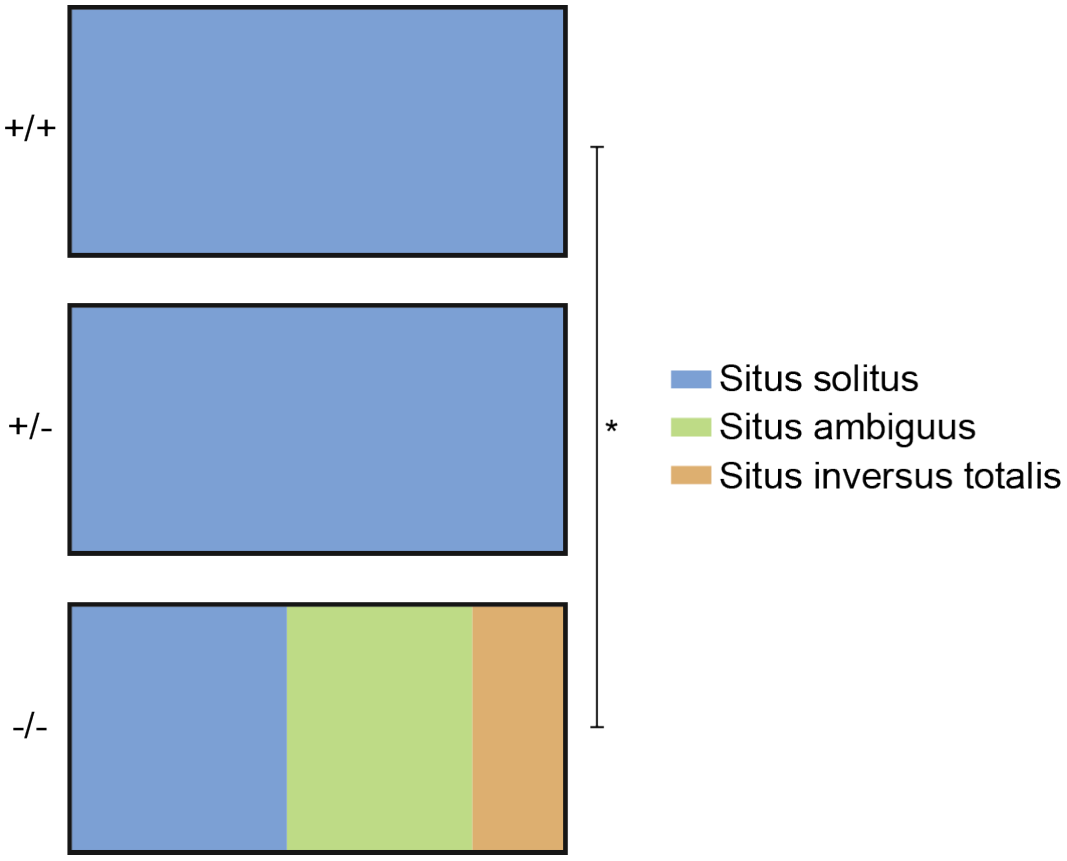


Figure 2.15 (top): Photographs of correctly patterned heart (a), right lung comprising four lobes (b) and left lung, single lobe (c) at 13.5 dpc. Scale bar shows 0.5 mm.

Figure 2.16 (bottom): Embryos homozygous for the *Pierce1-tm2b* allele exhibited visceral organ situs defects.

Bar chart showing the representation of situs solitus, situs ambiguus and situs inversus totalis in *Pierce1*$^{+/+}$, *Pierce1*$^{+/-}$ and *Pierce1*$^{-/-}$ embryos at 13.5 dpc. n= +/+ 16; +/- 47, -/- 16. *p<0.005, Fisher's exact t-test.

	Situs phenotype of SA embryos		
Embryo ID	*Heart apex (L/R)*	*Lung lobation (R: L)*	*Stomach situs (L/R)*
A	*R*	*1:1*	*R*
B	*L*	*1:1*	*L*
C	*R*	*1:2*	*L*
D	*R*	*1:1*	*R*
E	*R*	*1:1*	*R*
F	*R*	*1:2*	*L*

Table 2.2: situs phenotype for *Pierce1*$^{-/-}$ embryos marked as situs ambiguus in **Fig. 2.16**.

2.2.5: Defects in expression of left-right asymmetric genes at 8.0 dpc in *Pierce1*$^{-/-}$ embryos are concordant with later defective visceral organ situs.

Organ situs is a consequence of earlier asymmetric gene expression. I therefore analysed the expression of LR asymmetric genes to evaluate the molecular identity of the left and right sides of the embryo during its early development (7.5-8.5 dpc).

Pitx2 is a distal marker of molecular LR asymmetry in the early embryo. It is expressed bilaterally in the head folds throughout 7.5-8.5 dpc (Yoshioka *et al.*, 1998) and is expressed in the left, but not the right LPM from the 3 somite stage. As such, I assessed *Pitx2* expression by in situ hybridization to examine whether *Pitx2* expression abnormalities were observed in addition to the organ patterning defects discussed above.

In wild-type and heterozygous embryos, *Pitx2* was restricted to the left LPM (**Fig. 2.17: A, B**). In some *Pierce1*$^{-/-}$ embryos, physiological left LPM expression of *Pitx2* was detected (**Fig. 2.17: C**). However, *Pitx2* is also observed in the right LPM in isolation (**Fig. 2.17: D**); in both the left and right LPM simultaneously (**Fig. 2.17: E**); and absent from both left and right LPM (**Fig. 2.17: F**). These patterns of expression are abnormal and would likely lead to situs defects in later development. Right hand side *Pitx2* expression in the LPM is a precursor to the development of SIT; bilateral LPM *Pitx2* would lie upstream of left isomerism. Absent *Pitx2* expression would cause right isomerism, but it remains possible that there is delayed activation of *Pitx2*. A delay in expression would in itself would be abnormal; by the time point evaluated (4 somite stage) all wild-type and heterozygous embryos displayed left LPM localized expression. An increase in embryo numbers is needed for a more thorough and statistically significant evaluation of a delay in *Pitx2* expression in *Pierce1*$^{-/-}$ embryos. Overall proportions of *Pitx2* staining patterns occurring in wild-

type, heterozygous and *Pierce1*$^{-/-}$ were calculated (**Fig. 2.18**) and analysed using Fisher's exact t-test, demonstrating a significant difference between staining in wild-type or heterozygous and *Pierce1*$^{-/-}$ embryos.

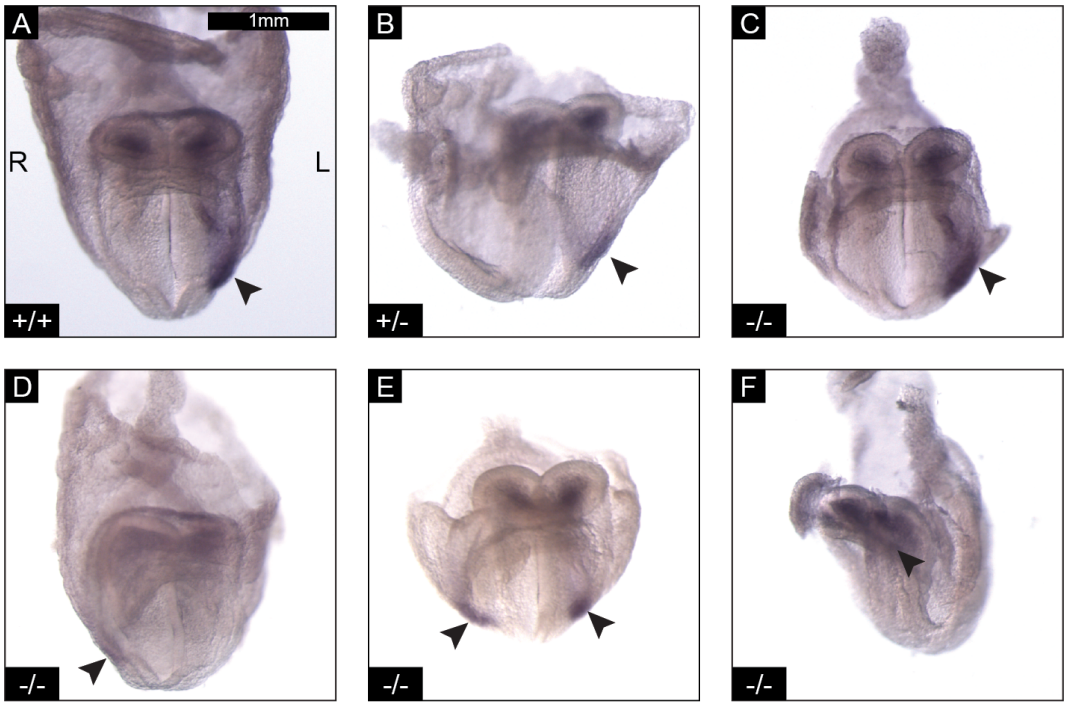


Figure 2.17: Embryos homozygous for the *Pierce1-tm2b* allele exhibited aberrant *Pitx2* gene expression.
Pitx2 in situ hybridisation patterns observed in *Pierce1*$^{+/+}$, *Pierce1*$^{+/-}$ and *Pierce1*$^{-/-}$ embryos. Stained areas are highlighted with arrows, and the left and right sides of the embryo are annotated. Embryos resulted from *Pierce1*$^{+/-}$ intercross matings at 8.0 dpc. Scale bar shows 1 mm.

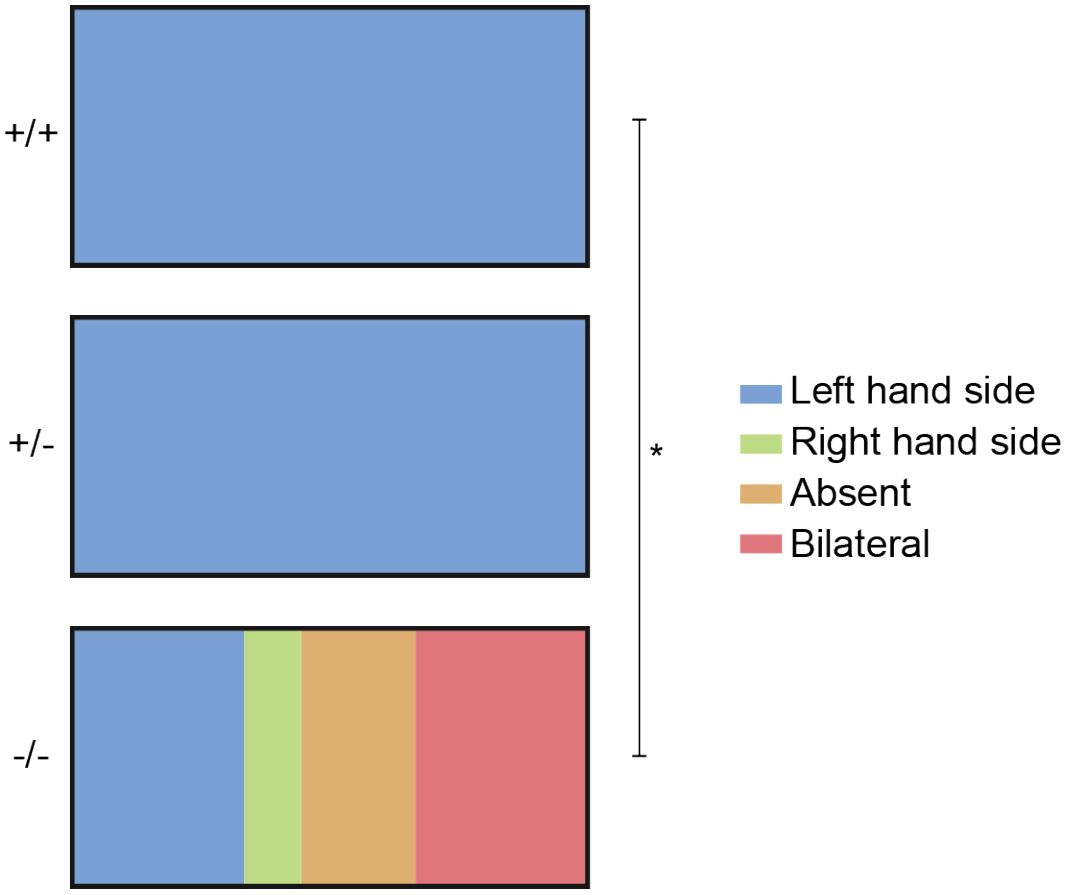


Figure 2.18: Embryos homozygous for the *Pierce1-tm2b* allele exhibited aberrant *Pitx2* gene expression.
Bar chart showing the representation of *Pitx2* in situ hybridisation staining patterns in *Pierce1*$^{+/+}$, *Pierce1*$^{+/-}$ and *Pierce1*$^{-/-}$ embryos. Embryos resulted from *Pierce1*$^{+/-}$ intercross matings at 8.0 dpc. n= +/+ 15; +/- 17, -/- 9. *p<0.005, Fisher's exact t-test.

Cerl2 is the first known asymmetrically expressed gene to act downstream of nodal flow, and therefore its expression provides the first read-out of asymmetry at the level of gene expression. As nodal flow analysis demonstrated defective flow in *Pierce1*$^{-/-}$ embryos, this should be reflected in altered *Cerl2* expression. As such, I analysed *Cerl2* expression in embryos between the 1 and 3 somite stages. In wild-type embryos, *Cerl2* is initially expressed symmetrically around the node from the early head fold stage, before *Cerl2* mRNA is degraded preferentially on the left-hand side of the node in response to fluid flow. This leads to an increase in *Cerl2* mRNA on the right hand side of the node which is readily apparent by 8.0 dpc, or after the late head fold stage.

Changes in *Cerl2* expression are challenging to evaluate by eye - C*erl2* asymmetry is not binary like that of *Pitx2,* with a simple presence or absence of expression to note. Differences in expression are not clear cut, and I deemed a manual determination of *Cerl2* expression levels on either side of the node insufficiently precise (**Fig. 2.19**: manual annotations of differential *Cerl2* expression). Instead, I quantified stain intensity using the region of interest tool in ImageJ (Schneider, Rasband and Eliceiri, 2012), and divided left-hand side stain intensity by right-hand side stain intensity to compare the expression of *Cerl2* on either side of the node. When left-hand side stain intensity is less than right-hand side stain intensity, as we would expect in wild-type embryos, the result from the intensity division is less than 1.

When comparing wild-type and heterozygous embryos to *Pierce1*$^{-/-}$ embryos, a significant increase in the result of left intensity divided by right intensity was observed (**Fig. 2.20**). This means that *Cerl2* mRNA asymmetry is less pronounced in *Pierce1*$^{-/-}$ embryos. We would expect this to result in defective situs patterning. An increase in left hand side *Cerl2* mRNA could be a harbinger of SIT, whilst a lack of nodal *Cerl2* asymmetry could precede isomeric visceral organ patterning.

I concluded that the mean increase in *Cerl2* expression symmetry around the node reflects an early defect in flow response in *Pierce1*$^{-/-}$ embryos. I hypothesise that this is due to ineffective nodal flow caused by defective ciliary motility.

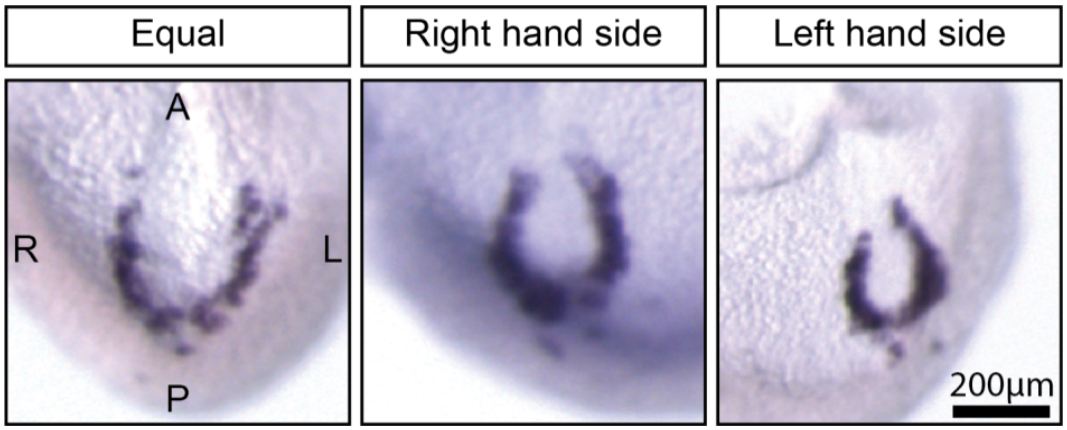


Figure 2.19: Manual annotation of *Cerl2* expression in *Pierce1*$^{-/-}$ embryos was inconclusive.
Cerl2 in situ hybridisation patterns observed in *Pierce1*$^{+/+}$, *Pierce1*$^{+/-}$ and *Pierce1*$^{-/-}$ embryos at 8.0 dpc. The anterior, posterior and left and right axes are annotated; scale bar shows 200 µm.

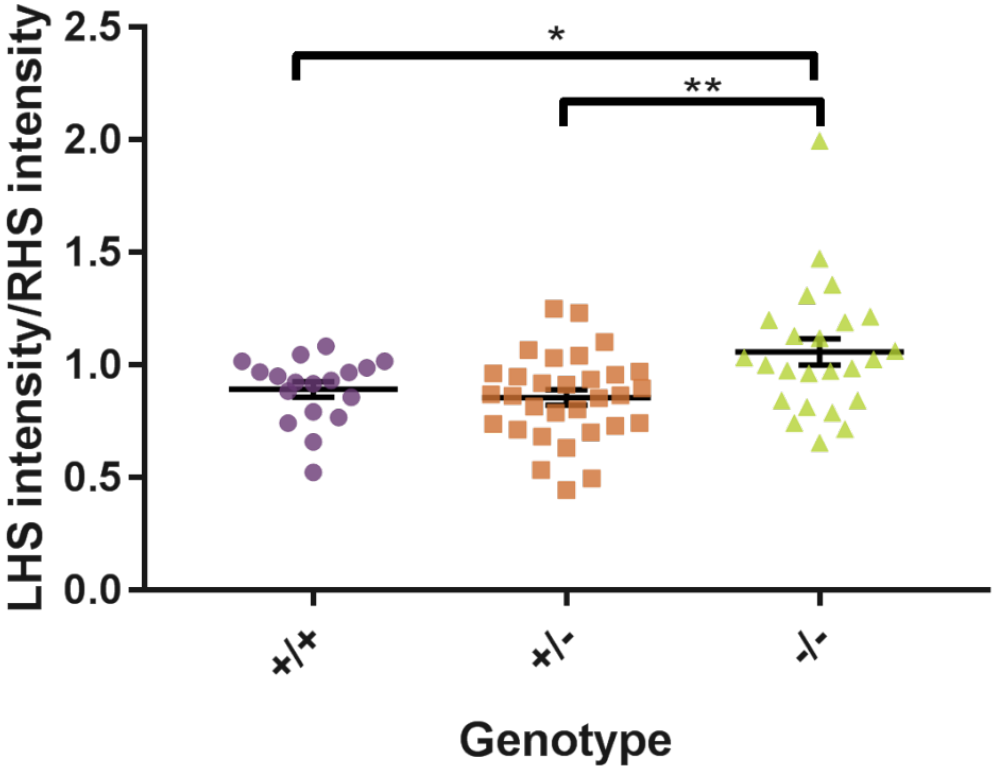


Figure 2.20: Computerised annotation of *Cerl2* expression in *Pierce1*$^{-/-}$ embryos demonstrated a significant difference in gene expression between wild-type, *Pierce1*$^{+/-}$ and *Pierce1*$^{-/-}$ embryos.
XY plot showing the *Cerl2* LHS in situ hybridisation stain intensity divided by RHS stain intensity observed in *Pierce1*$^{+/+}$, *Pierce1*$^{+/-}$ and *Pierce1*$^{-/-}$ embryos at 8.0 dpc. Embryos resulted from *Pierce1*$^{+/-}$ intercross matings. n= +/+ 18; +/- 31, -/- 24. *p<0.05, **p<0.005 (mixed model analysis). Bars show mean ± SEM.

2.2.6: Node morphology is grossly normal in *Pierce1*$^{-/-}$ embryos

It seemed possible that defective nodal flow could be due to disrupted ciliary or node morphology in *Pierce1*$^{-/-}$ embryos. This seemed unlikely as defects in ciliogenesis or gastrulation usually cause more severe embryonic phenotypes than those observed in *Pierce1*$^{-/-}$ embryos. Moreover, Sung et al (Sung *et al.*, 2016) reported no morphological defects in the nodes and nodal cilia of their *Pierce1*-null line.

I harvested wild-type and *Pierce1*$^{-/-}$ at 8.0 dpc, n=3 per genotype. Rosie Little (MRC Harwell MGU) processed and imaged these embryos using SEM. The nodes showed no gross genotype-dependent morphological differences (**Fig. 2.21**). Closer examination revealed no gross morphological ciliary differences, such as bulging at the tip or the base, or bifurcations, in *Pierce1*$^{-/-}$ (**Fig. 2.21: B, C, f-l**) or wild-type nodal cilia (**Fig. 2.21: A, d-e**).

Changes in ciliary length have been associated with defects in cellular signalling. They could also be reasonably expected to alter fluid flow dynamics as a result of ciliary rotational beating at the node. To test whether flow and LR patterning defects in *Pierce1*$^{-/-}$ mice could be downstream of alterations in ciliary length, I analysed the lengths of the cilia in the node of age-matched wild-type and *Pierce1*$^{-/-}$ embryos (n=1 embryo per genotype, n=20 cilia per embryo); this revealed no statistical difference (**Fig. 2.22**).

The lack of gross nodal or ciliary morphological changes in *Pierce1*$^{-/-}$ embryos, in combination with an absence of significant change in ciliary length, suggests that none of these factors underpin the nodal flow and LR patterning defects observed in *Pierce1*$^{-/-}$ mice.

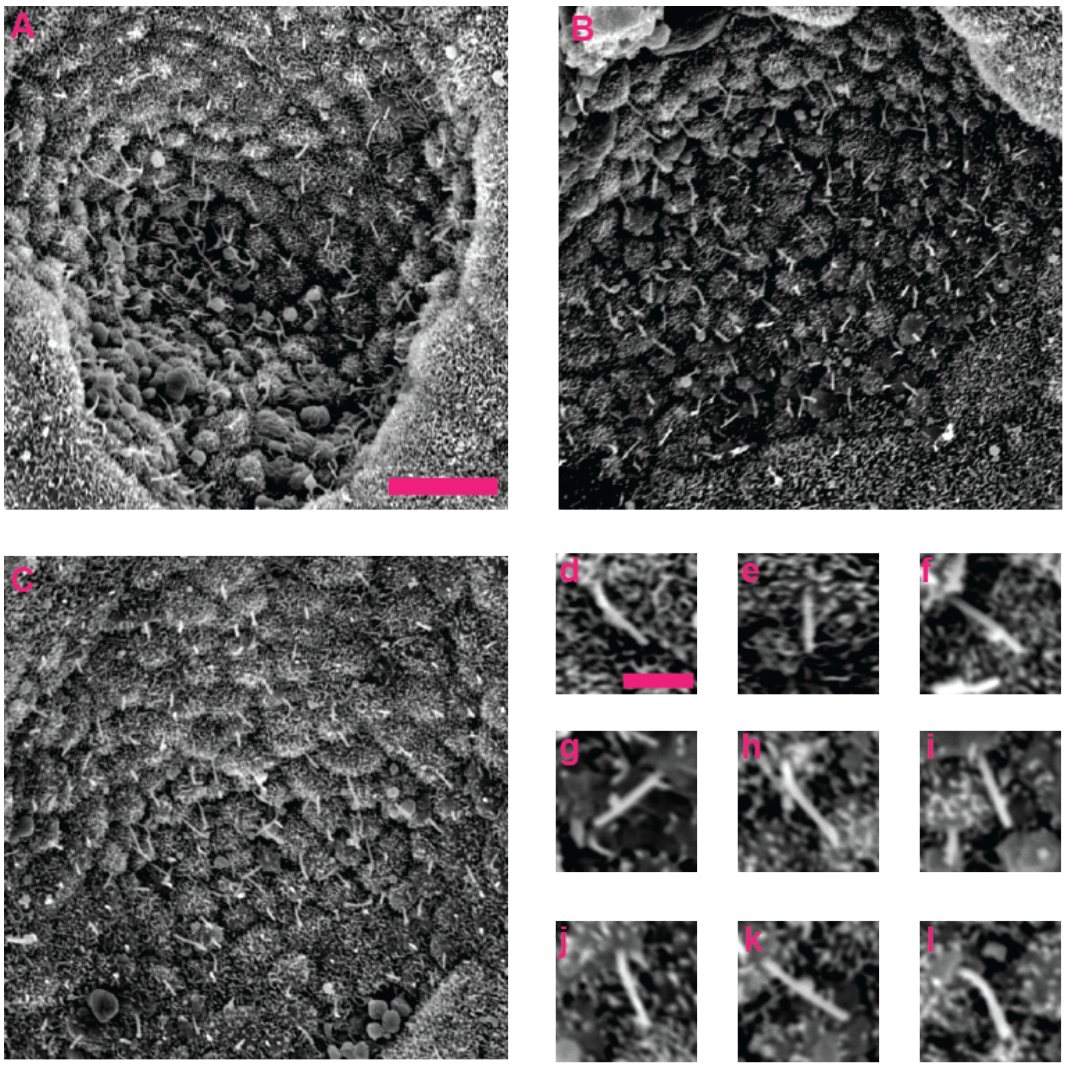


Figure 2.21: Cilia are morphologically normal in *Pierce1*$^{-/-}$ nodes.
SEM images of nodal cilia in *Pierce1*$^{+/+}$ (A, d, e) and *Pierce1*$^{-/-}$ (B, C, f-l) embryonic nodes. No morphological differences were noted. Scale bar in A = 10 µm, scale bar in d=2 µm.

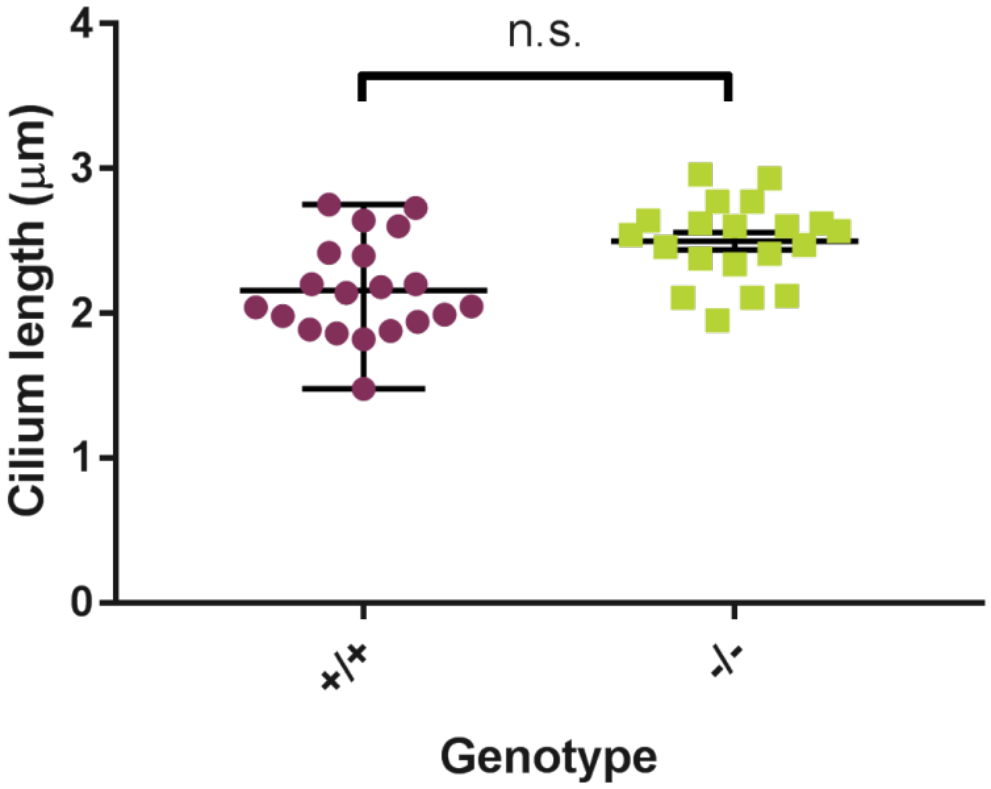


Figure 2.21: No difference in ciliary length was detected between wild-type and *Pierce1*$^{-/-}$ nodal cilia.
Cilium length in *Pierce1*$^{+/+}$ and *Pierce1*$^{-/-}$ age-matched embryonic nodes. 20 cilia measured in each node. No significant difference was found between wild-type (mean=2.160 μm) and *Pierce1*$^{-/-}$ (mean=2.499 μm) nodal cilia length (generalised linear mixed model). Error bars show range.

2.3: Discussion

2.3.1: Flow at the embryonic node

Nodal flow was abnormal in *Pierce1*$^{-/-}$ embryos. Although two embryos were observed with some leftwards flow at the node, the majority of embryos analysed showed disorganised flow, with varying degrees of velocity. The nodal flow in *Pierce1*$^{-/-}$ embryos was heterogeneous both with regards to speed, or lack thereof, and direction. This is perhaps unsurprising, given the variation observed in analysis of ciliary motility. Whilst CBF and CBP in some nodes were clearly abnormal and identifiable by eye, *Pierce1*$^{-/-}$ nodal cilia generally exhibited phenotypic overlap with their wild-type and heterozygous counterparts.

In this field, publications often present one or two PIV plots for each genotype or experimental condition to represent nodal flow (Shinohara *et al.*, 2012). Our mutant showed a more variable phenotype, and it would not have accurately represented the data to display only one or two plots. As such, more data was included. This was particularly important as I developed an in-house particle image velocimetry pipeline using readily available software and open source plug-ins (Thielicke and Stamhuis, 2014) (with assistance from Henrik Westerberg and Jenni Vibert, MRC Harwell Institute Biocomputing). Wild-type and heterozygous embryos were never observed to have abnormal nodal flow under standard experimental conditions using our analysis pipeline. We validated the analysis of previous data from the lab, demonstrating concordance with proprietary software analysis (data not shown).

2.3.2: Caveats and limitations of particle image velocimetry

PIV imaging is technically challenging. For correct imaging, the embryo needs to be sufficiently compressed under the coverslip to allow focusing on a plane of view that includes the leftwards fluid flow induced

by the cilia. Too far compressed, and the embryo is irreparably damaged; too little compression, and focusing on the plane including the fluid flow is difficult. Annotation of video quality blind to genotype and in advance of video processing is necessary to ensure that flow directionality and strength determined in processed videos reliably reflects the native state of the embryo, and is not due to damage to the node or altered focal plane. I annotated video quality and any technical issues alongside embryo ID during the recording process blind to genotype, to ensure that I wasn't biasing myself towards including *Pierce1*$^{-/-}$ videos that showed abnormal flow due to technical issues or artefacts.

Other factors that had to be kept constant in both PIV and DIC embryo analysis included maintaining temperature to promote embryo survival and prevent effects on CBF. I kept the embryos warm and used pre-warmed media; embryos were kept in a 37ºC incubator when not being dissected or videoed. I was also careful to be prompt with the videoing process, as leaving embryos under microscope lights for a longer period of time led to embryonic decay, with the embryo being damaged more easily. Without careful management of these factors, we would not reliably be able to conclude flow defects resulting from embryo genotype.

I carried out DIC video analysis manually, with ciliary beat frequencies counted and beat patterns assigned to classes. This analysis was carried out blind to embryo genotype; a machine learning approach would be an interesting avenue to explore in the future regarding CBP analysis. This could go some way to removing any potential observed bias from human data processors.

Although my statistical analysis included weighting against individual litters of embryos, to assess whether any embryo was more severely affected due to its litter of origin, I have shown my data by individual embryo as well. This demonstrates that there is a general trend

for reduced CBF across all *Pierce1*$^{-/-}$ embryos, as opposed to a small group of *Pierce1*$^{-/-}$ embryos being more severely affected and causing a significant drop in mean *Pierce1*$^{-/-}$ beat frequency. This analysis was important after the detection of *Pierce1*$^{-/-}$ embryos with seemingly normal leftwards nodal flow; I wanted to ascertain whether there was a dual population of embryos within this line with some *Pierce1*$^{-/-}$ embryos much more severely affected than others.

Through PIV analysis and DIC imaging of embryonic nodal cilia, I have demonstrated that ciliary motility is disrupted in *Pierce1*$^{-/-}$ embryos. This results in aberrant nodal flow and is the likely cause of the LR patterning defects observed in the *Pierce1*-null line created by Sung et al (Sung *et al.*, 2016).

2.3.3: Our allele shows similar phenotypes to those observed by Sung et al.

The results of gross situs phenotyping in our *Pierce1*$^{-/-}$ embryos at 13.5 dpc show that our allele exhibited a similar phenotype to that of the null allele analysed by Sung et al (Sung *et al.*, 2016). Consistent with the leftwards flow observed in the nodes of heterozygous and wild-type embryos, we only saw SS in these genotypes. The incidence of situs abnormalities, including SIT, in solely the *Pierce1*$^{-/-}$ genotype tallied with what we would have expected from the nodal flow data, and results from Sung et al (Sung *et al.*, 2016).

However, our results did show a greater incidence of situs abnormalities, in particular a higher incidence of SA, than has been documented in mouse lines exhibiting immotile cilia at the node (Lucas *et al.*, 2012) (**Appendices 3 & 4**). The *iv* line, a canonical model of defective LR visceral organ patterning in the mouse, is reported (Sundberg and Collins, 1993) as exhibiting 50% SIT, with a high proportion of SS (some reports state 50%) and a lower proportion of heterotaxy. However, this

varies dependent on background strain (Layton, 1976; Layton and Hummel, 1976; Layton *et al.*, 1993), and heterotaxy is likely to be under-reported unless embryonic situs analysis was conducted alongside post-mortem analysis of neonatal mice. I hypothesise that the increase in turbulent and disordered flow at the node of *Pierce1*$^{-/-}$ embryos, as opposed to an absence of or very minimal flow, led to this increase in heterotaxy.

My situs analysis was macroscopic, and would not have detected more subtle defects in LR patterning, for example defects exhibiting as subtle cardiac defects. In situ hybridisation using probes complementary to genes expressed solely in the left and right atria or ventricles, for example *Tbx5* (Bruneau et al. 1999; left ventricle), would help to create a more detailed picture of the situs defects that occur in homozygotes of the *Pierce1-tm2b* allele. Ultimately, μCT analysis of the visceral organs in *Pierce1*$^{-/-}$ animals would give the most detailed picture of adult organ situs in these animals. Such an analysis was carried out on the *Pierce1*-null line generated by Sung et al, and we did not replicate the μCT study here.

In addition to demonstrating a higher incidence of heterotaxy than observed in mouse lines with immotile nodal cilia, this line exhibits a higher incidence of heterotaxy than typically observed in human populations with PCD (12.1%; Shapiro et al. 2014). This could in part be due to an increase in susceptibility to patterning defects created by genetic modifiers within the C57BL/6N inbred mouse strain; as humans tend to have a much more heterogeneous genetic make-up than inbred mouse strains, there is a reduced likelihood in humans of conserved clustering of genetic modifiers altering SA risk. Another possibility is that situs patterning defects leading to SA do occur in human patients, but are so detrimental as to not be compatible with life. This would go some way to explaining the reduction in SA incidence in patient populations.

When evaluating the specific situs defects observed, lung lobation is a clear marker of situs in the mouse and aids our examination of patterning in this line. SS and SIT were both observed in *Pierce1*$^{-/-}$ embryos, along with left isomerism of the lung lobes. No right isomerism was detected in the lung lobation analyses; this may be due to the small numbers evaluated, or due to a lack of right isomerism in this line. I consider the latter option unlikely as Sung et al did detect right isomerism in their paper (Sung *et al.*, 2016).

2.3.4: Left-right asymmetric gene expression

I evaluated the expression of canonical LR asymmetrically expressed genes as their expression lies upstream of altered visceral organ situs. This provided further evidence that aberrant nodal flow is the primary cause of defective LR patterning in these mice.

2.3.4.1: Pitx2 expression

Pitx2 is a transcription factor that is argued to be the primary downstream effector of visceral organ left-hand sidedness in embryonic development. Physiologically, *Pitx2* shows strong expression restricted to the head folds and the left LPM (Belmonte *et al.*, 1998; Logan *et al.*, 1998; Yoshioka *et al.*, 1998). Head fold expression is independent of LR patterning and is implicated in eye development, meaning that head fold expression is unlikely to be affected in *Pierce1*$^{-/-}$ mice, as adults in this line show no optical phenotype. Thus, *Pitx2* head fold expression provides a positive control for the LPM expression evaluated in each embryo.

Pitx2 always retained its physiological expression pattern in wild-type and heterozygous embryos. These genotypes both exhibited leftwards nodal flow. In *Pierce1*$^{-/-}$ embryos, however, *Pitx2* expression showed varying lateralisation. Different patterns were observed, including solely right LPM expression, both left and right LPM expression, and solely

left LPM expression. A proportion of embryos also showed no LPM expression.

Pitx2 expression leads to left-hand side identity, and we would presume that embryos exhibiting *Pitx2* expression in both left and right LPM would go on to develop left isomerism of the visceral organs, which would result in a 1:1 lung lobation pattern. Those only expressing *Pitx2* in the right LPM would go on to develop SIT. Embryos with evidence of SIT and left isomerism were identified in the gross situs analysis, fitting with the gene expression pattern observed in the early embryo.

A complete absence of *Pitx2* in the LPM is also observed. This could result from later initiation of *Pitx2* expression in some *Pierce1*$^{-/-}$ embryos – wild-type and heterozygous embryos were examined at matched time points, and had all initiated *Pitx2* expression by this point in development (>3 somite pairs). A delayed initiation of LR asymmetric LPM gene expression has been reported in other mouse lines with defective ciliary motility (Grimes et al. 2016). Alternatively, this could reflect right hand side patterning on both the right and left hand sides of the embryo due to a lack of nodal flow, leading to right isomeric patterning of the visceral organs. To further evaluate the possibility of delayed *Pitx2* expression, a time course study could be carried out. This would require greater numbers of embryos than utilised in the results presented to reach significance.

Although no cases of right isomerism were identified through gross situs phenotyping at 13.5 dpc, the numbers evaluated were small, and Sung et al did detect right isomerism in their situs analysis (Sung *et al.*, 2016). I would conclude that as the in situ hybridisation staining work was carried out with greater numbers than the gross situs analysis, it is reasonable to infer that I detected right isomerism with *Pitx2* staining

experiments, and simply did not analyse sufficient numbers to detect right isomerism with regards to lung lobation.

In essence, *Pitx2* staining demonstrated abnormal situs patterning in *Pierce1*$^{-/-}$ embryos, mirroring the results of Sung et al.

2.3.4.2: Cerl2 expression

Cerl2 is the first genetic product to show asymmetry in response to nodal flow (Nakamura, Saito, *et al.*, 2012). By evaluating *Cerl2* expression, I was able to test more directly whether abnormal nodal flow causes aberrant downstream gene expression – if *Cerl2* expression was normal, there could be an intermediary mechanism affecting *Cerl2* and *Pitx2* expression in these mice. This putative mechanism could act between initial changes in *Cerl2* gene expression and later changes in *Pitx2* expression, as PITX2 is the transcription factor that directly upregulates left-hand-sidedness of visceral organs.

Cerl2 is initially expressed L-R symmetrically around the node at the early head fold stage on both sides of the node. Left hand side mRNA undergoes flow-induced degradation leading to an asymmetry that can first be detected from the late head fold stage (Marques *et al.*, 2004; Nakamura, Saito, *et al.*, 2012), and is readily apparent in wild-type by the onset of somitogenesis. This expression pattern made analysis of changes in *Cerl2* mRNA levels in *Pierce1*$^{-/-}$ embryos more challenging. The change in expression is not as readily identifiable as that of genes such as *Pitx2*, with its clear-cut asymmetric expression domain of the left LPM.

After attempting to classify left and right hand side overexpression by eye, I used a computational approach. I calculated the signal intensity created by the in situ hybridisation stain using ImageJ (Schneider, Rasband and Eliceiri, 2012) and evaluated the proportion of signal intensity on the left and right hand side of the embryo. This reduced potential bias in this work, and showed that there is a significantly more

equal distribution of stain intensity either side of *Pierce1*$^{-/-}$ embryonic nodes, compared to both wild-type and heterozygous embryos.

I analysed embryos at 0-2 somite stages for this work as the asymmetry in *Cerl2* expression is required early in LR patterning to ensure correct activation of the downstream genetic cascade. Theoretically, there could be delayed *Cerl2* asymmetry in these embryos, with it being reached at a later developmental time point than is typically observed in the wild-type. However, I hypothesise that any such delay would likely impact establishment of LR patterning, as it would prevent the coordinated onset of *Nodal* and *Pitx2* expression, and thus could still play a role in the heterotaxy phenotype observed in this line. To fully evaluate delays in *Cerl2* expression, a time-course study analysing a greater number of embryos would be needed, in a similar fashion to that suggested for *Pitx2* expression above.

Regardless of whether *Cerl2* expression does eventually become asymmetric, or is merely delayed, my work has shown that the expression of the first genetic product to show asymmetry in LR patterning is significantly disrupted. These results point to an event upstream of known genetic changes associated with LR patterning as the pathological factor in the development of *Pierce1*$^{-/-}$ embryos.

2.3.5: Node morphology

SEM of embryonic nodes and statistical analysis of nodal ciliary length revealed no gross differences in node or nodal cilia morphology. This correlates with the results of Sung et al (Sung *et al.*, 2016), and adds further support to the two different null alleles of *Pierce1* exhibiting equivalent phenotypes. There was no evidence for a reduction in the number of cilia, or motile cilia, at the node, based on SEM analysis and live imaging.

The absence of an effect on node morphology demonstrates that defective LR patterning observed in these mice is not downstream of an inability to pattern and form the node itself. Mice with defects in ciliary assembly components are often observed to have abnormal ciliary morphology such as shortened or absent cilia (Morris and Scholey, 1997; Nonaka *et al.*, 1998a; Huangfu and Anderson, 2005; Mueller, 2005; Nakamura, Saito, *et al.*, 2012), or cilia with bulging tips (Pazour, Wilkerson and Witman, 1998; G J Pazour, Dickert and Witman, 1999; Gregory J. Pazour, Dickert and Witman, 1999; Porter *et al.*, 1999; Signor *et al.*, 1999; Hou, 2004). The lack of ciliary morphology abnormalities tells us that absence of PIERCE1 is not causing a defect in ciliogenesis per se, but instead implies that the defect lies solely in the components required for motility. This fits with the overall phenotype observed in these mice. As previously discussed, defective ciliogenesis presents with a range of overt and severe phenotypes, in a large part due to the requirement for cilia in vertebrate Hh signalling (Goetz and Anderson, 2010). The developmental phenotypes observed in *Pierce1*$^{-/-}$ mice are limited to those immediately downstream of a requirement for ciliary motility, further supporting the proposition that the process of ciliogenesis itself is not affected.

Although the ciliary motility analysis of this line was fairly high resolution, crossing the *Pierce1*-null line with a line containing a fluorescent tag for motile cilia (e.g. DNAH11-GFP, McGrath et al. 2003) may improve resolution of motile cilia and reduce any error associated with the background subtraction involved in my analysis. Although time-consuming, crosses of this sort could provide further insight into the nodal ciliary motility defects observed in *Pierce1*$^{-/-}$ embryos.

2.4: Conclusions

A lack of functional PIERCE1 at the embryonic node affects ciliary motility, leading to a reduced beat frequency and an increase in the

incidence of aberrant beat pattern. I propose that aberrant ciliary motility leads to a lack of reliable effective leftwards flow in the node, and that this leads to an increase in LR patterning defects in the *Pierce1*$^{-/-}$ embryo population.

There are two key questions remaining after this work:

1. What is the function of the PIERCE1 protein such that its absence leads to ciliary motility defects in the node?
2. Does homozygosity for the *Pierce1*-null allele lead to ciliary motility defects in the adult?

As for the function of the PIERCE1 protein, results in this chapter give us limited insight. The protein does appear to be solely required for ciliary motility in the embryo, based on the lack of other classical ciliogenesis or ciliary signalling phenotypes such as polydactyly (**Chapter 1.2.5; Appendix 1**). A lack of PIERCE1 leads to altered ciliary motility and thus aberrant LR patterning. What then, do we know about other proteins that are required specifically for nodal ciliary motility? Many are components of the ultrastructural apparatus that is essential for effective motility; others are necessary for the trafficking and assembly of those components.

2.4.1: Areas for future study

A future avenue for exploration that could help us with functional analysis of the PIERCE1 protein would be the evaluation of nodal ciliary cross-section by TEM. TEM evaluation of respiratory motile cilia in cross-section enables us to detect potentially causative ultrastructural defects. An investigation into ultrastructural defects in the nodal motile cilia in *Pierce1*$^{-/-}$ mice would assist us in determining the function of this protein on a subcellular level, as a lack of particular ultrastructural features could imply a potential role in their assembly or trafficking. However, this work is technically challenging, particularly as the number and density of motile

cilia in the embryonic node is low. This makes collecting sufficient numbers of images for a thorough evaluation of ultrastructure challenging. As well as this, the topology of the node, i.e. its sunken nature on the posterior face of the embryo, means many sections must be checked before slices with motile cilia are reached. It is a time consuming process that is certainly not a low hanging fruit or it would have been more seriously considered during the course of this DPhil.

The question of whether the *Pierce1*-null allele leads to ciliary motility defects in the adult is particularly of note, as children and adults with reduced ciliary motility are said to suffer from PCD (**Chapter 1.4**). This condition can be caused by multiple genes, not all of which are known, and thus the investigation of potential candidate genes could be of use in diagnostics. Therefore, a study of ciliary motility in adult tissues of *Pierce1*$^{-/-}$ mice was undertaken, focusing on motile multicilia in the respiratory tract, and sperm flagellar motility. This work is presented and discussed in **Chapter 3**.

3: *Pierce1*$^{-/-}$ mice show ciliary motility defects in adult tissues.

Motile cilia play a key role in the function of several tissues and organs in the post-natal mammal, as well as in the embryonic node. In this chapter, I will first give an overview of the role of motile cilia in the physiological function of distinct tissues in the adult. I will then discuss the rationale for investigating motile cilia in *Pierce1*$^{-/-}$ mice, before presenting the results of investigations into adult tracheal epithelial and sperm flagella. A discussion of the results in each tissue follows. A more overarching discussion, considering both sets of results as complementary data, may be found in **Chapter 6**.

3.1: Motile cilia in the adult: an introduction

Post-natally, motile multiciliated epithelia are required for the physiological function of the airways, something that is underlined by the severe respiratory disease phenotype observed in patients with PCD. Multiciliated epithelia are also implicated in the function of the ventricles of the brain, and the oviduct of the female reproductive system; their importance in both of these organs may be reduced, and appears to vary between species. In the male reproductive system, the sperm flagellum shares much of the ultrastructure of the motile cilium, and is central to successful in vivo fertilisation.

3.1.1: The ventricular system

Ependymal cells are a specialised subset of glial cells lining the ventricles of the brain (Jiménez *et al.*, 2014). Multiple motile cilia protrude from each ependymal cell into the ventricles, and the beating of these cilia aids the circulation of CSF throughout the ventricular system (Narita and Takeda, 2015). The movement of this fluid conveys nutrients and growth factors to the brain (Sakka, Coll and Chazal, 2011).

The importance of the ependymal motile cilia in preventing the development of hydrocephalus in humans may be limited. We suspect this due to the low incidence of hydrocephalus (Lucas *et al.*, 2017) in patients with PCD. Although isolated cases of PCD in combination with hydrocephalus do occur (Greenstone *et al.*, 1984; Vieira, Lopes and Silva, 2012), the presence of hydrocephalus is not indicative of a diagnosis of PCD (Behan *et al.*, 2016). PCD patients do not show an elevated incidence of hydrocephalus when compared to the general population.

Unlike the patient population, mouse knock-outs of genes known to cause PCD in humans show a high incidence of hydrocephalus (**Appendix 3**). Different inbred strains of mouse exhibit differing rates of hydrocephalus; this variation is thought to be due to genetic modifiers that

lead to ventricular anatomical differences between each strain (Lee, 2013). These differences place a greater reliance on ependymal ciliary motility as a mechanism for CSF clearance in certain inbred strains.

3.1.2: The reproductive systems

Motile cilia are found in the lining of the oviduct, and form the basis for the sperm flagella.

Sperm flagellar motility is required for oocyte fertilisation without medical intervention (Turner, 2006). After the advent of *in vitro* fertilisation techniques in 1978 (Wang and Sauer, 2006), it became apparent that sperm samples with improved motility had a higher rate of ovum fertilisation. Further techniques were developed, culminating with the development of intra-cytoplasmic sperm injection (ICSI) in 1992 (Palermo *et al.*, 1992). Now, most cases of infertility resulting from asthenozoospermia (reduced sperm motility) can be successfully treated.

The rate of fertilisation and successful pregnancy following ICSI due to asthenozoospermia is variable, and is thought to be linked to the causative defects behind the individual cases of sperm immotility (ranging from metabolic deficiencies to aberrant flagellar ultrastructure) (Ortega *et al.*, 2011). If only the flagellar ultrastructure is affected, the sperm body itself, which contains the necessary genetic information for successful reproduction, is less likely to have been damaged than in the case of, for example, a metabolic defect, and thus ICSI is more effective.

Motile cilia line the oviduct, and are thought to play a role in transporting the fertilised ovum towards the uterus (Lyons, Saridogan and Djahanbakhch, 2006). Individual case reports may indicate a higher incidence of ectopic pregnancy (implantation of the fertilised egg outside of the uterus) in women with PCD (Blyth and Wellesley, 2008), presumably due to ineffective ovum and zygote transport in the oviduct. Larger and more definitive studies have not been carried out. There are

clearly documented cases of successful pregnancies in female patients with PCD (Sivaramakrishnan, Cottee and Coon, 2015), meaning that any fertility defects are not as penetrant as the lung pathology, situs defects and male infertility that are the hallmarks of the condition. Indeed, any reduced female fertility in PCD could result from chronic respiratory infection, chronic inflammation, and resultant health issues, as opposed to being a direct consequence of ciliary motility disruption. Asthma, another respiratory condition associated with chronic inflammation, is known to be associated with longer time to pregnancy; the underlying mechanism behind this is unclear (Gade *et al.*, 2014).

3.1.3: The respiratory system: the mucociliary escalator

Motile cilia are central to one of the most important innate immune defences in the body – mucociliary transport (Bartlett, Fischer and McCray, 2008). The epithelia of the respiratory tract and lungs are exposed to numerous pathogens and pollutants every day, yet in a physiological setting, mucociliary transport ensures that these epithelia mostly remain infection-free (Ganesan, Comstock and Sajjan, 2013). The pseudostratified multiciliated epithelium is composed of approximately 60% MCCs and 20% goblet cells (Norden, 2017); basal cells and Clara cells comprise the remainder of the epithelium. The cilia beat, providing the force to move mucus which is secreted by the goblet cells and glands in the submucosa (Williams *et al.*, 2006).

MCCs are found largely in the lower respiratory tract and the nasal sinuses (Brooks and Wallingford, 2014). As we move from the major airways of the lower respiratory tract into the smaller airways lacking in cartilaginous support and mucosal glands, the epithelium becomes progressively cuboidal and less ciliated (Norden, 2017).

3.1.3.1: Motile multiciliogenesis

During lung development, the progenitors of MCCs arise from multipotent precursor cells found in the terminal buds of the branching lung. These progenitors give rise to all the cell types that will go on to compose the pseudostratified epithelium, including both goblet cells and MCCs. As detailed in **Fig. 3.1**, there are four stages to multiciliated cell development, delineated by differences in gene expression and presence of ciliary components

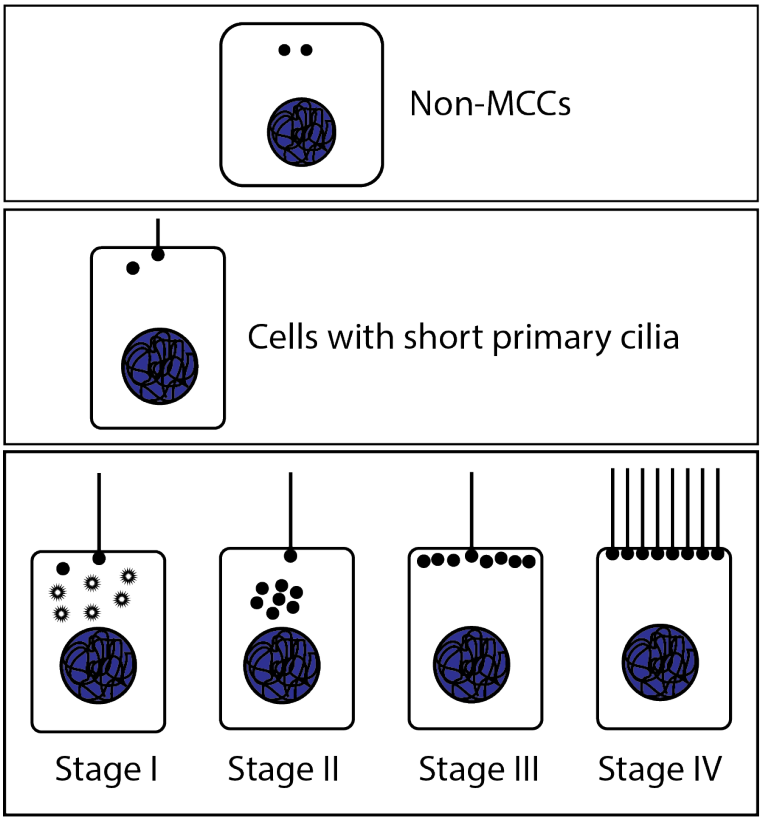


Figure 3.1: Diagrammatic representation of the differentiation of airway multiciliated cells. Non-MCCs refers to either non-differentiated basal cells, or to differentiated non-MCC cells such as goblet cells and Clara or club cells, the progenitor cells of the airway epithelium (Rokicki *et al.*, 2016). Cells with short primary cilia will differentiate into MCCs. Stage I cells are generating the components to reproduce centrioles and cilia, whilst Stage II cells are actively generating centrioles themselves. Stage III cells are recognised by centrioles migrating to the apical surface of the cell, where they will dock and form basal bodies. Stage IV cells are fully functional motile multiciliated cells (Vladar and Brody, 2013).

3.1.3.2: The airway surface layer

The airway surface layer is a layer of fluid and protein on the apical surface of the respiratory epithelium, comprised of both the periciliary and mucous layers. The rheological properties of the mucous layer are determined in a large part by macromolecular complexes termed mucins. These glycoproteins are rich in cysteines, which enables the formation of disulphide cross-bridges between mucin molecules (Bustamante-Marin and Ostrowski, 2017). Healthy mucus contains approximately 1% mucins, 1% salt, 1% other protein, and 97% water; this forms a 2-5 μm thick protective layer above the cilia that is present all the way from the bronchioles to the upper airway (Matthews LW; Spector S;Lemm J; Potter JL;, 1963; Hamed and Fiegel, 2014).

Salt concentration is central to regulating the hydration status of the mucus. In conditions where salt levels in the mucus are increased, effectively dehydrating the mucus, it becomes thick, sticky, and difficult to clear (Boucher, 2007). This occurs in CF due to mutation of the *CFTR* gene, which encodes an ion channel. A lack of this ion channel in the cell membrane leads to perturbation of the hydration status of the mucus, with thick and sticky mucus resulting. This mucus cannot be readily expelled by the motile multicilia, and thus pathogenic bacteria trapped by the mucus can proliferate in situ, causing chronic lung infection and inflammation (Randell and Boucher, 2006).

The periciliary layer (PCL) itself is as tall as the extended cilium (Button *et al.*, 2012), and lubricates ciliary movement whilst maintaining a pericellular environment. Its core components include specific mucins and glycolipids. As with the mucus layer, the hydration status of the PCL reflects its ion balance (Tarran *et al.*, 2005). In the face of inadequate hydration, the mucus layer collapses onto the PCL, hampering ciliary movement (Sleigh, Blake and Liron, 1988; Randell and Boucher, 2006).

Pulmonary surfactant is secreted by the non-ciliated cells of the epithelium (Whitsett, Wert and Weaver, 2010); some groups have proposed surfactant as lying between the mucus and PCL to facilitate kinetic energy transfer between cilia and mucus whilst preventing cilia becoming obstructed by the mucus itself (Girod De Bentzmann *et al.*, 1993; Wanner, Salathe and O'Riordan, 1996).

3.1.3.3: Ciliary beat pattern in the respiratory epithelium

Respiratory ciliary motility in the mouse is first observed post-natally as early as day 3 (Francis *et al.*, 2009). When fully developed, the respiratory motile cilia beat in a coordinated metachronal fashion. This refers to phase-shifted beating of the motile cilia along the plane of the effective stroke, with simultaneous activation of neighbouring cilia perpendicular to that plane (Sanderson and Sleigh, 1981; Brooks and Wallingford, 2014). Metachronal beating is required for effective mucociliary clearance, and is enabled by actin cross-bridges between the basal bodies of neighbouring cilia (Werner *et al.*, 2011). Correct PCP along the axis of ciliary beating is also a requirement for coordinated beating and permits appropriate orientation of the basal bodies, with the basal foot pointing in the direction of the beat (Vladar *et al.*, 2015).

3.1.4: Rationale for experimental work

The defects observed in embryonic nodal motile cilia in *Pierce1*$^{-/-}$ mice raised the question of whether motile cilia found in adult tissues displayed similar defects. X-gal staining as part of the IMPC has shown that *Pierce1* is expressed in all adult tissues with motile cilia (**Chapter 4**). This added further weight to the necessity of investigations into putative defects in the function of motile cilia in the adult.

Although there is conservation between the ultrastructure of nodal and other motile cilia in the human, there is evidence that certain proteins are only required in particular classes of motile cilia (Mitchison and

Valente, 2017). A gene that causes defects in nodal ciliary motility when deleted may have no effect on motile cilia in other tissues. Notably, distinct classes of motile cilia (nodal, multiciliated, flagella) have distinct forms of movement, so it follows that there may be ciliary components regulating this motility that are unique to each ciliary form. Moreover, there appear to be multiple gene families that contribute genetic products required for particular aspects of ciliary motility, and this could lead to degeneracy, with an effect on ciliary motility observed in some tissues and not others. As such, the finding of aberrant ciliary motility in the node did not necessarily mean that other classes of motile cilia would be similarly affected.

I hypothesised that motility defects may affect the tracheal epithelium and sperm flagella in *Pierce1*$^{-/-}$ mice. This would strengthen the argument for *Pierce1* to be considered as a candidate PCD-causative gene, and thus to be included in genetic screening for the disease. As the extent to which the motile cilia lining the fallopian tube are required for correct fertilisation and implantation of zygotes is uncertain, this was not a focus of my work.

3.2: Results of investigations into adult tracheal ciliary motility

3.2.1: Ciliary beat frequency is significantly reduced in *Pierce1*$^{-/-}$ mice.

Due to the reduced CBF often seen in patients with PCD, determining whether *Pierce1*$^{-/-}$ mice also showed any difference in CBF was a key part of tracheal ciliary motility analysis. I harvested tracheas from 12 wild-type, 10 heterozygous and 10 *Pierce1*$^{-/-}$ mice at 8-10 weeks of age. Tracheas were sent via same-day courier to the PCD team at Southampton Hospital, where James Thompson cleaned the tracheas and incubated individual tracheal rings overnight (**EM8.1, EM8.2**). He took DIC videos of motile cilia present in the tracheal epithelium of a maximum of five rings of cartilage from each individual mouse. An ImageJ plugin was used to conduct a Fourier Fast Transform analysis of mean tracheal CBF in each ring. I analysed the data, using a generalised linear mixed model to determine statistical significance. This accounted for individual mouse identity as a potential confounding factor in determining the significance of changes in mean population beat frequency.

I found that the mean CBF of the tracheal epithelium of *Pierce1*$^{-/-}$ mice was significantly lower than that of wild-type and heterozygous littermates (**Table 3.1, Fig. 3.2**). There was a significant ($p<0.05$) stepwise drop between the CBF of wild-type (23.261 Hz) and heterozygous (20.905 Hz) mice, and again between that of heterozygous and *Pierce1*$^{-/-}$ mice (19.243 Hz). It seemed possible that a sub-population of *Pierce1*$^{-/-}$ mice with a more severe phenotype could be underlying the statistical significance. I therefore used graphical analysis to display CBF results by mouse identity. This demonstrated no such subpopulation, with reduced CBF scores occurring throughout the *Pierce1*$^{-/-}$ population (**Fig. 3.3**).

I observed that the mean CBF values appeared to be clustering in two putative populations of motile cilia in the *Pierce1*$^{-/-}$ animals. I hypothesised that this could be due to the presence of two classes of motile cilia, with different physiological beat frequencies in wild-type animals, with a change in distribution between these classes in the *Pierce1*$^{-/-}$ mice and to a lesser extent in the heterozygous mice. I binned data points by mean CBF (**Fig. 3.4**) to create a histogram. There was no evidence of a "dual population" of tracheal motile cilia in the wild-type environment, and I concluded that a change in putative class allocation or cell fate was unlikely to be the determining factor in the significant drop in CBF observed in heterozygous and *Pierce1*$^{-/-}$ cilia.

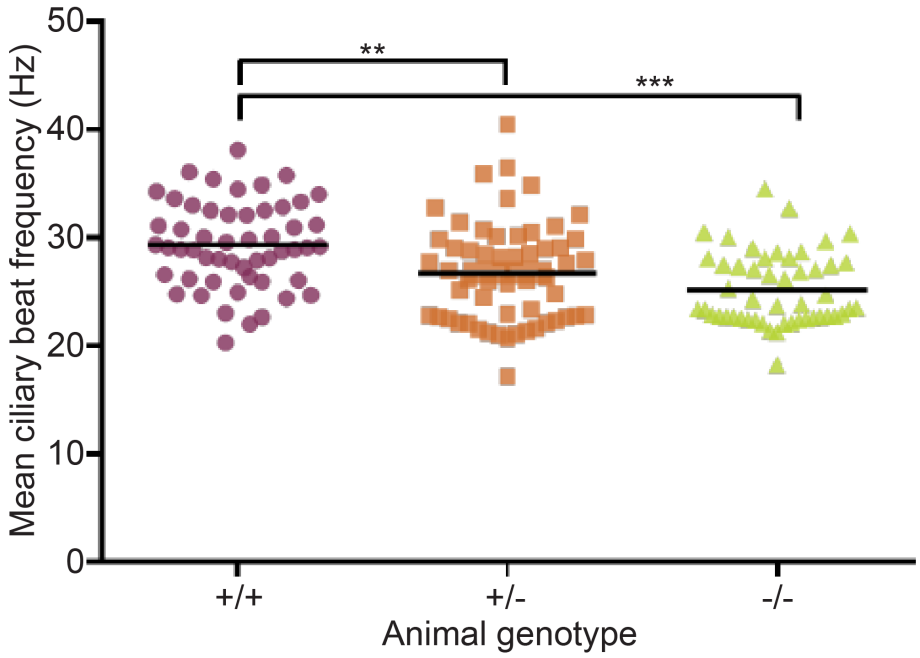


Figure 3.2: Ciliary beat frequency is significantly reduced in *Pierce1*$^{-/-}$ mice.
Mean ciliary beat frequency of tracheal motile cilia by genotype. 5 ring sections taken per animal. n= 10+/+, 10+/- and 10-/- **p = 0.024 ***p =0.001

Genotype	Ciliary beat frequency estimate (Hz)	Std. Error	df	t	Sig.	95% Confidence Interval	
						Lower Bound	Upper Bound
Pierce1*$^{+/+}$ *(intercept)	*23.2*	*1.1*	*164.6*	*20.6*	*0.000*	*21.0*	*25.5*
***Pierce1*$^{+/-}$**	*20.9*	*0.8*	*154.2*	*-3.1*	*0.003*	*-3.9*	*-0.8*
***Pierce1*$^{-/-}$**	*19.2*	*0.8*	*153.8*	*-5.0*	*0.000*	*-5.6*	*-2.4*

Table 3.1: Ciliary beat frequency is significantly reduced in *Pierce1*$^{-/-}$ mice.
Mean ciliary beat frequency of tracheal motile multicilia and statistical analysis of results. Intercept = mean value for wild-type cilia, when a normal distribution has been applied to the data .

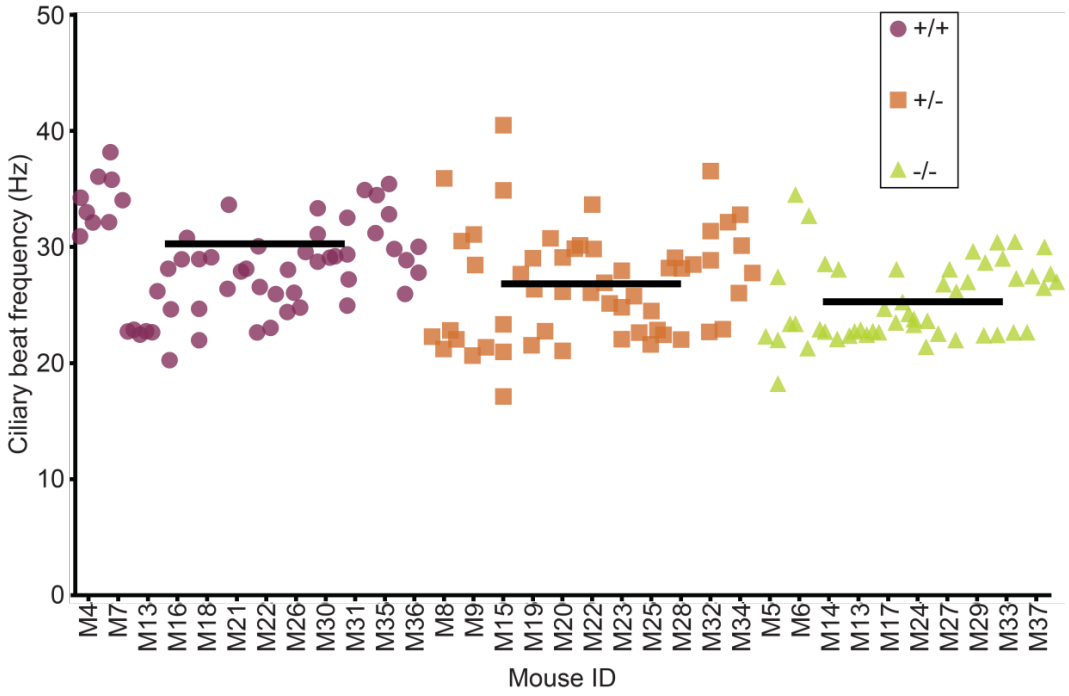
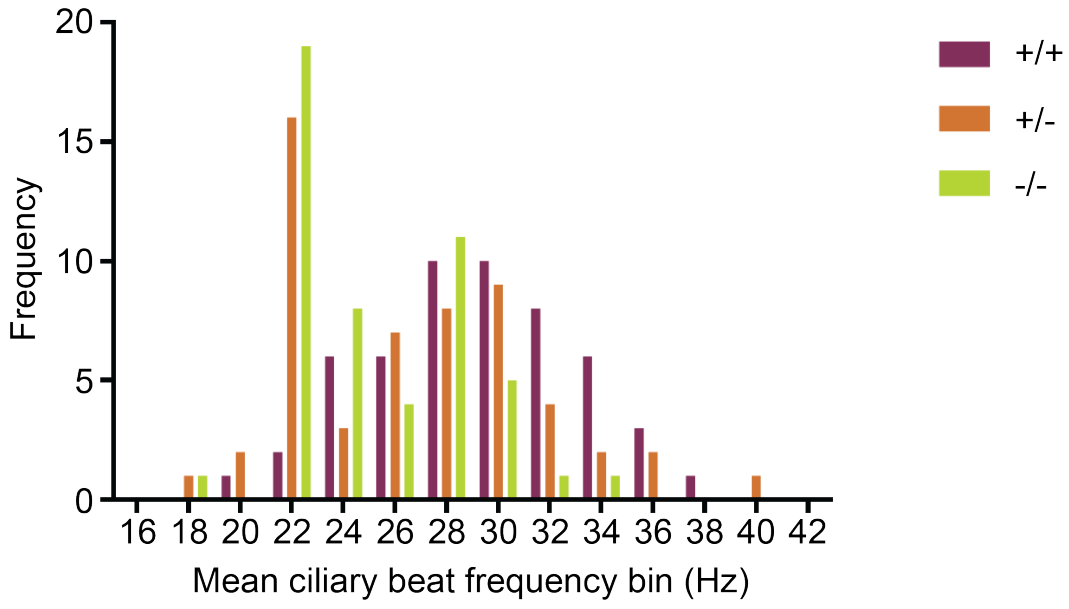


Figure 3.3 (top): Variation in ciliary beat frequency measurements does not arise from a small population of severely affected animals.
Tracheal ciliary beat frequency ordered according to identity of the mouse from which the tracheal rings were taken.
Figure 3.4 (bottom): A dual population of ciliary beat frequencies are not present in tracheal cilia.
Histogram of tracheal ciliary beat frequencies observed in *Pierce1*$^{-/-}$, heterozygous and wild-type animals, demonstrating no obvious existence of a dual population of motile cilia in the wild-type.



3.2.2: *Pierce1*$^{-/-}$ mice show an increase in stiff ciliary beat pattern.

Live imaging of the motile cilia in the tracheal epithelium has shown that patients with PCD often display altered CBP, for example stiff beating. A stiff beat pattern shows less of a whip-like recovery stroke, and so the power and recovery strokes are less easily distinguished (Bustamante-Marin and Ostrowski, 2017). **Fig. 3.5** shows the movement of one tracheal motile cilium through its beat cycle, with the effective or power stroke in black and the recovery stroke in turquoise. This diagram shows a full amplitude stroke; a beat stroke with reduced amplitude would exhibit a reduced range of motion. Another potential affected area of ciliary motility in patients with PCD is beat synchrony. Tracheal motile cilia should beat metachronally to facilitate effective mucociliary clearance. Beat synchronisation refers to this coordinated pattern of ciliary movement.

Differences in CBP and synchrony were also evaluated in *Pierce1*$^{-/-}$ mice (**Fig. 3.6, Table 3.2**). DIC videos of ciliary beating from tracheal sections of *Pierce1*$^{+/+}$, $^{+/-}$ and $^{-/-}$ animals were independently scored by three diagnostic scientists at the Southampton PCD Centre, blind to genotype. Videos were annotated with the predominant CBP observed; other beat patterns that were present but not predominant were also noted. Potential beat pattern scores included “normal”, “stiff”, “weak residual movement”, and “completely immotile”. Beat synchronisation and amplitude were also evaluated (**Fig. 3.7; Table 3.3, 3.4**). Beat synchronisation was scored as “present”, “absent” or “unable to analyse”. Beat amplitude was scored as “full range”; “diminished” or “unable to analyse”.

I unblinded the videos and analysed the resulting data. *Pierce1*$^{-/-}$ samples (n=10) show an increase in stiff beat pattern, with a total of 17 annotations of dominant beat pattern as stiff compared to 6 total

annotations for wild-type cilia (**Fig. 3.6, Table 3.2**). No wild-type (n=12) or heterozygous (n=10) videos were annotated with stiff beating by all three scientists concordantly, yet two *Pierce1*$^{-/-}$ videos were. Tracheas from two *iv/iv* male mice were included blind in the analysis. These mice carry a mutation in *Dnah11* and are known to have aberrant ciliary motility, both in the node (Okada *et al.*, 1999) and in the respiratory epithelium (Lucas *et al.*, 2012). *DNAH11* has been shown to cause PCD in humans (Bartoloni *et al.*, 2002; Schwabe *et al.*, 2008; Knowles *et al.*, 2012) when mutated.

Both *iv/iv* videos were annotated with stiff beat pattern by two out of three scientists, providing reference points for the threshold of potentially pathological disrupted CBP. A difference in beat synchronisation pattern between *Pierce1* genotypes was not observed (**Table 3.3**). There may be a difference in beat amplitude between wild-type, *Pierce1*$^{-/-}$ and heterozygous mice, but the large proportion of videos annotated with "unable to analyse" in the *Pierce1*$^{-/-}$ population made this difficult to confirm (**Fig. 3.7, Table 3.4**).

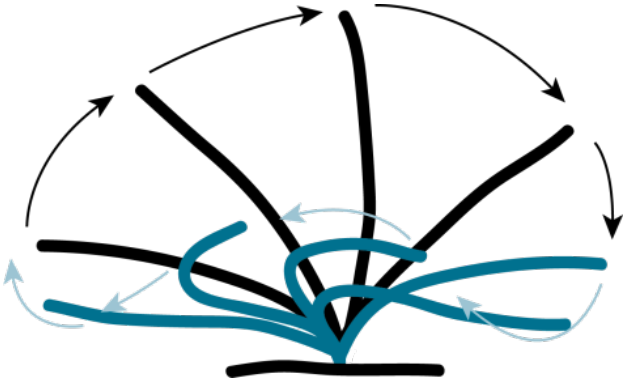


Figure 3.5: Diagrammatic representation of physiological beat pattern observed in MCCs. The power (black) and recovery (turquoise) strokes are shown; directionality is marked by arrows. Based on Raidt et al. 2014.

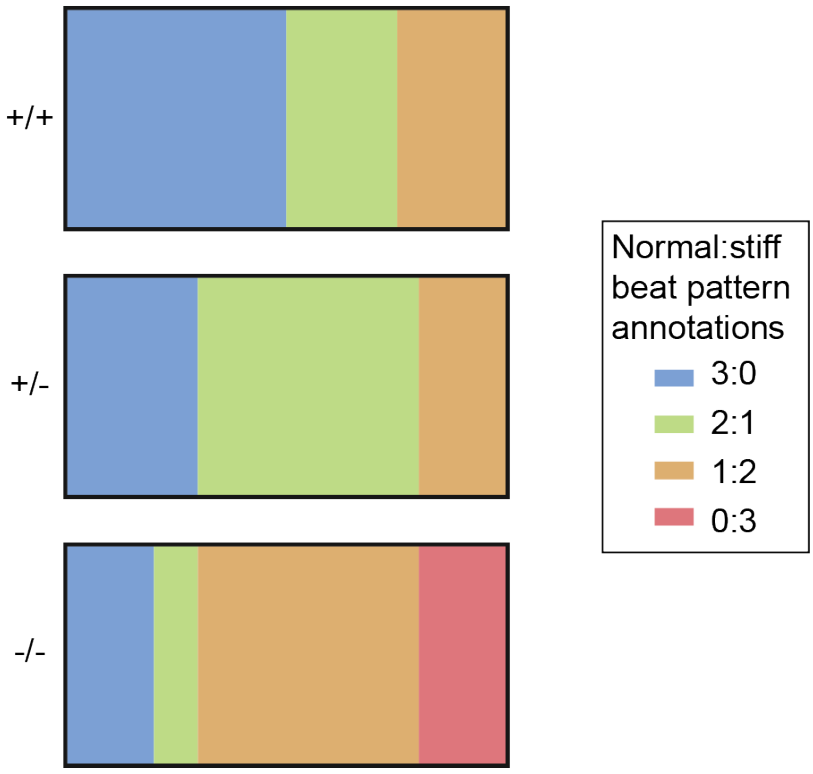


Figure 3.6 (top): *Pierce1*$^{-/-}$ mice have an increase in stiff ciliary beat pattern.
Bar chart showing ratio of ciliary beat pattern annotations by three diagnostic scientists upon viewing videos of tracheal cilia from *Pierce1*$^{+/+}$, *Pierce1*$^{+/-}$ and *Pierce1*$^{-/-}$ mice. 3:0 = three scientists annotated stiff beating; 0:3 = three scientists annotated normal beating.
Table 3.2 (bottom): Table showing distribution of annotation ratios.

		Ciliary beat pattern score			
		3/3 normal	2/3 normal	2/3 stiff	3/3 stiff
Genotype	*Pierce1*$^{+/+}$	6	3	3	0
	Pierce1$^{+/-}$	3	5	2	0
	Pierce1$^{-/-}$	2	1	5	2
	iv/iv	0	0	2	0

	Amplitude (number of annotations by three scientists across all videos)		
Genotype	*Full range*	*Diminished*	*Unable to analyse*
Pierce1$^{+/+}$	*25*	*3*	*5*
Pierce1$^{+/-}$	*20*	*1*	*12*
Pierce1$^{-/-}$	*15*	*10*	*5*

	Synchronisation (number of annotations by three scientists across all videos)		
Genotype	*Present*	*Absent*	*Unable to analyse*
Pierce1$^{+/+}$	*31*	*1*	*2*
Pierce1$^{+/-}$	*32*	*0*	*1*
Pierce1$^{-/-}$	*27*	*0*	*3*

***Pierce1$^{-/-}$* tracheal motile cilia may show a slight decrease in beat amplitude, but show no deficits in synchronisation.**
Table 3.3 (top): Table showing beat synchrony annotations by genotype for all videos analysed.
Table 3.4 (bottom): Table showing beat amplitude annotations by genotype for all videos analysed.

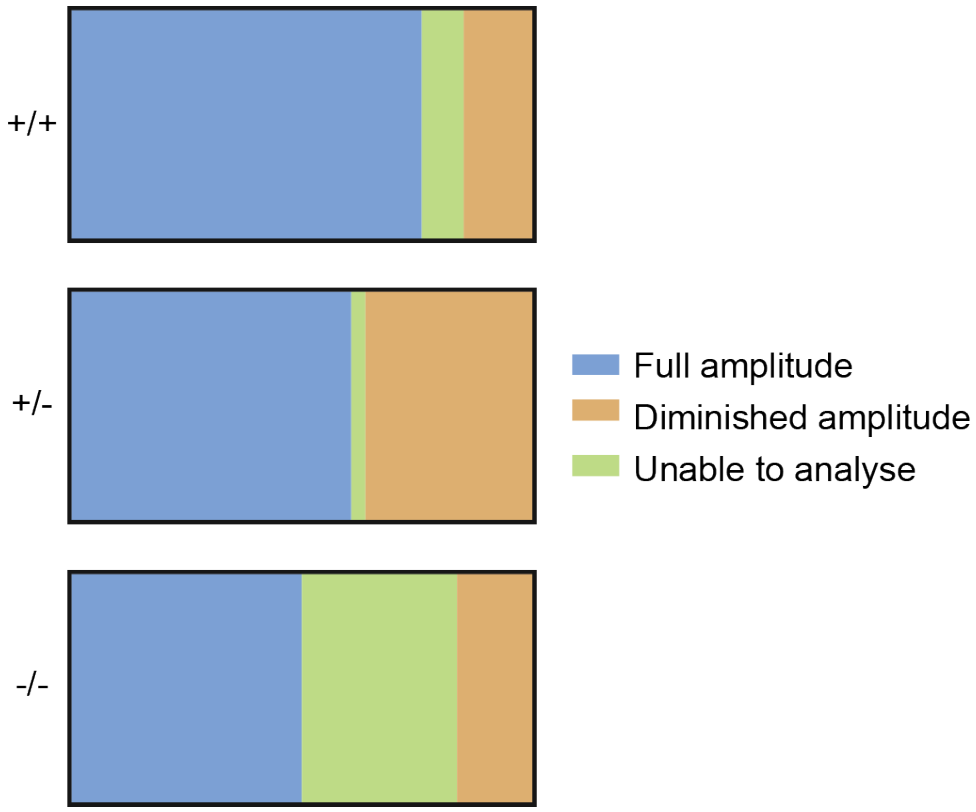


Figure 3.7: *Pierce1*$^{-/-}$ tracheal motile cilia may show a slight decrease in beat amplitude.
Amplitude annotations taken by diagnostic technicians, shown by genotype.

3.2.3: No significant differences in airway pathology are observed between *Pierce1*$^{+/+}$ and *Pierce1*$^{-/-}$ animals.

I hypothesised that *Pierce1*$^{-/-}$ mice may show similar respiratory illness to mouse models of PCD due to their defective tracheal ciliary motility. Patients with defective ciliary motility typically present with chronic respiratory infection and inflammation (Lucas *et al.*, 2017). Although humans with lung conditions such as PCD and CF exhibit bronchitis, sinusitis is more commonly observed in mouse models of both diseases (Zariwala, Knowles and Omran, 2007; Ostrowski *et al.*, 2010; Wilke *et al.*, 2011; Lucas *et al.*, 2012; Norris and Grimes, 2012). As such, investigations into the presence of airway inflammation in the nasal cavities were undertaken.

I investigated airway pathology by analysing aged wild-type and *Pierce1*$^{-/-}$ mice via histopathology (5 males, 5 females of each genotype, all aged to 6 months). Mice were sacrificed using Schedule 1 methods. The Histology Core Team at MRC Harwell Institute sectioned the heads and stained with haematoxylin and eosin to reveal the presence of any inflammatory exudate. No difference in nasal passage occlusion was observed in pathology slides, and a representative image for both male (**Fig. 3.8, top**) and female (**Fig. 3.8, bottom**) mice is shown, with sections at three different points through the skull (**Fig. 3.9**). Animal husbandry staff members were alerted to the possibility of respiratory distress as a welfare concern for *Pierce1*$^{-/-}$ animals; no such distress was observed.

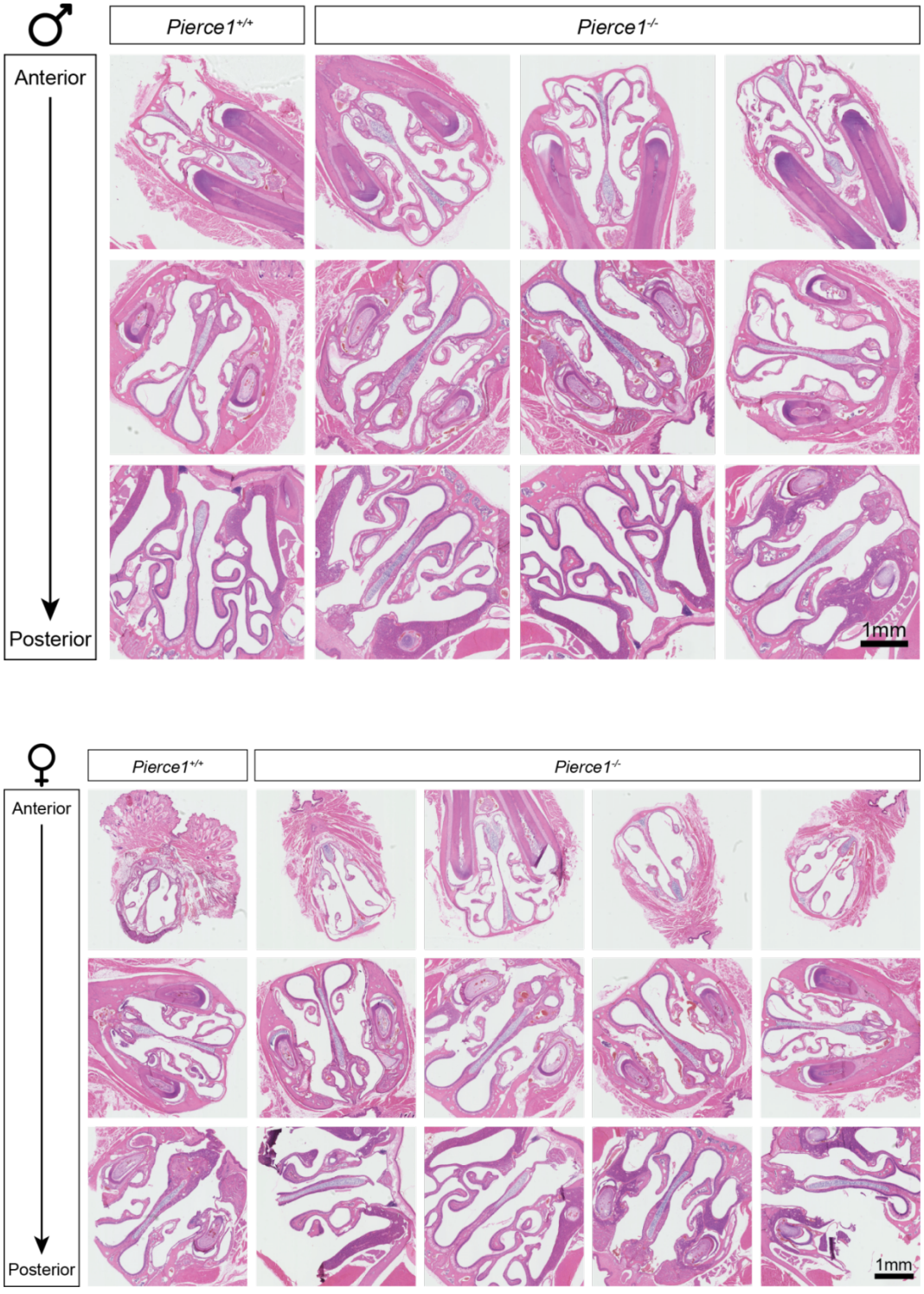


Figure 3.8: *Pierce1*$^{-/-}$ and wild-type nasal cavities show no mucus accumulation and are indistinguishable.
Haematoxilyn and eosin stained sections through the nasal cavities of *Pierce1*$^{+/+}$ and $^{-/-}$ mice, aged to six months. Male (top) and female (bottom) animals showed no evidence of an increase in airway inflammatory exudate or mucus accumulation when compared to wild-type. Scale bar shows 1 mm. n=6 mice evaluated per sex and genotype, 1 wild-type and 4 representative *Pierce1*$^{-/-}$ image sets displayed.

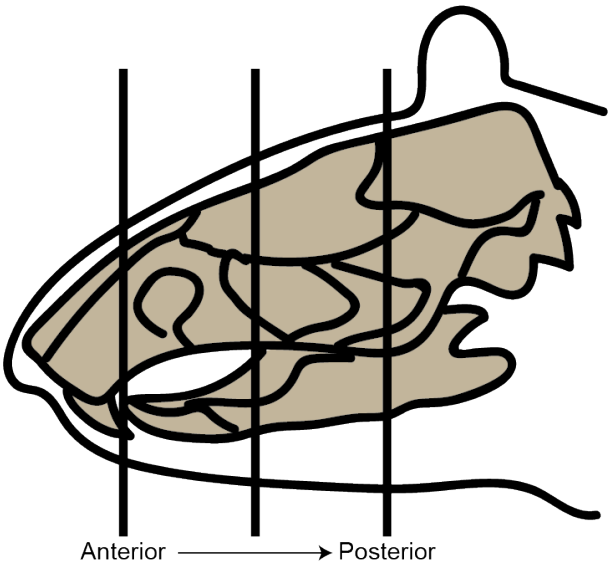


Figure 3.9: Schematic showing approximations of sections through murine nasal cavities, brightfield images are shown in **Fig. 3.8**.

3.2.4: *Pierce1*$^{-/-}$ mice show a significant increase in dynein arm defects in the motile cilia of the respiratory epithelium.

Where possible, investigation of beat frequency and pattern in PCD patients is carried out in parallel with immunofluorescence and TEM analysis of motile ciliary cross sections. These analyses can identify ultrastructural defects that may be responsible for aberrant ciliary motility. Ultrastructural components such as axonemal microtubules and dynein arms have a greater density when stained with osmium tetroxide, and TEM has played an important role in furthering our understanding of the structure of both motile and immotile cilia, in both physiological and pathological states. Although not all ultrastructural defects can be visualised with TEM, there are certain "hallmark defects" which have been associated with particular PCD-causing mutations (**Fig. 3.10**).

Defects can occur in the microtubule doublet arrangement in the axoneme, as well as in the dynein arms which are a requirement for correct ciliary motility. It should be noted that dynein arms are arranged in a spiral staircase fashion around the axonemal microtubules, and thus it is rare to find all 9 ODAs present at the same stage (Satir and Christensen, 2007). As such, a cilium would be tagged as defective for ODAs if less than 7 were present. IDAs are smaller and less easily annotated by TEM (Satir and Christensen, 2007); therefore less than 5 IDAs need to be present for an IDA defect to be annotated.

Particular defects have been associated with specific genes, and TEM analysis was carried out on motile cilia from *Pierce1*$^{-/-}$ mouse tracheas with the aim of comparing any detectable ultrastructural defect with other better-characterised genes. It was anticipated that this could provide an insight into a potential biochemical function for PIERCE1.

Tracheas harvested CBF analysis were used for this work (n=3 wild-type mice, n=4 from *Pierce1*$^{-/-}$ mice). Tracheal rings were prepared,

imaged and scored by James Thompson (Southampton University). I analysed the resulting data. Motile cilia in tracheas from *Pierce1*$^{-/-}$ mice were compared to those from wild-type littermate controls. For analysis of microtubule arrangement, n=749 cilia (+/+) and 1258 (-/-) were examined. Microtubules exhibited the canonical 9+2 arrangement in wild-type cilia (**Fig 3.11**: A; diagrammatic representation shown in panel F). This arrangement was also observed in from *Pierce1*$^{-/-}$ mice; no significant difference was detected by statistical analysis (**Fig. 3.12**).

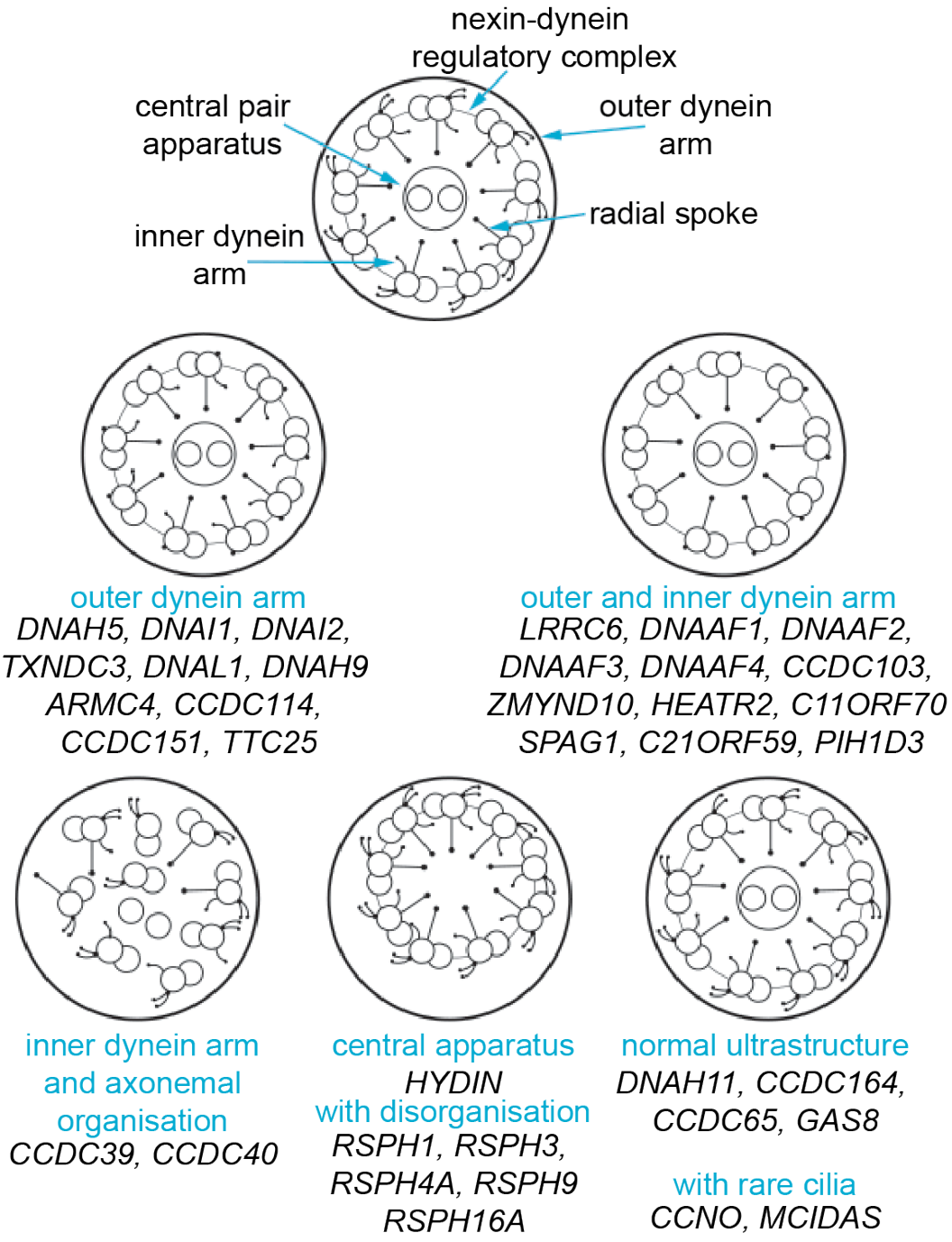


Figure 3.10: Diagrammatic representation of canonical ultrastructural defects detectable by TEM analysis, and the PCD-causative genes with which these defects are associated.

For evaluation of dynein arm defects, n=387 cilia +/+ and 597 cilia -/- were examined. In wild-type cilia, most dynein arms are present in each cross-section as described above (**Fig. 3.11; A**). A schematic of this dynein arm arrangement is shown for reference (**Fig. 3.11; F**). Dynein arms were not present to the same extent in cilia from *Pierce1*$^{-/-}$ samples, with a range of IDA and ODA defects observed (**Fig. 3.11, B-E**). When statistically analysed, a significant difference in dynein arm defects was evident between wild-type cilia and those from *Pierce1*$^{-/-}$ samples (**Fig. 3.13**; $p<0.0005$, Fisher's exact test). Dynein arms are required for ciliary motility, and thus the inner arm defect found in cilia from *Pierce1*$^{-/-}$ mice could be causative for the motility defects seen in these cilia.

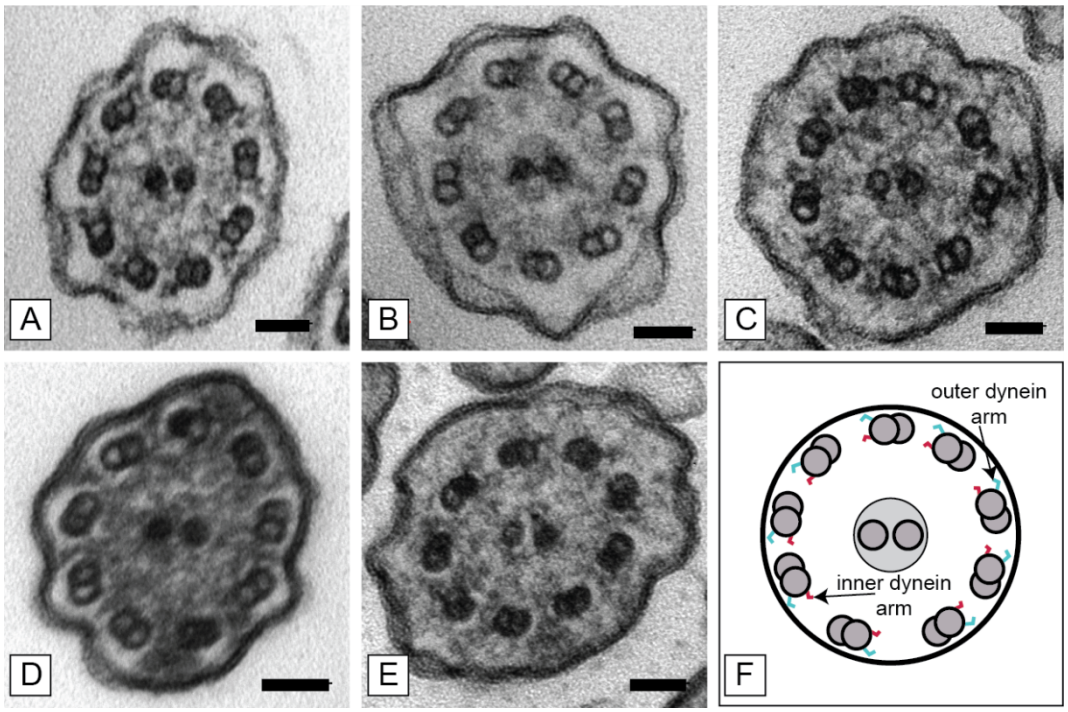


Figure 3.11: *Pierce1*$^{-/-}$ tracheal motile cilia exhibit inner and outer dynein arm defects.
High-resolution examples of wild-type (A) and from *Pierce1*$^{-/-}$ (B-E) cilia cross-sections, imaged by TEM. B-E show evidence of the dynein arm defects statistically analysed in **Fig. 3.12** and **Fig. 3.13**. Panel F shows a simplified diagram of structures that we would expect to be readily detected in a TEM cross-section. Scale bar shows 50nm.

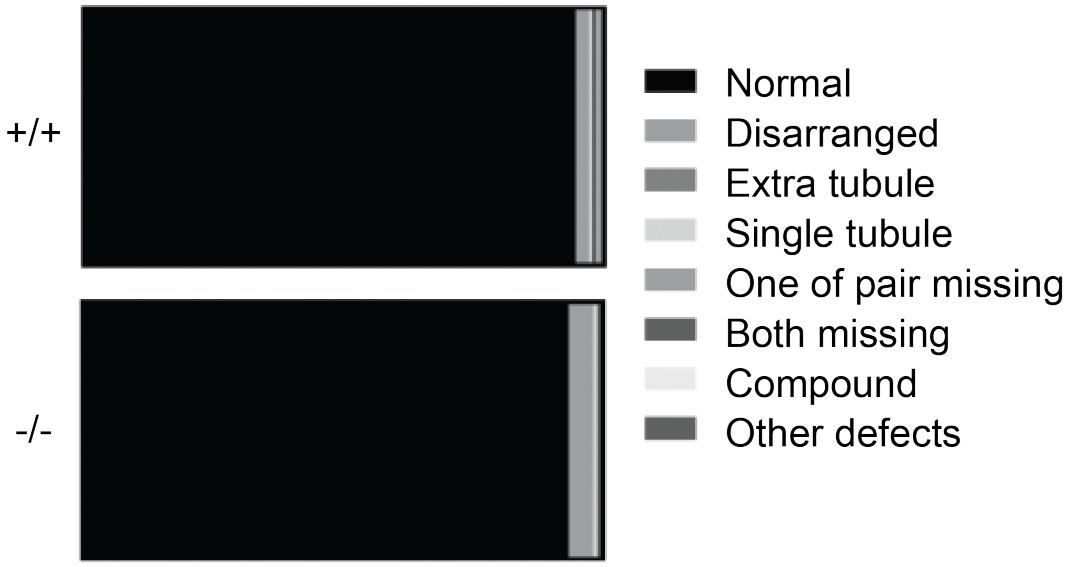
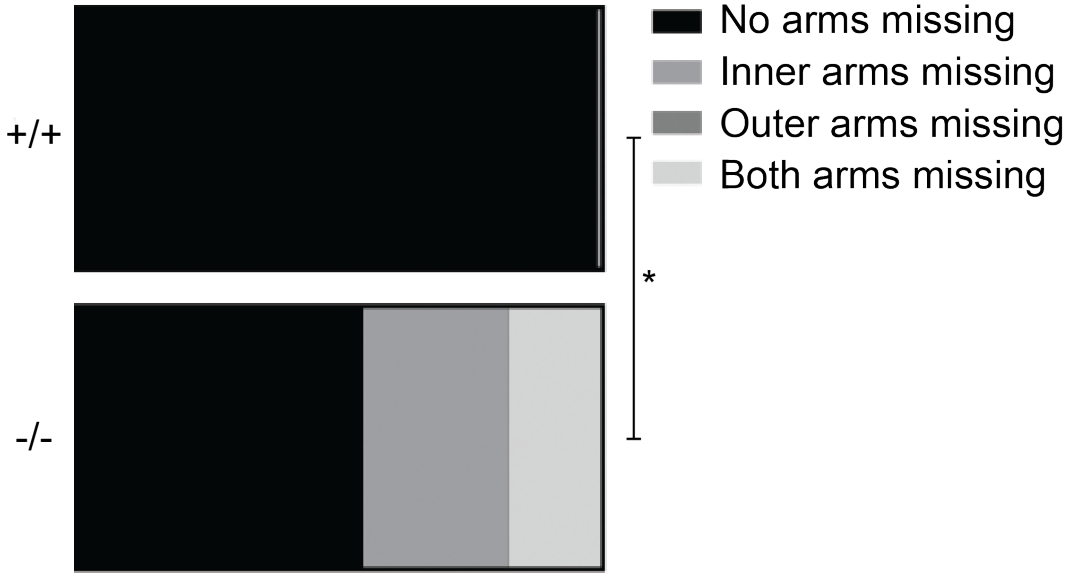


Figure 3.12 (top): *Pierce1*$^{-/-}$ tracheal motile cilia exhibit no microtubule defects.
Graphical depiction of proportion of microtubule defects observed. n= 3 animals +/+, 4-/-; n=749 cilia (+/+) and 1258 (-/-). N.S.
Figure 3.13 (bottom): *Pierce1*$^{-/-}$ tracheal motile cilia exhibit inner and outer dynein arm defects.
Graphical depiction of proportion of dynein arm defects observed in wild-type and *Pierce1*$^{-/-}$ mice. n= 3 animals +/+, 4-/-; n=387 cilia +/+ and 597 cilia -/-. *p<0.0005, Fisher's exact test.



3.3: Discussion of tracheal ciliary motility

Pierce1$^{-/-}$ mice showed a reduction in CBF and an increase in stiff beat pattern compared to wild-type littermate controls. This points to PIERCE1 as a likely modifier of ciliary motility in the tracheal epithelium, as well as in the motile cilia of the node.

I carefully controlled for experimental factors that can lead to altered CBF and/or pattern. Increases in temperature are known to lead to increased CBF, and vice versa, so tracheal rings were allowed to equilibrate at 37^{o}C in the microscope chamber for an hour prior to data collection. All samples were blinded with regards to genotype and sex. Mice used in this analysis were 8-10 weeks of age; statistical analysis of the effect of genotype on beat frequency included sex and mouse identity of tracheal rings as potential confounding factors. All *Pierce1*$^{+/+}$, $^{+/-}$ and $^{-/-}$ mice were littermates from *Pierce1*$^{+/-}$ intercross matings, controlling for any strain-specific differences in ciliary motility and ensuring that the genetic background of the mice was as similar as possible. This *Pierce1*-null allele is congenic on C57BL/6N, which again minimised genetic variation.

In the UK, most video analysis of tracheal CBF is carried out at 37^{o}C. Other laboratories follow different protocols, notably video recording at room temperature (25^{o}C) to more closely mimic the conditions experienced in vivo by the respiratory epithelium. Adding video recording at 25^{o}C as well as 37^{o}C to our protocol would have been minimally disruptive as concerns the labour required, as well as potentially unmasking a motility defect only present when CBF is naturally reduced by the lower air temperature.

It must be noted that many videos were tagged as poor resolution by the diagnostic scientists, meaning that the scientists were unable to analyse amplitude and synchronisation accurately. This poor resolution is due to the difference in sample preparation between patient and mouse

samples. Patients have nasal brushings taken and cultured, allowing a "top view" of the CBP, whilst mouse tracheal rings only provide a "side view" (**Fig. 3.14**). The analysis of tracheal rings also required a greater resolving distance, contributing to some of the resolution issues. Occasionally mucus or fibrous tissue can adhere to the epithelial face of the tracheal rings and obstruct cilia movement, causing secondary motility issues. This is easily identified by an experienced diagnostician and so is unlikely to have had a major impact on this analysis. Together, these issues may have hampered the accurate identification of beat pattern throughout all videos analysed.

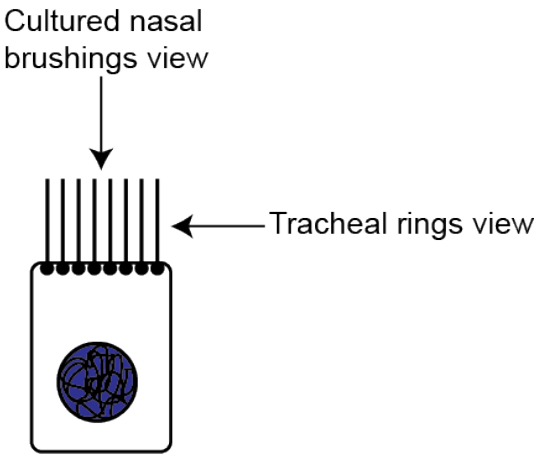


Figure 3.14: Diagrammatic representation of the differing viewpoints of tracheal ring and nasal cell cilia during diagnosis.

Airway pathology investigations did not show inflammatory exudate present in the nasal cavities of *Pierce1*$^{-/-}$ mice. This is potentially not surprising, as the approximately 17% drop in CBF is subtle in comparison to other mouse models of PCD. For example, a conditional knock-out of *Dnaic1* shows virtually immotile tracheal cilia (Ostrowski *et al.*, 2010), which is a much starker defect than that observed in this line. The more subtle defect may explain the lack of accumulation of inflammatory exudate in the nasal cavities of these mice. An additional factor to consider in evaluating this data is the housing of these mice in an SPF facility. This would have dramatically reduced their contact with pathogens, and moving mice to an SPF facility is known to drastically reduce the mucus accumulation phenotype in some PCD-causative gene null lines (personal communications, Heymut Omran).

There are other reasons to believe that the *Pierce1* knock-out leads to a less severe ciliary motility phenotype than knock-out mouse models of PCD – many of these cause severe hydrocephalus and perinatal lethality in homozygous affected mice (**Appendix 3**). Indeed, a desire to study adult ciliary motility without hydrocephalus-associated mortality was the driving factor behind the creation of the *Dnaic1* conditional knock-out model (Ostrowski *et al.*, 2010). Large-scale hydrocephalus was not observed in *Pierce1*$^{-/-}$ pups, and although we suspect some in utero/perinatal loss of *Pierce1*$^{-/-}$ mice due to heterotaxy resulting from defective LR patterning, we did not struggle to raise adult *Pierce1*$^{-/-}$ mice of either sex.

Hydrocephalus is not commonly associated with PCD in humans (Lucas *et al.*, 2014). This may be due to the differences in anatomy and posture between the two species that lead to a greater reliance in the mouse on ependymal motile cilia for circulation of CSF in the ventricles. We know that *Pierce1* is expressed in the ependyma through X-gal staining (**Chapter 4.2.1**, available at http://www.mousephenotype.org/data/genes/MGI:1916577). We hypothesise that PIERCE1 is either not a requirement for motile ciliary function at all in the ependymal environment, or that the residual levels of ciliary motility are sufficient to ensure CSF flow and avoid hydrocephalus-associated mortality.

An additional factor in the lack of airway pathology in these animals may have been the lack of an infectious “challenge”. The mice were maintained in a specific-pathogen free facility. This is in stark contrast to patients with PCD, who interact with pathogens on a regular basis, and for whom it is impractical to live in a largely sterile environment. Potentially, when appropriately exposed to a respiratory pathogen, the *Pierce1*$^{-/-}$ mice may have shown a greater susceptibility to infectious challenge than their

wild-type littermates due to their aberrant ciliary motility, and presumably altered mucociliary clearance.

Further investigations of mucociliary clearance itself are challenging. The trachea is a relatively thick, cartilaginous structure. The application and analysis of the movement of fluorescent microspheres, as utilised in the embryonic node, would be challenging on a practical level without seriously damaging the trachea itself, although a report of in vivo examination of mucociliary clearance of fluorescent beads in the mouse has recently been published (Rogers *et al.*, 2018). This protocol could be considered as a future area of investigation for this mouse line (Sears, Yin and Ostrowski, 2015; Bustamante-Marin and Ostrowski, 2017). The direct visualisation of mucociliary clearance in the *Pierce1*$^{-/-}$ state has its challenges but is a worthwhile area to explore.

Correlative differences in ciliary ultrastructure were evaluated by TEM. This work demonstrated a reduction in IDAs, and an increase in incidence of a dual outer and inner defect occurring simultaneously. We did not observe a decrease in ODAs alone; this hints that the *Pierce1* gene product is likely not acting as a dynein arm ultrastructural component, but instead as a trafficking or assembly factor (Horani and Ferkol, 2018). Defects in one structural component tend to cause absence of that component specifically, whereas assembly factor defects cause heterogeneous absence of both inner and outer arms.

Dyneins are believed to be synthesised in the cell body, before trafficking towards the base of the cilium. The Wallingford laboratory proposed the idea of dynein assembly factories in 2017 (Huizar *et al.*, 2017) and hypothesised that dynein assembly factors cluster at the apical surface of the cell along with chaperones and dynein arm components, in order to facilitate dynein arm assembly. This hypothesis was further explored in a recent publication (Huizar *et al.*, 2018), which identified a

liquid-phase separated putative organelle, termed the DynAP (dynein assembly particle), as the site of dynein assembly.

Multiple PCD-causing genes have been allocated a “dynein arm assembly factor (DNAAF)” identity based on their effect on dynein arms; that is to say, when mutated, these genes lead to variable dynein arm defects. Five DNAAFs (Omran *et al.*, 2008; Loges *et al.*, 2009; Horani *et al.*, 2012; Mitchison *et al.*, 2012; Tarkar *et al.*, 2013) have been identified thus far, largely due to their ciliary ultrastructure phenotype, their cytosolic localisation, and their interaction with each other, as assayed via co-immunoprecipitation (IP). DNAAF proteins appear to localise to DynAPs, where we would presume they play a role in assembling dynein arms.

TEM studies of *Pierce1*$^{-/-}$ mice show similar dynein arm defects to those observed in patients with DNAAF mutations (Horani and Ferkol, 2018), potentially hinting at a role for PIERCE1 in these assembly complexes. Many questions remain surrounding dynein assembly, and it is clear that we do not have a complete understanding of the requisite proteins; the TEM and ciliary motility phenotypes observed in the *Pierce1*$^{-/-}$ mice correlate with a putative role for PIERCE1 as a dynein assembly factor, potentially acting in the DynAP. Localisation studies to investigate this further appear to provide a compelling line of future study.

To demonstrate DynAP localisation patterns, the Wallingford group performed co-expression studies using tagged forms of DNAAFs and dynein arm components in *X. laevis* culture (Huizar *et al.*, 2018). Replicating a study of this style in the mouse has its challenges. Mouse tracheal epithelial cells can be cultured to develop a functional tracheal epithelium, including motile ciliated cells. However, transfection with tagged proteins is challenging, and transformation using lentivirus would be required. Antibodies against multiple DynAP components would be another way to demonstrate co-localisation of PIERCE1 with DynAPs;

however anti-mouse antibodies against dynein arm components and DNAAFs have not been successfully validated. Commercially available antibodies against PIERCE1, as well as a rabbit poly-clonal synthesised by us against PIERCE1, have not been successfully validated in our hands. These lines of enquiry would require a substantial amount of optimisation to ensure reliability.

3.4: Sperm flagellar motility

3.4.1: Introduction

Mammalian sperm consist of a head, a mid-section and a tail or flagellum (**Fig. 3.15**). The head contains tightly packaged DNA (Borg *et al.*, 2009) as well as an acrosomal tip, which contains the enzymes required to break down the zona pellucida of the ovum. The mid-section contains a large number of mitochondria to provide energy for the movement of the flagellum. The flagellum itself is a highly conserved, evolutionarily ancient, part of eukaryotic cells, and believed to derive from the last eukaryotic common ancestor (Margulis *et al.*, 2006). Sperm flagella are composed of an axonemal core similar to other motile cilia, such as those in the tracheal epithelium, and exhibit a 9+2 microtubule doublet structure.

The sperm flagellum contains a number of accessory structures in addition to the 9+2 microtubule axoneme (Borg *et al.*, 2009). These include the helical mitochondrial sheath, present in the mid-piece of the spermatozoon. The outer dense fibre is found in the mid- and principal pieces, whilst the fibrous sheath is found only in the principal piece. The outer dense fibre (Baltz, Williams and Cone, 1990) and fibrous sheath both provide structural rigidity to the flagellum, protecting it against the shear forces that it will endure during swimming. The outer dense fibre also has a proposed role in regulating tail motility (O'Bryan *et al.*, 1998; Nakamura *et al.*, 1999), whilst the fibrous sheath provides a site for ATP generation via glycolysis (Eddy, Toshimori and O'Brien, 2003; Miki *et al.*, 2004), as well as providing a scaffold for signal transduction cascades (Nakamura *et al.*, 1999; Eddy, Toshimori and O'Brien, 2003). None of these additional structures are found in motile cilia elsewhere in the body.

In light of our results showing that motile cilia are adversely affected elsewhere in *Pierce1*$^{-/-}$ mice, we hypothesised that a lack of functional

PIERCE1 would be unlikely to impact these more specialised structures unique to the sperm flagellum, but that a lack of PIERCE1 may affect axonemal construction and thus flagellar motility. Therefore, experiments were designed to assess sperm motility and any deficits in axonemal ultrastructure.

Computer-assisted sperm analysis (CASA) refers to analysis of sperm movement using light microscopy and a computer programme. CASA was first developed by several labs in the 1990s (Amann and Waberski, 2014), and is now standard practice for sperm quality assessment. CASA utilises computing analysis and a light microscope to track individual spermatozoa and analyse their motility patterns, assessing a variety of motility characteristics and assigning general motility classes to each sperm cell. It allows high through-put assessment of sperm motility by analysing each spermatozoon as a distinct clustering of object points, or diffraction spheres, which can be tracked from frame-to-frame. Due to the subtle differences in ciliary motility observed in the analysis of tracheal and nodal motile cilia, computer-aided analysis was clearly the preferred method for analysing sperm motility.

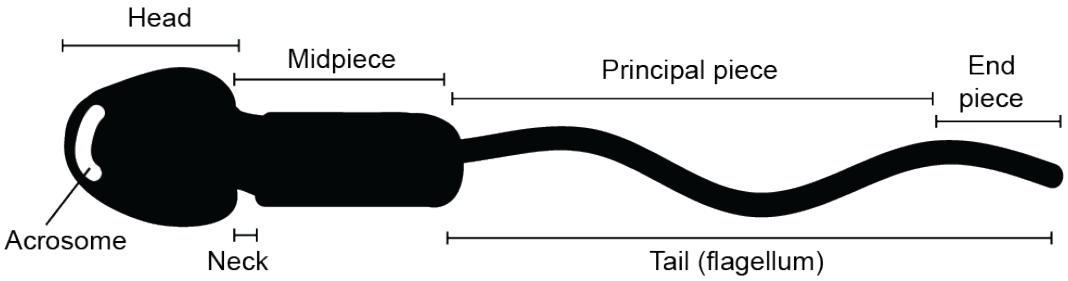


Figure 3.15: diagrammatic representation of spermatozoon structure.

Studies have demonstrated that CASA can predict male fertility rates with greater accuracy than traditional methods alone, across a range of species (Amann and Waberski, 2014). Distinct analysis settings are utilised for the spermatozoa of different species, to allow for species-specific differences in motility. Overlapping yet distinct sets of predictive

variables exist for different species, due to the differing natures of spermatozoa and fertilisation (**Fig. 3.16, Table 3.5**). For example, in humans lateral head displacement (ALH), and curvilinear velocity (VCL) have both been found to be predictive of fertility. No correlation was observed between beat cross frequency (BCF), average path velocity (VAP), linearity (LIN) and straightness (STR) (Hirano *et al.*, 2001) and fertility. However, in turkeys, a positive correlation has been found between straight line velocity (VSL), LIN and BCF and sperm mobility (King, Holsberger and Donoghue, 2000). A wide range of heterogeneity, both within samples from the same individual, and between distinct individuals from the same species, has been noted.

In addition to motility parameters, CASA can also assess sperm morphology. Abnormal sperm morphology (teratozoospermia) has long been assumed to play a role in male infertility (Kumar and Singh, 2015). However, this was questioned by a recent study that showed high rates of fertility in the face of abnormal morphology (Kovac *et al.*, 2016); the story is clearly not complete. Elongation and area are two parameters analysed by CASA that are indicative of altered sperm morphology.

CASA has in the past been used to demonstrate strain-specific differences in sperm motility in inbred mouse strains (Goodson *et al.*, 2011). As such, it was particularly important to use littermate controls in this work to ensure that we were properly controlling for strain-related sperm motility issues.

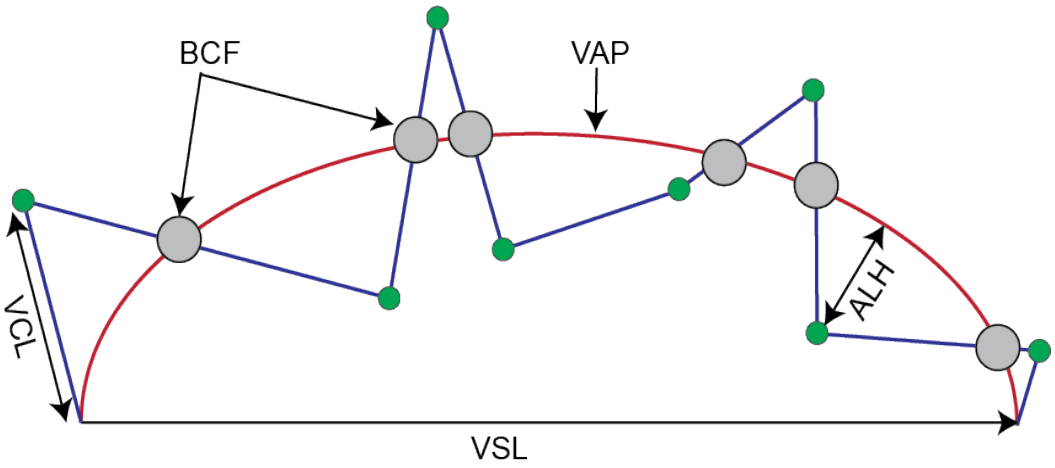


Figure 3.16: Diagrammatic representation of a CASA track. Actual track (VCL) = navy; smoothened track (VAP) =red. Straight line distance (VSL) and lateral head displacement (ALH) are denoted by black arrowed lines. Points at which the actual track crosses the smoothened track are marked by grey circles (BCF).

CASA attribute (Amann and Waberski, 2014)	***Definition***
Curvilinear velocity (VCL)	*The distance of the actual sperm track, including head movement deviations, divided by total track time.*
Average path velocity (VAP)	*The distance of a derived, smoothed path, divided by total track time.*
Straight line velocity (VSL)	*The straight line distance between the start and end points of the track, divided by total time.*
Lateral head displacement (ALH)	*Average deviation of the sperm head from the smoothened path.*
Beat cross frequency (BCF)	*The frequency with which the sperm head crosses the smoothened path.*
Linearity (LIN)	*The straight line distance divided by the sum of the incremental distances along the actual path (VSL/VCL)*
Straightness (STR)	*The straight line distance of the smoothed path divided by the distance of the smoothed path (VSL/VAP)*
Elongation	*Mean ratio of width: length of sperm head.*
Area	*Mean area of all analysed sperm heads*

Table 3.5: CASA attributes and their definitions.

3.5: Results of investigations into adult sperm flagellar motility.

3.5.1: Computer-assisted sperm analysis demonstrates significant differences in some motility attributes between *Pierce1*$^{+/+}$ *and Pierce1*$^{-/-}$ sperm.

To gain insight into sperm flagellar motility in *Pierce1*$^{-/-}$ mice, I utilised CASA. I harvested testes from 6 wild-type and 6 from *Pierce1*$^{-/-}$ mice and isolated a sperm sample from each cauda epididymides, collected via a "swim up" method (**EM8.3**). I analysed 10 fields of view from each sperm sample via CASA and processed the resulting data, which was analysed using a generalised linear mixed model to account for testis identity and mouse identity as potential confounding factors.

I found no significant difference ($p<0.05$) between wild-type and from *Pierce1*$^{-/-}$ sperm samples with regard to VCL, VAP and VSL (**Fig. 3.17, Table 3.6**). ALH was also found to show no significant difference. This implied that the overall velocity of the sperm is, on average unchanged irrespective of *Pierce1* genotype. However, BCF showed a significant increase between wild-type and *Pierce1*$^{-/-}$ animals, whilst LIN and STR showed a significant decrease. These data suggested that *Pierce1*$^{-/-}$ sperm had a disrupted track of motion, with more head twitching compared to distance travelled than their wild-type counterparts.

Table 3.6: *Pierce1*$^{-/-}$ sperm exhibit no gross flagellar motility defects. Statistical analysis of CASA data collected for wild-type and *Pierce1*$^{-/-}$ sperm, analysed by a generalised linear mixed model. Intercept = mean value for wild-type spermatozoa, when a normal distribution is applied to the data

Motion attribute	Estimate	Standard error	t value	p value	Lower 95% confidence interval (of odds ratio)	Upper 95% confidence interval (of odds ratio)
			Area (μm^2)			
Intercept	35.9	5.0	7.2	0.000	25.9	45.8
Pierce1$^{-/-}$	-11.7	6.7	-1.7	0.102	-25.1	1.6
			Beat cross frequency (Hz)			
Intercept	22.0	1.1	20.6	0.000	19.9	24.1
Pierce1$^{-/-}$	3.1	1.4	2.1	0.035*	0.2	5.9
			Elongation (%)			
Intercept	45.7	1.6	28.3	0.000	42.5	48.9
Pierce1$^{-/-}$	-3.4	2.2	-1.6	0.117	-7.8	0.9

	Lateral head displacement (μm)					
Intercept	*8.5*	*17.0*	*0.5*	*0.619*	*-25.3*	*42.2*
Pierce1$^{-/-}$	*21.0*	*23.1*	*0.9*	*0.365*	*-24.9*	*66.9*
	Linearity (%)					
Intercept	*39.1*	*0.9*	*42.1*	*0.000*	*37.2*	*40.9*
Pierce1$^{-/-}$	*-6.4*	*1.3*	*-4.9*	*0.000**	*-8.9*	*-3.8*
	Straightness (%)					
Intercept	*60.1*	*1.0*	*59.9*	*0.000*	*58.2*	*62.1*
Pierce1$^{-/-}$	*-5.8*	*1.4*	*-4.1*	*0.000**	*-8.5*	*-3.0*

	Curvilinear velocity (μm/s)					
Intercept	*134.1*	*11.4*	*11.8*	*0.000*	*111.5*	*156.7*
Pierce1$^{-/-}$	*24.6*	*15.5*	*1.6*	*0.117*	*-6.2*	*55.3*
	Average path velocity (μm/s)					
Intercept	*81.8*	*6.8*	*12.1*	*0.000*	*68.3*	*95.2*
Pierce1$^{-/-}$	*5.5*	*9.2*	*0.6*	*0.554*	*-12.8*	*23.8*
	Straight line velocity (μm/s)					
Intercept	*51.9*	*3.8*	*13.8*	*0.000*	*44.4*	*59.4*
Pierce1$^{-/-}$	*1.1*	*5.2*	*0.2*	*0.843*	*-9.2*	*11.3*

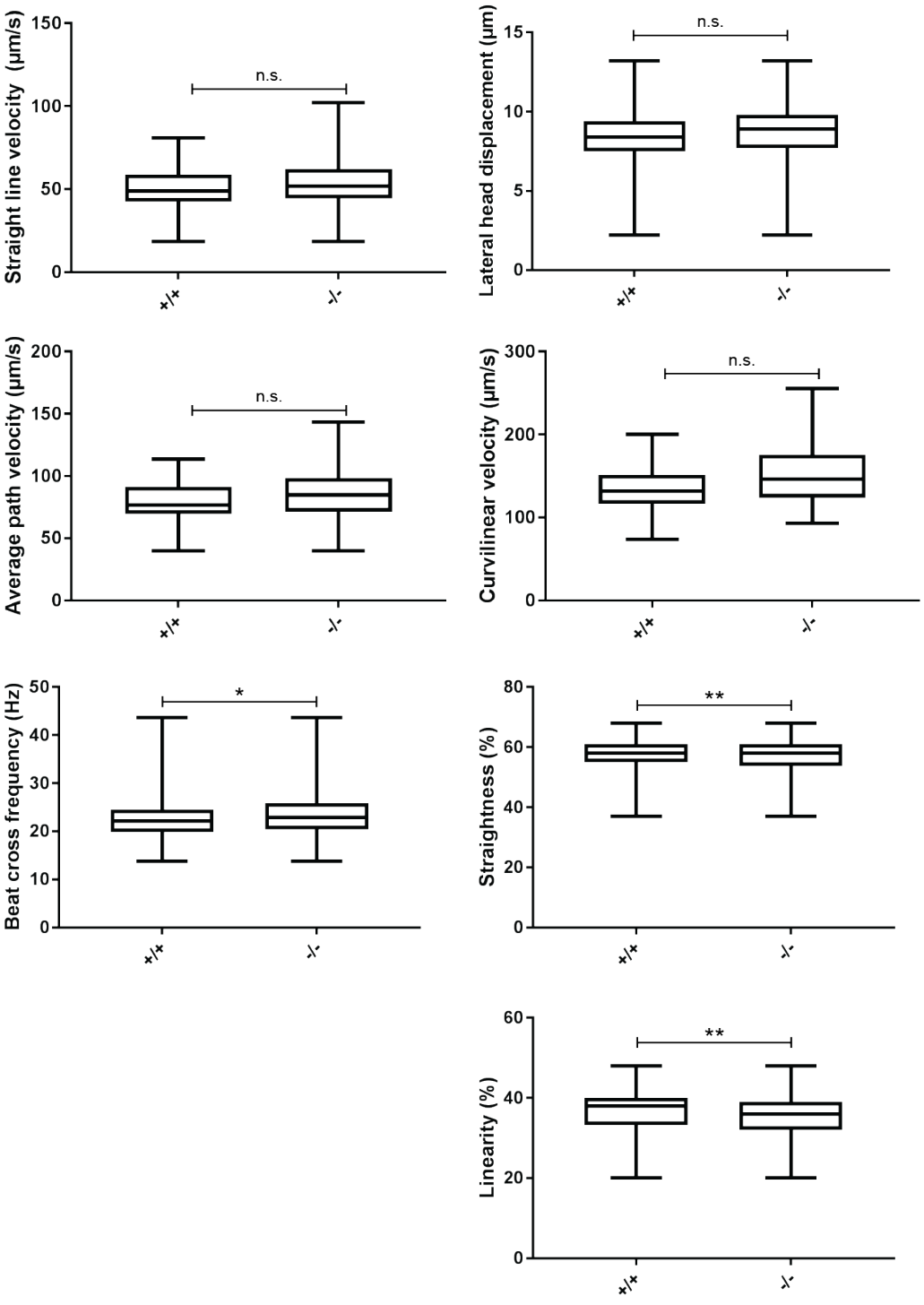


Figure 3.17: *Pierce1*$^{-/-}$ sperm exhibit no gross flagellar motility defects. Graphical representation of CASA motility attributes. Significant attributes are denoted by * ($p<0.05$) and ** ($p<0.005$). n = 5 mice per genotype, both testes evaluated individually. Five fields of view analysed per testis sample.

3.5.2: *Pierce1*$^{-/-}$ sperm show no significant difference in morphology attributes, compared to *Pierce1*$^{+/+}$ sperm.

I also used CASA to evaluate sperm morphology. I found no significant difference when comparing the area and elongation of *Pierce1*$^{-/-}$ and wild-type sperm (**Fig. 3.18, Table 3.6**). Abnormal sperm morphology was not detected in *Pierce1*$^{-/-}$ sperm in this study, nor was any difference obviously detectable by eye. There is debate within the field as to the extent to which abnormal morphology is associated with sperm motility defects; as no sperm morphology defects were detected, it is unlikely that this underlies the differences in sperm flagellar motility detected in the *Pierce1*-null line.

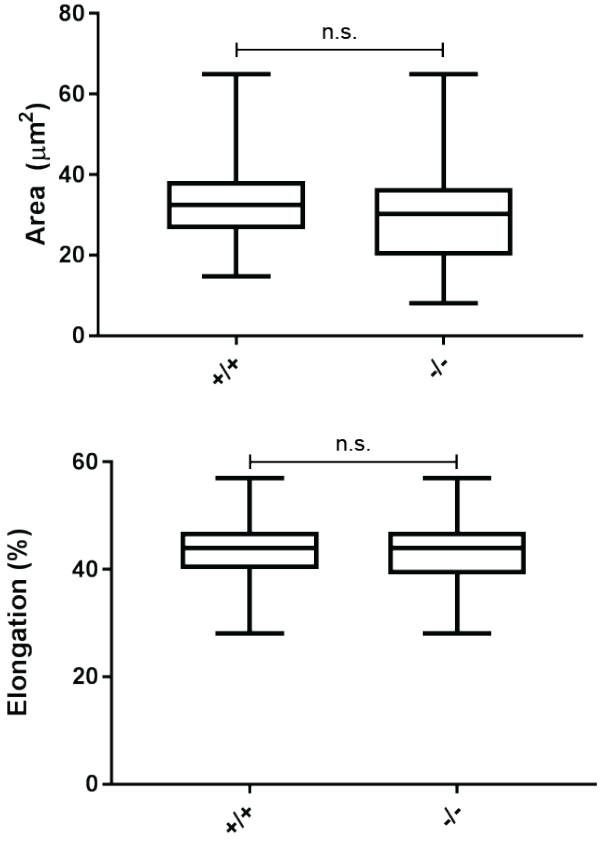


Figure 3.18: *Pierce1*$^{-/-}$ **sperm exhibit no gross flagellar morphology defects.** Graphical representation of CASA morphology attributes. n = 5 mice per genotype, both testes evaluated individually. Five fields of view analysed per testis sample.

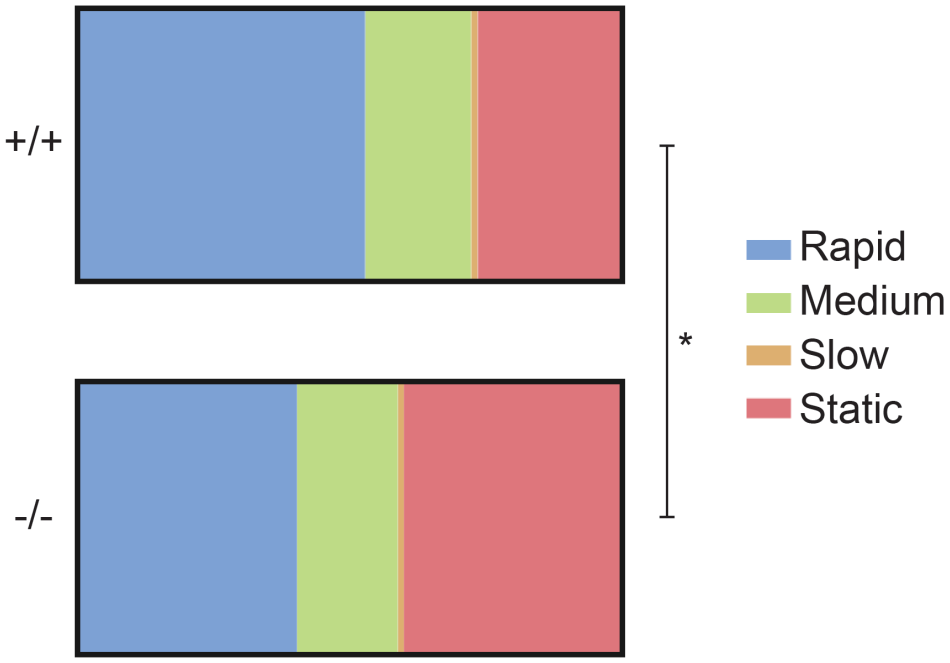
3.5.3: *Pierce1*$^{-/-}$ sperm samples show a decrease in "rapid" swimming and an increase in "static" sperm.

CASA classifies sperm as belonging to one of four motility categories: rapid (>50 μm/s), medium (25-50 μm/s), slow (<25 μm/s) or static. When I analysed these classifications I found a statistically significant difference in the proportions of the motility classes between the wild-type and Pierce1$^{-/-}$ sperm samples (**Fig. 3.19**). *Pierce1*$^{-/-}$ samples showed an increased proportion of static sperm, and a decreased proportion of rapid sperm, compared to wild-type sperm samples.

3.5.4: *Pierce1*$^{-/-}$ sperm samples show a significant decrease in total sperm count.

CASA evaluates motility parameters by averaging values across all sperm counted per genotype. To investigate whether there could also be differences in sperm count between wild-type and *Pierce1*$^{-/-}$ animals, I summed the number of sperm evaluated by genotype. Wild-type samples have a greater sperm count than *Pierce1*$^{-/-}$ samples (**Fig. 3.20**); I used a generalised linear mixed model to show that this difference is statistically significant.

Sperm samples utilised in CASA are collected through a "swim-up" method. I dissected each cauda epididymis away from the male reproductive tract and pricked it 10 times with a needle, before incubating each cauda in 1% bovine serum albumin (BSA) in PBS (phosphate-buffered saline) at 37^{o}C (**EM8.3**). This should bias the sample to contain fully developed motile sperm that literally "swam out" of the cauda epididymis. In the case of a reduced sperm count, it is difficult to ascertain whether this is due to a reduction in overall sperm production, or due to a reduction in sperm motility leading to fewer sperm being collected.



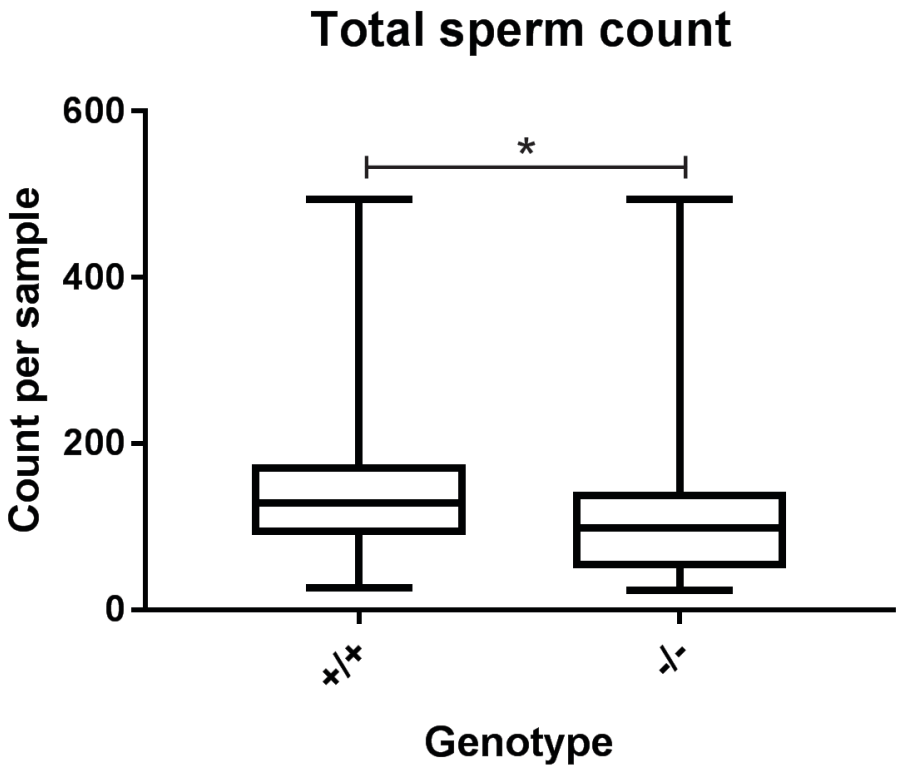


Figure 3.19 (top): *Pierce1*$^{-/-}$ sperm exhibit a decrease in the proportion of rapidly swimming sperm. Sperm motility classification by genotype. * = $p<0.05$. n = 5 mice per genotype, both testes evaluated individually. Five fields of view analysed per testis sample.

Figure 3.20 (bottom): *Pierce1*$^{-/-}$ sperm show a reduced sperm count. Mean sperm count per sample observed in wild-type and *Pierce1*$^{-/-}$ animals. Statistical analysis via a generalised linear mixed model, * = $p<0.05$. n = 5 mice per genotype, both testes evaluated individually. Five fields of view analysed per testis sample.

3.5.5: *Pierce1* expression initiates in concordance with a wave of flagellar motility-related genes.

The development of motile spermatozoa in the mouse testis is well characterised (Bellve *et al.*, 1977; Hess and Moore, 1993), and occurs in three successive stages: mitotic (approximately 10 days in length); meiotic (approximately 11 days in length) and post-meiotic (approximately 14 days in length) (Eddy, 2002). These stages are further subdivided (**Table 3.7**) (Borg *et al.*, 2009). The mitotic phase initiates immediately post-natally. Axonemal extension occurs from 20 days, and the first fully mature spermatozoa are produced by 35 days post-partum (dpp). Spermatogenesis then continues successively in waves throughout the seminiferous tubules, with developing spermatids at all described time points present chronologically along the length of the tubule. The time points given in **Table 3.7** mark the first occurrence of specific stages in spermatogenesis in the postnatal testis.

Table 3.7 (p134): Stages of spermatogenesis in the developing and post-natal mouse testis, including the time that each developing cell type is first observed.

Process	*Cell Type*	*Time of first appearance*
	Gonocyte	*12 dpc-1 dpp* (Burgoyne, 1987)
Spermatogonial specification	*Spermatogonia (As, Apr and Aal)*	*6 dpp* (Bellve *et al.*, 1977)
Spermatogonial differentiation	*Spermatogonia (A1-4, In- and B-)*	*8 dpp* (Bellve *et al.*, 1977)
	Pre-leptotene	*10 dpp*
Meiosis I (primary spermatocytes)	*Leptotene*	*10 dpp*
	Zygotene	*12 dpp*
	Pachytene	*14 dpp* (Bellve *et al.*, 1977)
	Diplotene	*17-18 dpp* (Nebel, Amarose and Hackett, 1961)
Meiosis II	*Secondary spermatocytes*	*18 dpp* (Bellve *et al.*, 1977)
	Round spermatids	*20 dpp* (Bellve *et al.*, 1977)
Spermiogenesis	*Condensing spermatids*	*30 dpp*
	Spermatozoa	*35 dpp* (Kramer and Erickson, 1981)

The field of transcriptomics has played an important role in furthering our understanding of changes in gene expression associated with spermatogenesis. Early research classified broad groups of gene expression change, and gene expression change associated with cell types present in the developing and adult testis (Almstrup *et al.*, 2004; Shima *et al.*, 2004). More recent work has associated gene expression change clusters with gene ontology (GO) terms and KEGG pathways (Laiho *et al.*, 2013), giving us a greater insight into the processes implicated by changes in gene expression. Notably, genes associated with "cilium" and "flagellum" show a significant increase in expression when comparing 17 dpp transcripts with those present at 21 dpp, concomitant with motile ciliogenesis in round spermatids. This provides evidence for onset of expression of transcripts required for sperm flagellar motility occurring in this timeframe.

The *Pierce1* allele used for this work includes a lacZ reporter. I was therefore able to use X-gal staining of testis cryosections to demonstrate whether or not we could see a spatiotemporal onset of *Pierce1* expression in the testis, related to the onset of sperm motility. At 14 dpp, sperm flagellar motility has not initiated, and we would expect no expression of genes associated with flagellar motility. At 18 dpp, flagellar motility is initiating, and any resulting changes in gene expression have strengthened by 22 dpp. At 35 dpp, the first sperm have reached complete maturity; we would expect continued expression of genes related to sperm motility to continue throughout adulthood. As such, testes were harvested from mouse pups at these time points, before cryosectioning and X-gal staining.

A tightly controlled expression pattern was observed as predicted, with onset of X-gal staining observed between p18 and p22 in *Pierce1*$^{+/-}$ and *Pierce1*$^{-/-}$ mice (**Fig. 3.21**), but not in wild-type mice (data not shown). Nuclear Fast Red counterstaining was used to make wild-type tissue with

no X-gal staining more visible (**Fig. 3.22**); staining after 18 dpp can still be observed in *Pierce1*$^{+/-}$ and *Pierce1*$^{-/-}$ counterstained tissue. An enlarged DIC image is also presented (**Fig. 3.23**) however it is difficult to conclude with certainty which cell types in the testis sections are showing expression. These results suggested that immunohistochemical analysis of PIERCE1 expression using an antibody may provide further insight into its localisation pattern in the testis.

Figure 3.21 (p138): *Pierce1* expression initiates with the onset of motile ciliary gene expression.
X-gal staining in testis cryosections shows initiation of lacZ reporter expression between 18 and 22 dpp in *Pierce1*$^{+/-}$ and *Pierce1*$^{-/-}$ mice. Tubules showing stained cells are denoted by arrows. Scale bar shows 100 μm. n = 2 mice per genotype at each time point. n = 8 sections per mouse.

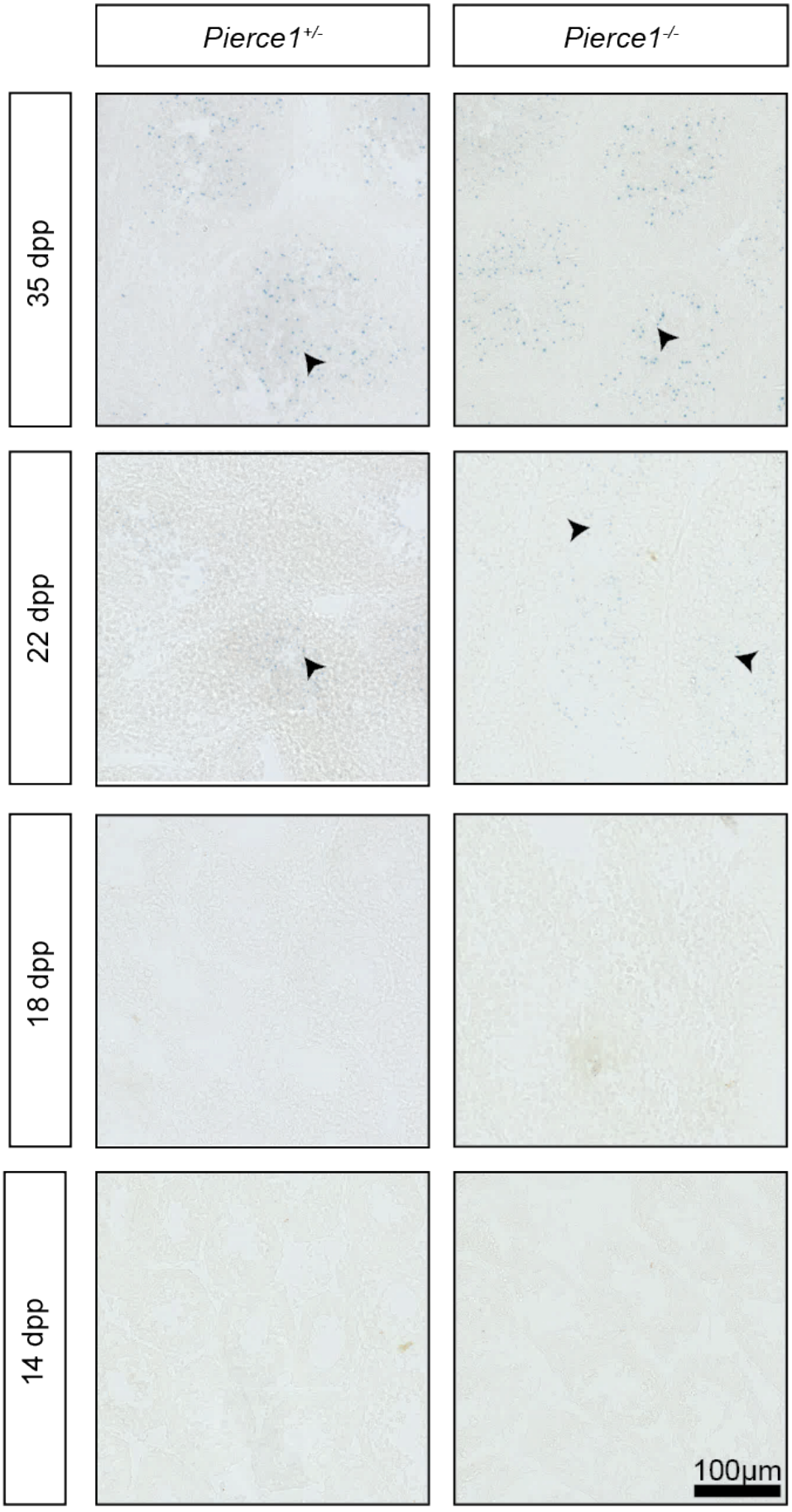
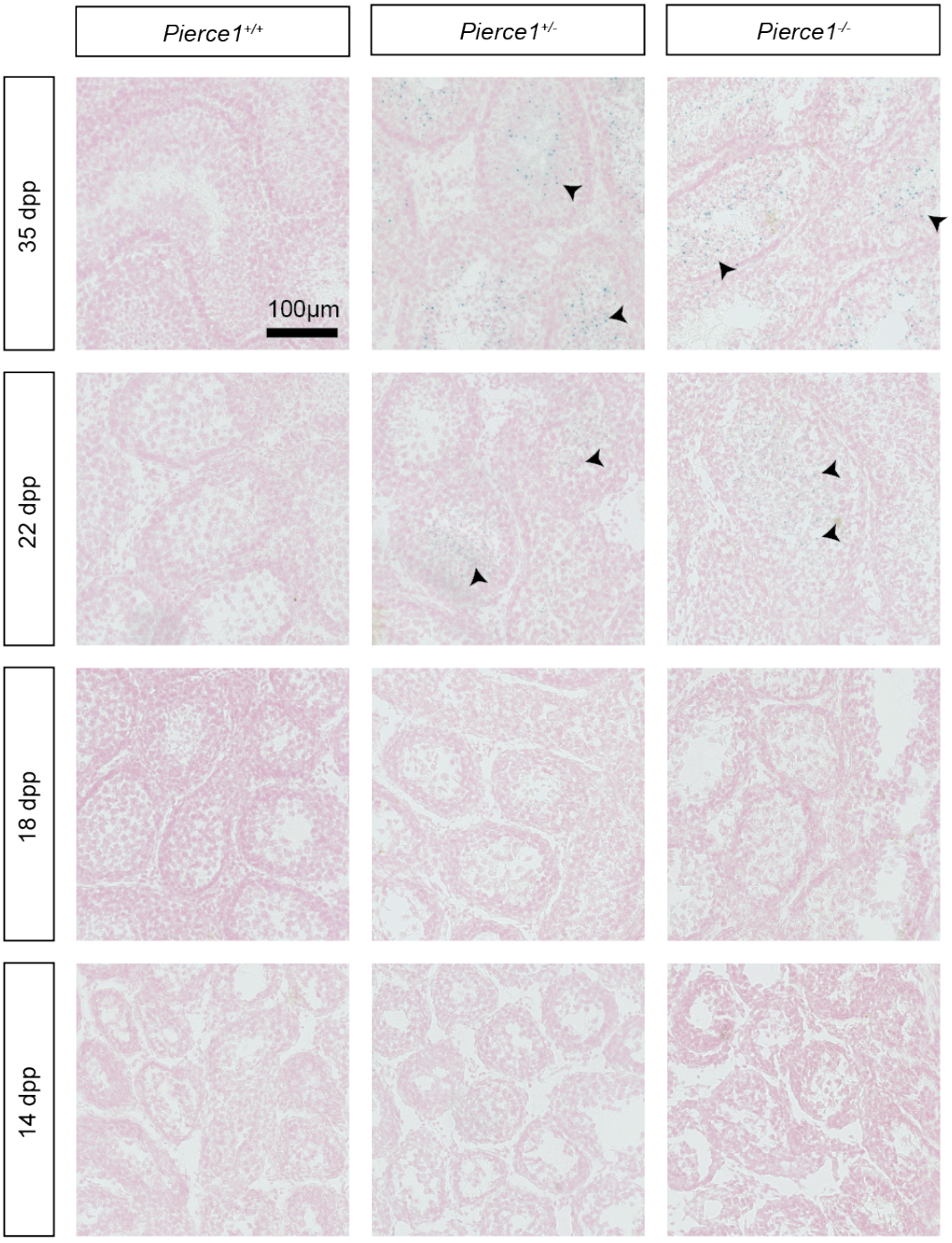

Pierce1+/-
Pierce1-/-
35 dpp
22 dpp
18 dpp
14 dpp
100µm

Figure 3.22: *Pierce1* expression initiates with the onset of motile ciliary gene expression. X-gal staining in testis cryosections shows initiation of lacZ reporter expression between 18 and 22 dpp. Sections are counterstained using Nuclear Fast Red. Wild-type tissue is included as a negative control due to lack of lacZ expression. Tubules showing stained cells are denoted by arrows. Scale bar shows 100 µm. n = 2 mice per genotype at each time point. n = 8 sections per mouse.



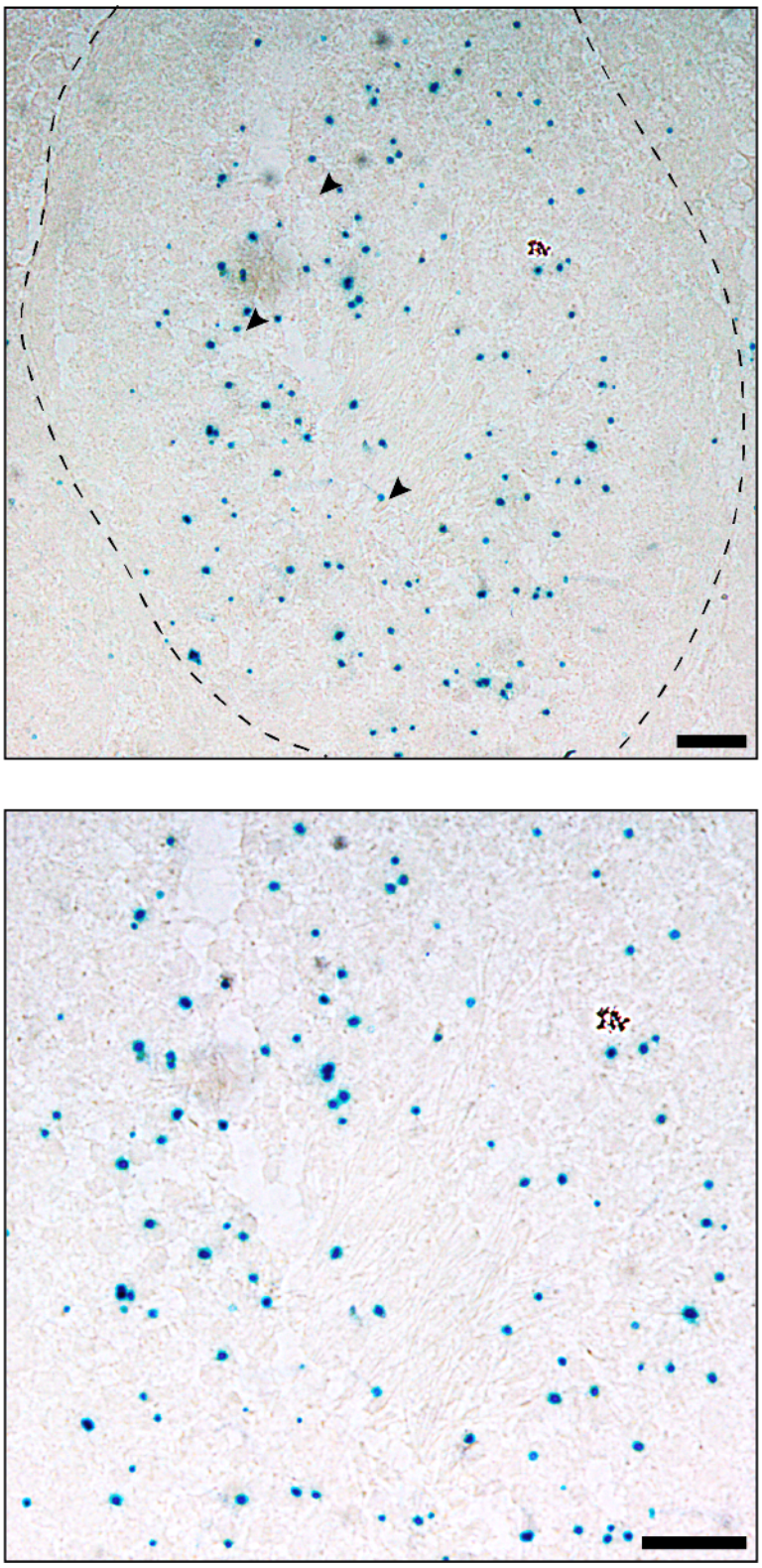


Figure 3.23: *Pierce1* expression initiates with the onset of motile ciliary gene expression.
X-gal staining in testis cryosections shows lacZ expression at 35 dpp is not in the flagellum. One tubule is outlined in top image with a dashed line. Examples of stained cells are denoted by arrows. Bottom image shows the same tubule at a higher magnification. Scale bar shows 20 μm in both images. n = 2 mice per genotype at each time point. n = 8 sections per mouse.

3.5.6: Transmission electron microscopy of sperm flagellar axonemes does not demonstrate ultrastructural defects in *Pierce1*$^{-/-}$ sperm flagella.

In light of the sperm motility defects detected, and the dynein arm defects associated with tracheal ciliary motility defects in *Pierce1*$^{-/-}$ mice, it seemed possible that similar dynein arm defects could be present in *Pierce1*$^{-/-}$ sperm flagella and causative for the observed motility defects. Therefore, sperm samples were collected for TEM analysis of sperm flagellar cross-sections.

The swim up method used during the CASA experiments failed to yield sufficient sperm number for analysis. Thus, epididymides from two wild-type and two *Pierce1*$^{-/-}$ males were fixed and analysed by TEM. Wild-type flagella showed a 9+2 microtubule arrangement with IDAs and ODAs present, in the distal and proximal mid-piece and end piece of the flagellum (**Fig. 3.24**). This staining pattern proved indistinguishable from *Pierce1*$^{-/-}$ sperm flagella.

Detailed counts of multiple sections were carried out to analyse microtubule arrangement (**Fig. 3.25**) and the presence of dynein arms (**Fig. 3.26**). Overall, these revealed no microtubule arrangement or dynein arm defects in *Pierce1*$^{-/-}$ murine spermatozoa.

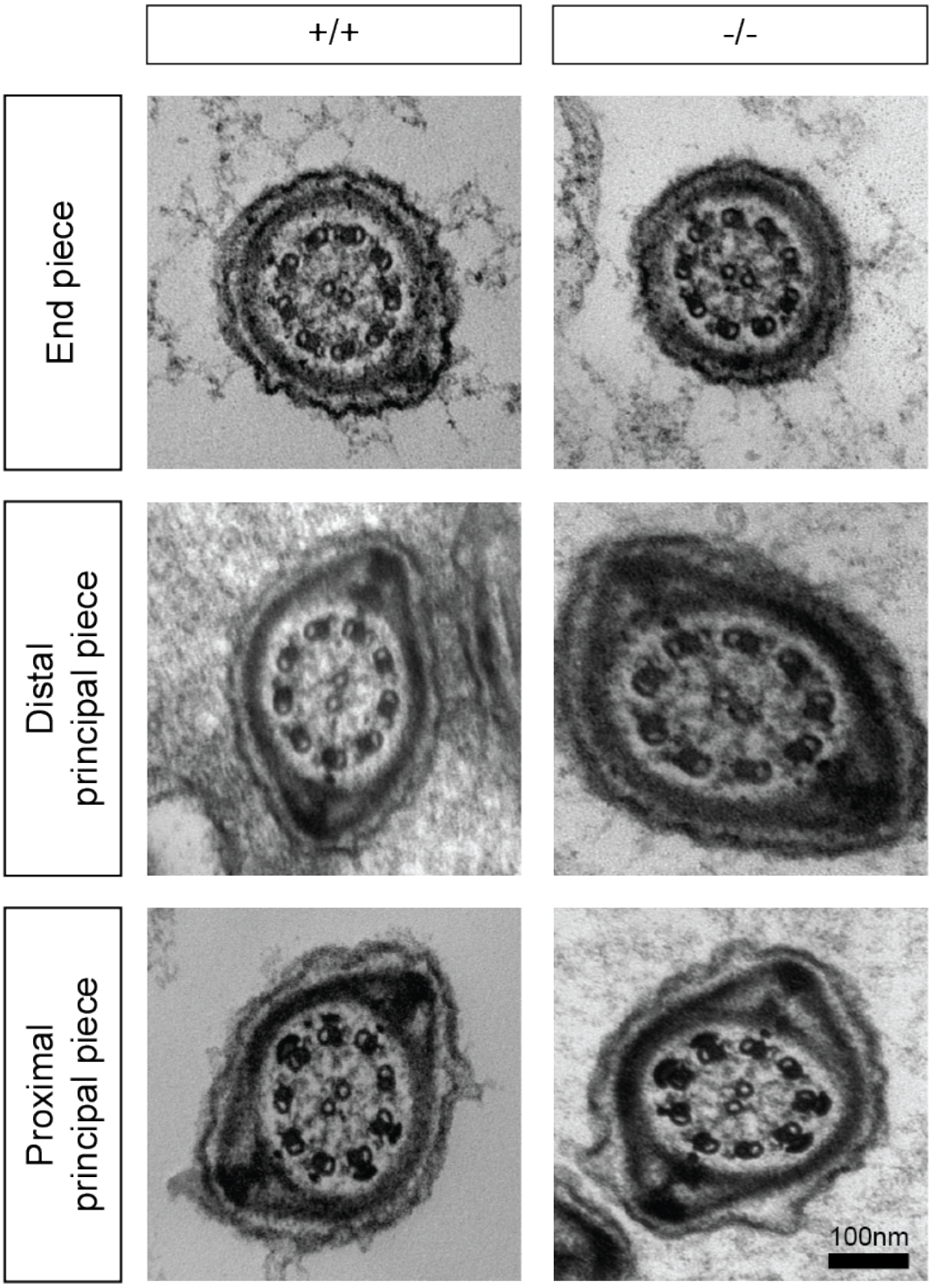


Figure 3.24: *Pierce1*$^{-/-}$ sperm exhibit no ultrastructural defects.
Flagellar cross-sections at the end piece and proximal and distal mid-pieces of *Pierce1*$^{+/+}$ and $^{-/-}$ spermatozoa flagella, showing an absence of microtubule and dynein arm defects. Scale bar shows 100nm. High resolution images taken from datasets referenced in **Fig. 3.25.**

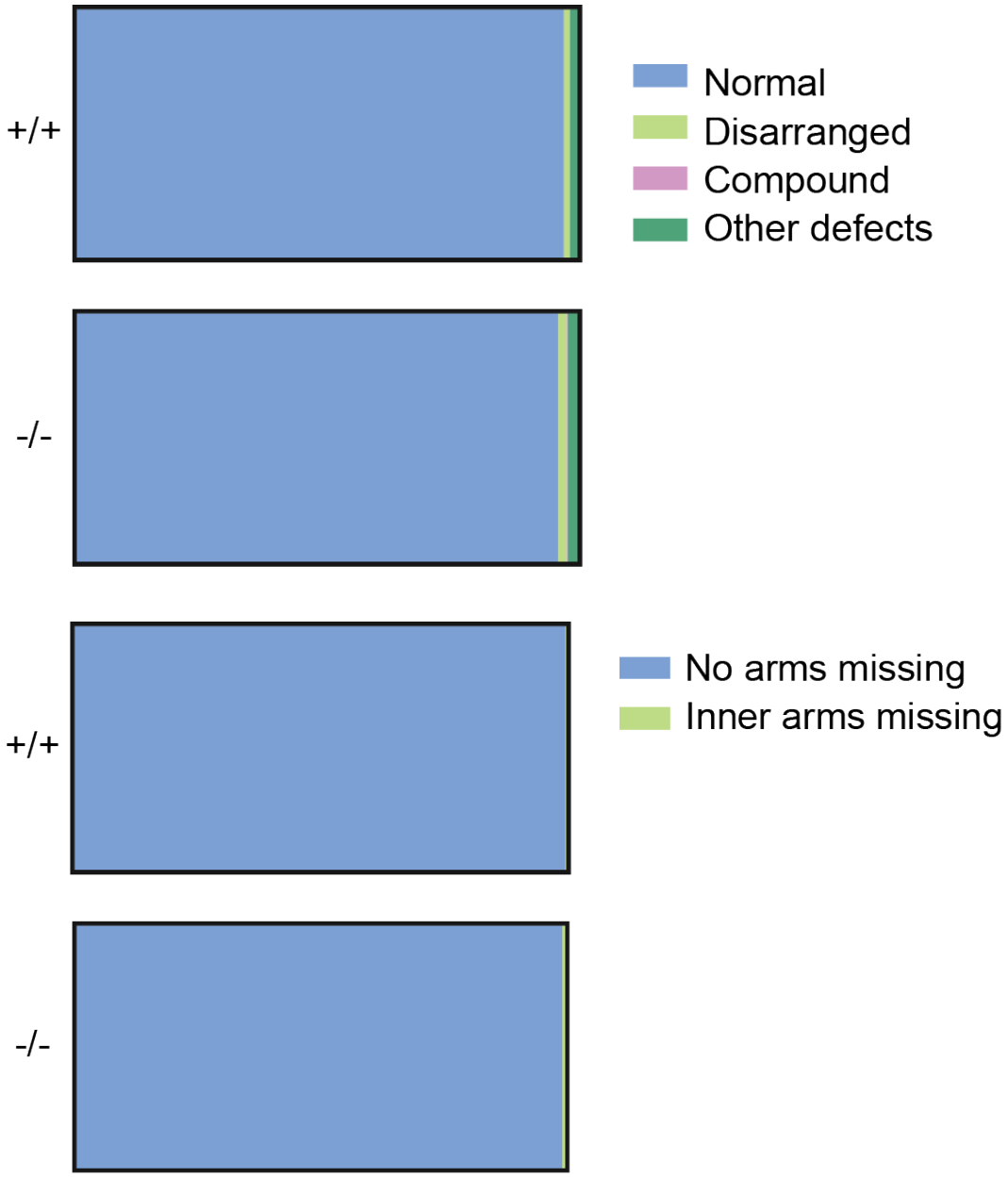


Figure 3.25 (top): *Pierce1*$^{-/-}$ sperm exhibit no microtubule defects. Proportion of microtubule defects observed. n= 2 animals +/+, 2-/-; n=650 flagella (+/+) and 638 (-/-). N.S.
Figure 3.26 (bottom): *Pierce1*$^{-/-}$ sperm exhibit no dynein arm defects. Proportion of dynein arm defects observed in wild-type and *Pierce1*$^{-/-}$ mice. n= 2 animals +/+, 2-/-; n=311 flagella +/+ and 307 flagella -/-. N.S.

3.6: Discussion of sperm motility defects in the mouse

CASA has become a key tool in the field of fertility as it allows a high-throughput and unbiased approach to sperm motility analysis. While useful in a variety of species (Amann and Waberski, 2014), it does have limitations. It is unclear how several motility parameters relate to overall fertility, and different factors have been found to have a significant correlation with fertility in different species (Van Der Horst, Maree and Du Plessis, 2018).

Moreover, CASA leads to the collection of many data points. Statistical significance does not necessarily equate to biological significance, and the collection of a very large number of data points increases the likelihood of achieving a significant difference between *Pierce1*$^{-/-}$ data and wild-type data simply by chance. Motility defects in the node and trachea in *Pierce1*$^{-/-}$ mice are relatively subtle, so perhaps a lack of clear differences among the many motility parameters is not surprising. In addition to this, the individual motility parameters are not independent of each other, with some being calculated from others. The difference in sperm count, and particularly in rapid sperm count, is potentially a greater indicator of biological significance than any one motility parameter alone. Sperm concentration and rapid sperm count are two CASA attributes that often show significant positive correlation with a reduction in male fertility, across multiple species.

A more accurate way of conducting the analysis would have been to carry out a large scale analysis of wild-type mouse sperm motility, with the aim of identifying categories of sperm movement based not only on velocity, but also other motion attributes such as beat cross frequency. This would have helped us to understand whether more subtle changes in sperm motility, or a distribution of classes, had occurred. With more time and resources, we could have also carried out a time course study, into

whether sperm motility deteriorated more rapidly in *Pierce1*$^{-/-}$ compared to wild-type animals. This is important as in their physiological role spermatozoa must maintain motility in the environment of the female reproductive tract after ejaculation. A rapid decline in motility may imply a physiological fertility defect that was not detected by the motility parameters examined in this study.

To underline this point, it must be stated that CASA is not a true examination of physiological sperm motility, in their native environment. The salt solution that the sperm sample is diluted in is not identical to the composition of the medium in the female reproductive tract. Indeed, we have shown that *Pierce1*$^{-/-}$ males are fertile, due to their use in creating *Pierce1*$^{+/-}$ litters that were used in X-gal staining work (**Chapter 4.2.1**). These matings were limited and subfertility may have been a limiting factor, but this was not directly assessed.

Hyperactivation refers to an over-excited figure of eight pattern of movement observed in mammalian sperm (Suarez, Varosi and Dai, 1993). An increase in hyperactivation is associated with reduced progressive velocity, and a reduction in male fertility. Defects in hyperactivation are specific to the spermatozoon and are often the result of signalling cascade defects. Whilst it remains a possibility that any dynein arm defects observed in tracheal motile cilia in the *Pierce1*-null line may be the result of defective signalling, it is highly unlikely that these are the result of a spermatozoon-specific process. There is also debate within the field as to whether CASA itself is sensitive enough to detect differences in hyperactivation. As such, hyperactivation studies were not carried out as part of my sperm motility analysis.

Background strain itself may have been a confounding factor in this work – B6N males have been shown to have significantly reduced sperm motility compared to other mouse lines (Goodson *et al.*, 2011). The Lee

lab have also shown that some aspects of motile cilia dysfunction in the mouse, such as hydrocephalus, appear to be noticeably more severe on a B6N background compared to mixed lines (Lee, 2013). Perhaps the deleterious effect of *Pierce1-tm2b* homozygosity could not be detected in full against this background. The opposing argument would be that the B6N background exaggerated the sperm motility defects, and that we could expect to find no significant differences at all if this gene was investigated on a different mouse background. However, with our knowledge of the genetic and epigenetic differences between inbred strains not entirely complete, it is difficult to make any prediction with certainty.

Many genes are expressed in the developing testis. We do not yet understand the functional significance of many of these, and a significant proportion of the genetic variation observed will be due to changes in the somatic cells as opposed to the germ cells which go on to form the sperm. Despite this, the field is concurrent that precisely controlled waves of gene expression exist in germ cells. GO datamining has shown particular waves to be associated with particular processes or components essential to the spermatocyte, including glycolysis and ciliary assembly. *Pierce1* expression initiating in parallel with the onset of gene expression related to sperm flagellar motility adds significant weight to a role for PIERCE1 in the onset and maintenance of flagellar or ciliary motility.

The involvement of PIERCE1 in sperm flagellar motility may occur via a similar mechanism to that in the trachea. Dynein arm and microtubule defects were not observed in TEM analysis of *Pierce1*$^{-/-}$ sperm flagella, which may imply that the function of PIERCE1 is being compensated for by other proteins in the flagellum. PIERCE1 could be functionally redundant in the wild-type spermatozoon, and its function compensated for by other proteins, leading to the absence of dynein arm defects.

Alternatively, our flagellar TEM may not have been precise enough to demonstrate what is a subtle defect in the tracheal epithelial cilia. There is the possibility that more defects may have been present in the mid-piece, which was not as thoroughly examined, and the examination of defects was not stratified by location along the sperm flagellum due to a reduced level of expertise in this area. Some dynein components have been shown to have distinct localisations in the distal and proximal portions of the axoneme, notably DNAH11 (Knowles *et al.*, 2012; Lucas *et al.*, 2012; Dougherty *et al.*, 2016) and DNAH9 (Fassad, Shoemark, Legendre, *et al.*, 2018; Loges *et al.*, 2018) in tracheal motile cilia (proximal and distal aspects respectively). However, there is evidence from the *Pihd3*$^{-/-}$ mouse that mice with sperm flagellar dynein assembly defects show these defects in both the principal piece and the mid-piece, i.e. along the length of the flagellum. As such, we would realistically expect defects to have been detected if present.

Another factor that must be taken into account is whether any resultant ultrastructural defect can be detected by TEM. For example, *DNAH11* mutations have been shown to lead to an ultrastructural defect in tracheal motile cilia that can be detected by electron tomography, but not by TEM (Shoemark, Burgoyne, *et al.*, 2018). Therefore, the lack of an observed defect in the sperm flagellum could result from any defect being subtle enough to escape detection via this method.

3.7: Conclusions

The conservation of PIERCE1 functionality across distinct classes of motile cilia in the mouse, in combination with the heterogeneous dynein arm defects observed in *Pierce1*$^{-/-}$ respiratory epithelium, add weight to PIERCE1's involvement in the assembly of dynein arms required for ciliary motility, or the regulation of this process. If PIERCE1 was a dynein arm component itself, we would expect to see a dynein arm defect that was more homogeneous when assessed via TEM, as observed in patients and model organisms with mutations in these genes (Horani and Ferkol, 2018). The fact that *Pierce1*$^{-/-}$ tracheal motile cilia show similar TEM abnormalities to those with defects in other dynein assembly factors increases the evidence for this conclusion.

However, our knowledge surrounding the dynein assembly factors themselves is limited. We have data from patients with assembly factor mutations showing dynein arm defects via TEM, and studies in cell culture have shown that the assembly factors appear to interact with each other. Other than that, our understanding of the biochemical function of dynein assembly factors in the cell, and particularly in the initiation and maintenance of ciliary motility is limited. This all makes the question of what exactly PIERCE1 is doing in the cell more intriguing. In the next chapter, I will summarise the bioinformatics and biochemical approaches used to address this problem.

4: Functional studies of PIERCE1

4.1: Introduction

Studies of ciliary motility in embryonic and adult *Pierce1*$^{-/-}$ tissues left unanswered the question of the biochemical function of PIERCE1. I will explore this further in this chapter, discussing the results of studies that aimed to uncover potential functions of PIERCE1, ranging from expression pattern analysis to in silico predictions as well as attempts to identify putative interactor proteins.

4.2: Results

4.2.1: Analysis of the expression of *Pierce1* genetic product

Due to experimental work detailed in previous chapters, we know that CBP and CBF are both affected to varying extents in tissues with motile cilia in *Pierce1*$^{-/-}$ mice, and thus it followed that *Pierce1* expression is required for appropriate ciliary motility. This hypothesis fit with previously described data from publications of *TAp73* targets that list *Pierce1* as a gene that is downstream of *TAp73* and upregulated during the onset of motile multiciliogenesis (Marshall *et al.*, 2016; Nemajerova *et al.*, 2016). Personal communication (Sudipto Roy) placed *Pierce1* downstream of *Foxj1*, the master regulator of all motile ciliogenesis. This led me to hypothesise that PIERCE1 would show restricted expression to tissues with motile cilia.

4.2.1.1: In the embryo

The embryonic node contains motile monocilia. It forms and becomes functional between 7.5 and 8.5 dpc in the mouse. Therefore, I collected embryos aged between these time points and used an in situ probe to analyse expression of *Pierce1* (**Fig. 4.1**). This demonstrated that *Pierce1* is expressed solely in the embryonic node at these stages. Its tight spatial restriction to the node provides evidence of its function being tied to that of the node, which is the LR organiser in mice and humans.

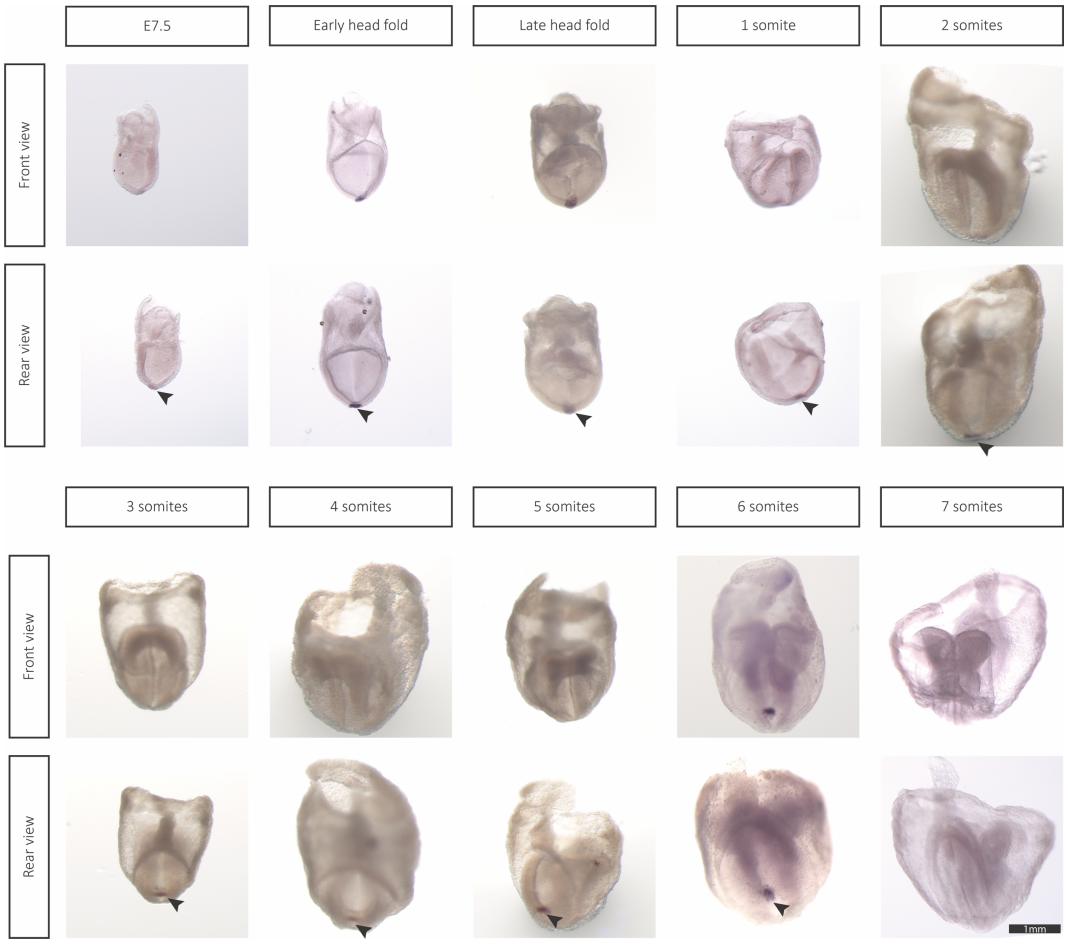


Figure 4.1: *Pierce1* expression is restricted to the embryonic node during early development.
Time series showing in situ hybridisation staining for *Pierce1* in embryos between 7.5 and 8.5 dpc. Front and back views are shown; staining is highlighted with an arrow. Scale bar shows 1 mm. Images are representative images from n = 10 images per time point.

The *Pierce1*-null allele contains a lacZ expression cassette in place of exon 2 of *Pierce1*. As such, X-gal staining was used to further analyse the expression pattern of *Pierce1* in the embryo. I conducted X-gal staining in embryos to determine whether protein localisation of the lacZ reporter in the embryo mirrors that of *Pierce1* mRNA, and found that X-gal staining also shows a tight localisation to the embryonic node (**Fig. 4.2**). As expected, the X-gal staining endures beyond the expression of *Pierce1* mRNA. This added further weight to a specific role for PIERCE1 in motile ciliated tissue.

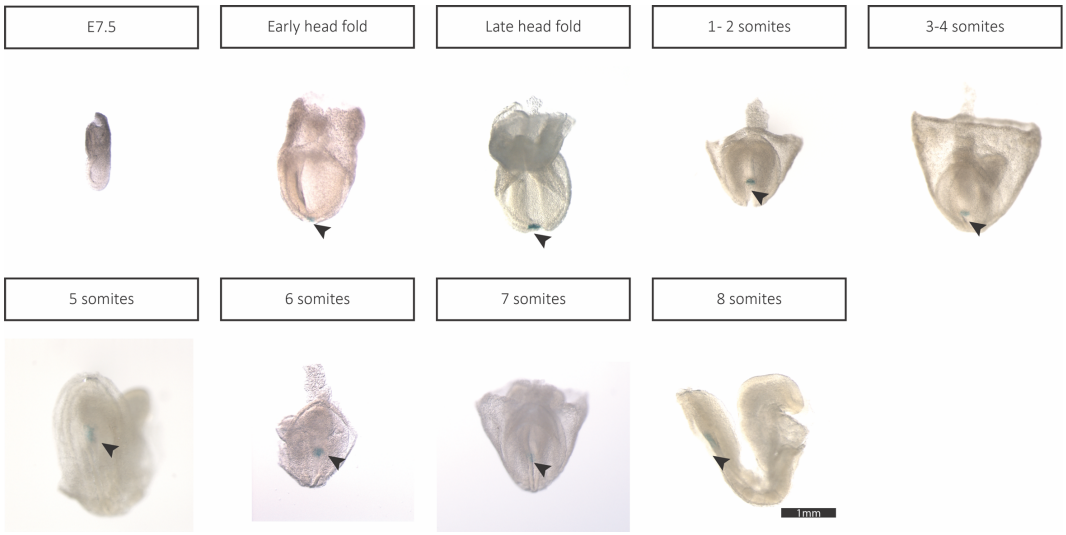


Figure 4.2: *Pierce1* expression is restricted to the embryonic node during early development. Time series showing X-gal staining for the *Pierce1-lacZ* reporter in embryos between 7.5 and 8.5 dpc. Front and back views are shown; staining is highlighted with an arrow. Scale bar shows 1 mm. Images are representative images from n = 10 images per time point.

4.2.1.2: Pierce1 expression in the adult

Expression of the *Pierce1-lacZ* reporter was assessed during analysis of the allele by the IMPC (IMPC, 2018). The resulting data is reproduced below (**Fig. 4.3**), and showed restriction to tissues with motile cilia. The oviduct in the female reproductive system contains a motile multiciliated epithelium to aid passage of the fertilised ovum to the uterus (Brooks and Wallingford, 2014). The male reproductive tract showed staining throughout, presumably due to the presence of sperm flagella; flagella contain a conserved ultrastructure that is shared with the motile cilium (Satir and Christensen, 2007). The airway is lined by motile MCCs that provide the power behind mucociliary clearance (Brooks and Wallingford, 2014), whilst the ependymal lining of the ventricles in the brain contains a motile multiciliated epithelium to aid the circulation of CSF (Brooks and Wallingford, 2014). Intriguingly, the spinal canal also showed staining. The existence of motile cilia in the spinal canal has recently been demonstrated in zebrafish, but has not been shown in mammals as of yet (Grimes et al. 2016).

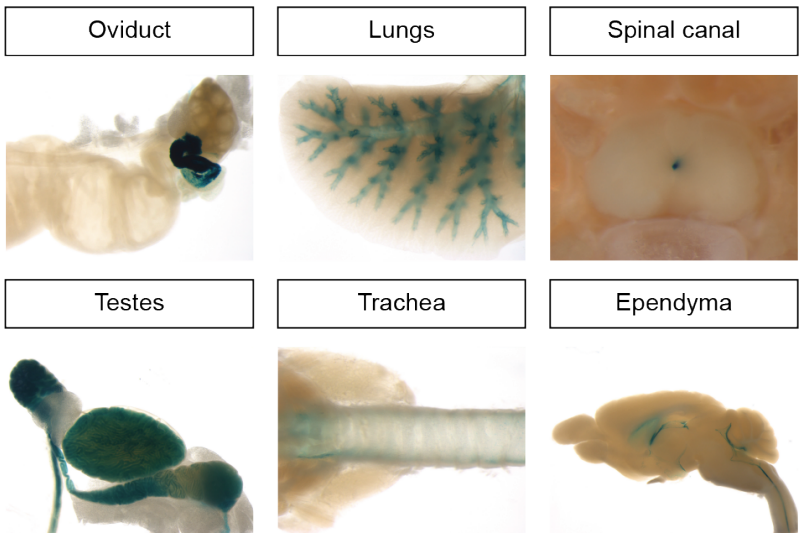


Figure 4.3: lacZ expression in adult tissues of *Pierce1*$^{+/-}$ mice shows expression is restricted to tissues thought to contain populations of cells with motile cilia or flagella. Data from: https://www.mousephenotype.org/data/genes/MGI:1916577

4.2.1.3: Analysing expression using an antibody to Pierce1

To enable a more precise analysis of PIERCE1 localisation pattern, a polyclonal rabbit antibody to full-length murine PIERCE1 was synthesised by Covalabs. Wax sections of tissues wild-type for *Pierce1* were hybridised with this antibody; antibody localisation was then visualised using DAB staining (Chris Esapa, MRC Harwell). Stain was clearly observed (**Fig. 4.4**) and, upon detailed analysis, showed localisation to the respiratory epithelium and elongating spermatids in the testis. Elongating spermatids are in the process of synthesising and extending their flagellar axoneme. This appeared to provide evidence that PIERCE1 not only localises to a motile ciliated tissue, but to a specific cell type in the process of building a motile cilium.

Pierce1$^{-/-}$ tissue was used as a negative control, as we predicted that no signal would be observed there. However, an identical staining pattern was observed (**Fig. 4.5**). We know that a genetic product is synthesised and converted into protein from the *Pierce1*-null allele locus due to X-gal staining studies. As our antibody was developed against the full-length sequence of murine PIERCE1, and the *Pierce1*-null allele still expresses exon 1, it seemed most likely that the identical signal observed in wild-type and *Pierce1*$^{-/-}$ tissue was due to the antibody reacting to an epitope in exon 1. Indeed, this area had been predicted to be the most strongly antigenic portion of the protein (data not shown).

To investigate whether or not the *Pierce1*-null allele expresses a protein that is detected by our polyclonal antibody, I carried out western blot analysis of wild-type and *Pierce1*$^{-/-}$ testes. The wild-type PIERCE1 protein is 41 kDa; the *Pierce1-lacZ* reporter allele is predicted to have a molecular weight of 135 kDa (assuming expression of exon1 spliced into lacZ). My Western blot analysis specifically detected a band in both wild-type and *Pierce1*$^{-/-}$ testis tissue of approximately 42 kDa (**Fig. 4.6**).

Overexpressed PIERCE1-GFP (68 kDa) was used as a positive control. Although a protein product that appears to be of the predicted size (42 kDa) is detected in wild-type tissues, the same band was observed in *Pierce1*$^{-/-}$ tissues. As such, this is unlikely to be due to specific binding to PIERCE1; even if there was some read-through or alternative splicing of exon1 into exon 3, the predicted molecular weight of that gene product is 35 kDa. The band observed in *Pierce1*$^{-/-}$ (approx. 42 kDa) could arguably be this alternatively spliced transcript; however I saw no evidence of a larger PIERCE1-LACZ band. Overall, we concluded that this antibody was unlikely to be a reliable experimental tool.

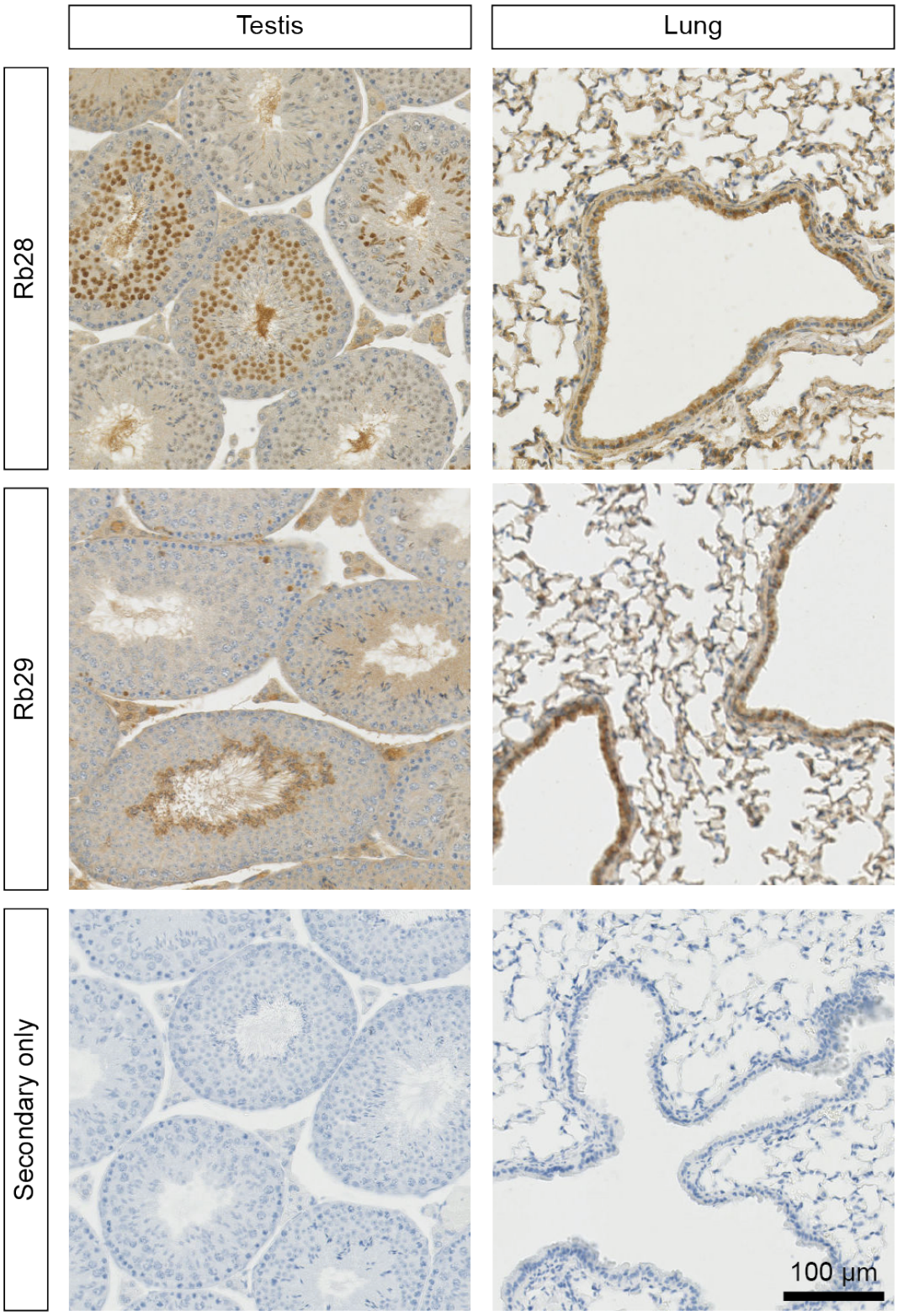


Figure 4.4: Anti-PIERCE1 staining appears to localise to cells with motile cilia or flagella.
DAB in wild-type testis and lung tissue. Results from both synthesised anti-PIERCE1 antibodies (Rb28; Rb29) are shown. Scale bar shows 100 µm.

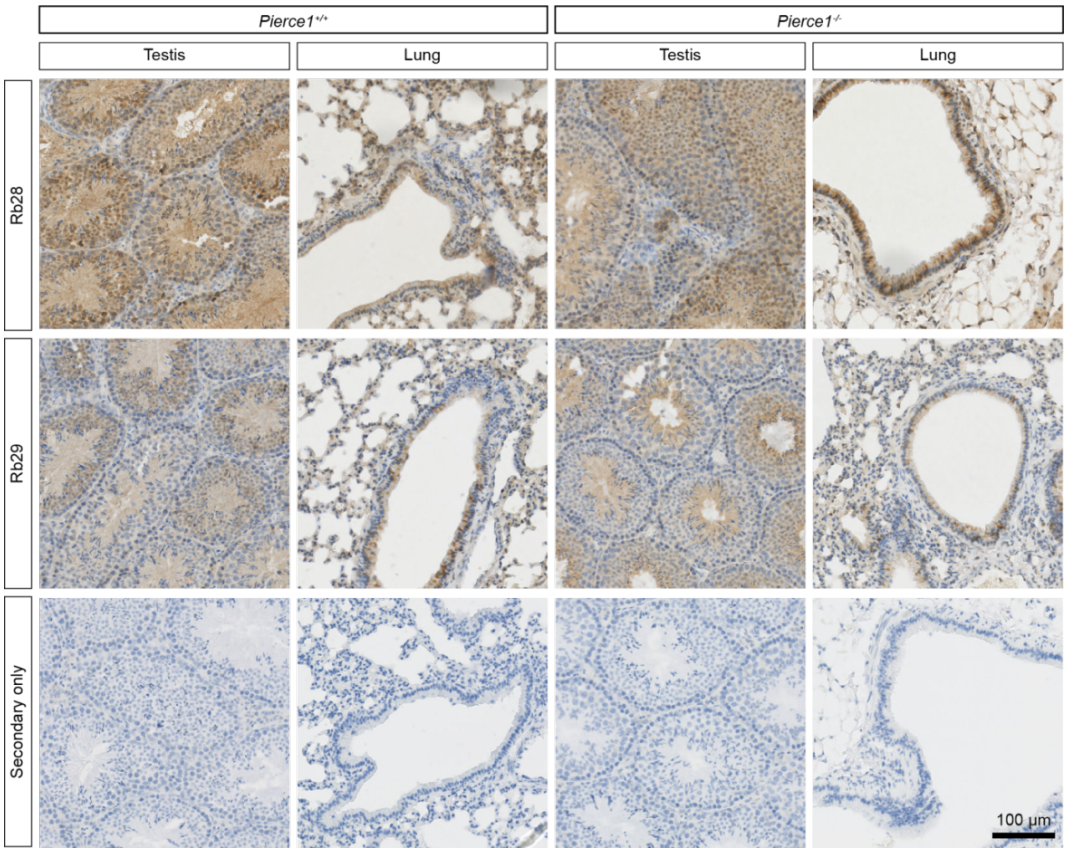
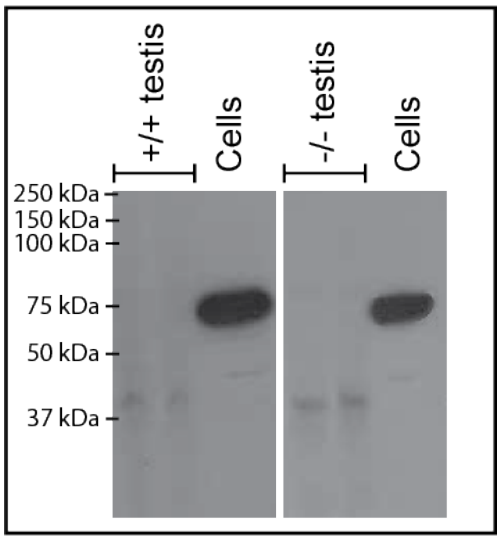


Figure 4.5 (top): Identical anti-PIERCE1 signal is observed in wild-type and *Pierce1*$^{-/-}$ tissues.
DAB in wild-type vs *Pierce1*$^{-/-}$ testis and lung tissue. Results from both synthesised anti-PIERCE1 antibodies (Rb28; Rb29) are shown. Scale bar shows 100 µm.

Figure 4.6 (bottom): Identically-sized proteins are detected by the anti-PIERCE1 antibody in wild-type and *Pierce1*$^{-/-}$ tissues.
Western blot analysis using anti-PIERCE1 shows bands of approx. 42 kDa in both wild-type and *Pierce1*$^{-/-}$ testis samples. A larger band of approx. 132 kDa (predicted to correspond to the *Pierce1-lacZ* gene product) was not observed in *Pierce1*$^{-/-}$ tissue. *Pierce1-EGFP*-transfected cell lysate was used as a positive control (68 kDa band).



4.2.1.4: Subcellular localisation

In light of the tissue-specific expression pattern of *Pierce1*, it seemed reasonable that the subcellular localisation of this protein might offer further clues as to its function. For example, it may traffic to a particular subcellular organelle, like the Golgi, or indeed to the primary cilium itself. This could help us to propose further functions and putative interactor proteins to investigate. Motile ciliated cells were not used for this analysis as their culture and transfection with tagged proteins is technically challenging and time intensive.

EGFP-tagged PIERCE1 was initially used, and showed no specific localisation pattern (not shown). As the EGFP tag is relatively large compared to the size of the PIERCE1 protein, we hypothesised that its size could be overwhelming any specific localisation signal encoded in the PIERCE1 protein. As such, tagged versions with small protein tags (FLAG and myc) were created. The FLAG tag was cloned into the N-terminus of the protein, and the myc tag into the C-terminus. This was to determine whether tagging at either terminus was disrupting any localisation signal.

I transfected and analysed tagged forms of PIERCE1 and investigated the localisation pattern of over-expressed PIERCE1 in cell culture to determine whether it showed a specific localisation that could point to putative functions. I transiently transfected IMCD3 cells with both tagged forms of PIERCE1. I investigated localisation under serum-containing and serum-starved conditions. Serum starvation was carried out to promote the formation of primary cilia in cells, to see whether PIERCE1 localisation pattern altered in the presence of a primary cilium.

FLAG-PIERCE1 (N-terminal tag) showed cytosolic localisation in IMCD3 cells when grown in media containing serum (**Fig. 4.7**). No nuclear localisation was observed. Anti-PDI was used as a positive control, and mock-transfected (Lipofectamine only) cells were used as a negative

control. Staining of transfected cells was also carried out with only the secondary antibodies to ensure that there was no non-specific secondary antibody staining present.

This localisation pattern was mirrored when the FLAG-PIERCE1 construct was transfected into cells that were then starved of serum to promote the formation of primary cilia (**Fig. 4.8**). Anti-ARL13B staining was used to demonstrate the presence of primary cilia, and thus to ascertain that no change in FLAG-PIERCE1 localisation was occurring in the face of primary ciliation. Mock-transfected and secondary-only controls were again used to demonstrate specific transfection and staining of the tagged protein.

Using the PIERCE1-myc (C-terminus) construct mirrored the localisation results of FLAG-PIERCE1 in both serum-containing (**Fig. 4.9**) and serum-free (**Fig. 4.10**) conditions. Expression of both constructs was also evaluated in NIH3T3 cells to ascertain whether the cell line itself was disrupting specific PIERCE1 localisation (data not shown); the same localisation pattern was observed.

Wild-type *Pierce1* was not expressed in these cells - primers designed for use in qPCR could only amplify *Pierce1* when used with cell lysates that had been transfected with tagged forms of *Pierce1* as their cDNA source. This is consistent with our knowledge of PIERCE1 as a protein that appears to exhibit restricted expression to tissues with motile cilia, but meant that we could not analyse endogenous PIERCE1 localisation in cell lines, and had to use transient transfection (and overexpression). Commercially available antibodies against human PIERCE1, and our own polyclonal antibody against mouse PIERCE1, were not successfully used in cell culture immunofluorescence studies to identify tagged forms of PIERCE1.

In summary, the subcellular localisation analysis did not offer specific clues as to the function of PIERCE1 due to a lack of localisation to subcellular structures with known functions. In addition to this, formulating hypotheses regarding the function of PIERCE1 from its protein sequence is challenging, as there no known structural annotations.

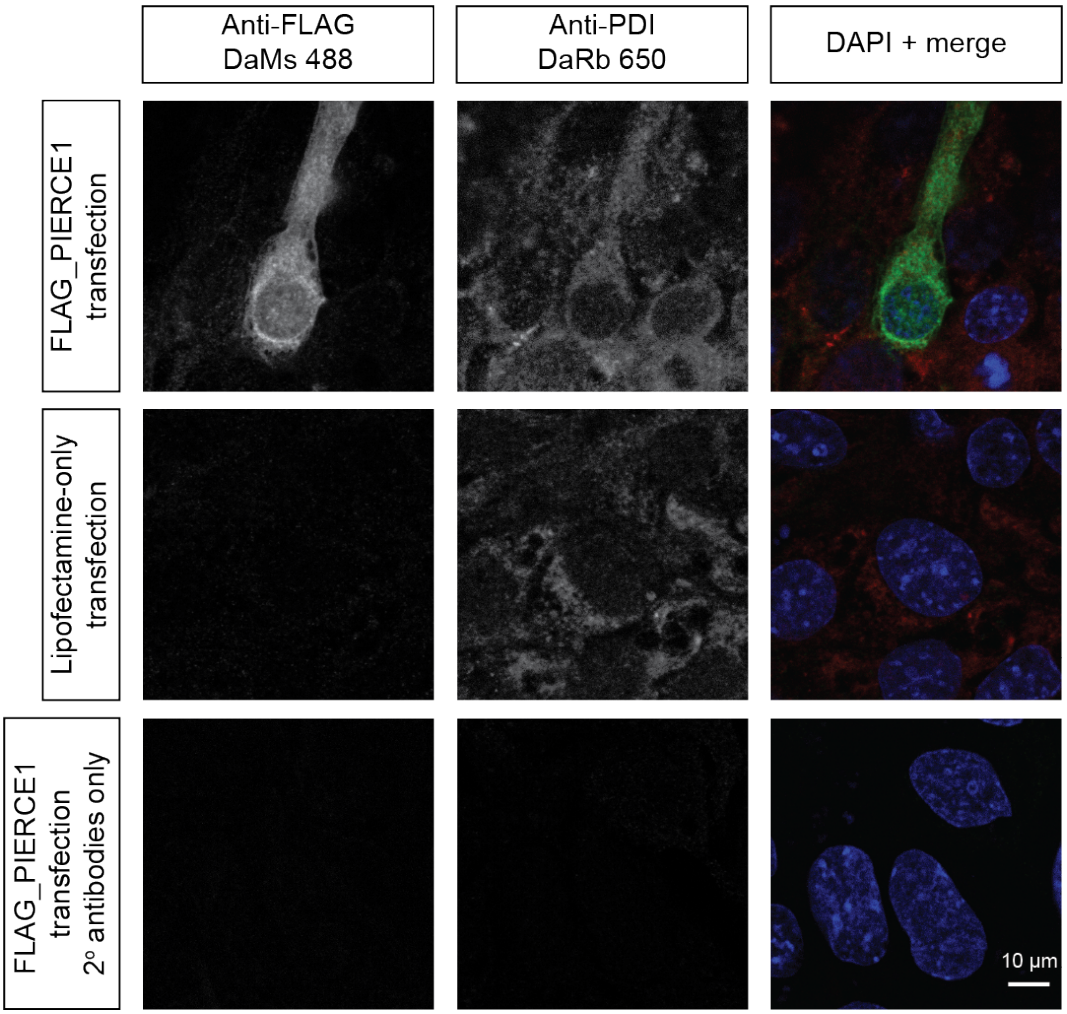


Figure 4.7: Tagged PIERCE1 does not show specific localisation in cell culture.
Immunofluorescence staining in IMCD3 cells for transiently transfected FLAG-PIERCE1 (media containing serum). Anti-FLAG (Ms; DaMs 488) and anti-PDI (Rb; DaRb650) antibodies used; anti-PDI used as a Golgi marker. Cells stained with DAPI pre-mounting. Secondary antibody only and Lipofectamine-only transfection controls also shown. Scale bar shows 10 µm. Cells transfected at 90% confluency in a 6 well plate. 50-60% rates of transfection efficacy observed.

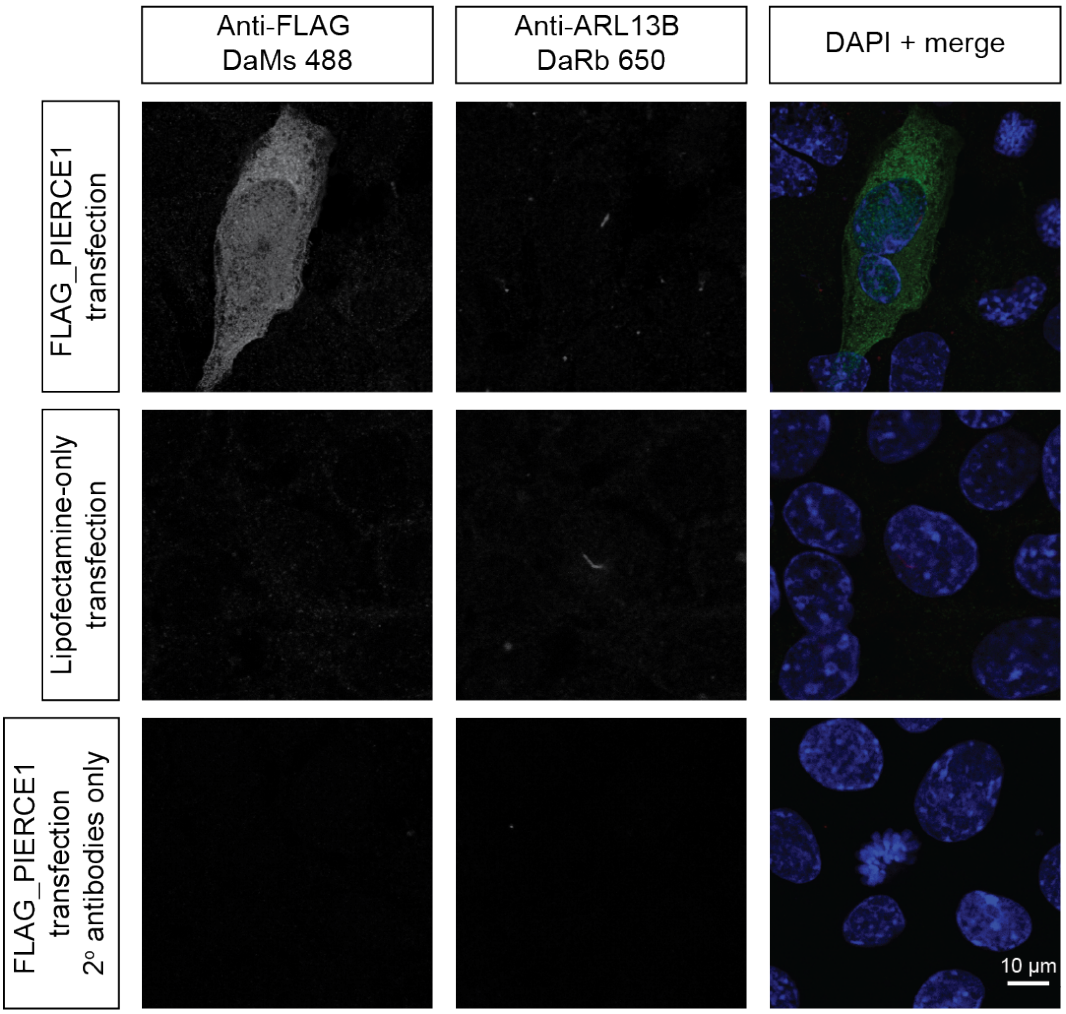


Figure 4.8: Tagged PIERCE1 does not show specific localisation in cell culture.
Immunofluorescence staining in IMCD3 cells for transiently transfected FLAG-PIERCE1 (serum-free media). Anti-FLAG (Ms; DaMs 488) and anti-ARL13B (Rb; DaRb650) antibodies used; anti-ARL13B used to mark cilia. Cells stained with DAPI pre-mounting. Secondary antibody only and Lipofectamine-only transfection controls also shown. Scale bar shows 10 µm. Cells transfected at 90% confluency in a 6 well plate. 50-60% rates of transfection efficacy observed.

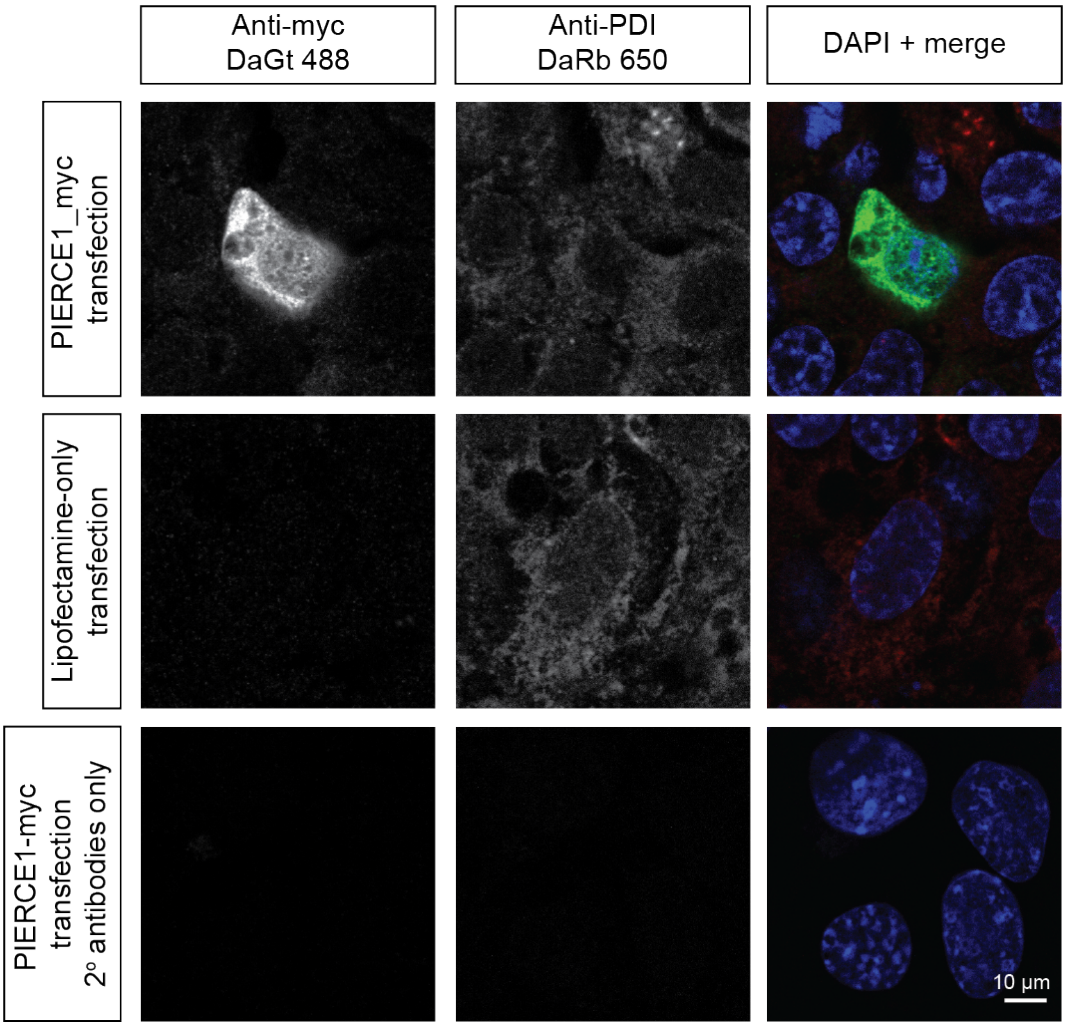


Figure 4.9: Tagged PIERCE1 does not show specific localisation in cell culture. Immunofluorescence staining in Imcd3 cells for transiently transfected PIERCE1-myc (media containing serum). Anti-myc (Gt; DaGt 550) and PDI (Rb; DaRb650) antibodies used; PDI used as a Golgi marker. Cells stained with DAPI pre-mounting. Secondary antibody only and Lipofectamine-only transfection controls also shown. Scale bar shows 10 µm. Cells transfected at 90% confluency in a 6 well plate. 50-60% rates of transfection efficacy observed.

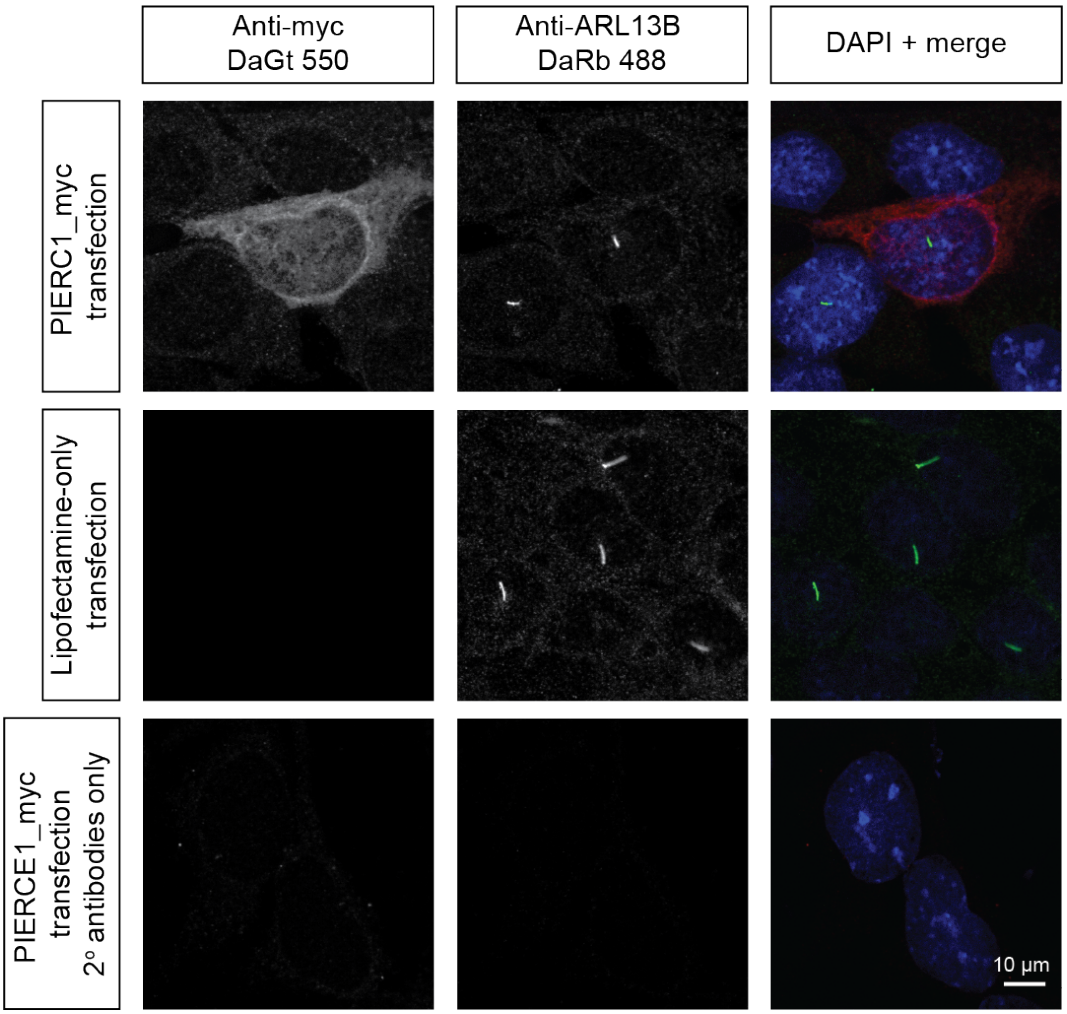


Figure 4.10: Tagged PIERCE1 does not show specific localisation in cell culture.
Immunofluorescence staining in IMCD3 cells for transiently transfected PIERCE1-myc (serum-free media). Anti-myc (Gt; DaGt 550) and Anti-ARL13B (Rb; DaRb650) antibodies used; anti-ARL13B used to mark cilia. Cells stained with DAPI pre-mounting. Secondary antibody only and Lipofectamine-only transfection controls also shown. Scale bar shows 10 µm. Cells transfected at 90% confluency in a 6 well plate. 50-60% rates of transfection efficacy observed.

4.2.2: In silico analysis of PIERCE1 structure

PIERCE1 contains a conserved domain of unknown function, DUF4490. I analysed *Pierce1* using a panel of bioinformatics programmes to assess structural or functional aspects of this domain, as well as of the PIERCE1 protein. These tools, and the results from their analysis, are summarised below.

PredictProtein (Yachdav *et al.*, 2014b) integrates multiple computer models that use a combination of neural networks and sequence comparison tools to evaluate different aspects of protein structure. It predicted that mouse PIERCE1 contained no transmembrane domains (Bigelow *et al.*, 2004) or disulphide bridges (Ceroni *et al.*, 2006). PIERCE1 is predicted to be a secreted protein, but due to the high percentage of predicted disorder (Schlessinger, Liu and Rost, 2007; Schlessinger, Punta and Rost, 2007; Schlessinger *et al.*, 2009), this result is given a reliability of only 33%. 6 putative protein-protein interaction sites (Ofran and Rost, 2007) were predicted in the protein, along with one polynucleotide interaction site.

I utilised PhosphoSitePlus to assess PTM sites in the mouse and human orthologues of PIERCE1 (**Fig. 4.11**). This data is presented as a lollipop plot, showing location of putative PTMs on the X axis and the number of supporting references on the Y axis. Datasets for both the human (top) and mouse (bottom) proteins are displayed.

The mouse protein contains predicted phosphorylation sites at Y28 (Akimov *et al.*, 2018) and Y78 (Cell Signalling Technology (CST) dataset), and a ubiquitination site at K136 (CST dataset). The human protein contains predicted phosphorylation sites at Y27 and Y47 (CST datasets), and ubiquitination sites at K16 and K105.

The Y27 site was identified through mass spectrometry of the MKN-45 gastric carcinoma cell line, whilst the Y47 site was identified through

mass spectrometry of the Jurkat human T cell line. The murine Y28 site was annotated as orthologous to the human Y27 site; the murine Y78 site was similarly annotated due to identification of the orthologous human Y47 site.

The ubiquitination site at K16 in the human protein was identified through a high throughput study using UbiSite, an antibody against ubiquitin, to enrich for ubiquitinated proteins in the Hep2 and Jurkat human cell lines and identify these modified proteins through mass spectrometry (Akimov *et al.*, 2018). The human K105 and mouse K136 ubiquitination sites were annotated as such due to the identification of the orthologous rat K105 site, through CST mass spectrometry of rat brain tissue.

All of the PTM sites for mouse and human orthologues of PIERCE1 were identified by mass spectrometry, and have only 1-2 supporting references. This means caution is required when evaluating these predicted sites. The K16 ubiquitination site comes from a published set of high-throughput data, and as such is indicated as being more reliable than the phosphorylation sites and other ubiquitination site, which were predicted using CST's in-house experimental data.

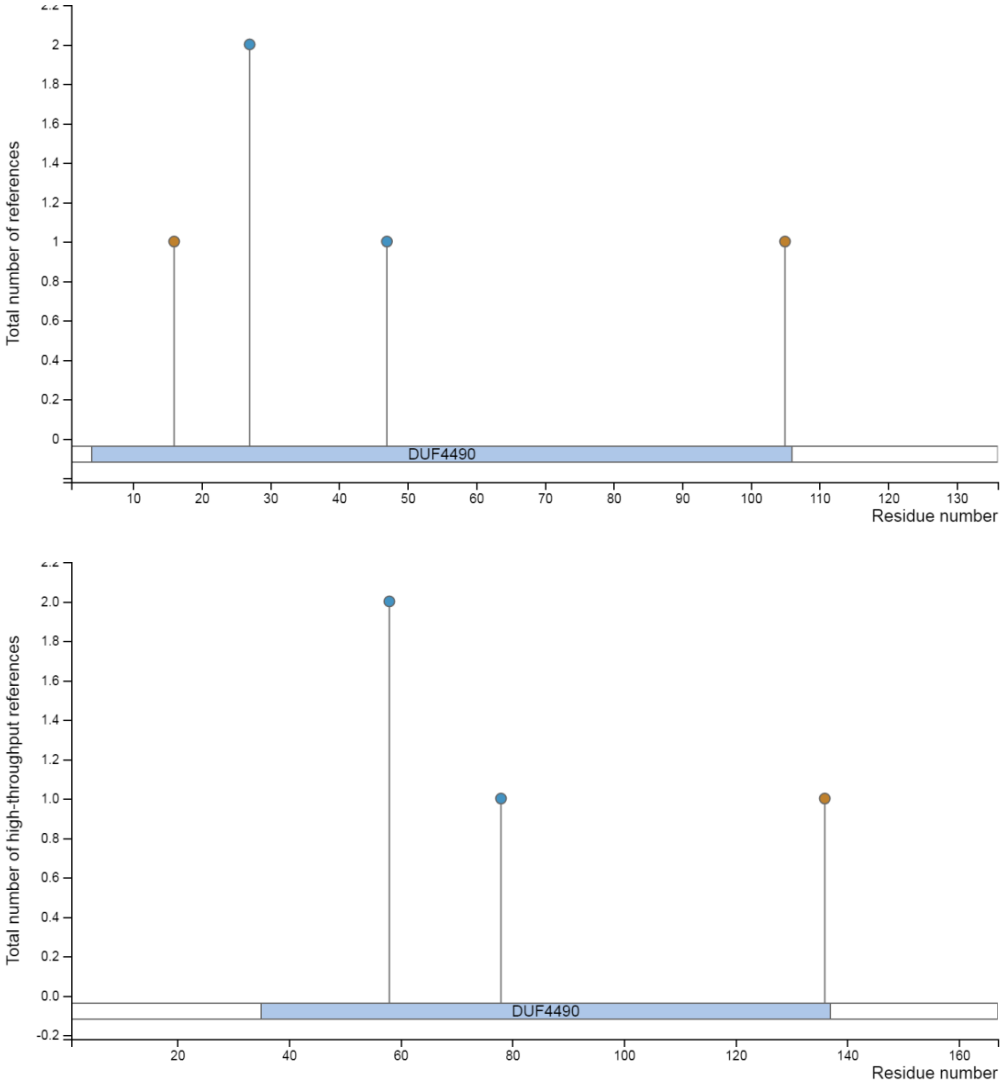


Figure 4.11: PhosphoSite does not predict any high-confidence phosphrylation or ubiquitination sites for PIERCE1.
PhosphoSite post-translational modification predictions for human C9ORF116 (top) and mouse PIERCE1 (bottom). Blue lollipops = predicted phosphorylation site; orange lollipops = predicted ubiquitinylation site. Y axis shows total number of references supporting each site prediction.

InterPro (Mitchell *et al.*, 2018) identifies conserved protein domains and structural protein properties. InterPro predicted no known functional domains or repeats in PIERCE1, and also could not associate any GO terms with this protein. The disordered region at the N terminus of the mouse protein was annotated polyampholite (mixed positive and negative charge; Piovesan et al. 2018; Potenza et al. 2015); this region is not conserved outside of the rodent taxa.

Using Phyre2 (Kelley *et al.*, 2015), a server which uses protein homology and analogy to recognize protein folding, I attempted to create a model of PIERCE1 protein structure. Due to the high level of predicted disorder (60%), 32% of residues were modelled with 75.6% confidence (a low confidence model). I also used IntFOLD3.0 to model PIERCE1 structure in silico; resulting models were annotated as low confidence and highly disordered. As such, these results were of no great utility.

I assessed regions of disorder in PIERCE1 homologues using IUPred (Dosztányi *et al.*, 2005) and ANCHOR (Dosztányi, Mészáros and Simon, 2009). I found a conserved, ordered sequence given a high probability of being a protein binding site in DUF4490. I then used bioinformatics datamining tools to attempt to place PIERCE1 in a network of its protein interactors, with the aim of identifying potential subcellular functions of PIERCE1. STRING (Szklarczyk *et al.*, 2015) (**Fig. 4.12**) and GeneMANIA (Warde-Farley *et al.*, 2010) (**Fig. 4.13, Fig 4.14**) were used to data mine for potential interaction partners of PIERCE1 that may be the targets of this putative binding site.

STRING is a network of known and predicted protein interactions that can be used to create networks of predicted functional interactors, based around a protein of interest. Low stringency settings had to be applied to enable detection of interaction partners for mouse and human proteins. This meant that the threshold for protein interaction scores was

set as 0.15 (low confidence interaction) as opposed to the default setting of 0.90 (high confidence interaction). Although we must bear in mind the lower stringency settings, which are likely to lead to an increased incidence of false positive results, it is worth noting the incidence of some genes known to be related to cilia and ciliary motility in these data mined networks. For example, the STRING network (**Fig. 4.12**) includes DYNLRB2, which is associated with GO annotations for dynein intermediate chain binding and ciliary assembly ('UniProt: a worldwide hub of protein knowledge', 2019), as well as SMRP1, which is associated with spermatogenesis and shows restricted expression to the lung (Haitchi *et al.*, 2009) and testis (Matsuoka *et al.*, 2008).

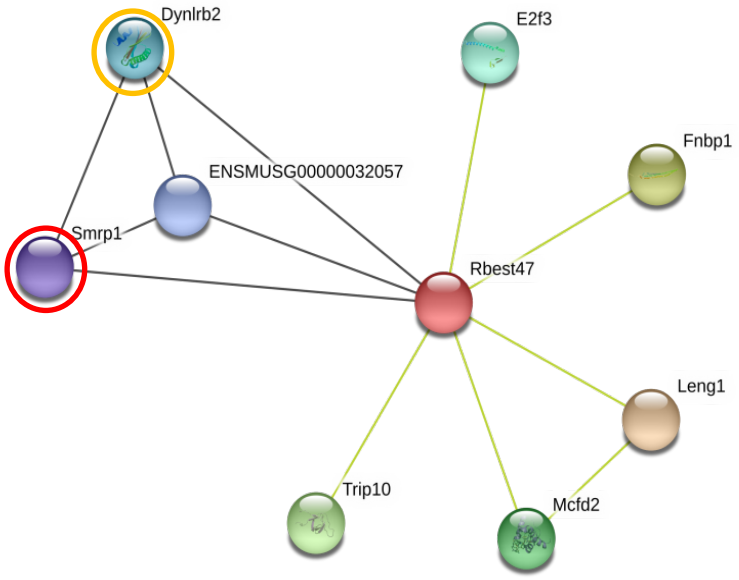


Figure 4.12: STRING does not predict any high-confidence interactors for PIERCE1.
STRING network (low confidence) for mouse PIERCE1 (red node; Rbest47). Light green links: partner determined by text mining. Black links: partner determined by co-expression data. Red circles indicate known links to ciliary/flagellar motility (UniProt ('UniProt: a worldwide hub of protein

The low confidence human GeneMANIA network (**Fig. 4.13**) includes CCDC40 and RSPH9, which are both known to cause PCD (Castleman *et al.*, 2008; Antony *et al.*, 2013), as well as PIFO, which is implicated in the ciliary targeting of Hh signaling components (Kinzel *et al.*, 2010). Also of note are two proteins with relevant functional annotations due to sequence similarity: B9D1 and IQCG. B9D1 is annotated as required for ciliogenesis and Hh signaling ('UniProt: a worldwide hub of protein knowledge', 2019), and IQCG (DRC9; dynein regulatory complex 9) is annotated as an N-DRC component and required for sperm flagellar assembly and motility.

Members of the mouse GeneMANIA network (**Fig. 4.14**) included FOXJ1, the master regulator of motile ciliogenesis. This is unsurprising due to personal communication (Sudipto Roy) listing FOXJ1 as an upstream regulator of PIERCE1 in the zebrafish. DYNLRB2 and PIFO also appear in this network, replicating the results from STRING datamining. TRAF3IP1 and CATIP add to the pool of ciliogenesis-associated proteins that are implicated in datamining studies. DNAH6 is a network member of particular note, as it has been shown to interact with other known heterotaxy and ciliary motility genes (Li *et al.*, 2016). In addition to this, two flagellar associated proteins (CFAP52 and CFAP126) also occur in this network, though their precise function in relation to cilia or flagella is poorly understood. RIIAD1 is highly expressed in tissues with a high degree of both motile ciliation, including the testis, trachea and olfactory epithelium (McClintock *et al.*, 2007), whilst AGR3 is implicated in the regulation of tracheal CBF (Bonser *et al.*, 2015). 1110017D1RIK is an alternate name for SMRP1, the spermatogenesis-associated protein that occurred in the STRING network (Matsuoka *et al.*, 2008; Haitchi *et al.*, 2009).

A unifying issue with these analyses, however, is that all of these networks largely consisted of genes or proteins identified by co-expression and co-localisation studies, as opposed to demonstrable biochemical

interactions. In addition, due to networks being constructed from data mining, a repeated result between STRING and GeneMANIA networks does not add to the reliability of that result, and thus is more likely to occur due to both programs having data mined from the same source material. There is very little publicly available information on biochemical interactors of PIERCE1, limiting the extent to which these networks can aid us in drawing conclusions about the functional nature of PIERCE1 in the motile cilium.

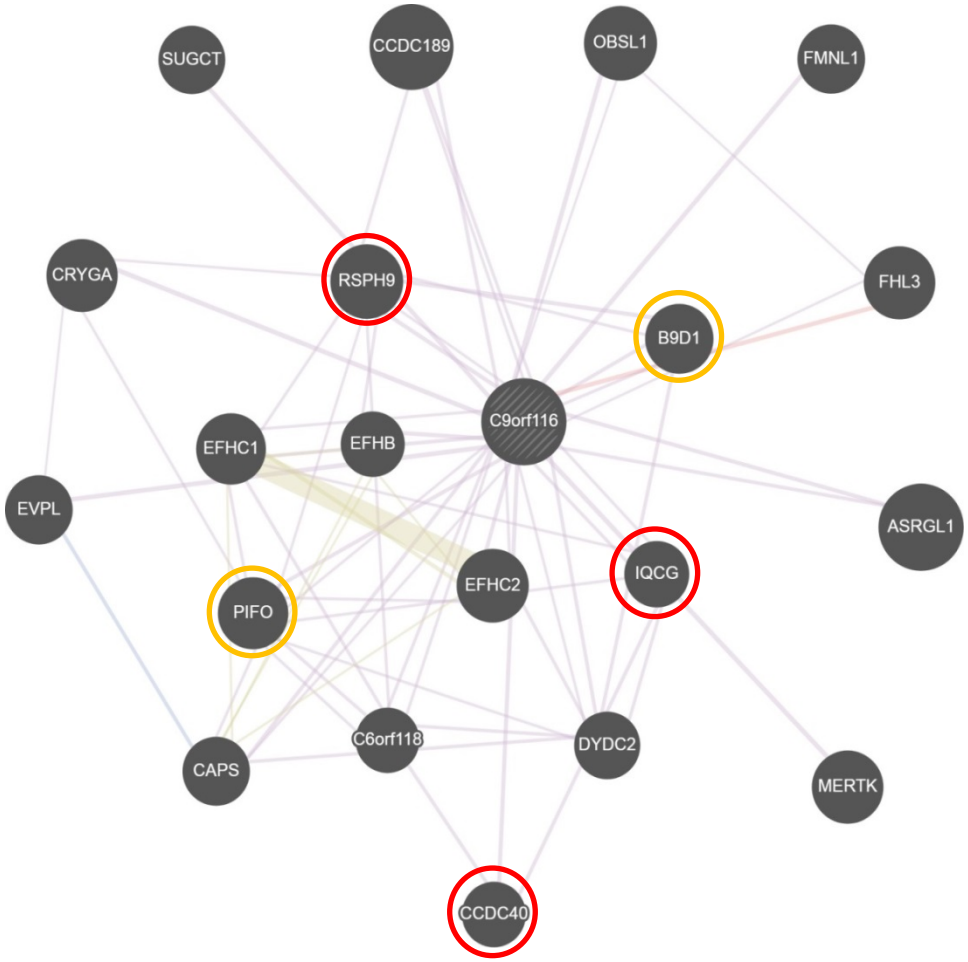


Figure 4.13: GeneMANIA does not predict any high-confidence interactors for C9ORF116.
GeneMANIA network (low confidence) for human C9ORF116 (hashed node). Light green links: partner determined by text mining. Black links: partner determined by co-expression data. Purple = co-expression data; red = physical interaction data. Red circles indicate known links to ciliary/flagellar motility (UniProt ('UniProt: a worldwide hub of protein knowledge', 2019)); orange circles indicate known links to primary cilia/ciliogenesis (Uniprot

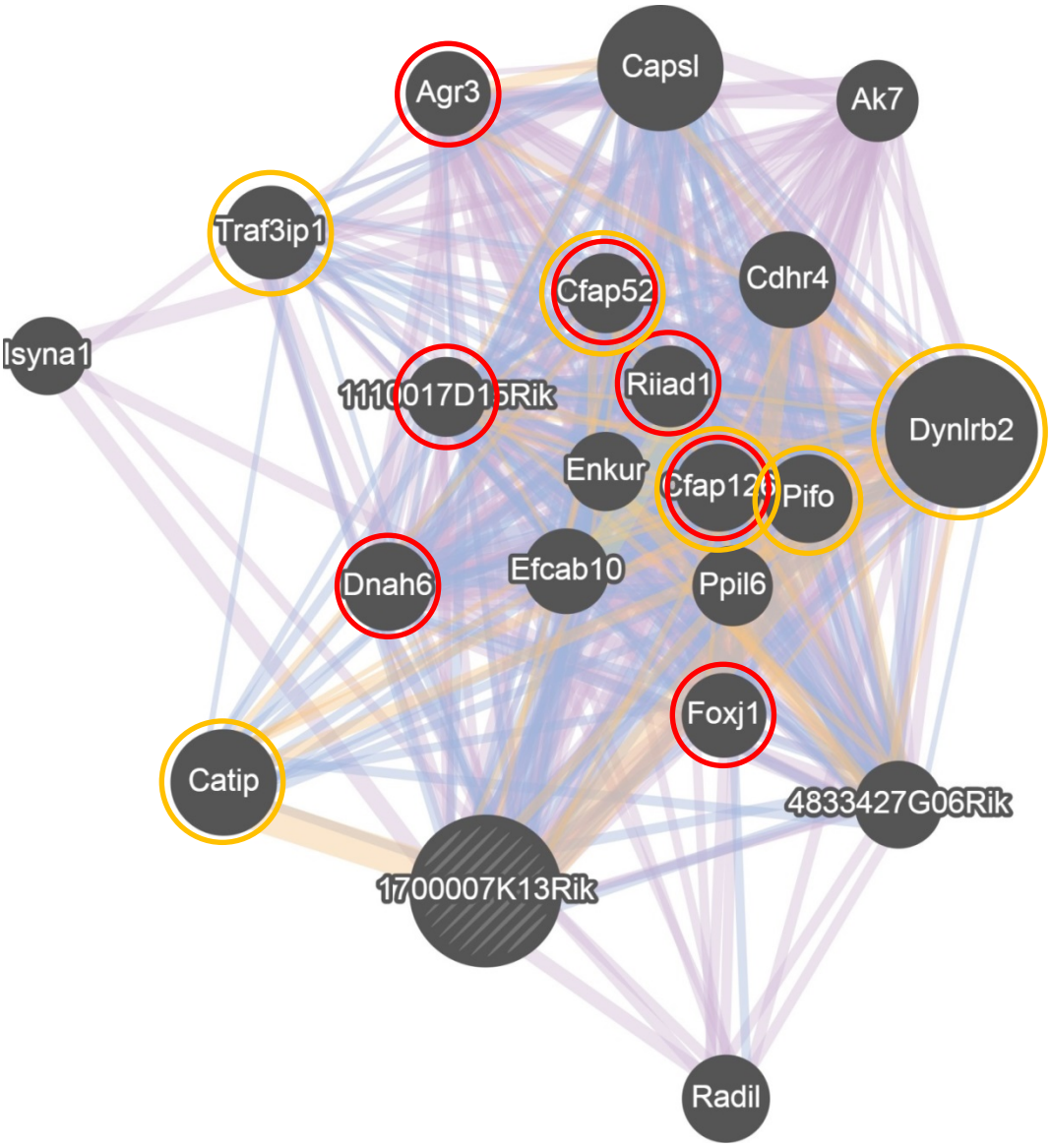


Figure 4.14: GeneMANIA does not predict any high-confidence interactors for 1700001K13Rik.
GeneMANIA network (low confidence) for mouse PIERCE1 (1700001K13Rik; hashed node). Purple = co-expression data. Blue = co-localisation. Orange = predicted interaction. Red circles indicate known links to ciliary/flagellar motility (UniProt ('UniProt: a worldwide hub of protein knowledge', 2019)); orange circles indicate known links to primary cilia/ciliogenesis (Uniprot ('UniProt: a worldwide hub of protein knowledge', 2019)).

4.2.3: Phylogenetic analyses of *Pierce1*

Bioinformatic analyses aimed at unpicking PIERCE1 protein structure and function were relatively unenlightening. As such, I re-focused on phylogenetic analyses of *Pierce1*. I aimed to determine similarities and differences between DUF4490-containing proteins in different organisms, and to test whether DUF4490 does not appear to exist in organisms without motile cilia.

DUF4490 did indeed appear to only be found in organisms with motile cilia, including species of fungi that form flagellated spores. It was not found in organisms that are known to lack motile cilia, such as *C. elegans*. In unicellular organisms of the plant lineage with motile cilia or flagella, such as *C. reinhardtii*, DUF4490 exists as part of a larger protein (FAP182, approximately 49 kDa) that also contains a coiled-coil domain and a nucleotide diphospho-sugar transferase. This makes it likely that at some point in its evolutionary history the protein has split, leaving its orthologues in the animal kingdom with only DUF4490. As there are many variants of nucleotide diphospho-sugar transferase proteins, it is difficult to determine exactly what happened to the other half.

I used ConSeq (Berezin *et al.*, 2004; Ashkenazy *et al.*, 2010; Celniker *et al.*, 2013; Yachdav *et al.*, 2014a) to combine functional and phylogenetic analyses, by detecting conserved residues of the human protein and assigning them putative structural or functional characterisations (**Fig. 4.15**). This predicted that core residues of DUF4490 are both highly conserved and functional.

One other protein in the mouse contains DUF4490 – *Ccpg1os*. I carried out a phylogenetic analysis of the more conserved region (as determined by the ConSurf analysis) of orthologues of these two proteins to test whether they are likely to share a common ancestor protein – whether evolution has been divergent or convergent in the emergence of

the DUF4490 domain (**Fig. 4.16**). *Pierce1* and *Ccpg1os* both tightly cluster in the phylogenetic analysis (**Fig. 4.17**). This makes it more likely that they have emerged from one ancestral protein than that multiple species have separately developed two proteins containing the same domain through convergent evolution.

I repeated the Phyre2 structural analysis with this more conserved sequence, hypothesising that a more reliable prediction was possible without less conserved sequence adding noise. The highest confidence resulting structural model had only 21.9% confidence, meaning that it was a very low confidence putative model that should be treated with caution. This new model did not show any structures of note.

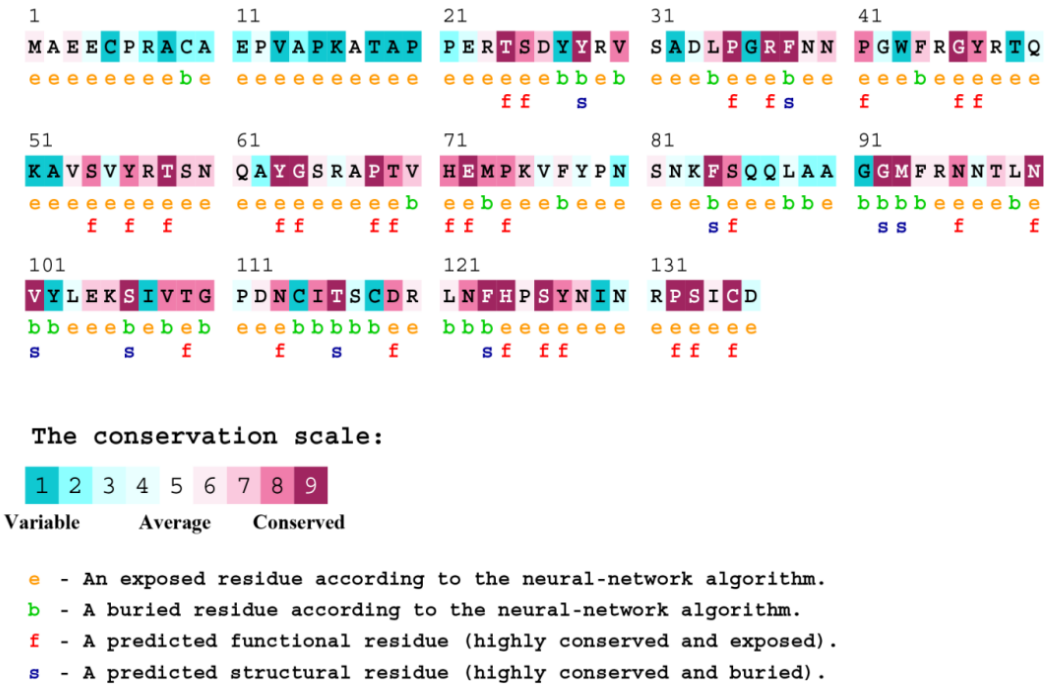


Figure 4.15: ConSeq predicts core conserved residues in DUF4490. ConSeq plot of *C9ORF116* human sequence, showing conservation of residues (background colour) and predicted exposed, buried, functional and structural residues (annotated). The ConSeq programme performs a BLAST for homologous sequences and aligns these using MAFFT, and this alignment is then used to build a phylogenetic tree using the Rate4Site algorithm (Pupko *et al.*, 2002). Conservation scores for each position are calculated using an empirical Bayesian method (Mayrose *et al.*, 2004). ConSeq detects predicts whether residues are likely to be exposed or buried according to a neural network algorithm; exposure and conservation are used to annotate likely structural or functional roles for individual amino acids.

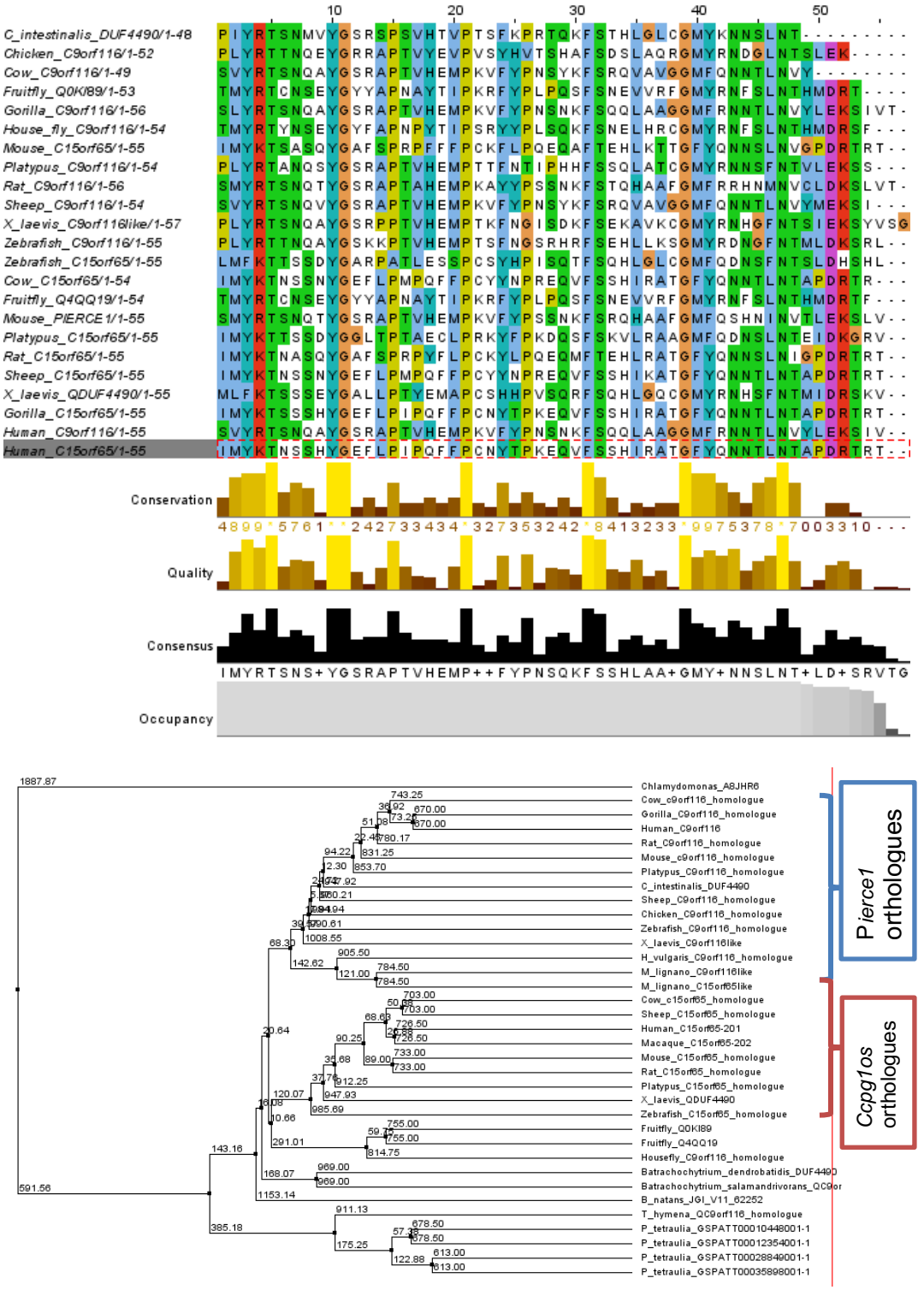


Figure 4.16 (top): Clustal V alignment demonstrates core conserved residues in DUF4490.
Clustal V alignment of the most conserved aspect of DUF4490 containing proteins, carried out in Jalview (Waterhouse *et al.*, 2009).
Figure 4.17 (bottom): The clustering of Pierce1 and Ccpg1os orthologues implies a common ancestor protein.
Phylogenetic tree of the sequences in **Fig. 4.16** (Clustal V method), showing clustering of sequences from *Ccpg1os* and *Pierce1* orthologues. This provides evidence for both proteins having evolved from a single common ancestor protein.

4.2.5: Evaluation of *Pierce1* paralogue expression

Following the identification of *Ccpg1os* as a DUF4490-containing putative *Pierce1* paralogue, I undertook expression analysis. I wanted to determine whether *Ccpg1os* showed a similar expression pattern to *Pierce1*, with restriction to tissues with motile cilia. A 2011 paper by Tamplin et al investigating FOXA2 target gene expression (Tamplin, Cox and Rossant, 2011) demonstrated *Ccpg1os* expression in the embryonic node, a structure tightly related to ciliary motility. I designed and synthesised an in situ hybridisation probe against *Ccpg1os* and my analysis confirmed node-specific expression (**Fig. 4.18**).

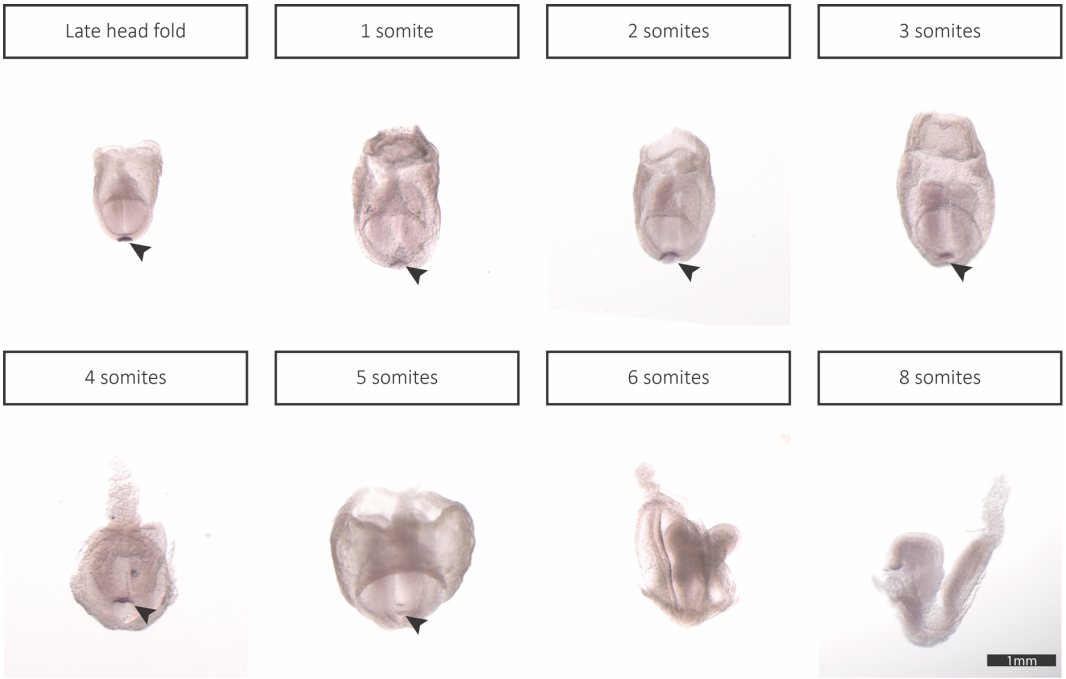


Figure 4.18: *Ccpg1os* expression is restricted to the node in the early embryo.
in situ hybridisation staining (arrowed) for *Ccpg1os*, showing expression restricted to the embryonic node between 7.5 and 8.5 dpc. Scale bar shows 1 mm. Images are representative images from n=5 images per time point.

Residual ciliary motility is present in *Pierce1*$^{-/-}$ embryos, thus I hypothesised that increased expression of *Ccpg1os* could be playing a

compensatory role, and that this could partially underlie the variable phenotype in these mice. I therefore investigated the expression of *Ccpg1os* in *Pierce1*$^{+/+}$, *Pierce1*$^{+/-}$ and *Pierce1*$^{-/-}$ embryos using in situ hybridisation (**Fig. 4.19, Fig. 4.20**). I scored relative expression levels blind to genotype as being very low, low, medium or high (**Fig. 4.19**). *Pierce1*$^{-/-}$ embryos appear to show a trend towards a decrease in *Ccpg1os* expression, though there is considerable heterogeneity across embryos of all genotypes (**Fig. 4.20**). This left me unable to calculate any statistical significance as to whether homozygosity for the *Pierce1*-null allele leads to a change in *Ccpg1os* expression.

Conducting a more precise gene expression study in the embryo using qPCR would require the collection of a large number of *Pierce1*$^{-/-}$ nodes. This was deemed to be impractical due to mouse numbers and time constraints. However, *Pierce1* also appeared to play a role in adult ciliary motility, and indeed, it could be argued that the ciliary motility phenotype in the adult *Pierce1*$^{-/-}$ mice was also partially penetrant - *Ccpg1os* could be playing a compensatory role here as well. I therefore investigated the expression of *Ccpg1os* in tissues with motile cilia (lung, brain, testis, oviduct) from *Pierce1*$^{+/+}$ and *Pierce1*$^{-/-}$ adult mice at 6 months of age. I harvested tissues and isolated RNA from 6 female mice and 8 male mice of each genotype, before synthesising cDNA for use in these experiments.

Analysis of *Ccpg1os* expression by qPCR (**Fig. 4.21**) showed variable but significant effects on *Ccpg1os* expression dependent on *Pierce1* genotype. In *Pierce1*$^{-/-}$ tissue compared to wild-type, we see differential effects between tissues. For example, in female mice, *Ccpg1os* expression was significantly upregulated in the lung and brain of *Pierce1*$^{-/-}$ mice compared to wild-type, but there was no significant effect in the oviduct. In male *Pierce1*$^{-/-}$ mice, when compared to wild-type expression levels, *Ccpg1os* was significantly downregulated in the testis. However,

there was no significant difference in expression in the lung or the brain. There was also a substantial difference in the variation of expression observed within tissues across this dataset. To take a clear example, there is a very broad range of expression changes in the female brain, with a much reduced range in the oviduct.

It is important to note that there appears to be substantial variation between expression changes in male and female samples. More variability and increases in *Ccpg1os* expression are observed in the female data, as opposed to less variation in expression, with a tendency towards downregulation of *Ccpg1os* in *Pierce1*$^{-/-}$ tissues compared to wild-type, in the male data. Our knowledge regarding the genetic network within which these genes may interact is insufficient to draw conclusions with certainty from this work, but there is no clear evidence that *Ccpg1os* consistently acts as a compensatory mechanism in *Pierce1*$^{-/-}$ tissues.

I hypothesised that the *Pierce1*-null allele could be upregulated in the face of its loss-of-function genetic alteration through a feedback mechanism in which a lack of PIERCE1 function within the cell leads to upregulation of the genes required for this function. My investigations into *Ccpg1os* expression in *Pierce1*$^{-/-}$ tissues assumed that *Pierce1* expression was simply abolished in *Pierce1*$^{-/-}$ tissues, with the potential for compensatory upregulation by genes that serve a similar function.

If the genetic regulatory landscape is actually much more complex than this, it could be confounding investigations into any alteration in *Ccpg1os* expression in wild-type and *Pierce1*$^{-/-}$ tissues, and underlying the variable and unpredictable changes in expression observed when comparing *Ccpg1os* expression in *Pierce1*$^{+/+}$ and *Pierce1*$^{-/-}$ tissues (**Fig. 4.21**). As such, I investigated relative expression of the wild-type and null *Pierce1* alleles in heterozygous testis tissue to determine whether there was any striking or unexpected change in the expression of either allele,

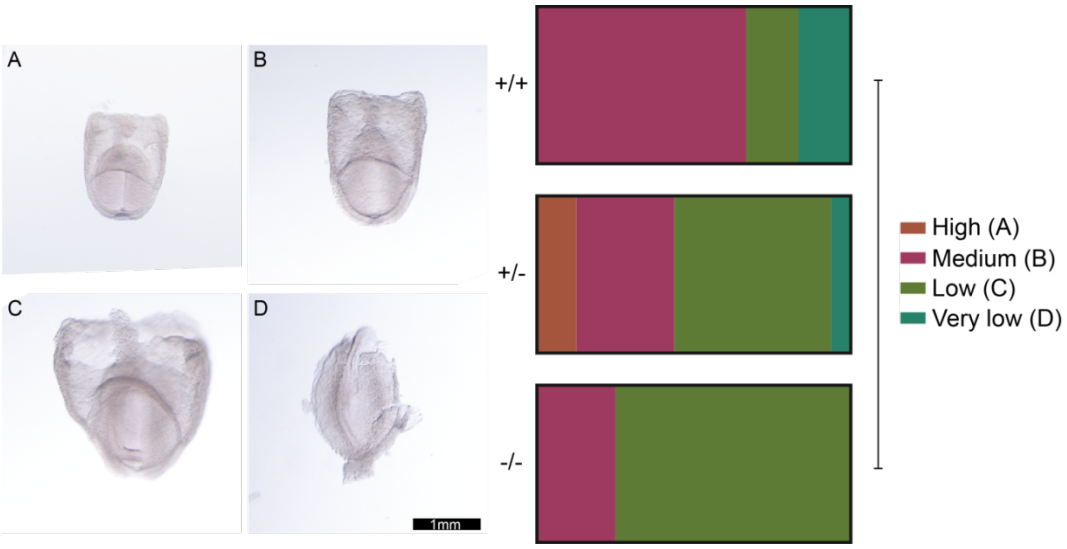
as this could partially account for the varied changes in *Ccpg1os* expression that I observed (**Fig. 4.22, Fig. 4.23**).

Due to the genetic alteration of *Pierce1* in the null allele, and the small size of the gene, different qPCR assays were used to each allele. The cycle threshold (CT) refers to the number of cycles of DNA replication required to produce sufficient fluorescent signal to be detected. Δ_{CT}, or the change in CT, refers to the difference between the number of cycles required to produce fluorescent signal for an assay designed against a housekeeping gene, and an assay designed against our gene or allele of interest.

When I used an assay designed against the wild-type allele, I saw a decrease in Δ_{CT} as wild-type *Pierce1* copy number decreased from wild-type to *Pierce1*$^{-/-}$ tissue (**Fig. 4.22**). This is as expected; more cycles are required to create sufficient levels of DNA amplification for the concurrent fluorescent signal to be detected. *Pierce1*$^{-/-}$ tissue did eventually lead to a detected signal, but this was due to background noise and thus was not considered an indication of physiological detection of allele expression.

A similar story unfolds with an assay designed to detect expression of the *Pierce1*-null allele (**Fig. 4.23**). A stepwise change in Δ_{CT} was observed as *Pierce1*-null allele copy number increased. Overall, no extraordinary changes in allele expression were observed, making it unlikely that any dramatic upregulation of the *Pierce1*-null allele expression in *Pierce1*$^{-/-}$ mice, relative to wild-type *Pierce1* expression in *Pierce1*$^{+/+}$ mice, is the root of the variable changes in *Ccpg1os* expression observed in qPCR experimental work.

Overall, through phylogenetic analysis I have provided strong evidence that *Ccpg1os* and *Pierce1* evolved from a shared common ancestor. It is at present unclear whether *Ccpg1os* acts to compensate for *Pierce1* in vivo. Although changes in expression can be detected, these



are inconsistent. A detailed knowledge of the genetic network of which *Pierce1* is a part will aid in their interpretation.

***Ccpg1os* expression tends to decrease in *Pierce1*$^{-/-}$ embryonic nodes.**
Figure 4.19 (left): *Ccpg1os* expression patterns observed in *Pierce1*$^{+/+}$, *Pierce1*$^{+/-}$ and *Pierce1*$^{-/-}$ embryos. High (A), Medium (B), Low (C) and Very low (D) staining pattern reference images are displayed. Scale bar shows 1 mm.
Figure 4.20 (right): Proportion of expression patterns observed in *Ccpg1os* expression analysis [illegible] pattern is observed.

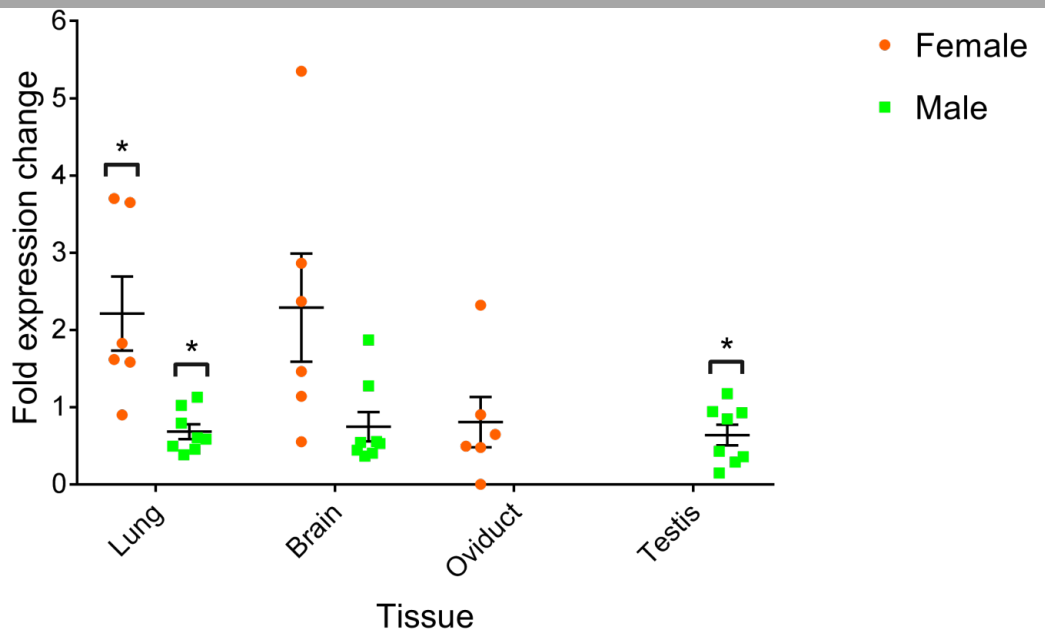
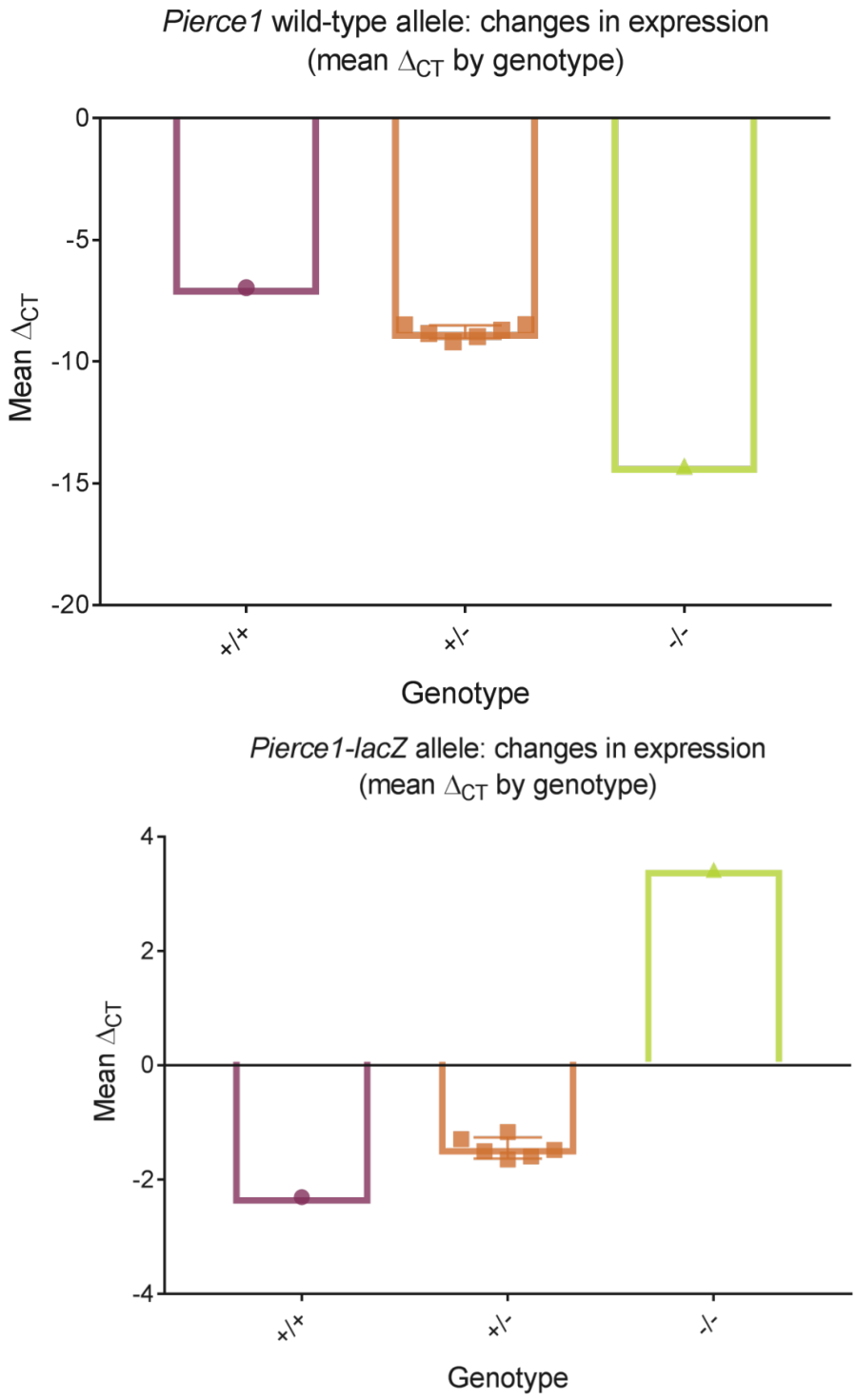


Figure 4.21: *Ccpg1os* shows changes in expression between *Pierce1*$^{-/-}$ and wild-type mouse tissues.
RQ values denoting fold change in gene expression for *Ccpg1os* in *Pierce1*$^{-/-}$ relative to wild-type tissues. Results for female (orange) and male (green) tissue samples are displayed. Mean and SEM for each tissue by sex are indicated.



No extraordinary changes in the expression of either *Pierce1* allele expression are observed in wild-type, *Pierce1*$^{+/-}$ and *Pierce1*$^{-/-}$ mouse tissues.

Figure 4.22 (top): Expression of *Pierce1* wild-type allele in *Pierce1*$^{+/+}$, *Pierce1*$^{+/-}$ and *Pierce1*$^{-/-}$ testis samples. Δ_{CT} refers to the change in cycle threshold for each genotype; a higher Δ_{CT} value means that the target of the PCR assay is more highly expressed. n=1 (+/+), n=6 (+/-), n=1 (-/-)

Figure 4.23 (bottom): Expression of *Pierce1*-null allele in *Pierce1*$^{+/+}$, *Pierce1*$^{+/-}$ and *Pierce1*$^{-/-}$ testis samples. n=1 (+/+), n=6 (+/-), n=1 (-/-)

4.2.6: Regulation of *Pierce1* expression

Recent papers published on the role of TAp73 as a master regulator of motile multiciliogenesis identified *Pierce1* as a TAp73 target (Marshall *et al.*, 2016; Nemajerova *et al.*, 2016). An initial paper by Sung et al (Sung *et al.*, 2010) posited that *Pierce1* expression lay downstream of p53, and identified a putative p53 binding site upstream of *Pierce1*. *p53* is a canonical tumour suppressor gene, and is not typically associated with motile ciliogenesis. I designed in situ probes against *TAp53*, hypothesising that if *TAp53* did have an as yet undiscovered role in motile ciliogenesis, it may show restricted nodal expression pattern in the embryo. These probes revealed ubiquitous expression in 7.5-8.5 dpc embryos (**Fig. 4.24**).

I also designed and synthesised in situ hybridisation probes against *TAp73*. These showed no expression in the embryo at 7.5-8.5 dpc (**Fig. 4.24**), but did show expression in the embryonic lung at 13.5 dpc (**Fig. 4.25**). This provided a positive control for the probe, as we would expect expression of *TAp73* to initiate as the development of the multiciliated epithelium of the trachea begins. This fit with the proposed role of TAp73 in motile multiciliogenesis, and the lack of LR patterning defects observed in *TAp73*$^{-/-}$ mice (Marshall *et al.*, 2016; Nemajerova *et al.*, 2016).

The published *p53* binding site shows strong similarities with that of *p73* (**Fig. 4.26**); the two transcription factors are members of a family that also contains *p63* (Yang and McKeon, 2000; Belyi *et al.*, 2010; Sung *et al.*, 2016). I propose that overexpression of *p53* in the initial paper that identified *Pierce1*, and the similarity of the *p53* and *p73* DNA binding sites, may have led to the incorrect categorisation of *Pierce1* as a gene regulated by *p53*. In a biological setting, I believe that the p53 family member it is more likely to be associated with is *TAp73*.

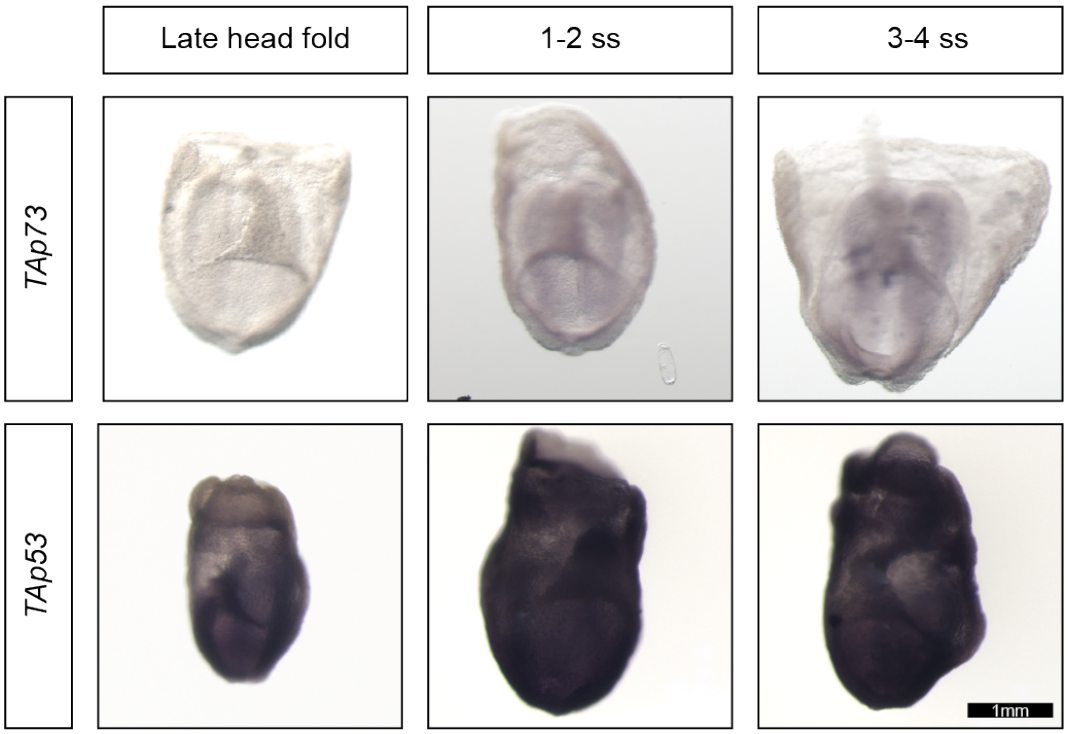


Figure 4.24: *TAp73* shows no expression in the early embryo, whilst *TAp53* shows ubiquitous expression.
TAp73 (top row) and *TAp53* (bottom row) expression in the early embryo (8.0-8.5 dpc), as evaluated by in situ hybridisation. No specific nodal expression of *TAp73* or *TAp53* is observed. *TAp53* expression is ubiquitous whilst *TAp73* expression is absent. Scale bar shows 1 mm. Images are representative of 5 images per time point for each probe.

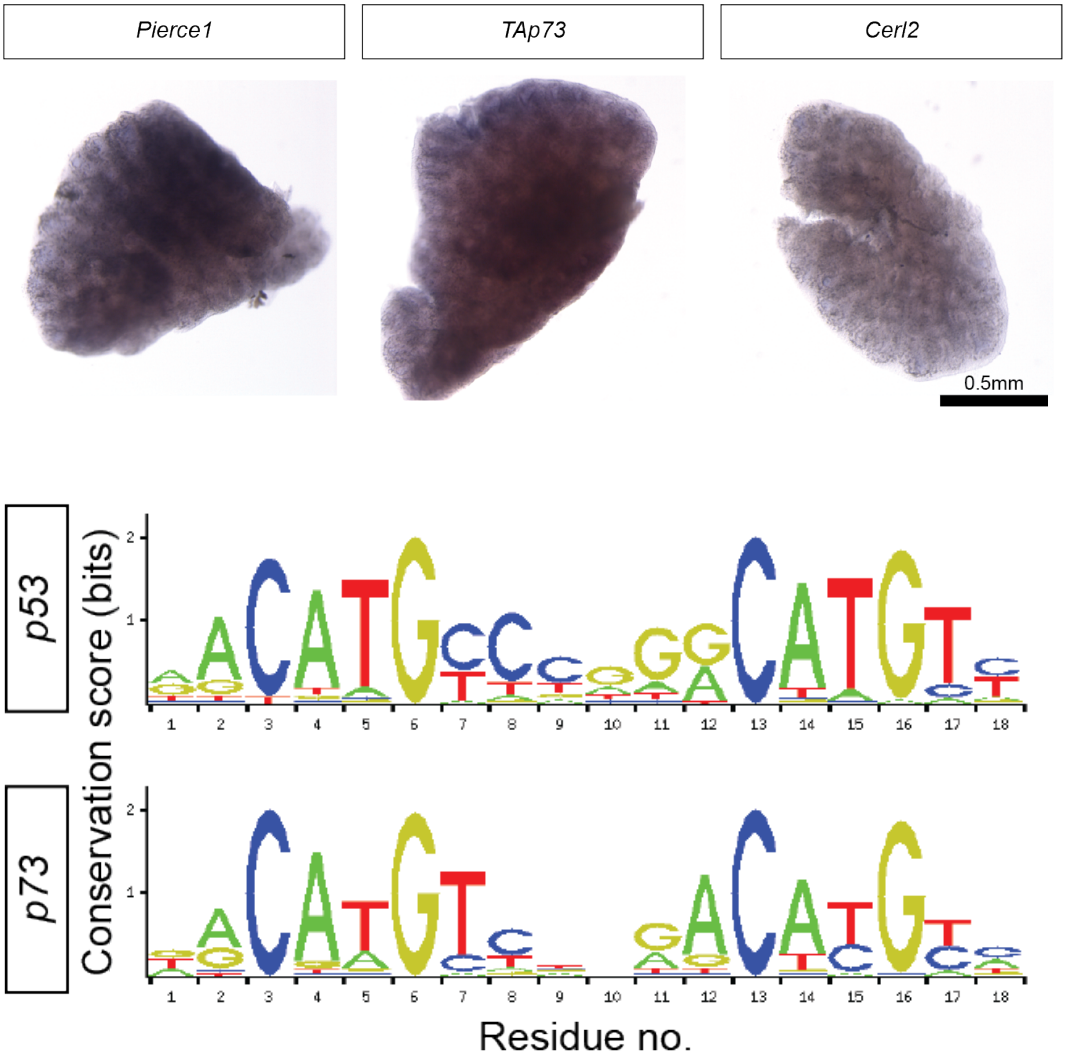


Figure 4.25 (top): *TAp73* and *Pierce1* are expressed in the developing lung at E13.5.
TAp73 expression in the embryonic lung at 13.5 dpc. Expression is observed in the *TAp73* probe and the *Pierce1* probe. No expression is observed in the *Cerl2* probe. Scale bar shows 0.5 mm. Images are representative of 10 images per probe.
Figure 4.26 (bottom): The p53 and p73 consensus DNA binding sequences are similar.
Graphic demonstrating similarity of p53 and p73 transcription factor binding sites.

4.2.7: Yeast two-hybrid screen and investigation of putative interactors

In an effort to identify putative interaction partners of PIERCE1 to ascertain its subcellular function, commercial yeast two-hybrid (Y2H) screens were carried out. This process involves the expression of proteins in yeast cells. If a “bait” protein (usually the protein of interest) binds to a “prey” protein (potential interactor), the transcription of a selector gene cassette is activated due to their proximity. These reporter genes enable colony survival or a colour change (Fields and Song, 1989; Criekinge and Beyaert, 1999; Brückner *et al.*, 2009). Amino acids 1-136 of human C9ORF116 were used as the bait; prey libraries of human lung and human testis were both evaluated. Levels of confidence were assigned to these data: A-C interactors were deemed high confidence, whereas D and E were considered as low confidence interactors likely to contain false positives. These high confidence interactors and any known information regarding protein function and expression are detailed in **Table 4.1**.

The commercial Y2H screen assigns each interaction a confidence values based on Predicted Biological Score, which represents the probability of that interaction being non-specific. As such, the score lies between 0 and 1. Likelihood is mainly based on the number of independent interactions detected compared to the chance of finding these interactions at random as background noise. The cut off between different levels, e.g. A-B, are arbitrarily defined, but a D confidence interaction generally represents an interaction where one unique prey fragment was identified. These interactions are either biological interactions that are hard to detect using Y2H, for example due to low mRNA levels or prey toxicity in yeast, or are false-positive interactions.

Table 4.1: Summary of high confidence interactors discovered in the yeast two-hybrid screen using C9ORF116 as a bait protein with human lung and testis prey libraries. Function and localisation data taken from NCBI RefSeq (O'Leary *et al.*, 2016).

Library/screen	Protein	Confidence interactor	Protein function (O'Leary *et al.*, 2016)	Protein localisation
Human testis	BOLL	A	Probable RNA-binding protein; may be required during spermatogenesis	Restricted expression to testis.
Human testis	COL1A2	B	Collagen α 2 (I). Member of a fibrillar collagen forming family.	Broad expression in 14 tissues, higher in gall and urinary bladders
Human testis	CTSB1 var1	C	Cathepsin B. Peptidase – involved in proteolytic cleavage of amyloid precursor protein.	Broad expression in 21 tissues, higher in thyroid.
Human lung	CTSB1 var1	C		
Human testis	GLUL	B	Glutamate ammonia ligase (glutamine synthetase).	Broad expression in 27 tissues, higher in fat and

				brain.
Human testis	HNRNPF	C	Heterogeneous ribonucleoprotein F. Involved in packaging and transporting pre-mRNA.	Broad expression in 25 tissues, higher in appendix and lymph node.
Human testis	IFT88	A	Intraflagellar transport 88.	Broad expression in 27 tissues, higher in testis and thyroid.
Human testis	METAP1	C	Methionine aminotransferase 1. Removes N-terminal methionine from naïve proteins; essential for progress through the cell cycle.	High expression in 21 tissues, elevated in oesophagus and testis.
Human testis	MLST8	C	mTOR associated protein, LST8 homologue. Subunit of both mTORC1 and mTORC2, which regulate cellular growth and survival in response to nutrient and hormonal signals.	Broad expression in 27 tissues, higher in testis, brain, kidney and thyroid.

Human testis	MMP15	C	Matrix metallopeptidase 15. Involved in the breakdown of extracellular matrix in development and disease.	Broad expression in 24 tissues, elevated in thyroid and placenta.
Human testis	ORC2	B	Origin recognition complex 2. Required for initiation DNA replication in eukaryotic cells	Ubiquitous expression, higher in testis.
Human lung	ORC2	B		
Human testis	PIAS2 var α	C	Protein inhibitor of activated STAT2. PIAS proteins function as E3 SUMO ligases and play a role in many cellular processes by mediating the SUMOylation of targeted genes.	Broad expression in 25 tissues, elevated in testis and thyroid.
Human lung	PIAS2 var α	C		
Human testis	SEPT12	B	Filament-forming cytoskeletal GTPase. Involved in spermatogenesis.	Restricted expression to testis.
Human testis	TUBG1	C	Tubulin γ 1 chain. Major component of microtubules.	Broad expression in 25 tissues, higher in testis and bone marrow.

Human testis	UBQLN3	C	Ubiquilin 3. Thought to associate the proteasome and the ubiquitination machinery to facilitate in vivo proteasomal degradation.	Restricted expression to testis.
Human lung	CCDC80	C	Coiled coil domain containing 80. GO annotations include heparin binding and glucosaminoglycan binding.	Broad expression in 19 tissues, elevated in gall bladder and endometrium.
Human lung	PAM	B	Peptidyl-glycine α-amidating monooxygenase. Implicated in the α-amidation of neuropeptides. Implicated in ciliary motility in unicellular flagellates.	Broad expression in 17 tissues, elevated in heart and adrenal glands.
Human lung	SDHA	C	Succinate dehydrogenase. Involved in complex II of the mitochondrial electron transport chain.	Ubiquitous expression in 27 tissues, elevated in heart and kidney.

4.2.7.1: Results replicated in both lung and testis screens

After reviewing GO terms and other data held in NCBI RefSeq (O'Leary *et al.*, 2016), few of the interactors identified in the Y2H study were found to have known links to ciliary motility or ciliogenesis. A decision was made to focus on candidate interactors that were replicated in both lung and testis prey library screens, namely *CTSB1* variant A, *ORC2* and *PIAS2α.*

CTSB1 is a peptidase involved in proteolytic cleavage, notably in the clearance of amyloid precursor protein (Dinnes *et al.*, 2016). *ORC2* is required for the initiation of DNA replication in cells (Kawakami *et al.*, 2015). We reasoned that these proteins both seemed to play a broader role in cellular function that would lead to a more severe phenotype if they, or any of their interaction partners, were disrupted. *PIAS2α*, however, is involved in SUMOylation, a PTM process which has been implicated in ciliary trafficking (Li *et al.*, 2012; McIntyre *et al.*, 2015). As such, *PIAS2α* was considered the most likely biological interactor of the three, and in vitro experiments were carried out to validate the Y2H interaction.

4.2.7.2: Co-immunoprecipitation of tagged Pierce1 and Pias2 does not show interaction.

Tagged forms of PIAS2 and PIERCE1 were used to investigate their interaction via co-IP studies. I had previously cloned *EGFP-Pierce1* (N-terminal) for used in sub-cellular localisation work. *Pias2-HA* (C-terminal) was purchased from the MRC Protein Phosphorylation and Ubiquitinylation (PPU) unit at the University of Dundee. These plasmids were co-transfected and expressed in 293T cells. Cell lysates were harvested and taken through a co-IP protocol (**EM3.9**).

There is no enrichment for HA signal (red) in the EGFP IP well, and no enrichment of EGFP signal (green) in the HA IP well. One interpretation of the resulting Western blot (**Fig. 4.27**) was demonstration of no interaction between tagged forms of *Pias2* and *Pierce1*. However, *Pias2*-expression was much lower in co-transfected cells than that of *Pierce1-EGFP* (data not shown). I titrated proportions of each plasmid as well as sequentially transfecting the 293T cells, but *Pias2-HA* expression remained low. This could be a confounding factor affecting this work. Efforts are currently being made to clone *Pias2* into a different vector to boost its expression sufficiently to avoid this issue, which would allow co-expression studies to be carried out with more accuracy.

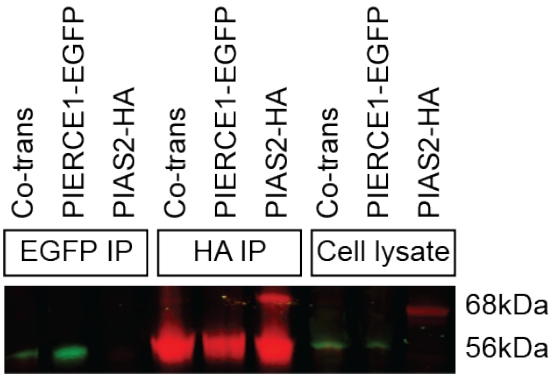


Figure 4.27: PIERCE1 and PIAS2 do not interact in cell culture. Co-immunoprecipitation blot showing the presence of PIERCE1-EGFP (green, 56 kDa) and PIAS2-HA (red, 68 kDa) bands. Top column labels show cellular transfection identity (Co-transfected with both *Pierce1-EGFP* and *Pias2-HA*; *Pierce1-EGFP*; *Pias2-HA*). Boxed labels show antibody used in immunoprecipitation (anti-EGFP; anti-HA; no antibody [cell lysate only]).

4.2.7.3: Expression pattern of Pias2 does not support an interaction with Pierce1.

I investigated whether *Pias2* showed expression in tissues with motile cilia. Although *Pias2* could have other partner interaction proteins, and play other roles, in tissues without motile cilia, it seemed logical that for *Pias2* to interact with *Pierce1*, *Pias2* must be expressed in the tissues to which we know *Pierce1* expression is restricted. A literature search revealed that *Pias2* is expressed in the neural folds and cardiogenic region of the developing embryo at the time of the break in LR symmetry (8.0 dpc) (Costa *et al.*, 2011). The images published by Costa et al (Costa *et al.*, 2011) do not clearly show the node itself, and nodal *Pias2* expression is not remarked upon in their work. As *Pierce1* is only expressed and present in the node, we would expect that any biologically relevant interacting partner would also be expressed in the node. Efforts have been made to contact the authors of this paper, and although the original data has not been recovered, *Pias2* was noted as exhibiting no nodal expression. Simultaneously, work is ongoing to develop our own *Pias2* in situ hybridisation probes to further evaluate this.

4.3: Discussion

4.3.1: *Pierce1* expression is restricted to tissues with motile cilia.

In both the embryo and the adult, expression of *Pierce1* is restricted to tissues with motile cilia. In the early embryo (7.5-8.5 dpc), we see expression tightly restricted to the embryonic node, which contains motile monocilia that are required for effective patterning of the LR axis. In the adult, X-gal staining showed that *Pierce1* is expressed in organs such as the lungs, the respiratory tract, the ependyma of the brain and the reproductive organs. These are all known to contain motile cilia or flagella. This expression pattern was consistent with *Pierce1* playing a cellular role that is connected with initiating and/or maintaining ciliary motility.

The restriction of *Pierce1* expression to tissues with motile cilia made it less likely that this gene has a broader role, for example in cell-cell signalling – if *Pierce1* does play such a role, it appears to be solely in the context of promoting effective ciliary motility. This is mirrored by phenotyping data from the IMPC, which does not show any other gross phenotype in *Pierce1*$^{-/-}$ mice (http://www.mousephenotype.org/data/genes/MGI:1916577).

In situ hybridisation and X-gal staining studies are limited in their resolution to the cellular level, and left us asking where PIERCE1 is found in cells with motile cilia. Its location within the cell, for example at the base of or indeed within the cilium, could provide further clues as to its function; current super-resolution microscopy methods allow the resolution of the membranes bounding either side of the ciliary axoneme and beyond. If a specific and reliable immunofluorescence signal could be obtained with an antibody, we could resolve the localisation of hypothetical ciliary PIERCE1 to the ciliary membrane, or to the axoneme itself.

4.3.2: Immunohistochemistry using an anti-PIERCE antibody is inconclusive.

The creation of a polyclonal antibody against full-length mouse PIERCE1 has proved inconclusive. DAB staining of wax-embedded tissue sections appeared to demonstrate expression of PIERCE1 in cell types known to contain motile cilia or flagella, including the respiratory epithelium and elongating (round) spermatids. The restriction to round spermatids in particular was thought to add weight to a role for *Pierce1* in ciliary and flagellar motility, as the round spermatid stage is when the developing spermatid initiates gene expression related to ciliary and flagellar motility (Laiho *et al.*, 2013). However, identical signal was observed in DAB staining of both wild-type and *Pierce1*$^{-/-}$ tissue. In western blot analysis, a band of similar size was detected in wild-type and *Pierce1*$^{-/-}$ tissues, and the predicted exon 1-lacZ fusion band was not detected at all. Overexpressed EGFP-PIERCE1 did appear to be detected, with a clear band of the predicted size. The uncertainty surrounding the specificity of our anti-PIERCE1 polyclonal antibody makes it difficult to treat the DAB staining results with confidence.

The antibody could be binding to an exon 1–exon 3 alternative splice variant in *Pierce1*$^{-/-}$ tissue, which would in part explain the signal observed in the DAB staining, and the band detected in western blot analysis. For this to be the case, we would have to assume that the epitope to which both synthesised antibodies are binding lies in exon 3, which we presume is not present in the exon 1-lacZ gene product. This would explain why a larger band was not detected in *Pierce1*$^{-/-}$ tissue sample western blot analysis, whilst also explaining why a band corresponding to the PIERCE1-EGFP fusion was detected. To fully investigate this possibility, cloned versions of *Pierce1* lacking individual exons could be produced and transiently over-expressed in cell culture, to assay their detected via western blot and DAB staining.

Another method to determine antibody specificity would be to pre-incubate the anti-PIERCE1 antibody with PIERCE1 peptide to block the antibody, and compare the strength of signal of the blocked antibody with control antibody. If the antibody is specific to PIERCE1, pre-incubation with PIERCE1 peptide will mean that all binding sites are occupied, and therefore staining signal will be much weaker with the blocked antibody compared to the control.

4.3.3: Subcellular localisation of PIERCE1 in cell culture

I used tagged versions of *Pierce1* to investigate subcellular localisation of PIERCE1. I used both serum-containing and serum-free medium in this work, with serum-free media used to promote the formation of primary cilia. I hypothesised that the presence of a primary cilium may lead to an altered localisation pattern of PIERCE1 – a cilium-targeted protein cannot traffick to a cilium that is not present. However, I observed no altered localisation pattern in serum-free media compared to serum-containing media. This is perhaps unsurprising given the ciliary motility phenotype in these mice – the primary cilia induced in my cell culture were not motile, and all evidence collected supports *Pierce1* expression being restricted to motile ciliated cells. As such, any localisation in cell culture may not be representative of the expression pattern in cells with motile cilia.

Using the anti-PIERCE1 polyclonal antibody for reliable immunofluorescence to investigate PIERCE1 subcellular localisation in cells with motile cilia has been challenging. The tagged forms of PIERCE1 could be used to assay subcellular localisation in motile ciliated cells with the use of murine tracheal epithelial cell culture, or by transfecting into animal cap cultures. Both of these techniques are currently under investigation by our lab and collaborators.

4.3.4: In silico analysis of PIERCE1

I hypothesised that bioinformatics analysis may prove useful in unravelling the functional role of PIERCE1, for example by identifying known functional domains of the protein, or revealing interaction partners that are known to play a broader role in ciliary motility. However, little reliable protein structure prediction has come out of this analysis. This is perhaps unsurprising; *Pierce1* is an orphan gene, with very little known about its cellular function. The high level of predicted disorder may be due to the fact that DUF4490 is exactly that – a domain of unknown function, and thus structural prediction tools struggle to compute it.

PTM sites could also have given us a clue as to the functional role of PIERCE1. Putative conserved sites for phosphorylation and ubiquitinylation were identified, but these must be viewed with the caveat that the data source was high throughput mass spectrometry; although the sites are predicted, they are not validated as functionally relevant PTMs. Indeed, whilst the ubiquitinylation site came from published data, all of the other PTM sites are from CST's in-house data, which means that it has not necessarily been as rigorously analysed as published data. Each PTM site also had only one or two citations as the data source, further lowering the reliability of these predictions.

Data mined genetic networks also proved of limited use. There were no KEGG pathways hits for the mouse and human orthologues of *Pierce1*. STRING was only able to create an interaction network when stringency was reduced and low confidence interactors were included. Although the GeneMANIA networks did include genes typically associated with ciliary motility, such as *Foxj1* and *Rsph9*, the majority of interactions included in the GeneMANIA network come from co-expression or co-localisation studies. As such, they were not necessarily direct interactors. Many interactions in the mouse PIERCE1 network are actually predicted

interactions. Only one interaction in the human GeneMANIA network was due to physical interaction – that of C9ORF116 with FHL3.

FHL3 (four and a half lim domains 3) is a member of a protein family containing an FHL domain - a highly conserved double zinc finger motif. It is a highly conserved protein, and has been shown to regulate the expression of the SMAD transcription factors, which have been implicated in tumorigenesis and development through their mediation of TGF-β super-family signalling. FHL3 has been shown to localise to the nucleus (Coghill *et al.*, 2003) - none of our studies have shown PIERCE1 to have nuclear localisation, although any interaction with FHL3 could theoretically be taking place outside of the nucleus.

Phylogenetic analysis showed that DUF4490, the predicted functional domain conserved across *Pierce1* and its homologues, is highly conserved amongst organisms with motile cilia. The tight conservation of the DUF4490 region, particularly when compared with other aspects of the protein, for example the divergent N-terminal sequence in rodents, adds weight to this gene as playing an important functional role in the cell. The lack of *Pierce1* orthologues in organisms known to lack motile cilia, such as *C. elegans*, further underlines that this role is likely to be in ciliary and flagellar motility.

4.3.5: *Ccpg1os*, the *Pierce1* orthologue

The identification of a *Pierce1* orthologue could have indicated that there may be some kind of compensatory mechanism taking place in our *Pierce1*$^{-/-}$ mice. The *Pierce1*$^{-/-}$ mice had a less severe ciliary motility phenotype than mouse models of PCD, which typically exhibit immotile cilia and a high rate of perinatal mortality due to hydrocephalus. This is not the case in the *Pierce1*-null line.

This compensatory hypothesis was supported by publicly available data showing *Ccpg1os* to be expressed specifically in the embryonic node.

Further experimentation evaluating differences in expression in *Pierce1*$^{+/+}$ and *Pierce1*$^{-/-}$ mice was inconclusive. There is no overall pattern of *Ccpg1os* upregulation in *Pierce1*$^{-/-}$ tissues. There are multiple factors that could be contributing to this. The *Ccpg1os* qPCR data shows varying expression across different tissues. A tissue-specific differential requirement for PIERCE1 could lead to altered changes in *Ccpg1os* expression. We know that motile cilia appear to be affected to different extents in *Pierce1*$^{-/-}$ tissues with motile cilia; however, different analytical techniques were used to evaluate ciliary motility in each tissue. This makes any overall difference in motility hard to ascertain when comparing distinct tissues. We did not detect a dynein arm defect in *Pierce1*$^{-/-}$ sperm (**Fig. 3.24**). Potentially, a differing need for PIERCE1 in order to assemble motile cilia could underlie differential changes in *Ccpg1os* expression.

Another explanation that I considered was differential expression of the two alleles. If the null allele is being upregulated in response to its lack of functional output, this may reduce any compensatory upregulation in *Ccpg1os*. Due to the design of the *Pierce1*^{tm2b} allele and the small size of *Pierce1*, evaluating any change in specific allele expression was challenging. Probes designed for use with the wild-type *Pierce1* allele would not work for the *Pierce1*-null allele, as they were designed to span an exon-exon boundary that wouldn't appear in *Pierce1*$^{-/-}$ animals. Probes designed to be specific for the *Pierce1*-null allele would likewise fail to effectively amplify the wild-type allele.

I decided to analyse relative expression of each allele in *Pierce1*$^{+/-}$ animals and compare Δ_{CT} values with those of *Pierce1*$^{-/-}$ and wild-type tissue for each probe. This showed expected decreases in expression of each allele in heterozygous tissue. Overexpression of the *Pierce1*-null allele in the *Pierce1*$^{-/-}$ tissue samples is unlikely to be a factor underlying changes in *Ccpg1os* expression.

A key factor to consider when evaluating these data is that *Pierce1* and *Ccpg1os* are both poorly characterised genes. We have little idea as to their cellular function and their regulatory network – there are undoubtedly other genes and regulatory factors at play here. Finally, both genes are not highly expressed in the embryonic node. It could be that upregulation of expression is not required for compensation of function on a protein level.

4.3.6: Regulation of *Pierce1* expression

Although *p53* was initially described as an upstream regulator of *Pierce1* expression, I believe that an important consideration in evaluating the data collected by Sung et al on the regulation of *Pierce1* by *p53* is the similarity of the *p53* and *p73* binding sites. There is strong evidence for *TAp73* as an upstream regulator of *Pierce1* expression; the result of *p53* as a regulator of *Pierce1* expression may be a false positive due to the similarity of the *p53* and *p73* binding sites. I propose that artificial overexpression of *p53* may have led to it binding to sequences that are actually *p73* sites.

Although ciliogenesis is in part associated with the cell cycle – centrioles form the basal body of the cilium, and thus in physiological conditions, the cell cycle must be arrested for ciliogenesis to occur – any defect disrupting the connection between the cell cycle and ciliogenesis would tend to disrupt primary ciliogenesis. As previously discussed, the *Pierce1*$^{-/-}$ mouse does not show a suitably severe phenotype for us to believe that *Pierce1* is required for primary ciliogenesis; indeed, we know primary ciliogenesis is not affected due to live imaging of motile cilia and SEM imaging of nodal cilia. The cilia appear to be present and morphologically normal.

4.3.7: Yeast two-hybrid studies

We hypothesised PIERCE1 plays a role in dynein assembly, due to the dynein assembly defects observed in TEM sections of tracheal motile cilia. Any defect in dynein assembly could disrupt ciliary motility, and thus be causative for the motility defects detected in *Pierce1*$^{-/-}$ mice. However, the results from the Y2H screen did not identify interactions with known dynein assembly factors. This did not support our initial hypothesis. I researched the proposed interaction partners to prioritise which of them to validate, using co-IP of tagged proteins in cell culture. My work did not demonstrate an interaction between PIERCE1 and PIAS2.

Plans are underway to clone *Pias2* into another expression vector in an attempt to repeat this work and address issues with expression levels. If PIERCE1 and PIAS2 still do not co-express, this may reflect some kind of biological interaction occurring between them. All of the research conducted thus far is not supportive of an interaction between PIERCE1 and PIAS2. They do not appear to co-express in tissues where we know that PIERCE1 is required for ciliary motility, and we have not validated the Y2H protein interaction results.

Although few of the proteins identified in the Y2H screen appear to have an obvious link to motile cilia, the time has come to consider these other candidate interactors more seriously. Lower confidence interactors that include a high proportion of false positives could still include a biologically relevant protein, and should be examined further. To do this, I would conduct a more thorough literature search, particularly looking for knock out model organisms of these genes, to determine whether a typical ciliary motility phenotype is observed, for example male infertility in *D. melanogaster* or hydrocephalus in the mouse.

In addition to this, we must consider the potential for PIERCE1 playing an organism-specific role. There is divergence between the N-

terminus of the rodent PIERCE1 protein and that of the human orthologue, and we have no evidence as yet of any human patients affected by mutations in *C9ORF116*. The Y2H screen was conducted using libraries of human proteins. There is a possibility that the human protein no longer functions in ciliary motility. However, I consider this unlikely. DUF4490 is still present and conserved in the human orthologue; the zebrafish *Pierce1* orthologue also shows a functional role in ciliary motility, adding weight to this being a conserved role of PIERCE1.

There are additional factors to consider regarding the lack of human patients diagnosed with mutations in *C9ORF116*. If C9ORF116 plays a similar biological role in humans as the mouse and zebrafish orthologues do in their respective organisms, we would expect mutations in *C9ORF116* to have a modifying effect on ciliary motility. Although stereotypical PCD may be the result, I consider that it is more likely any mutations in *C9ORF116* would result in LR patterning defects due to alterations in nodal ciliary motility; this is the primary phenotype observed in the mouse line. Although we do see modifying effects on ciliary motility in other tissues, these effects are not sufficiently substantial to cause pathology such as rhinitis and male infertility.

If homozygous *C9ORF116* mutations in humans lead to nodal ciliary motility dysfunction similar to that observed in the mouse, we would expect a variety of phenotypes to arise. It is of note that a significant proportion of these would be SS, which is unremarkable, and SIT, which is not pathological. As such, it may not be diagnosed in the absence of other PCD-associated co-morbidities, such as chronic bronchiectasis or male infertility.

A proportion of *C9ORF116* mutations would be expected to lead to heterotaxy. If the associated cardiac patterning defects were severe, this may lead to miscarriage or termination of pregnancy. Even if carried to

term, severe heterotaxic visceral organ patterning defects would be a significant morbidity burden on the neonate. As such, the hypothetical population of surviving patients affected by a *C9ORF116* mutation could well be exceedingly small, and statistically unlikely to be identified. In addition to this, *C9ORF116* (and *Pierce1*) are small genes; the chances of a mutation affecting their conserved DUF4490 in particular are low. Of course, all this does not mean that *C9ORF116* mutations could not be a cause for PCD; further insight into the functional interactors of this protein could aid us in evaluating the likelihood of this.

4.4: Conclusions

Overall, I have shown that *Pierce1* is likely to be expressed solely in cells with motile cilia. *Pierce1* and its paralogue *Ccpg1os* appear to have evolved from a shared common ancestor, and show similar expression patterns, with the potential for some level of functional compensation. *Pierce1* has not been identified as an interactor of known dynein assembly factors; both in silico and Y2H studies have not identified *Pierce1* as a member of known ciliary assembly protein networks. Work continues to further evaluate potential interaction partners of *Pierce1* in order to fully ascertain its functional role in the cell.

4.4.1: Future work

The functional studies into the PIERCE1 protein have left some key questions to be answered. Notably, the issue remains of which proteins PIERCE1 is interacting with in its biological niche. This will help us understand the ciliary motility defects caused in the mouse by *Pierce1* knock-out. Avenues of exploration currently underway include expression of tagged *Pierce1* in motile multiciliated epithelial cell culture, to isolate tagged PIERCE1 protein and proximal interactors. As well as this, overexpression in animal cap cells derived from *Xenopus* in underway. A similar premise underlies this work – overexpression of *Pierce1*, isolation

of proteins in close proximity to PIERCE1, and comparison with the protein population present in native cells.

5: *Ccdc103* and ciliary motility in the mouse

5.1: Introduction

Analysis of *Pierce1*$^{-/-}$ tracheal ciliary ultrastructure via TEM demonstrated dynein arm defects in these cilia with a similar level of penetrance to those observed in patients with PCD carrying certain *CCDC103* mutations (personal communication, James Thompson). *CCDC103* encodes a coiled coil domain-containing protein that is known to localise along the ciliary axoneme (Panizzi *et al.*, 2012).

CCDC103 was first identified as a PCD-causative gene through genetic screening of patients with PCD and dynein arm defects (Panizzi *et al.*, 2012). Zebrafish carrying mutations in this gene present with abolished ciliary motility, and the orthologous gene product in *C. reinhardtii* was shown to bind tightly to the flagellar axoneme (Panizzi *et al.*, 2012). This initial paper identified several distinct mutations in *CCDC103* that were considered likely causes of PCD. Three British Pakistani families carried frameshift mutations leading to a premature stop codon (p.Gly128fs25*). Patients homozygous for this mutation exhibited complete paralysis of motile cilia from nasal brushings, with severe dynein arm defects apparent when investigated by TEM.

Four individuals from three families, two of British Pakistani origin and one of German origin, were identified as being homozygous for *CCDC103* p.His154Pro. This mutation was predicted to cause protein disruption, with a damage score of 0.972 when evaluated by Polyphen-2 (Adzhubei, Jordan and Sunyaev, 2013), where 1.0 is the most disruptive score. Patients homozygous for the *CCDC103* p.His154Pro mutation exhibited a more heterogeneous ciliary motility phenotype, including reduced beat amplitude, a loss of coordination, and some areas of cells exhibiting complete paralysis. This was reflected in the variability observed in their dynein arm phenotype, with some patients having no detectable

dynein arm defects, and other *CCDC103* p.His154Pro patients showing a complete loss of dynein arms. Heterogeneity was observed between siblings in the same family, who were both homozygous for *CCDC103* p.His154Pro. The single nucleotide change causing this change in protein sequence appeared to be less pathological, and less penetrant, than the frameshift loss-of-function mutation also detected in this initial paper.

Other case reports of PCD patients homozygous for mutations in *CCDC103* followed. A distinct frameshift mutation (*CCDC103* p.Pro129Valfs*24) reported in 2014 (Raidt *et al.*, 2014) led to completely immotile cilia. The *CCDC103* p.His154Pro mutation, with its more variable phenotype, was also detected in an Irish Traveller family (Casey *et al.*, 2015), with children presenting with PCD in combination with developmental delay due to a 17q12 microdeletion. TEM analyses of this family showed that whilst affected probands did display more dynein arm defects than the general population, the level of defects was not as severe as that typically observed in the PCD patient population.

However, despite these instances of homozygosity for *CCDC103* p.His154Pro occurring in PCD patients, it remained unclear whether this was a causative genetic defect for PCD, or merely a high frequency non-pathological variant. The *CCDC103* p.His154Pro variant has a high allele frequency (Shoemark, Moya, *et al.*, 2018), whilst PCD is itself a rare disease – we would expect a disease-causing variant with such a high allele frequency to be causing a disease that is more common than PCD.

Shoemark et al (Shoemark *et al.*, 2017) investigated the penetrance and disease phenotype of the *CCDC103* p.His154Pro mutation in families of British South Asian origin. 86 patients were screened for the *CCDC103* p.His154Pro mutation. In homozygous carriers exhibiting PCD symptoms, a range of diagnostic test results were observed. These included normal CBF and CBP; normal TEM results; and normal nasal nitric oxide levels.

Low nasal nitric oxide levels have been associated with many, but not all, patients with PCD; the biological reasons behind this association are unclear (Behan *et al.*, 2016). Despite the variety in diagnostic tests, many of these patients were presenting with the respiratory disease phenotype associated with PCD.

The presence of SIT, a major indicator of abnormal ciliary motility during development, increases the likelihood that PCD is considered by diagnosing clinicians (Lucas *et al.*, no date). 94% of the patients found to be homozygous for the *CCDC103* p.His154Pro mutation either exhibited SIT themselves, or SIT was found in their siblings, which may indicate that a high proportion of these patients are not being diagnosed. Alternatively, there could be an additional effect on nodal ciliary motility or downstream LR patterning due to the *CCDC103* p.His154Pro mutation; a low rate of diagnosis is considered more likely due to the high incidence of normal diagnostic test results in this patient population.

Shoemark et al also showed that *CCDC103* p.His154Pro disrupts the oligomerisation capacity of CCDC103 (Shoemark *et al.*, 2017), with dimers able to form, but larger oligomers not present. Little is known about the functional requirement of CCDC103 in ciliary motility, but we would presume that this capacity to form oligomers is functionally important, and leads to the disrupted ciliary motility and lung pathology observed in patients homozygous for *CCDC103* p.His154Pro.The capacity for CCDC103 to exist as monomers and dimers was reported by Panizzi et al (Panizzi *et al.*, 2012), who reported that the protein appeared to be highly stable and required harsher denaturing conditions than were standard. CCDC103 exhibits a high α-helix content and a molecular weight of approximately 29 kDa (King and Patel-King, 2015).

CCDC103 contains an RPAP3_C domain flanked by N and C terminal coiled coil domains, and this central domain is believed to be

involved in oligomer and dimer formation. RPAP3_C domains were initially identified at the C-terminus of RNA polymerase II associated proteins, and contain tetratricopeptide repeats towards the N terminus of the domain (Itsuki *et al.*, 2008). King & Patel-King proposed a role for CCDC103 in directing the precise positioning of ODA docking on the microtubule axoneme, either through editing the microtubule lattice to facilitate docking, or through a direct interaction with ODA components themselves (King and Patel-King, 2015). *CCDC103* p.His154Pro lies in the middle of the RPAPC_3 domain. This could explain why oligomerisation is disrupted in patients homozygous for this mutation. However, there is much left to understand regarding the nature of CCDC103 and its role in ciliary motility.

The *CCDC103* p.His154Pro mutation was engineered into B6N mice via CRISPR-Cas9 as part of the Genome Editing Mice for Medicine project. *CCDC103* p.His154Pro lies in a region of the protein that is conserved between mice and humans, and is predicted to disrupt protein structure (Shoemark, Moya, *et al.*, 2018). This allele is henceforth referred to as *Ccdc103*^{H154P}. A mouse with a 13 nucleotide deletion in the gene, at approximately the same locus as the single nucleotide change leading to p.His154Pro, was also created (*Ccdc103*^{del13}; **Fig. 5.1**). An alternative *Ccdc103* transcript that is expressed in the mouse is also displayed.

As part of collaborative work with the Mitchison group (University College London), I set out to analyse nodal flow and nodal ciliary motility in both the *Ccdc103*^{del13} and *Ccdc103*^{H154P} mouse lines, to give further insight into motility issues underlying the increase in incidence of SIT in patients carrying the *CCDC103* p.His154Pro mutation. I also planned analyses of organ situs at 13.5 dpc, to investigate whether the introduction of these mutations into the mouse led to LR visceral organ patterning defects.

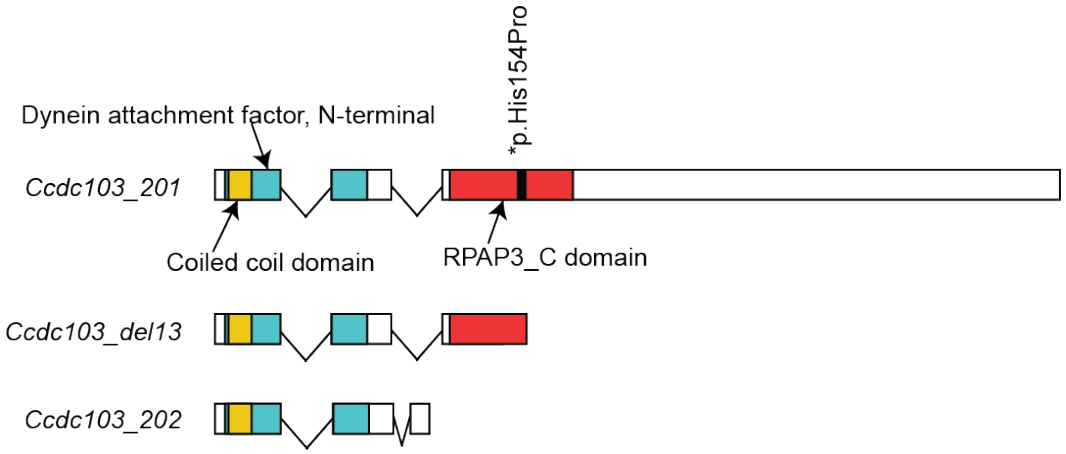


Figure 5.1: Diagram showing the protein domains present in *Ccdc103* transcripts, and the location of the p.His154Pro and del13 mutations. *Ccdc103_202* refers to an additional Ccdc103 transcript that is expressed in the mouse.

5.2: Results

5.2.1: *Ccdc103* shows restricted expression to the mouse node.

The expression pattern of *Ccdc103* in the mouse had not previously been investigated. I designed and synthesised in situ hybridisation probes against *Ccdc103* (**Fig. 5.2**) and the expression of this gene showed nodal localisation between 7.5 and 8.5 dpc. *Ccdc103* expression does appear to initiate and terminate earlier than that of Pierce1 by a few hours – staining is not clearly seen after the 3 somite stage. However, this specific nodal localisation at this time point in embryonic development is concurrent with a role for *Ccdc103* in the establishment of LR asymmetry, putatively through effects on nodal ciliary motility.

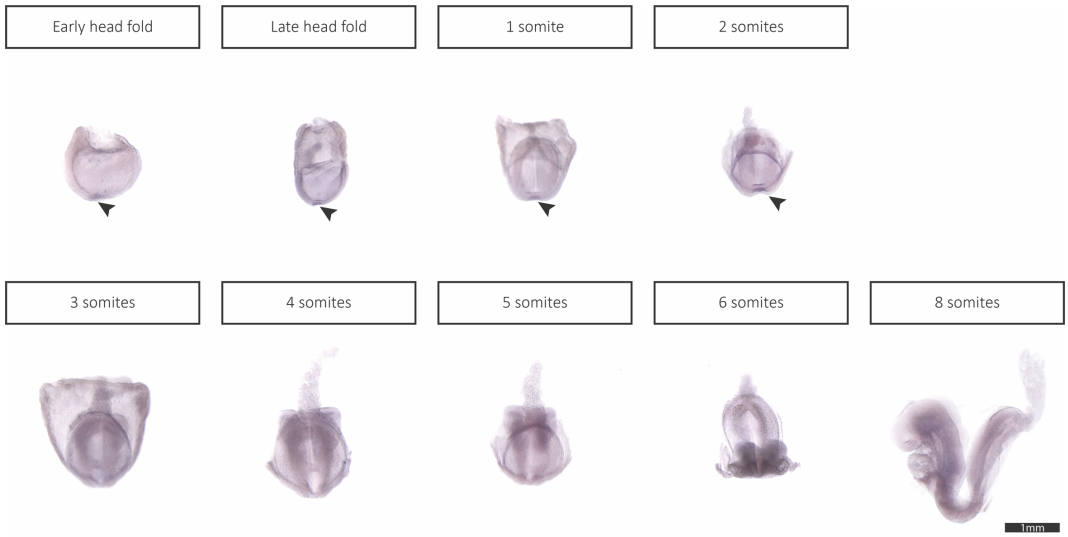


Figure 5.2: *Ccdc103* is expressed in the embryonic node in the early mouse embryo.
In situ hybridisation staining (arrowed) for C*cdc103*, showing expression restricted to the embryonic node between 7.5 and 8.5 dpc. Scale bar shows 1 mm. Images are representative images from n=5 images per time point.

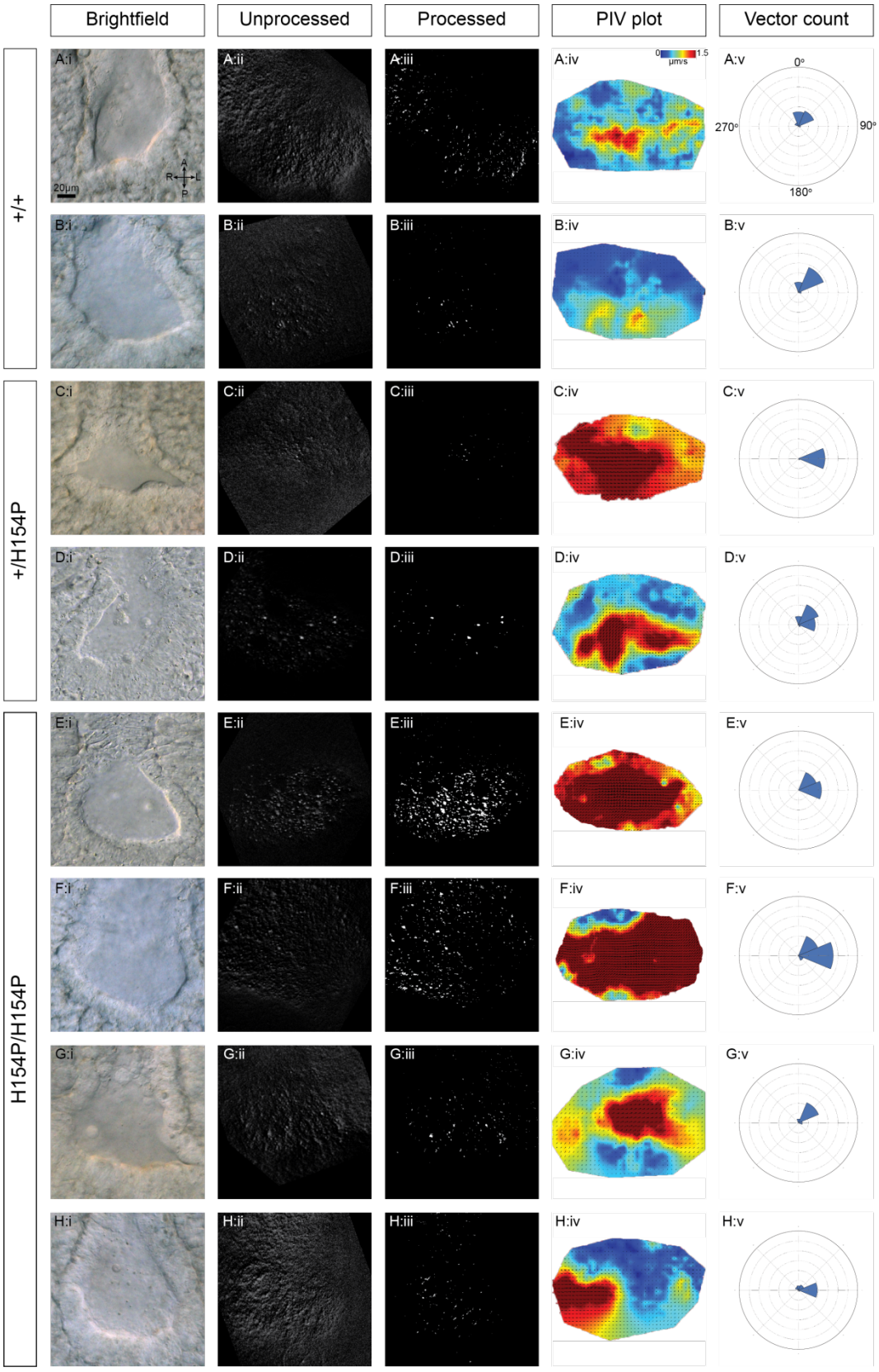
5.2.2: *Ccdc103*$^{H154P/H154P}$ mice show leftwards nodal flow.

Leftwards nodal flow is required for effective LR patterning. I utilised PIV (Nonaka *et al.*, 1998a; Shinohara *et al.*, 2012) to examine flow in the nodes of *Ccdc103*$^{H154P/H154P}$ mice. By using this technique to track the movement of fluorescent beads between frames of a video, I determined fluid flow velocity at the embryonic node. Embryos dissected at 8.0 dpc in DMEM + 10% FBS. Embryos were incubated at 37^{o}C in media when not being dissected or imaged. I mounted individual embryos with their nodes facing upwards in a mixture of fluorescent beads (0.2 μm in diameter) and media. In wild-type embryos, beads were moved across the surface of the node due to leftwards flow created by the rotation of posteriorly oriented cilia (**Fig. 5.3, A-B**).

I used the same detection settings and processing pipeline as with the nodal flow analysis of *Pierce1*$^{-/-}$ embryos (**EM6.6**). Figures are presented with brightfield images of the node analysed (**i**), showing a lack of gross deformities. The first frame of the resulting video, both unprocessed (**ii**) and processed (**iii**), is displayed to demonstrate the presence of fluorescent beads in the node. Heat maps, showing mean velocity magnitude across the node (red = 1.5 μm/s; dark blue = 0 μm/s) and directional arrows (black) are displayed in (**iv**). Enlarged heat maps are shown in **Fig. 5.4** and **Fig. 5.5** to optimise visibility of directional arrows. The final column (**v**) shows the vector count for each sector of flow direction. In this representation, the anterior pole of the node is at 0^{o}, and the posterior pole at 180^{o}. Nodal flow in wild-type and heterozygous embryos show a concentration of vectors towards 90^{o} (leftwards flow, see panels **A-D: v**).

Wild-type (A, B; n=2) and heterozygous embryos (C, D; n=2) showed an organised, leftwards band of fluid flow across the node. This was also observed in *Ccdc103*$^{H154P/H154P}$ embryos (E-H; n=4).

Figure 5.3 (p211):*Ccdc103*$^{H154P/H154P}$ embryos show leftwards nodal flow. Particle image velocimetry (PIV) plots of 8.0dpc embryonic nodes wild-type (A, B), heterozygous (C, D) and homozygous (E-H) for *Ccdc103* p.His154Pro. Panels show: (i) a brightfield image of the node (scale bar shows 20 μm), (ii) an unprocessed image showing fluorescent beads in the node, (iii) a processed image with beads binarised and dilated, (iv) a mean velocity magnitude plot and (v) a rose plot showing vector counts in direction segments. All embryos show leftwards flow. Data collected over 17 experimental sessions. n=4 +/+ (2 shown), n=4 +/H154P (2 shown), n = 6 H154P/H154P (4 shown).


Brightfield
Unprocessed
Processed
PIV plot
Vector count
+/+
+/H154P
H154P/H154P
A:i
A:ii
A:iii
A:iv
A:v
B:i
B:ii
B:iii
B:iv
B:v
C:i
C:ii
C:iii
C:iv
C:v
D:i
D:ii
D:iii
D:iv
D:v
E:i
E:ii
E:iii
E:iv
E:v
F:i
F:ii
F:iii
F:iv
F:v
G:i
G:ii
G:iii
G:iv
G:v
H:i
H:ii
H:iii
H:iv
H:v
20µm
A
R
L
P
0
1.5
µm/s
0°
90°
180°
270°

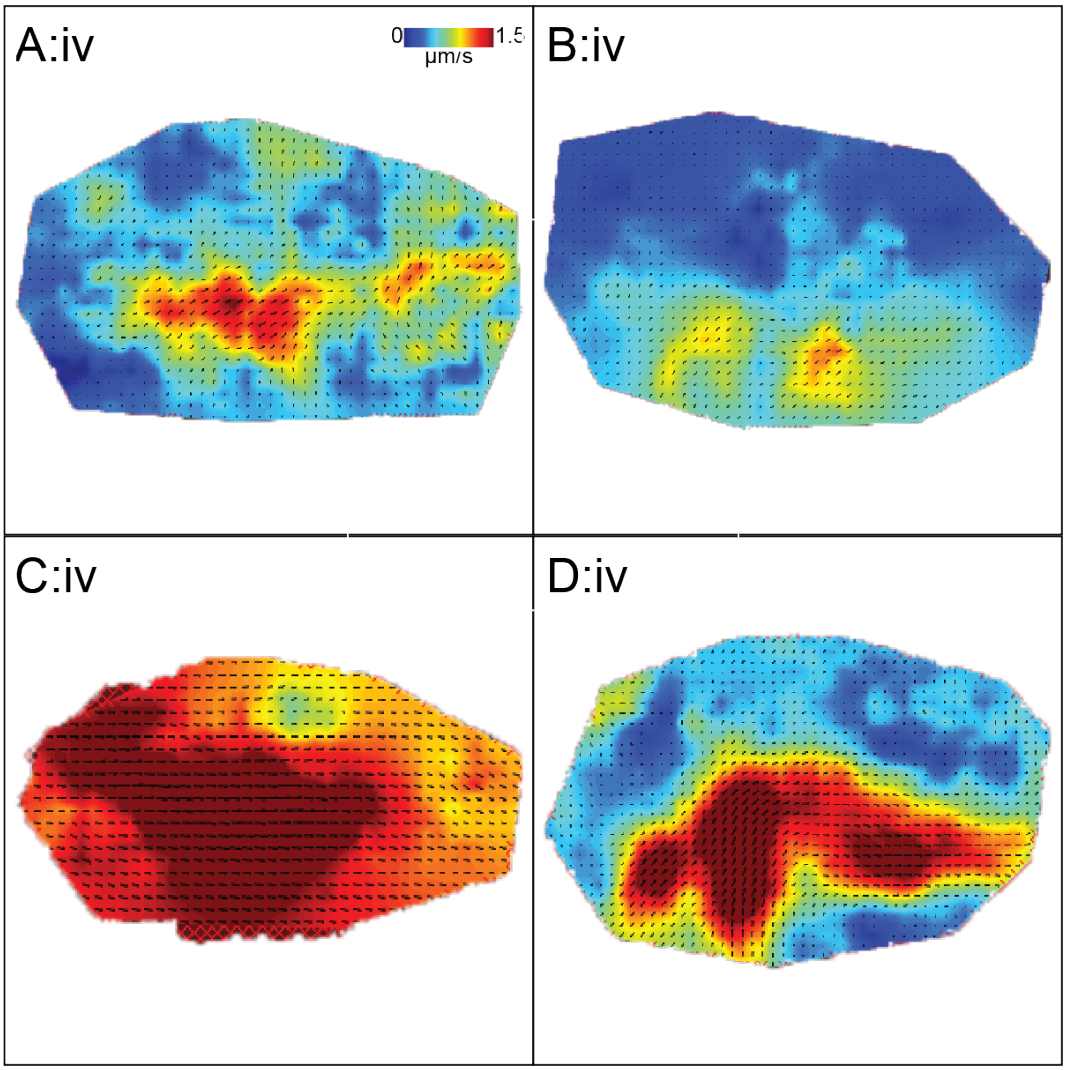


Figure 5.4: *Ccdc103*$^{H154P/H154P}$ embryos show leftwards nodal flow.
Enlarged particle image velocimetry (PIV) plots of embryonic nodes wild-type (A, B), and heterozygous (C, D) for *Ccdc103* p.His154Pro at 8.0 dpc. All embryos show leftwards flow. Velocity is colour coded; dark red refers to high velocity (1.5 µm/s), whilst dark blue refers to low velocity (0 µm/s); a scale bar is shown in A:iv. Directionality of vectors is shown by black arrows.

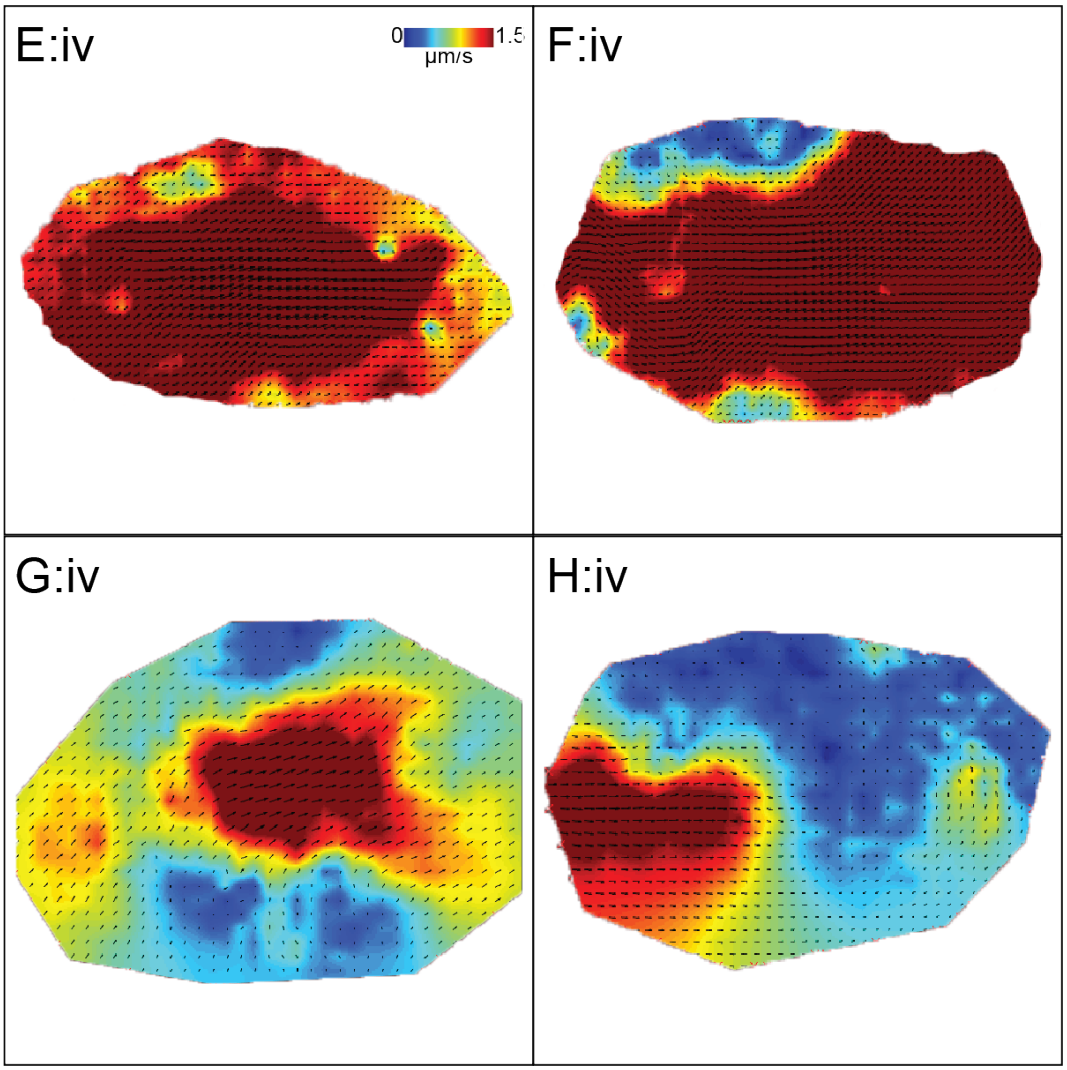


Figure 5.5:*Ccdc103*$^{H154P/H154P}$ embryos show leftwards nodal flow.
Enlarged particle image velocimetry (PIV) plots of embryonic nodes homozygous (E-H) for *Ccdc103* p.His154Pro at 8.0 dpc. All embryos show leftwards flow. Velocity is colour coded; dark red refers to high velocity (1.5 µm/s), whilst dark blue refers to low velocity (0 µm/s); a scale bar is shown in E:iv. Directionality of vectors is shown by black arrows.

5.2.3: *Ccdc103*$^{H154P/H154P}$ mice show normal ciliary beat frequency and motility.

Patients carrying the *CCDC103* p.His154Pro mutation show subtle and varying defects in ciliary motility. Although these deficiencies lead to situs defects in humans, it seemed possible that any motility defects present in mouse embryos homozygous for *Ccdc103*^{H154P} could leave sufficient residual activity to maintain leftwards nodal flow. As such, I undertook live imaging of motile cilia in the node of *Ccdc103*$^{H154P/H154P}$ embryos to investigate the presence of any subtle motility defects.

Analysis revealed no obvious CBP (data not shown) or CBF (**Fig. 5.6**) defects; wild-type, heterozygous and *Ccdc103*$^{H154P/H154P}$ nodal motile cilia were indistinguishable by eye whilst blind to genotype. A more detailed analysis of CBF (n=6 embryos *Ccdc103*$^{+/+}$, 30 cilia; 6 embryos *Ccdc103*$^{+/H154P}$, 30 cilia; 5 embryos *Ccdc103*$^{H154P/H154P}$, 25 cilia) showed no significant difference between mean nodal CBF (*Ccdc103*$^{+/+}$=6.189 Hz; *Ccdc103*$^{+/H154P}$=5.716; *Ccdc103*$^{H154P/H154P}$=6.540 Hz) when evaluating embryos of each genotype ($p>0.05$, generalised linear mixed model).

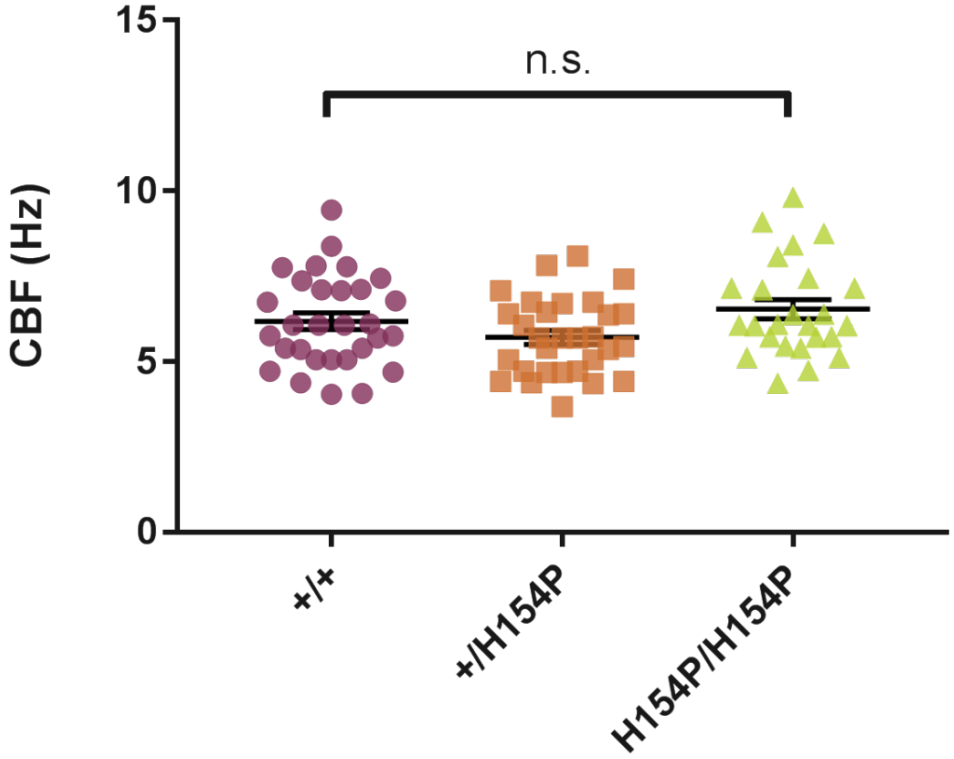


Figure 5.6:*Ccdc103*$^{H154P/H154P}$ embryos show no difference in ciliary beat frequency when compared to wild-type and heterozygote littermates.
Ciliary beat frequency measurements from embryos +/+, +/- and -/- for *Ccdc103* p.His154Pro. No significant difference in ciliary beat frequency was detected by statistical analysis (p>0.05, generalised linear mixed model). n=6 embryos +/+, 30 cilia; 6 embryos +/-, 30 cilia; 5 embryos -/-, 25 cilia. Data collected over 9 experimental sessions.

5.2.4: *Ccdc103*$^{H154P/H154P}$ mice show no evidence of gross situs defects.

The lack of ciliary motility defects, in combination with the leftwards nodal flow observed in *Ccdc103*$^{H154P/H154P}$ mice, prompted the question as to whether this line exhibited organ situs defects. Therefore, I analysed gross organ situs at 13.5 dpc, investigating the situs of the heart, lungs, and stomach. These are all indicators of LR organ patterning, and readily observable at 13.5 dpc. In the wild-type embryo, the heart apex points to the left, the lungs exhibit a 4:1 (R: L) lobation pattern, and the stomach is situated on the left hand side of the abdomen.

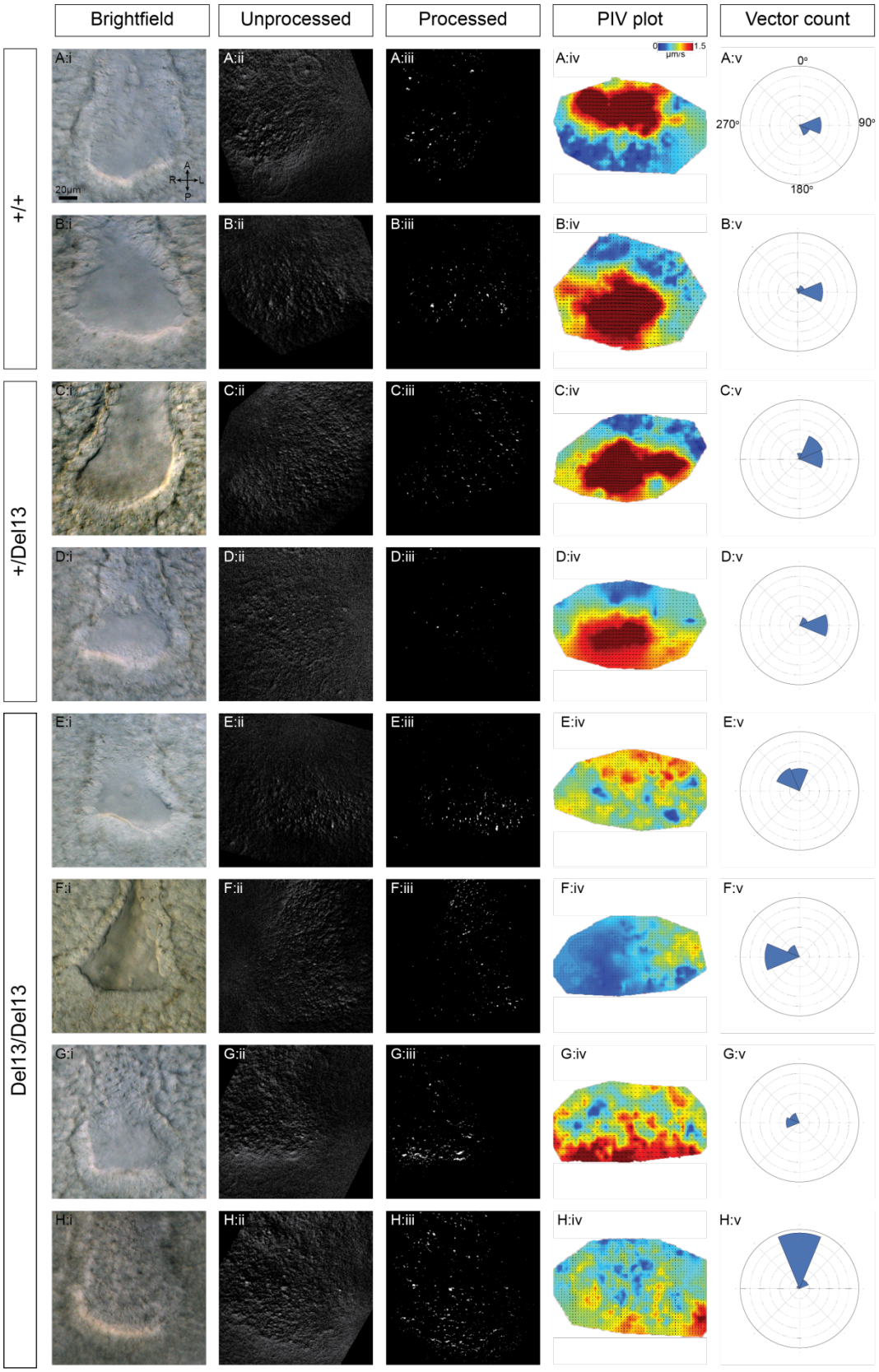
Strikingly, no situs defects were evident in any *Ccdc103*$^{H154P/H154P}$ embryos examined. For this analysis, 12 *Ccdc103*$^{+/+}$, 40 *Ccdc103*$^{+/H154P}$ and 16 *Ccdc103*$^{H154P/H154P}$ embryos were scored. In combination with the CBF and nodal flow analysis results, this strongly suggests that the *Ccdc103* p.His154Pro mutation does not cause LR patterning defects in mice.

5.2.5*: Ccdc103$^{del13/del13}$* mice show abnormal nodal flow.

The lack of a nodal flow phenotype in mice homozygous for *Ccdc103* p.His154Pro raised the question as to whether this mutation was not sufficient to disrupt nodal ciliary motility in the mouse, or whether this gene itself was not required for murine nodal ciliary motility. Ciliary motility in a mouse carrying a mutation in *Ccdc103* had not previously been investigated. Patients with more deleterious mutations in *CCDC103* exhibit essentially immotile cilia, and thus we hypothesised that mice homozygous for the 13 nucleotide deletion in *Ccdc103 (Ccdc103^{del13})* would show ciliary motility defects if this gene was required for murine ciliary motility in a conserved manner.

I evaluated nodal flow using particle image velocimetry (**Fig. 5.7**) as described earlier in this chapter and elsewhere in this thesis. Wild-type and *Ccdc103$^{+/del13}$* embryos showed leftwards flow at the embryonic node (**Fig. 5.7, A-D; Fig. 5.8**), as observed in all other wild-type and heterozygous embryos that I have evaluated. *Ccdc103$^{del13/del13}$* mice exhibited defective nodal flow in all embryos examined (**Fig. 5.7, E-H; Fig. 5.9**). Most embryos exhibited essentially no flow across the pit of the node. Some embryos show patches of medium velocity flow. This led me to hypothesise as to whether residual ciliary motility is present in the nodes of *Ccdc103$^{del13/del13}$* embryos, causing patchy abnormal flow.

Figure 5.7 (p218):*Ccdc103$^{del13/del13}$* embryos show a loss of nodal flow.
Particle image velocimetry (PIV) plots of embryonic nodes wild-type (A, B), heterozygous (C, D) and homozygous (E-H) for *Ccdc103^{del13}* at 8.0 dpc. Panels show: (i) a brightfield image of the node (scale bar shows 20 μm), (ii) an unprocessed image showing fluorescent beads in the node, (iii) a processed image with beads binarised and dilated, (iv) a mean velocity magnitude plot and (v) a rose plot showing vector counts in direction segments. Wild-type (A, B) and heterozygous (C, D) embryos show leftwards fluid flow, *Ccdc103$^{del13/del13}$* embryos (E-H) show no overall directionality of nodal flow. Data collected over 19 experimental sessions. n=4 +/+ (2 shown), n=4 +/Del13 (2 shown), n = 6 Del13/Del13 (4 shown).


Brightfield
Unprocessed
Processed
PIV plot
Vector count
+/+
+/Del13
Del13/Del13
A:i
A:ii
A:iii
A:iv
A:v
B:i
B:ii
B:iii
B:iv
B:v
C:i
C:ii
C:iii
C:iv
C:v
D:i
D:ii
D:iii
D:iv
D:v
E:i
E:ii
E:iii
E:iv
E:v
F:i
F:ii
F:iii
F:iv
F:v
G:i
G:ii
G:iii
G:iv
G:v
H:i
H:ii
H:iii
H:iv
H:v
20µm
A
R
L
P
0
1.5
µm/s
0°
90°
180°
270°

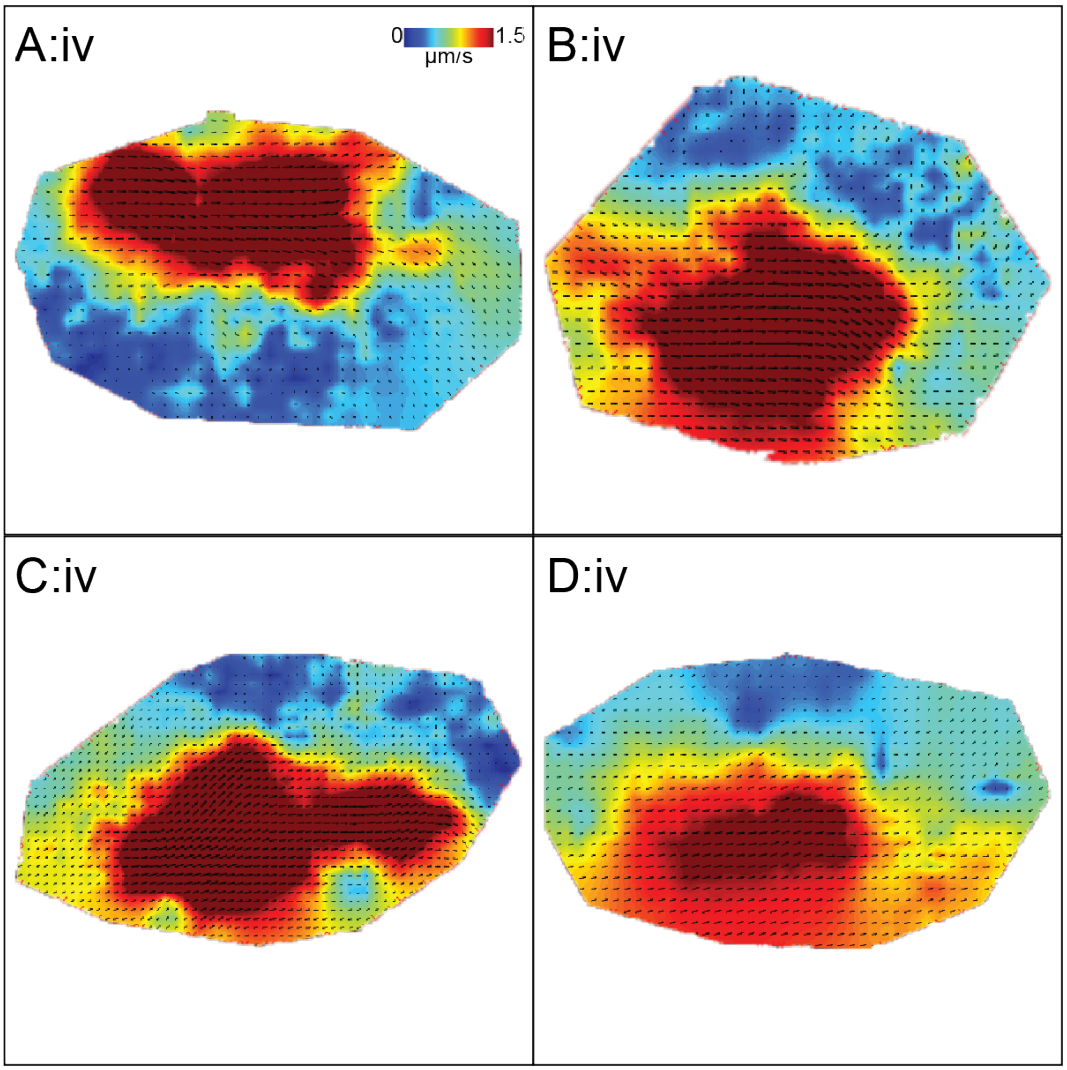


Figure 5.8:*Ccdc103*$^{del13/del13}$ embryos show a loss of nodal flow.
Enlarged particle image velocimetry (PIV) plots of embryonic nodes wild-type (A, B), and heterozygous (C, D) for *Ccdc103*^{del13} at 8.0 dpc. All embryos show leftwards flow. Velocity is colour coded; dark red refers to high velocity (1.5 µm/s), whilst dark blue refers to low velocity (0 µm/s); a scale bar is shown in A:iv. Directionality of vectors is shown by black arrows.

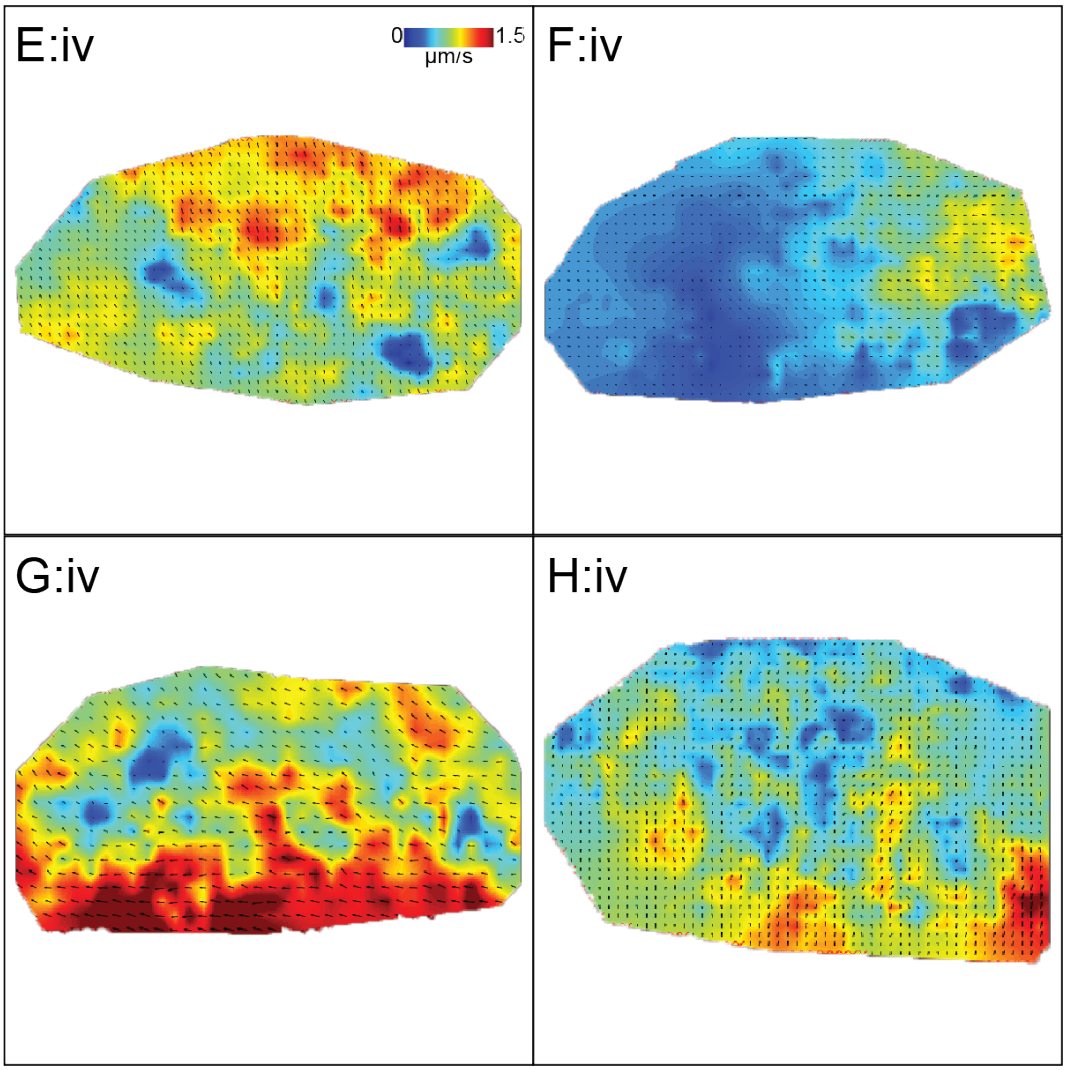


Figure 5.9:*Ccdc103*$^{del13/del13}$ embryos show a loss of nodal flow.
Enlarged particle image velocimetry (PIV) plots of embryonic nodes homozygous (E-H) for *Ccdc103*^{del13} at 8.0 dpc. All embryos show a lack of leftwards nodal flow. Velocity is colour coded; dark red refers to high velocity (1.5 µm/s), whilst dark blue refers to low velocity (0 µm/s); a scale bar is shown in E:iv. Directionality of vectors is shown by black arrows.

5.2.6: *Ccdc103*$^{del13/del13}$ mice have largely immotile nodal cilia.

To investigate the defects underlying the lack of leftwards flow in the *Ccdc103*$^{del13/del13}$ nodes, CBF was assessed as previously described (n=10 embryos per genotype). Wild-type and heterozygous cilia showed a range of motility values and were indistinguishable from each other. In contrast, *Ccdc103*$^{del13/del13}$ cilia showed a striking reduction of motility (**Fig. 5.10**). Statistical tests confirmed these differences.

The vast majority of cilia were immotile in *Ccdc103*$^{del13/del13}$ mice, though one node with a patch of motile cilia was identified. Other *Ccdc103*$^{del13/del13}$ nodes examined (n=3) contained one detectable motile cilium. The beat frequency of these residual motile cilia overlapped with CBF values that occur in wild-type and heterozygous embryos; this group does have a lower average CBF, but the small numbers of *Ccdc103*$^{del13/del13}$ cilia that remain motile made it difficult to evaluate the significance of this difference. It should be noted that the majority of residually motile cilia occurred in one embryo (n=4 motile cilia), and this may be due to residual heterozygosity permitting a stochastically less penetrant phenotype in this case.

Although the *Ccdc103*^{del13} mutation is maintained on a congenic B6N background, de novo mutations can arise between generations. A do novo mutation may be particularly pertinent in this case, where 4 motile cilia were clustered together; potentially a mutation has permitted sufficient rescue in a precursor cell that derivatives can form motile cilia. Multiple immotile cilia were also found in that particular node.

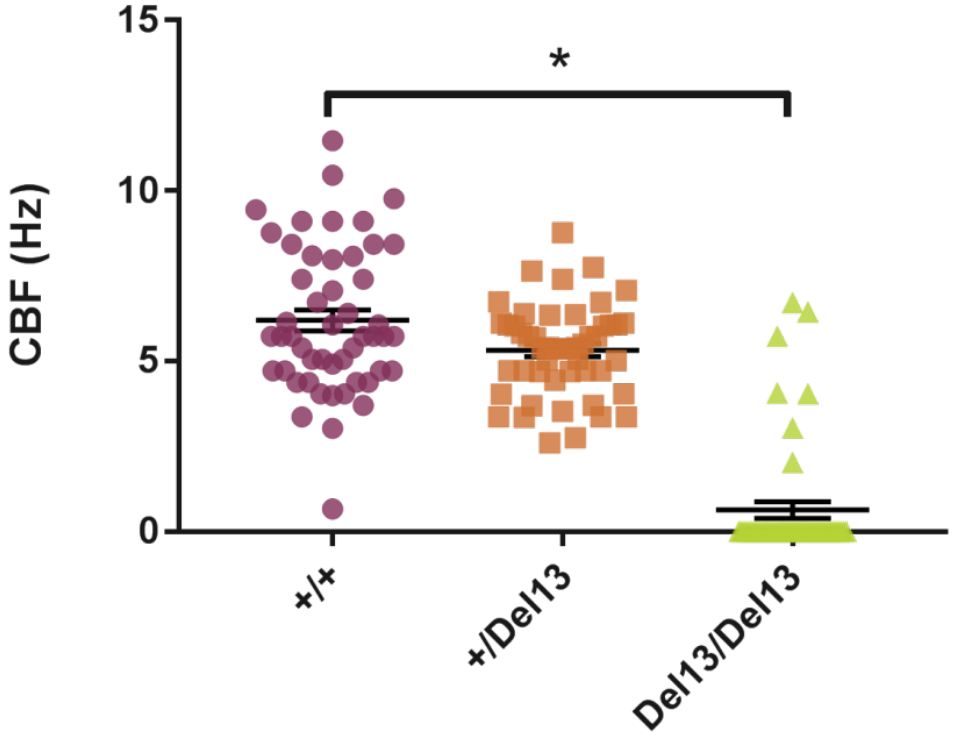


Figure 5.10:*Ccdc103*$^{del13/del13}$ embryos exhibit a massive reduction in nodal ciliary beat frequency.
XY plot showing ciliary beat frequency values (Hz) calculated for *Ccdc103*$^{+/+}$, *Ccdc103*$^{+/del13}$ and *Ccdc103*$^{del13/del13}$ embryos. n=10 embryos per genotype, 5 cilia evaluated per node. *p<0.0005, generalised linear mixed model. Data collected over 8 experimental sessions.

5.2.7: *Ccdc103*$^{del13/del13}$ mice exhibit a high incidence of situs defects.

To investigate whether the observed defects in ciliary motility and nodal flow lead to situs defects, I next examined the situs phenotype of *Ccdc103*$^{del13/del13}$ embryos as previously described (**Fig. 5.11**). In contrast to wild-type (n=34) and heterozygous (n=54) embryos, *Ccdc103*$^{del13/del13}$ embryos (n=35) exhibited a situs phenotype indicative of stark abnormalities in LR patterning (**Fig. 5.11; Table 5.1**). Out of the *Ccdc103*$^{del13/del13}$ embryos, 10 exhibited SS and 12 exhibited SIT. Among the population of embryos annotated as SA (n=9, **Table 5.1**), a high proportion of left isomerism was observed; this is typical of a "lack of nodal flow" phenotype on the B6N background in our hands (data not shown). A significant proportion of *Ccdc103*$^{del13/del13}$ embryos were found dead, with situs unable to be analysed due to embryo decay (n=4).

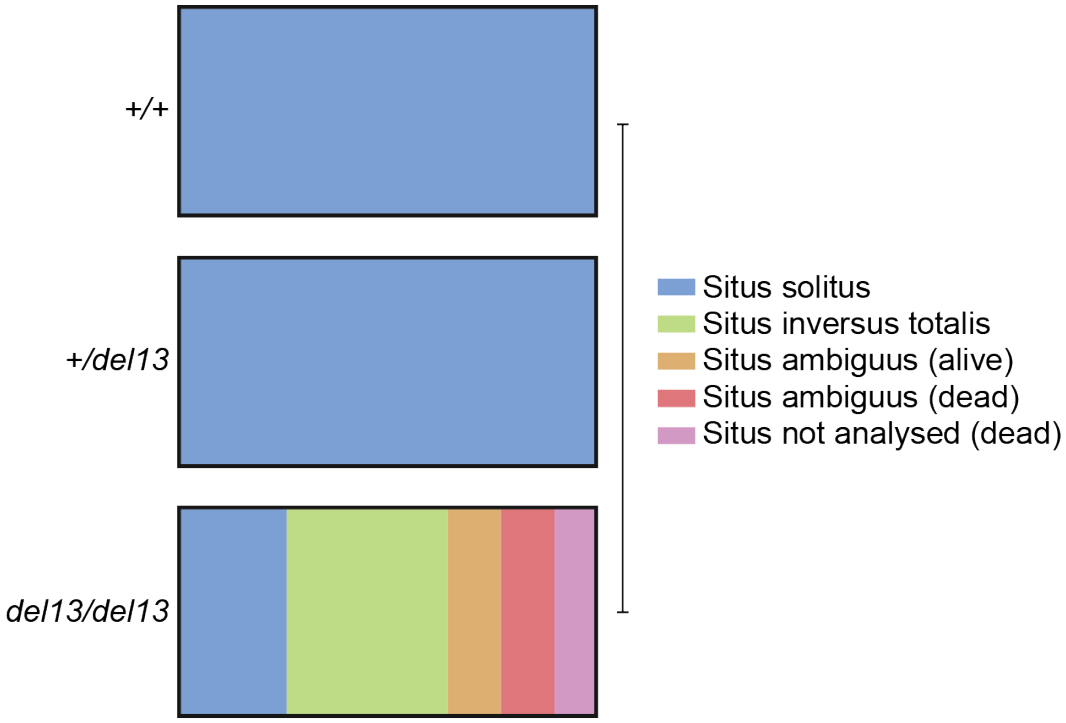


Figure 5.11:*Ccdc103*$^{del13/del13}$ embryos show severe situs defects. Bar chart showing the proportion of situs abnormalities observed in *Ccdc103*$^{del13/del13}$ embryos compared to wild-type and heterozygous littermates. n=34 +/+, n= 54 *+/del13*; n=35 *del13/del13*.

	Situs phenotype of SA embryos		
	Heart apex (L/R)	*Lung lobation (R: L)*	*Stomach situs (L/R)*
A	*L*	*1:1*	*L*
B	*L*	*1:1*	*L*
C	*L*	*1:1*	*L*
D	*L*	*1:1*	*R*
E	*R*	*1:1*	*L*
F	*R*	*1:1*	*L*
G	*L*	*1:1*	*L*
H	*R*	*1:1*	*R*
I	*L*	*1:1*	*L*

Table 5.1: Situs phenotype of *Ccdc103*$^{del13/del13}$ embryos annotated with SA (n=9).

5.3: Discussion

In this chapter I investigated nodal ciliary motility and nodal flow in two mouse lines carrying mutations in *Ccdc103*. The *Ccdc103* p.His154Pro mutation did not cause a nodal ciliary motility or nodal flow defect when homozygous on a B6N background, and thus did not cause situs defects. This seems strange in light of the high conservation of this gene. Moreover, the mutation is predicted to be deleterious to protein structure (Shoemark, Moya, *et al.*, 2018). However, there are significant genetic differences between mouse and human. Although there is 90-95% conservation between protein coding sequences, the stringency of this conservation depends on protein function, with tighter conservation shown between proteins that are required for life. Non-coding sequences exhibit reduced conservation, which is likely to underpin species-dependent variation in gene expression (Adams, 2007). Variation in expression levels could mean that the same protein components of a pathway are required to different extents in different species, providing a possible explanation for the lack of phenotype in *Ccdc103*$^{H154P/H154P}$ mice.

The majority (5/6) of *CCDC103* p.His154Pro mutations have been detected in consanguineous patients with PCD. There may be potential background effects in these patients that are not recapitulated in the mouse by the single amino acid change alone. We know that consanguinity leads to a reduction in heterozygosity, which increases the likelihood of pathogenic recessive genetic variants leading to overt disease. Equally, consanguinity may have led to linkage disequilibrium in the area around *CCDC103*, with co-inherited genetic variation leading to differential expression of *CCDC103*, a known PCD causative gene, with *CCDC103* p.His154Pro simply co-inherited with deleterious variation that has not yet been detected. The *CCDC103* p.His154Pro variant was detected in all studies referenced by whole exome sequencing and thus

any intronic or *cis* regulatory sequence changes would not have been detected via this method. Whole genome sequencing around the *CCDC103* locus may shed further light on the situation; in particular, linkage disequilibrium and co-inherited deleterious variation, of which *CCDC103* p.His154Pro may be a marker, must be ruled out.

There may be a reduction in CBF or CBP in the *Ccdc103*$^{H154P/H154P}$ mouse that was not detected due to the numbers analysed (n=5 *Ccdc103*$^{H154P/H154P}$ embryos); 15 mouse nodes of each genotype were evaluated in the analysis of the *Pierce1*-null line. The lack of LR patterning defect, as evaluated by embryonic organ situs, is consistent with *Ccdc103*^{H154P} having no pathological consequences for ciliary motility at the mouse node.

The *Ccdc103*^{del13} mutation, however, showed almost total ciliary immotility, with a concurrent disruption in nodal flow. This resulted in a high proportion of LR patterning defects, with partial embryonic mortality observed before 13.5 dpc. This severe ciliary motility defect is perhaps unsurprising as patients with more severe frameshift *CCDC103* mutations exhibit complete tracheal ciliary immotility, with a more severe and consistent respiratory phenotype, as opposed to patients with *CCDC103* p.His154Pro mutations, some of whom present with no overt respiratory disease.

The ciliary motility defect in *Ccdc103*$^{del13/del13}$ mice was clearly more severe than that observed in *Pierce1*$^{-/-}$ mice, and there was a dramatic increase in the incidence of situs defects. No *Ccdc103*$^{del13/del13}$ pups have been raised past weaning (personal communication, Hannah Mitchison). This likely speaks to pre- and post-natal death occurring in this line. This is may be resulting from hydrocephalus, a common phenotype in mouse models of PCD (**Appendices 2 & 3**), in addition to mortality due to cardiac and other LR organ patterning defects. Changing the background strain

that this mutation is on may reduce the penetrance of hydrocephalus sufficiently to permit our raising adult *Ccdc103*$^{del13/del13}$ mice, with the aim of analysing adult tracheal ciliary and sperm flagellar motility (Lee, 2013).

The situs phenotypes in the *Ccdc103*$^{del13/del13}$ mouse made it clear that CCDC103 does play a role in nodal ciliary motility and LR patterning in the mouse. This adds weight for SIT in patients carrying *CCDC103* p.His154Pro mutations to be considered as a result of ciliary motility defects. *CCDC103* p.His154Pro is clearly not as penetrant as more disruptive loss-of-function mutations in the same gene, which is likely to add heterogeneity to patient presentations and compound the diagnostic puzzle.

Although there did not appear to be nodal ciliary motility defects in the *Ccdc103*^{H154P} line, a full examination of adult ciliary motility, particularly after challenge with pathogenic bacteria, would offer further insight into the role of this mutation in disease. Ciliary motility defects may be apparent upon precise analysis in the adult, in parallel with no nodal ciliary motility defect. Initial data from adult ciliary motility phenotyping in *Ccdc103*$^{H154P/H154P}$ mice shows an abnormality in sperm motility (personal communication, Hannah Mitchison). Investigation of adult tracheal ciliary and sperm flagellar motility remains to be completed.

The *Pierce1*$^{-/-}$ mouse showed a more severe ciliary motility defect than that observed in the *Ccdc103*$^{H154P/H154P}$ mouse. As this mutation is associated with milder respiratory disease in humans when compared to classical PCD, this comparison adds weight for mutations in *PIERCE1* to be considered when evaluating patients exhibiting similar respiratory disease to those homozygous for *CCDC103* p.His154Pro. As more severe mutations in *CCDC103* result in a more severe ciliary motility phenotype in the mouse, I would hypothesise that only a more severe loss-of-function

mutation in *PIERCE1* would be likely to result in a clinical presentation in a patient.

6: Overall discussion and conclusions

6.1: Ciliary motility is disrupted in the *Pierce1*$^{-/-}$ node, causing aberrant nodal flow and downstream left-right patterning defects.

My investigations of nodal cilia in the *Pierce1*$^{-/-}$ embryo have demonstrated that these cilia show abnormal motility, both with regards to beat frequency and beat pattern. This is associated with disruption of canonical leftwards fluid flow at the node which is known to be required for the reliable establishment of LR asymmetry. I propose that the disrupted motility is therefore a causative defect underlying the heterotaxy and abnormal situs patterning observed in these mice. Mirroring the results of Sung et al (Sung *et al.*, 2016), we see no evidence of altered ciliary morphology at the node, and would instead propose an ultrastructural defect to be underpinning the aberrant ciliary motility.

6.2: Ciliary motility is disrupted in *Pierce1*$^{-/-}$ adult tissues, but this disruption is not sufficient to cause associated pathology.

My analysis of tracheal cilia demonstrated that the abnormal ciliary motility observed in the embryonic node extended to the adult respiratory epithelium. This, in combination with the defects observed in sperm flagellar motility, and the motile ciliated tissue-specific X-gal staining, implies that PIERCE1 plays a conserved role in ciliary motility in the mouse, across all classes of 9+2 and 9+0 motile cilia.

Loss of PIERCE1 activity appeared to have differing impacts on the function of motile cilia in distinct locations. In the node, abnormal ciliary motility disrupted nodal flow, and consequently LR patterning. The typical effect of abnormal ciliary motility in the tracheal epithelium is impeded mucociliary clearance. In mouse models of respiratory disease, this

manifests as upper airway inflammation, i.e. rhinitis and sinusitis. This is in contrast to the human, where upper airway pathology is present in addition to lower respiratory tract infections. We did not observe any upper airway inflammation or mucus accumulation in the nasal cavities of *Pierce1*$^{-/-}$ mice aged to 6 months, despite there being significant differences in tracheal ciliary motility and ultrastructure. Removing PIERCE1 appeared to leave the motile cilia with sufficient residual function to maintain mucociliary clearance. It is important to note that these mice were not challenged with pathogens; potentially, in the face of this or altered environmental conditions which are known to impact mucociliary clearance, a defect could have manifested.

In the testis, *Pierce1* expression initiated in tandem with the onset of sperm flagellar motility during the initial wave of spermiogenesis. Significant defects in the motility of *Pierce1*$^{-/-}$ sperm are evident, notably a reduction in the number of rapid sperm present. Male fertility appeared to be unaffected, but the superficial fertility analysis conducted would only have been sufficient to identify severe fertility defects, such as complete infertility. Further analysis involving litter size counts and records of plugged (i.e., mated), but not pregnant, females may prove helpful in assessing any reduction in male fertility in *Pierce1*$^{-/-}$ mice.

While both lacZ expression and motility analysis implicate PIERCE1 in sperm flagellar motility, no defect in the flagellar ultrastructure was detected by TEM. This result can be interpreted in multiple ways. One conclusion could be that there is no defect in the flagellar ultrastructure of *Pierce1*$^{-/-}$ spermatozoa. However, it follows that the observed motility defects, and onset of gene expression at the same time point as other flagellar motility genes, result from some kind of ultrastructural defect in *Pierce1*$^{-/-}$ spermatozoa. The defect may be too subtle to be detected by our TEM analysis, or our TEM study may not have been sufficiently powered or precise to reveal a difference in the ultrastructure.

The presence, and deleterious effects observed in the absence, of PIERCE1 add weight to this protein being implicated in a conserved aspect of axonemal assembly and function. It seems unlikely that PIERCE1 is involved solely in a specialised process in one of these classes of cilia, for example manchette-dependent flagellar assembly in spermatozoa. Factors involved in this appear to be specific to the sperm flagellum, and have not been shown to play a role in ciliary motility elsewhere in the body.

While tissue-specific regulatory genetic cascades are known to be involved in the implementation of the motile ciliogenic transcription programme, e.g. *TAp73* for multi-motile ciliated cells, there are aspects of the downstream motile ciliogenic process itself that do not appear to be tissue-specific. For example, *PIH1D3* was initially thought to have been identified as a testis-specific dynein assembly factor, with mutations in this gene causing only flagellar dysmotility (Dong *et al.*, 2014),combined with motile nodal and tracheal cilia, in a mouse model. However, this gene was later shown to be causative for PCD (Olcese *et al.*, 2017; Paff *et al.*, 2017). The flagellar immotility observed in isolation in the mouse stemmed from the redundancy of additional transcripts in the mouse – these additional transcripts do not occur in humans, and therefore *PIH1D3* mutations in humans cause PCD affecting all tissues with motile cilia, as opposed to solely male infertility due to immotile sperm. To date, no tissue-specific dynein assembly factors have been described. The involvement of PIERCE1 in multiple classes of motile cilia adds evidence for this protein playing a universal role in ciliary motility.

6.3: PIERCE1: a putative DynAP component?

Studies into the cellular function of PIERCE1 have not yet reached full fruition. Anti-PIERCE1 antibodies have not been successfully validated, limiting their utility in the mouse. In addition to this, in silico

analyses of protein structure have shown limited success due to the unknown nature of DUF4490. However, the identification of a paralogue with a seemingly similar expression pattern to *Pierce1* opens up new avenues of investigation. Although data thus far has been inconclusive, a key future area of study is the creation of a *Ccpg1os*-null mouse line, with the eventual aim of creating *Pierce1*$^{-/-}$ *Ccpg1os*$^{-/-}$ double knock-out animals. These animals will enable the investigation of any compensatory effects between the two genes and their protein products.

The identification of potential interaction partners of PIERCE1 was an aim of this project, due to the likely insight they would give as to the biochemical function of PIERCE1. Studies thus far have been contradictory, as the results of Y2H screens did not identify reliable interactions with proteins that have known functions in motile cilia. One possibility is that PIERCE1 forms part of an as yet poorly characterised network of interacting proteins. Mass spectrometry could be used to good effect here to identify putative PIERCE1 interaction components, particularly through differences in the protein composition of *Pierce1*$^{+/+}$ and *Pierce1*$^{-/-}$ motile ciliated tissues.

Having evaluated recent data from the Wallingford group, I initially hypothesised that PIERCE1 is a DynAP member (**Chapter 3.3**). This fits with our TEM data showing disrupted dynein arm assembly, and a specific requirement for PIERCE1 protein in motile ciliated cells – DynAPs have thus far been exclusively observed in cells with multiple motile cilia. DynAPs have not been identified as of yet in the sperm flagellum; potentially, other compensatory mechanisms could exist in this environment, which could explain the lack of dynein arm defects in the *Pierce1*$^{-/-}$ spermatozoa. A key avenue of future research for *Pierce1* will be the investigation of co-localisation of PIERCE1 with DynAPs. Although this work is more challenging in the mouse, largely due to a lack of validated antibodies, it would provide such an insight into protein function that it

should be seen as a priority. Collaboration with scientists working in other model organisms may be needed to bring this to pass.

Although the dynein arm defects detected in *Pierce1*$^{-/-}$ cilia do appear to align with a defect in the assembly and trafficking of arms, as opposed to a specific defect in a particular component, a role for PIERCE1 outside of the DynAP complex should also be considered. For example, PIERCE1 may be involved in the trafficking of assembled arms to the cilium. PIERCE1 could also act as an adaptor for IFT of dynein arms, enabling their transport in an anterograde direction along the cilium. We know that different dynein heavy chains are found in proximal (DNAH11; Dougherty et al. 2016) and distal (DNAH9; Loges et al. 2018)outer dynein arms; it is reasonable to consider that PIERCE1 could be involved in directing the specific proximo-distal trafficking of these components in the cilium.

Immunofluorescence studies using anti-DNAH9 and anti-DNAH11 antibodies would enable us to determine whether this trafficking is affected, as we would see a specific defect in either of these proteins along the length of the cilium – either their absence, or their improper localisation. Utilising key mouse lines in this field, for example the lrd-GFP mouse (McGrath *et al.*, 2003), would enable us to further investigate any more general disruption of dynein arm trafficking in motile cilia, as we may observe GFP-tagged DNAH11 in the cytoplasm but not the motile cilium. Either of these defects in dynein arm trafficking is unlikely to be completely penetrant, bearing in mind that *Pierce1*$^{-/-}$ motile cilia retain a good degree of motility, but these avenues are worth investigating.

6.4: *Ccdc103* p.His154Pro does not associate with a phenotype in the C57BL/6N mouse, but a 13 nucleotide deletion in the same gene causes a severe ciliary immotility phenotype.

CCDC103 p.His154Pro has remained a point of interest to researchers and clinicians since its initial identification in 2012 (Panizzi *et al.*, 2012), with the heterogeneity in patient phenotype provoking discussion as to whether this mutation is merely a common SNP coinciding with PCD-like disease, or a pathological disease-causing variant. A penetrant phenotype in the *Ccdc103*$^{H154P/H154P}$ mouse could have helped to answer these questions.

However, a lack of phenotype in the mouse does not rule out *CCDC103* p.His154Pro as a pathogenic variant in humans. In part, this is due to the previously discussed differences in the mouse and human genomes, particularly in non-protein coding sequences. Inter-specific variation in non-coding regulatory sequences could mean that differential expression of an identical protein coding sequence leads different phenotypes in different species, due to differing levels of expression. In addition to this, *CCDC103* p.His154Pro is largely found in consanguineous families. There may be an additional genetic burden in these families due to lack of heterozygosity that is impacting disease phenotype in ways that are not fully understood. The increase in homozygosity for other recessive variants could alter ciliary motility itself, or provide an additional stress to cells and tissues leading to downstream effects on ciliary function.

Alternatively, consanguinity in many patients homozygous for *CCDC103* p.His154Pro may point towards linkage disequilibrium in the region surrounding this gene, with other co-inherited genetic variants causing the PCD phenotype present in some of the patients. Notably, the whole exome sequencing that has identified many of these patients would not have detected intronic or cis-regulatory variants, and a full evaluation

of linkage disequilibrium will be necessary to comprehensively understand these results. Studies continue in the *Ccdc103*^{H154P} line to further evaluate ciliary motility in the adult mouse.

Frameshift mutations in *CCDC103* cause a classical PCD disease phenotype in patients, and an increase in mouse phenotype severity with a 13 nucleotide deletion fits with this pattern. However, the *Ccdc103*$^{del13/del13}$ mouse showed a high level of embryonic death and heterotaxy. It is unclear why these embryos were so harshly affected. In the *Pierce1*$^{-/-}$ mice, some embryos showed a degree of leftwards flow and it seems reasonable to speculate that this led to a relative increase in the proportion of embryos exhibiting SS. In spite of this, there was still a considerable degree of heterotaxy in the *Pierce1*$^{-/-}$ embryo population, without the associated mortality observed in the *Ccdc103*$^{del13/del13}$ line.

There were differences in the flow phenotypes observed between the *Pierce1*$^{-/-}$ and *Ccdc103*$^{del13/del13}$ embryos. The *Pierce1*$^{-/-}$ embryos showed disordered nodal flow due to widespread defective ciliary motility, with reduced CBF and altered CBP. Overall, *Ccdc103*$^{del13/del13}$ nodes showed no real flow; however, there were occasional residual motile cilia in low numbers. As a previous paper in the field has demonstrated that two rotating cilia in the node are sufficient to break LR symmetry (Shinohara *et al.*, 2012), we must not underestimate the potential for even one motile cilium to have a significant effect on nodal flow, such that downstream gene expression is affected.

In addition, stochastic differences in the location of the residual motile cilia in the *Ccdc103*$^{del13/del13}$ nodes could further complicate the effects of flow in the node. Overall, the differences in nodal flow phenotypes between the two lines could lead to different phenotypes regarding activation of downstream LR patterning genes; this will become more apparent following investigation of *Cerl2* and *Pitx2* expression in

Ccdc103$^{del13/del13}$ embryos. This could then account for differing incidences of particular situs phenotypes between the two lines.

In spite of this, if the LR patterning defects in both lines result from defective fluid flow and an ineffective initial break in LR symmetry, it does logically not follow that we see an increase in embryo mortality between the two lines. Heterotaxy is observed in *Pierce1*$^{-/-}$ embryos without any evidence of the embryonic mortality observed in *Ccdc103*$^{del13/del13}$ embryos. I have only evaluated three gene-altered lines for situs defects (*Pierce1*$^{-}$*, Ccdc103*^{H154P}, *Ccdc103*^{del13}); potentially, the defects observed in the *Ccdc103*^{del13} line are similar to those that are observed in other ciliary immotility mouse lines on the C57BL/6N background.

However, interpreting the literature around this is difficult. If situs phenotyping has been carried out as part of an investigation into a mouse with suspected ciliary motility defects, often this occurs post-natally, meaning that differential timing of in utero mortality cannot be assessed. There is commonly significant morbidity and mortality of mice with ciliary motility defects is common, but can be due to hydrocephalus, situs defects, or a combination of the two. An analysis purely of Mendelian ratios does not inform the researcher as to the incidence of situs defects, as situs defects are not the sole cause of neonatal mortality in ciliary motility mice.

Furthermore, much of the evidence for situs defects in mice with mutations in genes that cause PCD in humans comes from one large-scale mutagenesis screen (Li *et al.*, 2015), and extensive phenotyping data on each individual mutant line is not provided. Until more is known about the function of CCDC103, it is important that future researchers bear in mind the possibility of additional developmental roles for this protein that may lead to increased embryonic mortality in *Ccdc103*$^{del13/del13}$ mice.

An additional motive in investigating ciliary motility in the *Ccdc103*$^{H154P/H154P}$ mouse was to compare any observed defects to those seen in the *Pierce1*$^{-/-}$ mouse. I hypothesised that this might enable me to better assess the likelihood of mutations in *C9ORF116* causing PCD in humans. *Ccdc103*$^{H154P/H154P}$ mutations caused no detectable ciliary motility defect in the mouse, but the same mutation in humans causes a range of PCD-like phenotypes, from classical PCD to a much milder rhinitis and sinusitis disease. This, combined with phenotyping data from elsewhere in this project, leads me to conclude that *C9ORF116* is more likely to be a ciliary modifier, and cause what is essentially a mild form of PCD, than to be a candidate gene for classical PCD itself.

6.5: *C9ORF116*: a candidate gene for human heterotaxy

I propose that, if the function of *Pierce1*, and DUF4490, is conserved between mouse and human, *C9ORF116* mutations in humans are most likely to be pathologically associated with congenital heart defects as a result of defective LR patterning. These patients may also exhibit reduced respiratory function, without overtly presenting with PCD; some mutations, for example *CCDC103* p.His154Pro, do not always cause fully penetrant PCD symptomology.

I hypothesise that ciliary motility-related disorders lie along a spectrum, with classical PCD at the extreme end. Delineating the genes contributing to this spectrum, through a combination of fundamental science and clinical research, will enable us to provide more personalised medicine to patients with ciliary motility disorders and may open up new avenues for therapeutic investigation.

Ciliopathy	Clinical signs and symptoms
Joubert syndrome and related disorders	*Hypotonia; ataxia; psychomotor delay; irregular breathing pattern; oculomotor apraxia; vermis hypoplasia/agenesis; renal degeneration, cystic kidney disease (cystic dysplasia and nephronophthisis); ocular colobomas; occipital encephalocoele; hepatic fibrosis; polydactyly; oral hamartomas; endocrine abnormalities*
Meckel-Gruber syndrome	*Phenotypic overlap with JBTS.* *Occipital encephalocoele; cystic dysplastic kidneys; hepatic bile duct proliferation; polydactyly*
Senior-Løken syndrome	*Phenotypic and genotypic overlap with JBTS and other ciliopathies, including BBS and NPHP.* *Retinitis pigmentosa; renal disease*
Oro facial digital syndrome type 1	*Rare X-linked disorder; affected males die pre-natally.* *Malformation of the oral cavity, face and digits; CNS abnormalities; cystic kidney disease*
Leber's congenital amaurosis	*Severe retinal dystrophy*
Bardet-Biedl syndrome	*Rod/cone dystrophy; polydactyly; obesity; learning disabilities; hypogonadism; renal abnormalities*
McKusick-	*Hydrometrocolpos; post-axial polydactyly; congenital*

Kaufman syndrome	*heart disease*
Alström syndrome	*Cone-rod dystrophy; obesity; progressive sensorineural hearing impairment; dilated cardiomyopathy; insulin resistance syndrome; developmental delay; relative preservation of cognitive function and lack of polydactyly (c.f. BBS)*

Appendix 1: Presentations associated with primary ciliopathies.

Appendix 2: Causative PCD genes

Gene	Results in	Mutation in	Mouse KO?
DNAH5 (Omran *et al.*, 2000; Olbrich *et al.*, 2002)	**ODA truncation**	Structural ODA motor protein	Yes
NME8 (TXNDC3) (Duriez *et al.*, 2007)			No
DNAI1 (Zariwala *et al.*, 2006)			Yes
DNAI2 (Loges *et al.*, 2008)			No
DNAL1 (Horváth *et al.*, 2005; Mazor *et al.*, 2011)			No
CCDC114 (Knowles, Leigh, *et al.*, 2013)		ODA-docking-complex components	No
ARMC4 (Hjeij *et al.*, 2013; Onoufriadis, Shoemark, Munye, *et al.*, 2014; Li *et al.*, 2016)			Yes
CCDC151 (Alsaadi *et al.*, 2014; Hjeij *et al.*, 2014)			Yes
TTC25 (Wallmeier *et al.*, 2016)			Yes
DNAH9 (Fassad, Shoemark, Legendre, *et al.*, 2018)		Structural ODA motor protein	No
CCDC103 (Panizzi *et al.*, 2012; Shoemark *et al.*, 2017)	**Outer and inner dynein arm truncation**	Unknown	No
LRRC6 (Kott *et al.*, 2012)		Cytoplasmic dynein-arm-	No
HEATR2 (Horani *et al.*, 2012)			No

DNAAF4 (DYX1C1) (Tarkar *et al.*, 2013)		assembly machinery	Yes
DNAAF1 (LRRC50) (Omran *et al.*, 2008)			No
DNAAF2 (KTU) (Loges *et al.*, 2009)			Yes
DNAAF3 (Mitchison *et al.*, 2012; Li *et al.*, 2016)			Yes
SPAG1 (Knowles, Ostrowski, *et al.*, 2013)			No
C21ORF59 (Austin-Tse *et al.*, 2013; Jaffe *et al.*, 2016)			No
ZYMND10 (Moore *et al.*, 2013; Zariwala *et al.*, 2013)			No
C11ORF70 (Fassad, Shoemark, le Borgne, *et al.*, 2018; Höben *et al.*, 2018)			No
HYDIN (Olbrich *et al.*, 2012)	**Central pair defect**	Central pair protein	Yes
STK36 (Edelbusch *et al.*, 2017)	**Cilia mis-orientation (due to central pair defect)**	Central pair protein	Yes (Nozawa *et al.*, 2013)
RSPH4A (Castleman *et al.*, 2008)	**Central pair defect + microtubule disorganisation**	Radial spokehead protein	No
RSPH16A (El Khouri *et al.*, 2016)		HSP chaperone	No
RSPH9 (Castleman *et al.*, 2008)		Radial spokehead	No

RSPH3 (Jeanson, Copin, Papon, Dastot-Le Moal, *et al.*, 2015)		protein	No
RSPH1 (Kott *et al.*, 2013; Knowles *et al.*, 2014; Onoufriadis, Shoemark, Schmidts, *et al.*, 2014)			No
GAS8 (GAS11, DRC4) (Olbrich *et al.*, 2015)	**No obvious ultrastructural defect; subtle beating abnormalities**	N-DRC protein	No
CCDC164 (DRC1) (Wirschell *et al.*, 2013; Li *et al.*, 2016)		N-DRC protein	Yes
CCDC65 (DRC2) (Austin-Tse *et al.*, 2013; Horani *et al.*, 2013)			No
CCDC39 (Merveille *et al.*, 2011; Solomon *et al.*, 2017)	**Disorganised axoneme (varied)**	Ruler proteins - maintain 9+2 integrity; N-DRC and IDA attachment	Yes
CCDC40 (Becker-Heck *et al.*, 2011)			Yes
CCNO (Wallmeier, 2014)	**Rare cilia**	Cyclin O	No
MCIDAS (Mieke Boon *et al.*, 2014)		Transcriptional regulator	No
DNAH11 (Bartoloni *et al.*, 2002; Schwabe *et al.*, 2008)	**Normal ultrastructure (immotile)**	Structural ODA motor protein	Yes
RPGR (Moore *et al.*, 2006)	Varied structural/beating defects	IFT protein	No
DNAH8 (Watson *et al.*, 2014)	Not reported	Not reported	No

Appendix 3: Genes known to cause PCD in humans, and their phenotype when knocked-out in the mouse.

Human PCD gene	Type of mutation	Tracheal cilia function	Nodal cilia function	Embryonic/pre-wean lethality	Hydrocephalus	Situs defects	Rhinosinusitis
DNAH5 (Ibañez-Tallon, Gorokhova and Heintz, 2002; Solomon *et al.*, 2017)	Functional null (transgene insertion)	Residual motility	Not scored	Yes – majority of homozygotes die by p21	Yes	Yes	Yes + otitis
	ENU – missense mutation	Reduced CBF	Not scored	Some survive to adulthood	Yes	Yes	Not scored
DNAI1 (Ostrowski *et al.*, 2010; Francis *et al.*, 2012)	Null	Not scored (lethal)	Immotile	N/A	Not scored (lethal)	Yes	Not scored (lethal)
	Conditional	Immotile	Not scored	N/A	No	No	Yes

	deletion in adults						
CCDC151 (Hjeij *et al.*, 2014)	ENU loss of function	Residual motility	Not scored	Yes	No	Yes	No
DNAAF4 (Tarkar *et al.*, 2013; Li *et al.*, 2015)	Exons 2-4 deleted ENU - mutation in start codon.	Dysfunctional motility	Not scored Not scored	Yes – 2/3 die in utero. Hydrocephalus - death by p21	Yes	Yes	Not scored (Poor survival)
DNAAF2 (Matsuo *et al.*, 2013)	Exon 1 deleted	Immotile	Not scored	Yes - >90% of homozygotes die pre-weaning	Yes	Yes	Not scored (Poor survival)
HYDIN (Davy and Robinson, 2003; Lechtreck *et al.*,	Spontaneous frameshift	Dysfunctional motility	Not scored	Yes – majority of homozygotes die by p21	Yes	No	Not scored (Poor survival)

2008)							
CCDC40 (Becker-Heck *et al.*, 2011)	ENU induced nonsense mutation	Shorter; motility not examined	Not scored	Yes - majority die pre-weaning	Yes	Yes	Not scored (Poor survival)
DNAH11 (Lucas *et al.*, 2012)	Spontaneous missense	Immotile	Immotile	No	No	Yes	Yes
DNAAF1 (Ha *et al.*, 2016)	ENU induced splice donor site mutation	Motility not examined	Not scored	Yes – no homozygotes recovered at p21	Yes	Yes	Yes
ARMC4 (Li *et al.*, 2015)	ENU – missense mutation	Not scored	Not scored	Not stated	Not stated	Yes	Not scored
DNAAF3 (Li *et al.*, 2015)	ENU – missense mutation	Immotile	Not scored	Not stated	Not stated	Yes	Not scored

CCDC164 (Li *et al.*, 2015)	ENU – missense mutation	Not scored	Not scored	Not stated	Not stated	Yes	Not scored
CCDC39 (Li *et al.*, 2015; Solomon *et al.*, 2017)	ENU - mutation in start codon.	Immotile	Not scored	Embryonic or post-natal lethality by 5-7 dpp	Yes	Yes	Not scored
TTC25 (Wallmeier *et al.*, 2016)	Exon 2-3 deletion	Residual motility	Not scored	Yes – some prenatal lethality	Yes	Yes	Not reported
STK36 (Vogel *et al.*, 2012)	Exon 25 (partial)	Motility not examined	Not scored	Yes – majority euthanised 3-6 weeks of age	Yes	No	No; middle ear inflammation

Appendix 4: Mouse knock-outs associated with ciliary motility phenotypes.

Gene name	Type of mutation	Tracheal cilia function	Nodal cilia function	Embryonic/pre-wean lethality	Hydrocephalus	Situs defects	Rhinosinusitis
Lrrc48 (Ha *et al.*, 2016)	ENU - missense at conserved residue	Not scored	Not scored	No	Yes	Yes	Yes
Pcdp1 (Lee *et al.*, 2008)	Spontaneous 400kb deletion	Reduced tracheal cilia beat frequency	Not scored	Yes – background strain dependent	No	Yes	Yes – background strain dependent
Spef1 (Sironen *et al.*, 2011)	Spontaneous missense & nonsense mutations (Lambe	Reduced tracheal cilia beat frequency	Not scored	Yes – majority of homozygotes die by p28	Yes	No	Yes

	et al., 2009)						
Poll (Kobayashi *et al.*, 2002; Zariwala *et al.*, 2004; Vogel *et al.*, 2010)	Gene trap (two lines)	Not scored	Not scored	Yes, 50% lethality in homozygotes by p21	Yes	Yes	Yes
Nme7 (Vogel *et al.*, 2010)	Gene trap in intron 1.	Not scored	Not scored	Not stated	Yes	Yes	No
Ulk4 (Vogel *et al.*, 2012)	Exons 4-8 deleted	Not scored	Not scored	Yes – high	Yes	Not stated	Yes
Nme5 (Vogel *et al.*, 2012)	Exon 1 deleted	Not scored	Not scored	Not stated	Yes	No	Yes
Kif27 (Vogel *et al.*, 2012)	Gene trap in intron 1	Not scored	Not scored	Yes – dead or euthanised by 8 weeks of age	Yes	No	Yes
Ak7 (Vogel *et al.*,	Gene trap	Not scored	Not scored	Yes – most	Yes	No	Yes

2012)	insertion in intron 6			homozygotes died by 8 weeks of age			
Cfap54 (McKenzie *et al.*, 2015)	Gene trap – insertion in intron 1	Reduced CBF	Not scored	Yes – dependent on background strain	Yes	No	Yes
Hsf1 (Inouye *et al.*, 2003; Takaki *et al.*, 2006, 2007)	Exons 2-4 deleted	Reduced CBF and amplitude	Not scored	Not stated	Yes	Not stated	Yes
Mns1 (Zhou *et al.*, 2012)	Exons 3-8 deleted	Not scored	Not scored	Not stated	Yes	Yes	Not stated
Wdr69 (Solomon *et al.*, 2017)	ENU – missense mutation	Dyskinetic	Not scored	Some survive to adulthood	Yes (some)	Yes	Not scored

Appendix 5: Experimental Methods

Animals were maintained in accordance with the Medical Research Council's guidance "Responsibility in the Use of Animal for Medical Research" (July 1993), and in accordance with the Animals (Scientific Procedures) Act, 1986.

Ethical approval for all studies involving mouse work was obtained as part of an application for a UK Home Office Project License (30/2980) and all mice were kept in accordance with UK Home Office welfare guidance and project license restrictions. Mice were bred in a specific pathogen-free environment at the Mary Lyon Centre, MRC Harwell Institute. Mice were maintained in controlled light with a 12 hour light/dark cycle, with controlled temperature (21^{o}C±2^{o}C) and humidity (55±10%). Mice had free access to water (10-12 ppm [parts per million] chlorine) and were fed ad libitum on a commercial diet (5.3% fat [corn oil], 21.2% protein, 57.4% carbohydrate, 4.6% fibre; Rat and Mouse Diet No. 3 [RM3], Special Diet Services, Essex, UK). All mice were socially housed in groups of 2-5 mice.

All mice were maintained on a C57BL/6N background strain. The *1700007K13Riktm2b* (European Conditional Mouse Mutagenesis Program) Wtsi allele was created at the Wellcome Trust Sanger Institute. It is a reporter-tagged deletion allele without conditional potential, and is isogenic on C57BL/6N background **(Fig. EM1**).

The *Ccdc103^{H154P}* and *Ccdc103^{del13}* alleles were created at MRC Harwell Institute Mary Lyon Centre using CRISPR-Cas9. The *Ccdc103^{H154P}* allele contains a single nucleotide change (A>C). The *Ccdc103^{del13}* allele contains a 13 nucleotide deletion (**Fig. 5.1**).

EM1: Genotyping *1700007K13Rik^{tm2b}*

The *1700007K13Rik^{tm2b}* allele contains a deletion of exon 2 with an insertion of lacZ (**Fig. EM1**). Mice carrying this allele were genotyped by a PCR assay.

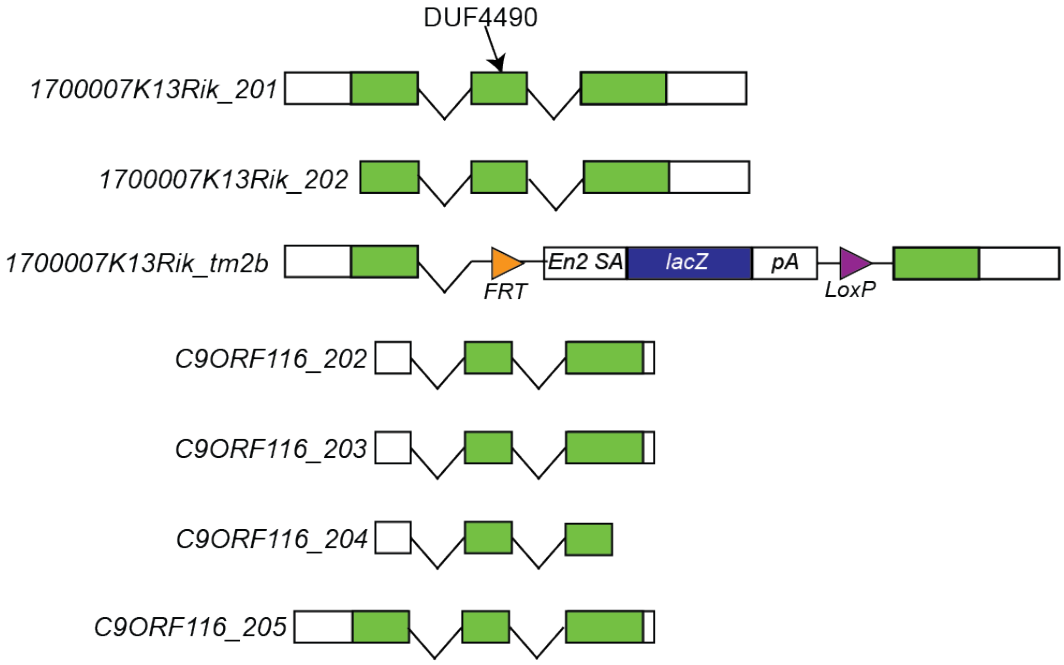


Figure EM1: Diagram showing the domains present in PIERCE1 (mouse 1700007K13Rik; human C9ORF116) transcripts, and design of the *Pierce1 (1700007K13Rik)* tm2b allele.

EM1.1: Tissue preparation:

Adult ear clips/tail samples: tissue samples were boiled in 90 µl 50 mM NaOH for 1 hour, before neutralisation with 10 µl Tris-HCl pH 4.5.

Embryonic yolk sac: tissue samples were boiled in 45 µl 50 mM NaOH for 1 hour, before neutralisation with 5 µl Tris-HCl pH 4.5.

The PCR set up was as follows: 10 µl Taq 2X Master Mix (QIAGEN, 201445); 0.5 µl (100 µM) each of *1700007K13Rik-5arm-WTF*, *1700007K13Rik-Crit-WTR*, and 5mut-R1 primers; 1 µl genomic DNA; 7.5 µl ddH_2O.

PCR reactions were run out in a 2% agarose gel, with the wild-type allele producing a band of 245 base pairs and the *1700007K13Riktm2b* allele producing a band of 184 base pairs.

PCR protocol:

- 98°C 30 seconds
- 40°C cycles:
    - 98°C 10 seconds
    - 57.7°C 30 seconds
    - 72 15°C seconds
- 72°C 2 minutes
- 10°C ∞

EM2: Genotyping CCDC103^{H154P}

Allele-specific FAM-labelled assays were used to genotype tissue from these lines. A VIC-labelled *DOT1* probe was used as an internal control. In samples that contain a modified allele, wild-type assay copy number drops by 1 and mutant assay copy number increases by 1.

EM2.1: Tissue preparation:

DNA Extract All Reagents kit (ThermoFisher, 4403319) was used for DNA extraction. For adult samples, 50 µl DNA lysis buffer was added (25 µl for embryonic samples). The sample was then heated to 95°C for 3 minutes, cooled, and an equal volume of DNA stabilisation buffer added. A plate shaker was used (approx. 1 minute) to mix the buffers, then the plate was either immediately frozen then stored at -20°C, or a 1:10 dilution in ddH_2O made and used as the qPCR template DNA.

The qPCR reaction set up is as follows:

Component	Volume (µl)
ABI GTX TaqMan™ Master Mix (ThermoFisher, 4401892)	5
Dot1L_2F (20 µm) primer	0.025

Dot1L_R (20 µm) primer	0.025
DotL_2M probe (5 µm)	0.2
Allele-specific FAM labelled assay (probe 5 µm and primers 15 µm each)	0.3
ddH_2O	1.5
DNA (1:10 dilution of prep)	2.5

7500 and CopyCaller software (both ThermoFisher) were used to analyse genotyping qPCR results.

EM3: Molecular biology

EM3.1: Agarose gel electrophoresis

1% agarose, TBE gels with 0.5% ethidium bromide were submerged in TBE buffer. TAE gels were used for cloning, with TAE buffer. 2% agarose gels with TBE buffer were used for genotyping *1700007K13Rik^{tm2b}* mice. Samples were mixed with 20% w/v Ficol OrangeG and DNA ladders (1 kb plus, New England Biolabs) were loaded into wells. A constant voltage of 80V was applied across the gel for 40-75 minutes (75 minutes for *1700007K13Rik^{tm2b}* genotyping gels) to separate linear DNA fragments by size. Fluorescence under ultraviolet light was achieved by the use of ethidium bromide as a DNA intercalatant. DNA separation was visualised using a Gel Doc system (BioRad).

EM3.2: Purification of PCR products

PCR products were purified using a QIAquick PCR purification kit (QIAGEN, 28106) or a QIAquick gel extraction kit (QIAGEN, 28706), according to manufacturer's instructions.

EM3.3: DNA sequencing

Purified DNA was sequenced by GATC Biotech and Source Biosciences, using primers targeted to the sequence of interest. Samples were prepared according to the guidelines of the relevant company.

EM3.4: cDNA synthesis

Applied Biosystems™ High-Capacity cDNA Reverse Transcription Kit (4368814) was used to synthesise cDNA from isolated RNA, according to manufacturer's instructions.

EM3.5: Restriction enzyme digestion

Restriction endonucleases purchased from New England Biolabs (NEB) were used with the recommended buffer and incubation temperature. 1 unit of restriction enzyme is defined as the activity required to fully cleave 1 µg of λ DNA in a 50 µl reaction in 1 hour.

Digests were routinely performed with the following set up: 1 µg purified DNA, 5 µl 10X restriction enzyme buffer (NEB), 10 U restriction enzyme, and ddH_2O to give a final volume of 50 µl. The success of restriction digestion was determined by DNA gel electrophoresis.

EM3.6: RNA isolation from tissues

Tissues were snap-frozen in liquid nitrogen. RNA was extracted using the appropriate QIAGEN RNeasy kit (mini [74106]: lung, testis, oviduct; fibrous [74704]: trachea; lipid: brain).

EM3.7: RT-qPCR

Fast SYBR® Green Master Mix (ThermoFisher, 4385612) was used to determine relative gene expression. Primers were designed to be uniquely complementary to the cDNA of interest. Standard curves and melting temperature analysis were carried out on each primer pair before use in quantification to ensure efficient amplification of a single product.

Isolated RNA was collected and used in cDNA synthesis as previously described. Reactions were set up as follows:

Component	Volume (µl)
Fast SYBR Green Master Mix	10
Forward primer (10 µM)	0.6
Reverse primer (10 µM)	0.6
ddH_2O	3.8
cDNA (10 ng per well)	5

An Applied Biosystems™ 7500 Fast Real-Time PCR System was used to run reactions, and 7500 Software v2.3 used to analyse results.

EM3.8: Western blotting

EM3.8.1: Tissue preparation:

Tissues were snap frozen in liquid nitrogen and stored at -80^{o}C before homogenisation in liquid N_2 using a pestle and mortar. 2 ml of lysis buffer was added per 200 mg tissue and mixed, before centrifugation (12,000 RPM, 4^{o}C, 20 minutes). Samples were heat inactivated at 95^{o}C, 10 minutes.

EM3.8.2: Cell preparation:

Cells were gently washed with ice-cold PBS. 500 µl ice-cold PBS was added to each well; cells were scraped and aspirated from the dish before centrifugation (12,000 RPM, 4^{o}C, 5 minutes). Cells were snap frozen in dry ice and stored at -20^{o}C. 500 µl RIPA buffer (150 mM NaCl; 50 mM Tris pH 7.5; 1% NP-40; 0.5% sodium deoxycholate; 0.1% SDS in ddH_2O) + 1X protease inhibitor (Roche, 04693159001) was added to each

pellet (2 wells of a 6 well plate); cells were re-suspended and passed through a 23G needle using a 1 ml syringe. The lysate was incubated for 30 minutes on ice then centrifuged (12,000 RPM, 4°C, 5 minutes). NuPAGE™ LDS Sample Buffer (4X; Invitrogen, NP0008) and 1 M DTT were added to cell lysates to give a final concentration of 1X Sample Buffer and 50 mM DTT, before heat inactivation at 95°C for 5 minutes.

EM3.8.3: SDS-PAGE and transfer

NuPAGE™ 4-12% Bis-Tris Protein Gels (Invitrogen, NP0321BOX & NP0322BOX), and NuPAGE™ MES SDS Running Buffer (Invitrogen, NP0002) were used in SDS-PAGE. Precision Plus Protein™ Dual Color Standard (Bio-Rad, 1610374) was used to determine band size. The iBlot transfer system (Invitrogen) was used to transfer protein bands to membrane.

Membranes were blocked in 5% skimmed milk powder in Tris buffered saline, 10% Tween (TBST; Biorad, 1706435) for 1 hour at room temperature (RT) with gentle agitation. Membranes were incubated with primary antibodies diluted in 5% milk in TBST for 1 hour at RT, or overnight at 4°C, with gentle agitation. Membranes were washed (3 x 5 minutes) with TBST before incubation with secondary antibodies diluted in 5% milk + TBST for 1 hour at RT, with gentle agitation. Membranes were washed again with TBST (3 x 5 minutes) before developing.

EM3.8.4: Enhanced chemiluminescence

The EZ-ECL kit (Biological Industries, 20-500-120) was used to develop Western blots with horseradish-peroxidase-conjugated secondary antibodies, according to manufacturer's instructions. An MI-5 X-ray processer was used to develop films (Amersham Hyperlink™ MP; GE 28906842). The default exposure time was 5 minutes, but was adjusted if necessary according to stain intensity.

EM3.8.5: LI-COR system

The LI-COR system (Odyssey CLx) was used to image Western blots with fluorescent-conjugated secondary antibodies, as manufacturer's instructions. Membranes were dried in the dark for >10 minutes before imaging.

EM3.9: Co-immunoprecipitation

Cells were washed with PBS before 250 µl of RIPA buffer + protease inhibitor (described above) was added to each well. Cells were scraped and passed through a 23G needle using a 1 ml syringe to disrupt clumps. Cells were incubated on ice for 30 minutes before centrifugation (12,000 RPM, 4^{o}C, 15 minutes) to pellet debris. Supernatant was transferred to a clean 1.5 ml tube; 50 µl was reserved for Western blot analysis.

Protein G Sepharose® Fast Flow beads (Sigma-Aldrich, P3296-5ML) were prepared by washing in RIPA buffer. Beads were spun at 2000 RPM for 1 minute to pellet and stored at 4^{o}C until pre-clearing.

Lysate supernatant was made up to 500 µl in volume per well of cells (from a six-well plate). Cell lysates were added to Protein G beads and rotated for 1-2 hours at 4^{o}C to pre-clear lysates. Beads were then spun at 3000 RPM for 1 minute to pellet beads, and the supernatant was split into two equal aliquots. Each aliquot was incubated with the appropriate antibody over night at 4^{o}C on the rotator.

Fresh protein beads were prepared on the following day as in step 2. 20 µl of beads were prepared for each IP reaction. IP reactions were added to beads and rotated at 4^{o}C for 1-2 hours to capture IP complexes. The reactions were then centrifuged (3000 RPM, 1 minute) to pellet beads and the supernatant discarded. Beads were washed 3X with 500 µl RIPA, with the supernatant discarded each time. 30 µl of 1X LDS Sample Buffer,

containing 50 mM DTT, was added directly to bead-IP complexes before proceeding with heat inactivation at 95°C for 5 minutes. Western blotting was carried out as described above.

EM4: X-Galactosidase staining

EM4.1: Whole embryos (7.5-8.5 dpc)

Embryos were dissected and washed with PBS before fixation (1% formaldehyde, 0.2% glutaraldehyde, 2 mM $MgCl_2$, 5 mM EGTA, 0.02% NP-40 in PBS). Embryos were washed 3 times (0.02% NP-40, 2 mM $MgCl_2$ in PBS). Embryos were then moved into stain for 18 hours at 37°C (10 mM $K_3Fe(CN)_6$, 10 mM $K_4Fe(CN)_6$, 2 mM $MgCl_2$, 0.01% sodium deoxycholate, 0.02% NP-40, 0.5 mg/ml X-gal). Embryos were washed 3x 5 minutes with PBS, and then post-fixed for 30 minutes with 4% paraformaldehyde (PFA) or fixative as detailed above. Embryos were stored in PBS prior to imaging.

EM4.2: Cryosectioned tissue

Testes were collected and frozen in OCT, in an isopentane bath on a bed of dry ice. Samples were stored at -80°C before cryosectioning. Slides were removed from freezer and allowed to thaw/dry for 1 hour. Samples were rinsed with PBS and then post-fixed in 4% PFA for 10 minutes, before 3 x 5 minute washes in PBS. Samples were then incubated with the X-gal staining solution (2 mM $MgCl_2 \bullet 6H_2O$, 0.01% sodium deoxycholate, 0.02% IGEPAL CA-630, 5 mM potassium ferrocyanide, 5 mM potassium ferricyanide, 0.1% X-gal in N,N-dimethylformamide, all made up in cold, freshly made PBS pH 8; 12 µl 4-Nitro blue tetrazolium chloride per 100 ml of stain solution added immediately before incubation) for 48 hours at 37°C.

After staining, samples were rinsed with PBS, post-fixed in 4% PFA for 10 minutes, and washed in PBS (2 minutes) and ddH_2O (3 x 1 minute).

Samples were then counter-stained with Nuclear Fast Red (Sigma-Aldrich, 6409-77-4) for approx. 7 seconds, before a 10 second wash in ddH_2O. Slides were dried and then dehydrated with sequential washes in industrial methylated spirits (1 minute in 70%, 3 x 1 minute in 100%). Slides were placed in Histo-Clear (National Diagnostics, HS-200) and mounted with coverslips and HistoMount (National Diagnostics, HS-103), before leaving to dry overnight and imaging.

EM5: Cell culture

Stringent aseptic technique was maintained throughout cell and tissue culture work.

EM5.1: Thawing cells

Vials to be thawed were removed from liquid nitrogen stores and kept frozen on dry ice before thawing. Each vial was swirled in a 37^oC water bath and removed with all but a slither of cells thawed. Cells were then added dropwise to a 10 cm dish containing 14 ml of appropriate cell culture medium. Medium was exchanged within 18 hours.

EM5.2: Splitting cells

Cells were washed with pre-warmed PBS and 1-1.5 ml 5-10% trypsin was added, as appropriate for the cell line. Once cells had completely detached, the trypsin was neutralised with 9 volumes of medium, and the cells were split into at least two plates, dilution dependent on the growth rate of the cell line. Cells were then incubated at 37^oC, 4% CO_2, until confluency was reached.

EM5.3: Counting cells

Trypsinised cells were pelleted by centrifugation at 800 RPM for 5 minutes. The supernatant was aspirated away and the pellet re-suspended in 10 ml pre-warmed medium. 10 µl of this suspension was added to a haemocytometer by capillary action. Cells were counted if

inside the grid or touching the left or bottom walls. A 1 mm^2 square (volume 100 nl) was counted and an average of three counts taken. This average was then multiplied by 10^4 and corrected for the dilution factor to give the number of cells/ml in the original suspension.

EM5.4: Transfection of constructs

Cells were transfected at 80-95% confluency. Lipofectamine® 2000 (ThermoFisher, 11668027) was prepared according to manufacturer's instructions. DNA to be transfected was purified using the PureYield™ Plasmid Midiprep kit (Promega, A2492). Cells were incubated for 24 hours before a media change or serum starvation (if used).

EM5.5: Immunocytochemistry

Cells were seeded onto coverslips in a 6 well plate and allowed to grow to confluency. If necessary, cells were serum starved to promote the growth of primary cilia. Coverslips were washed with ice-cold PBS and fixed with ice-cold methanol for 5 minutes or with RT 4% PFA for 30 minutes. Dishes were tilted to align cilia during fixation. Cells were washed 3 times with PBS and permeabilised with 1% NP-40 in PBS for no more than 3 minutes. Cells were washed 2 times with PBS and blocked with 4% BSA in PBS for 30 minutes at RT. Primary antibodies were diluted in 4% BSA and 50 µl per coverslip was dotted onto parafilm in a humidified chamber. Coverslips were dried gently and placed face-down on the primary antibody solution for 1 hour at RT. Cells were washed for 3 x 5 minutes in PBS, and then incubated on parafilm with the secondary antibodies in 4% BSA for 30 minutes at RT in the dark. Coverslips were washed 3 x 10 minutes in PBS before mounting. Antibodies used as in table.

EM6: Dissection of embryos

Using a light microscope at 0.63X magnification, decidua were dissected out from the oviduct. At 1X magnification, individual decidua were dissected. Reichart's membrane was removed, and if required, the yolk sac was taken for genotyping. DNA extraction and genotyping either occurred immediately, or the samples were frozen and stored at -20^{o}C for later processing.

EM6.1: Situs phenotyping of 13.5 dpc embryos

Using a light microscope, the head was removed and the thoracic cavity opened. Embryos were scored according to lung lobation (wild-type; 4:1 R:L), heart apex situs (wild-type; L) and stomach situs (wild-type; L). The tail was taken for genotyping. DNA extraction and genotyping either occurs immediately, or the samples are frozen and stored at -20^{o}C for later processing.

EM6.2: Whole mount immunofluorescence (7.5-8.5 dpc):

EM6.2.1: Protocol 1:

Embryos were dissected, washed with PBS and fixed in 4% PFA for 15 minutes. Embryos were permeabilised with sequential washes in TX-100 dilutions in PBS (3 x 5 minutes 0.1% TX-100 in PBS; 2 x 10 minutes 0.25% TX-100 in PBS; 2 x 5 minutes 0.1% TX-100 in PBS), before blocking in block solution (2.5% horse serum, 3% BSA in 0.1% Tween in PBS) for 1 hour at RT. Primary antibodies were diluted in 25% block solution, 25% 0.1% TX-100 in PBS and incubated with embryos for 18 hours at 4^{o}C. Embryos were then washed (4 x 30 minutes, 0.04% TX-100 in PBS). Secondary antibodies were diluted in 25% block solution, 25% 0.1% TX-100 in PBS, before incubation with embryos in a darkened chamber for 1 hour at RT. Embryos were then washed (3 x 30 minutes, 0.04% TX-100 in PBS), and then stored in PBS at 4^{o}C before imaging.

EM6.2.2: Protocol 2 (higher detergent concentration):

Embryos were dissected, washed with PBS and fixed in 4% PFA for 15 minutes. Embryos were permeabilised and blocked in detection secondary antibody serum (e.g. goat serum if secondary antibody was raised in goat) diluted 1:10 in 0.5% TX-100 in PBS, for 1 hour at RT with gentle agitation. Embryos were washed with PBS then the primary antibody was diluted in the permeabilisation/blocking buffer and applied, before incubation overnight at 4^{o}C with gentle agitation. Embryos were washed 3 times with PBS before the secondary antibody was diluted in the permeabilisation/blocking buffer. Embryos were incubated in this in the dark for 1 hour at RT, with gentle agitation. Embryos were washed 3 times with PBS before storage in PBS at 4^{o}C.

EM6.3: Whole mount in situ hybridisation

Fixed embryos were rehydrated through sequential 5 minute washes in 75%, 50% and 25% methanol in PBS. Embryos were washed with PBS + 0.1% Tween 20 (PBT; 2 x 5 minutes). Embryos were bleached for 1 hour in 6% H_2O_2 in PBT, before 3 x 5 minutes PBT washes. Embryos were permeabilised with 10 µg/ml Proteinase K in PBT for 5 minutes; Proteinase K was inactivated with a 20 mg/ml glycine in PBT wash (5 minutes). Embryos were washed (2 x 5 minutes, PBT) and post-fixed in 0.2% glutaraldehyde in 4% PFA in PBS for 20 minutes, followed by washing (2 x 5 minutes, PBT) and blocking at 70^{o}C for 1 hour in warmed pre-hybridisation solution. Probes were inactivated by heating to 70^{o}C for 30 minutes. Probes were diluted to 1:500 in hybridisation solution and incubated with embryos for 18 hours at 70^{o}C. Embryos were then washed for 3 x 30 minutes in wash solution I (70^{o}C/70^{o}C/65^{o}C) followed by 3 x 30 minutes in wash solution II (all 65^{o}C). Embryos were washed in TBST and pre-blocked in 10% heat-inactivated sheep serum (HISS) in Tris-buffered saline, 0.1% Tween 20 (TBST) for 2.5 hours at RT. Antibody was prepared

by blocking in 1% HISS in TBST with heat-inactivated embryo powder for 1 hour, with gentle agitation at 4ºC.The probe and antibody were then hybridised overnight at 4ºC in 1% HISS in TBST. Embryos were washed with TBST at RT (sequentially: 3 x 5 minutes, 5 x 1 hour, overnight). Embryos were then washed with NTMT at RT (5 minutes, 2 x 15 minutes). A solution of 5 µl NBT/BCIP per ml NTMT was used to stain areas of probe hybridisation. Embryos were then washed for 3 x 5 minutes in NTMT or PBS before post-fixation in 4% PFA for 30 minutes at RT. Embryos were stored in PBS at 4ºC prior to imaging; yolk sac was taken upon imaging for genotyping where appropriate.

NTMT (alkaline phosphatase buffer)	20X SSC (saline sodium citrate buffer)
For 50 ml: 1 ml 5 M NaCl, 5 ml 1 M Tris (pH 9.5), 2.5 ml 1 M $MgCl_2$	800 ml ddH_2O, 175.3 g NaCl (3M), 88.2 g trisodium citrate (NaCit; 300 mM). Adjust pH to 7.0 with a few drops of 1M HCl. Adjust volume to 1L with ddH_2O. Autoclave.

Pre-hybridisation solution	Hybridisation solution	Wash solution I	Wash solution II	10X TBST (Tris-buffered saline, 0.1% Tween 20)
For 10 ml: 5 ml formamide, 2.5 ml 20X SSC (pH4.5), 2.5 ml ddH_2O, 100 µl 10% Tween, 5 µl 100 mg/ml heparin	Add 10 µl of 10 mg/ml yeast RNA and 10 µl of 10 mg/ml salmon sperm DNA per 1 ml of pre-hybridisation solution	For 20 ml: 10 ml formamide, 4 ml 20X SSC (saline sodium citrate buffer) pH 4.5, 1 ml 20% SDS, 5 ml ddH_2O	For 20 ml: 10 ml formamide, 2 ml 20X SSC pH 4.5, 8 ml ddH_2O	40 g NaCl, 1 g KCl, 125 ml Tris-HCl (pH 7.5), 50 ml 10% Tween, 335 ml ddH_2O. Add Tween after autoclaving, store at RT.

EM6.3.1: In situ hybridisation probe synthesis

EM6.3.1.1: Plasmid linearization:

2 µg of plasmid DNA was digested with the appropriate enzyme for 1 hour in a 5-fold over-digestion, including an enzyme heat-kill temperature step. Agarose electrophoresis was used to demonstrate complete linearization, and QIAquick PCR purification kit (QIAGEN, 28106) was used to purify the template.

EM6.3.1.2: Probe synthesis:

Probes were synthesised using a DIG RNA labelling mix (Roche, 11277073910), with reactions set up as follows:

- 4 µl 10X transcription buffer
- 4 µl DIG labelling mix
- 1 µg linearized plasmid DNA
- 2 µl (40 units) appropriate RNA polymerase T3/T7 (ThermoFisher, EP0101/EP0111)
- 0.25 µl (25 units) RNase OUT™ (ThermoFisher, 10777019)
- RNase-free H_2O to 40 µl

Reaction mixture was incubated in a 37^{o}C water-bath for 2+ hours. 100 µl of H_2O, 15 µl of 3 M sodium acetate (pH 5.2), and 300 µl of ice-cold 100% ethanol were added, and the reaction mixture was incubated at -20^{o}C overnight to precipitate RNA. The reaction mixture was centrifuged at 14,000 RPM in a benchtop centrifuge for 20 minutes at 4^{o}C. The pellet was washed twice with 70% ethanol (5 minute spin at 14,000 RPM 4^{o}C between washes), before air drying and re-suspending in 200 µl of TE buffer. Synthesised probes were stored at -80^{o}C.

EM6.3.1.3: TA cloning for in situ hybridization probe plasmid synthesis

Primers were designed against the cDNA sequence of the gene of interest and optimised for synthesis using Taq polymerase (QIAGEN, 201445). Agarose electrophoresis was used to confirm product size; QIAquick PCR purification kit (QIAGEN, 28106) was used to purify the product.

The T vector was produced by blunt cutting 2 µg of pBluescript II KS (-) with EcoRV-HF (2 µg DNA, 20 U EcoRV-HF, 2 µl CutSmart® [NEB]) and ddH_2O to 20 µl. The digest was run for 2 hours at 37^oC with a 20 minute heat-kill at 65^oC. Complete digestion was confirmed by agarose electrophoresis. Thymidine bases were added to the cut vector (2 µg DNA, 10 µl 10X PCR Buffer, 5 µl Taq Polymerase, 1.5 µl 100 mM dTTP, ddH_2O to 100 µl) during a 2 hour incubation at 72^oC. The product was purified using a QIAGEN PCR purification kit and quantified.

Insert and vector were ligated in a molar ratio of 1:4 (vector: insert), with 60 ng of T-vector used in each ligation. Vector and insert only controls were included. A Quick Ligase kit was used for ligations (NEB, M2200S). 10 µl of the reaction was used in the transformation.

EM6.3.1.4: Analysis of transformants: blue/white selection

Blue/white selection was used to visually screen for successful cloning into pBluescript. Antibiotic-containing LB agar plates were coated with 100 µl of 100 mM IPTG and 35 µl of 25 mg/ml X-gal.

EM6.3.1.5: Analysis of transformants: polymerase chain reaction

Colonies were picked with a clean p10 pipette tip, which was wiped in the bottom of a PCR plate well, then dropped into a culture tube with 3 ml selective LB, and stored at 4^oC. The plate was sealed and spun for 2 minutes at 2,000 RPM. Taq 2X Master Mix (QIAGEN, 201445) and insert

primers were used (per well: 10 µl Master Mix, 1 µl forward primer, 1 µl reverse primer, 8 µl ddH_2O).

PCR programme:

- 96°C 3 minutes
- 35°C cycles
    - 94°C 40 seconds
    - 51°C 40 seconds
    - 72°C 60 seconds
- 72°C 10 minutes
- 10°C ∞

Products were analysed using agarose electrophoresis and correct inserts were sent for DNA sequencing.

EM6.3.1.6: Transformation of cloning quality E. coli

Cloning quality *E.coli* was defrosted on ice. 50 µl of *E.coli* was used for each ligation and dispensed into a culture tube, including tubes for negative (no DNA) and positive (parental plasmid) controls. 10 µl of ligation was added to *E. coli* and mixed gently, then incubated on ice for 30 minutes before a heat shock at 42°C for 45 seconds, and incubation on ice for 1 minute. 1 ml of antibiotic-free LB was then added to each tube, and tubes were incubated in a 37°C shaker incubator for 1 hour at 250 RPM. Antibiotic-containing plates were pre-warmed and high and low density cultures of each transformation were incubated overnight at 37°C, 4% CO_2.

EM6.4: Scanning electron microscopy

Embryos were dissected in PBS, and fixed overnight in 0.1 M sodium cacodylate, 2.5% glutaraldehyde in ddH_2O. Embryos were washed with 0.1 M sodium cacodylate (2 x 10 minutes), and then post-fixed in 1% osmium tetroxide in 0.1 M sodium cacodylate for 1 hour. Embryos were then washed in ddH_2O (6 x 3 minutes). Embryos were sequentially dehydrated in ethanol (50%, 70%, 100%; 10 minutes each) and washed

with 100% acetone for 10 minutes before storing in fresh acetone at 4°C. Embryos were dried using a critical point dryer, mounted on stubs and sputter coated before imaging. Images were taken using a Jeol SEM 6010LV.

EM6.5: Differential interference contrast imaging of embryonic nodal cilia

Embryos resulting from *Pierce1*$^{+/-}$ intercross matings were harvested at 8.0 dpc and dissected in pre-warmed DMEM (ThermoFisher, 210630-29) + 10% FBS (Sigma-Aldrich, F2442). DIC imaging was carried out at 100X using a Hamamatsu C9300 camera attached to a Leica DM2500 microscope. Embryos at 1-6 somite stages were used for this analysis. Quantitation was performed by counting cilia rotations from movies taken at approximately 100 frames per second for at least 5 cilia per embryo and at least 18 embryos per genotype.

EM6.6: Particle image velocimetry of embryonic nodal cilia

Embryos resulting from heterozygote intercross matings were harvested at 8.0 dpc and dissected in pre-warmed DMEM + 10% FBS. FluoSpheres™, 0.2 µm diameter (ThermoFisher F8848) were diluted in DMEM + 10% FBS before use. Videos were taken at 40X using an AxioCam HRm camera with a VivaTome attachment, on a Zeiss Observer.Z1 microscope. Data points were binarised and dilated using ImageJ, before PIV analysis using PIVLab plugin (Thielicke and Buma, 2014; Thielicke and Stamhuis, 2014) in MatLab. Embryos at 2-3 somite stages were used for this analysis.

EM7: Histological techniques

EM7.1: Immunofluorescence of cryosectioned tracheae

Mouse trachea were cut in 25 µm sections, thawed and dried. The samples were surrounded with liquid blocker, and rinsed twice with PBS. Samples were fixed in 4% PFA in PBS for 15 minutes before washing 3 x 5 minutes in 0.1% Triton X-100 in PBS. Samples were blocked for >2 hours in 0.1 Triton-X-100/1% BSA in PBS, before overnight incubation at 4°C in a pre-humidified chamber. Antibodies were diluted in in 0.1 TX-100/1% BSA in PBS. After primary antibody incubation, samples were washed 3 x 15 minutes in 0.1% TX-100 in PBS. In the dark, secondary antibodies were diluted in 0.1 TX-100/1% BSA in PBS and incubated with samples for 1 hour at RT. Samples were then incubated in a 1:20,000 dilution of DAPI stain in PBS for 5 minutes, before 3 x 5 minute washes with PBS. 1-2 drops of fluorescence mounting medium was applied to each sample and a coverslip carefully added. Mounting medium was allowed to dry in the dark before imaging.

EM7.2: DAB Staining

Slides were washed with ddH_2O and incubated with 3% H_2O_2 in isopropanol for 30 minutes at RT. Slides were washed twice with PBS, tapped dry and samples outlined with a wax pen. Samples were blocked with 10% serum in PBS for 30 minutes at RT, and then incubated with the 1° antibody for 1 hour at RT, or overnight at 4°C. Slides were washed twice with PBS and then incubated with a biotinylated 2° antibody for 30 minutes at RT:

a. Goat anti-rabbit biotinylated 2° (ThermoFisher, 32020), 1:200 in 10% goat serum
b. Rabbit anti-goat biotinylated 2° (Dako, K4065) @ 1:400 in 10% rabbit serum

The 3° ABC Solution was made up and incubated for 30 minutes at RT (5 ml PBS; 100 µl / 2 drops reagent A; 100 µl / 2 drops reagent B). Slides were washed twice with PBS and then incubated with 3° ABC Solution for 30 minutes at RT before washing twice with PBS. 200 µl DAB stain was added to each slide; slides were incubated until brown staining was visible. The reaction was quenched in PBS before counter staining with haematoxylin staining and coverslipping.

EM8: Live imaging of adult tissues

EM8.1: Trachea preparation

Animals were sacrificed between 10-14 weeks of age in accordance with Schedule 1 methods, before tracheas were dissected and shipped in RT Ham's F12 (ThermoFisher, 11765054) + 1% penicillin-streptomycin (ThermoFisher, 15140148). Researchers were blind to genotype and situs. Tracheas were cleaned by removing excess tissue and contaminants under a dissection microscope and cut into rings approximately the width of one cartilage ridge.

EM8.2: High-speed video microscopy of tracheal motile cilia

After incubating overnight at 37°C (5% CO_2) in MEM medium including penicillin, streptomycin and nystatin, rings were allowed to settle for 20 minutes on the bottom of the culture well on the stage of an inverted Olympus IX71 microscope in an environmental chamber at 37°C. High speed video microscopy recordings were taken at 500 frames per second using a 60X magnification (Olympus LUCPlan FLN) objective with a Photron MC 2.1 FastCam camera. CBF was measured by fast Fourier transform analysis of HSVs using an ImageJ plugin to provide a beat frequency map of the video images and a mean frequency for each video. All results were reviewed to exclude values from debris or non-ciliated

areas of the image. CBP was independently assessed by 3 expert reviewers viewing videos at 30 frames per second playback.

EM8.3: Computer-assisted sperm analysis

Male reproductive tracts were dissected from mice sacrificed using Schedule 1 methods, and travelled in pre-warmed PBS. Caudae were then dissected out, pierced 20X with a needle, and individually incubated in 500 µl pre-warmed 1% BSA in PBS. Caudae were incubated at 37^{o}C for 20 minutes, with samples agitated at 10 minutes and immediately before a 30 µl sample was taken for analysis.

Samples were loaded into a 100 µm deep counting chamber (Leja, SC-100-01-02-B), and equilibrated on a warm stage (37 °C) for 2 minutes. Images were acquired at 10X magnification using a negative contrast phase objective (Nikon Eclipse80i with DS-Ri camera). A minimum of 5 fields were evaluated in each sample. Motility assessment was performed using a CASA system (HTM-Ceros v.12.3, Hamilton Thorne).

EM9: Transmission electron microscopy

EM9.1: Sperm flagella:

Male reproductive tracts were dissected from mice sacrificed using Schedule 1 methods, and fixed in 3% glutaraldehyde in 0.1 M cacodylate buffer, post fixed in 2% osmium tetroxide in 0.1 M cacodylate buffer, dehydrated and embedded in Spurr's resin following a standard protocol. Ultra-thin sections (100 nm) were cut, stained with lead citrate and examined and micrographed using a Hitachi HT7700 TEM. Ultrastructural defects were scored from 300+ ciliary cross-sections per sample.

EM9.2: Tracheal motile cilia:

Rings were fixed in 3% glutaraldehyde in 0.1 M cacodylate buffer, post fixed in 2% osmium tetroxide in 0.1 M cacodylate buffer, dehydrated and embedded in Spurr's resin following a standard protocol. Ultra-thin

sections (100 nm) were cut, stained with lead citrate and examined and micrographed using a Hitachi HT7700 TEM. Ultrastructural defects were scored from 300+ ciliary cross-sections per sample.

Table EM1 (p271-273): Primers and probes used in the experimental work of this thesis.
Table EM2 (p274-276): Antibodies used in the experimental work of this thesis.

Table EM1: primers and oligonucleotides

Primer	Sequence
1700007K13Rik-5arm-WTF	ACAGGAGCTTGGCCTCTGTA
1700007K13Rik-Crit-WTR	AGAGCACTCTCTCCCAGCAG
5mut-R1	GAACTTCGGAATAGGAACTTCG
CCDC103H154P-WT1_F	GTGGCATTGGCTGAGCAC
CCDC103H154P-WT1_R	AATCCCCAGCACTGCTGTC
CCDC103H154P-WT1_Probe	AGGCTGAGCGACCGGAC
CCDC103H154P-DONORMUT2_F	GTGGCATTGGCTGAGCC
CCDC103H154P-DONORMUT2_R	CAAGTTGAACCGCCCAGTGTT
CCDC103H154P-DONORMUT2_Probe	CTGAGCGACCGCACAGCAGT
Dot1L_F	GCCCCAGCACGACCATT
Dot1L_R	TAGTTGGCATCCTTATGCTTCATC
Dot1L_Probe	CCAGCTCTCTCAAGTCG
CCDC103_DEL13_UNIV_Probe	CTGCTGGTGGCATTGGCTGA
CCDC103_DEL13_WT_R	ACTGCTGTCCGGTCGCTCAG
CCDC103_DEL13_UNIV_F	GCCACCTCTTCCAGATGGATG
CCDC103_DEL13_MUT_R	CCCAGCACTGCTGCCTC
Ccpg1os_FOR (qPCR)	ATGCAGAAATGAGACCTGAACC
Ccpg1os_REV (qPCR)	TGCTCTGTAAACGCTTGCTCT
ActinB_FOR (qPCR)	GGCTGTATTCCCCTCCATCG
ActinB_REV (qPCR)	CCAGTTGGTAACAATGCCATGT

Alpha_tubulin_FOR (qPCR)	CCTAAACAGGTTGATAGGCCAAA
Alpha_tubulin_REV (qPCR)	CTCGCCTTCCACAGAATCCA
Ccpg1os_FOR (cDNA amplification; in situ probe synthesis)	ACTCCGATCGTCTTGCTGTT
Ccpg1os_REV (cDNA amplification; in situ probe synthesis)	TGCTCTGTAAACGCTTGCTCT
Pierce1_FOR (cDNA amplification; in situ probe synthesis)	GCACAGACTTGATCTGGGCTA
Pierce1_REV (cDNA amplification; in situ probe synthesis)	CTGTCAGCATCTTTCCTGTGTG
Ccdc103_FOR (cDNA amplification; in situ probe synthesis)	GTTGAGCAAAGGGTGCCTTC
Ccdc103_REV (cDNA amplification; in situ probe synthesis)	AGGGTGATTTCTCCTGGGGT
Pias2_201_FOR (cDNA amplification; in situ probe synthesis)	AATGGCGGATTTCGAGGAGT
Pias2_201_REV (cDNA amplification; in situ probe synthesis)	CACGGGATTGTCAGCCTCAT
Pias2_202_FOR (cDNA amplification; in situ probe synthesis)	GCCCCCTGAACATTACGTCT
Pias2_202_REV (cDNA amplification; in situ probe synthesis)	GAGGTGAGACTGGGGATCAA
Pias2_203_FOR (cDNA	AGGAGTTGCGTTTAGGGAGC

amplification; in situ probe synthesis)	
Pias2_203_REV (cDNA amplification; in situ probe synthesis)	AGGTGGGCTTAGTGTCTTGC
1700007K13Rik-LacZ_primer1	CTCGCCACTTCAACATCAAC
1700007K13Rik-LacZ_primer2	TTATCAGCCGGAAAACCTACC
1700007K13Rik-LacZ_probe	TCGCCATTTGACCACTACCATCAATCC
PIERCE1_pEGFP-N1_for	GGAACTCGAGATGTCTGAAGAAAAACCTCAACAG
PIERCE1_pEGFP-N1_rev	GGAAGAATTCTGTCACAGATGGACGGC
PIERCE1_pcDNA3_for	GGAAGAATTCGCATGTCTGAAGAAAAACC
PIERCE1_pcDNA3_rev	GGAACTCGAGTTAGTCACAGATGGAC
PIERCE1_pLVX_for	GGAACTCGAGATGTCTGAAGAAAAACC
PIERCE1_pLVX_rev	GGAAGAATTCTTAGTCACAGATGGACG
pcDNA3.1/myc-His A_Pierce1_for	GGAAGAATTCATGTCTGAAGAAAAACCTCAACAGTCCG
pcDNA3.1/myc-His A_Pierce1_rev	GAGAGGGCCCGTCACAGATGGACGGCCTG

Table EM2: antibodies

Company/cat. no.	Against	Dilution	Raised in	Uses
Abcam ab11317	Γ tubulin	1:500	Rabbit	Immunofluorescence
Sigma-Aldrich T7451	Acetylated tubulin	1:500	Mouse	Immunofluorescence
Abcam ab52649	GM130	1:500	Rabbit	Immunofluorescence
Applied Design/ SPA-891	PDI	1:500	Mouse	Immunofluorescence
Abcam ab3672	PDI	1:500	Rabbit	Immunofluorescence
Sigma-Aldrich C3956.2MG	α-myc	1:500	Rabbit	Immunofluorescence
Abcam ab18181	HA	1:1000	Mouse	Immunofluorescence, western blotting
Sigma-Aldrich F3165.2MG	FLAG	1:500	Mouse	Immunofluorescence
N/A	PIERCE1	1:250	Rabbit	Western blotting

N/A	GFP	1:1000	Rabbit	Western blotting
ThermoFisher SA5-10041	Rabbit IgG H+L (DyLight 650)	1:500	Donkey	Immunofluorescence
Abcam ab6894	Rabbit	1:500	Donkey	Immunofluorescence
Abcam ab96883	Rabbit IgG H&L (DyLight® 488)	1:500	Goat	Immunofluorescence
Abcam ab96891	Rabbit IgG H&L (DyLight® 488)	1:500	Donkey	Immunofluorescence
Abcam ab96879	Mouse IgG H&L (DyLight® 488)	1:500	Goat	Immunofluorescence
Abcam ab96935	Goat IgG H&L (DyLight® 488)	1:500	Donkey	Immunofluorescence
LI-COR 926-32210	Mouse IgG (IRDye®800CW)	1:10,000	Goat	Western blotting (LI-COR)

LI-COR 926-68071	Rabbit IgG (IRDye®680RD)	1:10,000	Goat	Western blotting (LI-COR)
Sigma-Aldrich A6154	Rabbit IgG (HRP conjugated)	1:10,000	Goat	Western blotting (enhanced chemiluminescence)
Vector Labs BA-1000	Biotinylated Rabbit IgG	1:200	Goat	DAB staining
Agilent Dako E0466	Biotinylated Goat Immunoglobulins (affinity isolated)	1:400	Rabbit	DAB staining

Bibliography

Absalon, S. *et al.* (2008) 'Intraflagellar transport and functional analysis of genes required for flagellum formation in trypanosomes.', *Molecular biology of the cell*. doi: 10.1091/mbc.E07-08-0749.

Adachi, H. *et al.* (1999) 'Determination of left/right asymmetric expression of nodal by a left side-specific enhancer with sequence similarity to a lefty-2 enhancer.', *Genes & development*. Cold Spring Harbor Laboratory Press, 13(12), pp. 1589–600. Available at: http://www.ncbi.nlm.nih.gov/pubmed/10385627 (Accessed: 26 August 2016).

Adams, M. D. (2007) 'The Mouse Genome', in *The Mouse in Biomedical Research*. doi: 10.1016/B978-012369454-6/50018-2.

Adzhubei, I., Jordan, D. M. and Sunyaev, S. R. (2013) 'Predicting functional effect of human missense mutations using PolyPhen-2', *Current Protocols in Human Genetics*. doi: 10.1002/0471142905.hg0720s76.

Afzelius, B. A. (1976) 'A human syndrome caused by immotile cilia.', *Science (New York, N.Y.)*. American Association for the Advancement of Science, 193(4250), pp. 317–9. doi: 10.1126/science.1084576.

Ait-Lounis, A. *et al.* (2007) 'Novel function of the ciliogenic transcription factor RFX3 in development of the endocrine pancreas', *Diabetes*. doi: 10.2337/db06-1187.

Akimov, V. *et al.* (2018) 'UbiSite approach for comprehensive mapping of lysine and N-terminal ubiquitination sites', *Nature Structural and Molecular Biology*. doi: 10.1038/s41594-018-0084-y.

Almstrup, K. *et al.* (2004) 'Analysis of Cell-Type-Specific Gene Expression During Mouse Spermatogenesis1', *Biology of Reproduction*. doi: 10.1095/biolreprod.103.026575.

Alsaadi, M. M. *et al.* (2014) 'Nonsense mutation in coiled-coil domain containing 151 gene (CCDC151) causes primary ciliary dyskinesia.', *Human mutation*, 35(12), pp. 1446–8. doi: 10.1002/humu.22698.

Alten, L. *et al.* (2012) 'Differential regulation of node formation, nodal ciliogenesis and cilia positioning by Noto and Foxj1', *Development*. doi: 10.1242/dev.072728.

Amann, R. P. and Waberski, D. (2014) 'Computer-assisted sperm analysis (CASA): Capabilities and potential developments', *Theriogenology*. doi: 10.1016/j.theriogenology.2013.09.004.

Ansley, S. J. *et al.* (2003) 'Basal body dysfunction is a likely cause of pleiotropic Bardet-Biedl syndrome', *Nature*. doi: 10.1038/nature02030.

Antony, D. *et al.* (2013) 'Mutations in CCDC39 and CCDC40 are the Major Cause of Primary Ciliary Dyskinesia with Axonemal Disorganization and Absent Inner Dynein Arms', *Human Mutation*, 34(3), pp. 462–472. doi: 10.1002/humu.22261.

Arakel, E. C. and Schwappach, B. (2018) 'Formation of COPI-coated vesicles at a glance', *Journal of Cell Science*. doi: 10.1242/jcs.209890.

Ashique, A. M. *et al.* (2009) 'The Rfx4 transcription factor modulates Shh signaling by regional control of ciliogenesis.', *Science signaling*, 2(95), p. ra70. doi: 10.1126/scisignal.2000602.

Ashkenazy, H. *et al.* (2010) 'ConSurf 2010: calculating evolutionary conservation in sequence and structure of proteins and nucleic acids.', *Nucleic acids research*. Oxford University Press, 38(Web Server issue), pp. W529-33. doi: 10.1093/nar/gkq399.

Austin-Tse, C. *et al.* (2013) 'Zebrafish Ciliopathy Screen Plus Human Mutational Analysis Identifies C21orf59 and CCDC65 Defects as Causing Primary Ciliary Dyskinesia.', *American journal of human genetics*, 93(4), pp. 672–

86. doi: 10.1016/j.ajhg.2013.08.015.

Avidor-Reiss, T. *et al.* (2004) 'Decoding cilia function: Defining specialized genes required for compartmentalized cilia biogenesis', *Cell*. doi: 10.1016/S0092-8674(04)00412-X.

Baas, D. *et al.* (2006) 'A deficiency in RFX3 causes hydrocephalus associated with abnormal differentiation of ependymal cells', *European Journal of Neuroscience*. doi: 10.1111/j.1460-9568.2006.05002.x.

Badano, J. L. *et al.* (2006) 'The Ciliopathies: An Emerging Class of Human Genetic Disorders', *Annual Review of Genomics and Human Genetics*. doi: 10.1146/annurev.genom.7.080505.115610.

Baltz, J. M., Williams, P. O. and Cone, R. A. (1990) 'Dense fibers protect mammalian sperm against damage', *Biology of reproduction*. doi: 10.1095/biolreprod43.3.485.

Bangs, F. and Anderson, K. V. (2017) 'Primary cilia and Mammalian Hedgehog signaling', *Cold Spring Harbor Perspectives in Biology*. doi: 10.1101/cshperspect.a028175.

Barratt, K. S., Glanville-Jones, H. C. and Arkell, R. M. (2014) 'The Zic2 gene directs the formation and function of node cilia to control cardiac situs', *Genesis*. doi: 10.1002/dvg.22767.

Bartlett, J., Fischer, A. and McCray, P. B. (2008) 'Innate immune functions of the airway epithelium', *Contributions to Microbiology*. doi: 10.1159/000136349.

Bartoloni, L. *et al.* (2002) 'Mutations in the DNAH11 (axonemal heavy chain dynein type 11) gene cause one form of situs inversus totalis and most likely primary ciliary dyskinesia.', *Proceedings of the National Academy of Sciences of the United States of America*, 99(16), pp. 10282–6. doi: 10.1073/pnas.152337699.

Becker-Heck, A. *et al.* (2011) 'The coiled-coil domain containing protein CCDC40 is essential for motile cilia function and left-right axis formation.', *Nature genetics*, 43(1), pp. 79–84. doi: 10.1038/ng.727.

Beckers, A. *et al.* (2007) 'The mouse homeobox gene Noto regulates node morphogenesis, notochordal ciliogenesis, and left right patterning.', *Proceedings of the National Academy of Sciences of the United States of America*. National Academy of Sciences, 104(40), pp. 15765–70. doi: 10.1073/pnas.0704344104.

Behan, L. *et al.* (2016) 'PICADAR: A diagnostic predictive tool for primary ciliary dyskinesia', *European Respiratory Journal*, 47(4), pp. 1103–1112. doi: 10.1183/13993003.01551-2015.

Bellve, A. R. *et al.* (1977) 'Spermatogenic cells of the prepuberal mouse. Isolation and morphological characterization', *Journal of Cell Biology*. doi: 10.1083/jcb.74.1.68.

Belmonte, J. C. I. *et al.* (1998) 'Pitx2 determines left|[ndash]|right asymmetry of internal organs in vertebrates', *Nature*. Nature Publishing Group, 394(6693), pp. 545–551. doi: 10.1038/29004.

Belyi, V. A. *et al.* (2010) 'The origins and evolution of the p53 family of genes.', *Cold Spring Harbor perspectives in biology*. doi: 10.1101/cshperspect.a001198.

Benadiba, C. *et al.* (2012) 'The Ciliogenic Transcription Factor RFX3 regulates early midline distribution of guidepost neurons required for corpus callosum development', *PLoS Genetics*. doi: 10.1371/journal.pgen.1002606.

Benmerah, A. (2013) 'The ciliary pocket', *Current Opinion in Cell Biology*. doi: 10.1016/j.ceb.2012.10.011.

Berbari, N. F. *et al.* (2008) 'Bardet: Biedl Syndrome Proteins Are Required for the Localization of G Protein-Coupled Receptors to Primary Cilia', *Proceedings of the National Academy of Sciences of the United States of America*. doi: 10.2307/25461402.

Berezin, C. *et al.* (2004) 'ConSeq: The identification of functionally and structurally important residues in protein sequences', *Bioinformatics*. doi: 10.1093/bioinformatics/bth070.

Berman, S. A. *et al.* (2003) 'A novel MAP kinase regulates flagellar length in Chlamydomonas', *Current Biology*. doi: 10.1016/S0960-9822(03)00415-9.

Bershteyn, M. *et al.* (2010) 'MIM and cortactin antagonism regulates ciliogenesis and hedgehog signaling', *Developmental Cell*. doi: 10.1016/j.devcel.2010.07.009.

Besschetnova, T. Y. *et al.* (2010) 'Identification of Signaling Pathways Regulating Primary Cilium Length and Flow-Mediated Adaptation', *Current Biology*. doi: 10.1016/j.cub.2009.11.072.

Bigelow, H. R. *et al.* (2004) 'Predicting transmembrane beta-barrels in proteomes', *Nucleic Acids Research*. doi: 10.1093/nar/gkh580.

Bisgrove, B. W. *et al.* (2012) 'RFX2 is essential in the ciliated organ of asymmetry and an RFX2 transgene identifies a population of ciliated cells sufficient for fluid flow.', *Developmental biology*. NIH Public Access, 363(1), pp. 166–78. doi: 10.1016/j.ydbio.2011.12.030.

Blackshear, P. J. *et al.* (2003) 'Graded phenotypic response to partial and complete deficiency of a brain-specific transcript variant of the winged helix transcription factor RFX4', *Development*. doi: 10.1242/dev.00661.

Blanchoin, L. *et al.* (2014) 'ACTIN DYNAMICS, ARCHITECTURE, AND MECHANICS IN CELL MOTILITY', *Physiological Reviews*. doi: 10.1152/physrev.00018.2013.

Blatt, E. N. *et al.* (1999) 'Forkhead transcription factor HFH-4 expression is temporally related to ciliogenesis', *American Journal of Respiratory Cell and Molecular Biology*. doi: 10.1165/ajrcmb.21.2.3691.

Blyth, M. and Wellesley, D. (2008) 'Ectopic pregnancy in primary ciliary dyskinesia', *Journal of Obstetrics and Gynaecology*. doi: 10.1080/01443610802058742.

Bonnafe, E. *et al.* (2004) 'The transcription factor RFX3 directs nodal cilium development and left-right asymmetry specification.', *Molecular and cellular biology*. American Society for Microbiology (ASM), 24(10), pp. 4417–27. Available at: http://www.ncbi.nlm.nih.gov/pubmed/15121860 (Accessed: 26 August 2016).

Bonser, L. R. *et al.* (2015) 'The endoplasmic reticulum resident protein AGR3: Required for regulation of ciliary beat frequency in the airway', *American Journal of Respiratory Cell and Molecular Biology*. doi: 10.1165/rcmb.2014-0318OC.

Boon, M *et al.* (2014) 'Mcidas mutations cause ciliary aplasia', *Pediatric Pulmonology*.

Boon, Mieke *et al.* (2014) 'MCIDAS mutations result in a mucociliary clearance disorder with reduced generation of multiple motile cilia.', *Nature communications*, 5, p. 4418. doi: 10.1038/ncomms5418.

Borg, C. L. *et al.* (2009) 'Phenotyping male infertility in the mouse: How to get the most out of a "non-performer"', *Human Reproduction Update*. doi: 10.1093/humupd/dmp032.

Boucher, R. C. (2007) 'Airway Surface Dehydration in Cystic Fibrosis: Pathogenesis and Therapy', *Annual Review of Medicine*. doi: 10.1146/annurev.med.58.071905.105316.

Brazelton, W. J. *et al.* (2001) 'The bld1 mutation identifies the Chlamydomonas osm-6 homolog as a gene required for flagellar assembly', *Current Biology*. doi: 10.1016/S0960-9822(01)00485-7.

Brennan, J., Norris, D. P. and Robertson, E. J. (2002) 'Nodal activity in the node governs left-right asymmetry', *Genes & Development*. Cold Spring Harbor Laboratory Press, 16(18), pp. 2339–2344. doi: 10.1101/gad.1016202.

Brokaw, C. J. (1994) 'Control of flagellar bending: A new agenda based on dynein diversity', *Cell Motility and the Cytoskeleton*. doi: 10.1002/cm.970280303.

Brokaw, C. J. and Kamiya, R. (1987) 'Bending patterns of Chlamydomonas flagella: IV. Mutants with defects in inner and outer dynein arms indicate differences in dynein arm function.', *Cell motility and the cytoskeleton*. doi: 10.1002/cm.970080110.

Brooks, E. R. and Wallingford, J. B. (2014) 'Multiciliated Cells', *Current Biology*. doi: 10.1016/j.cub.2014.08.047.

Brown, S. D. M., Hancock, J. M. and Gates, H. (2006) 'Understanding mammalian genetic systems: The challenge of phenotyping in the mouse', *PLoS Genetics*. doi: 10.1371/journal.pgen.0020118.

Brückner, A. *et al.* (2009) 'Yeast two-hybrid, a powerful tool for systems biology', *International Journal of Molecular Sciences*. doi: 10.3390/ijms10062763.

Bruneau, B. G. *et al.* (1999) 'Chamber-specific cardiac expression of Tbx5 and heart defects in Holt- Oram syndrome', *Developmental Biology*. doi: 10.1006/dbio.1999.9298.

Bryant, C. D. (2011) 'The blessings and curses of C57BL/6 substrains in mouse genetic studies', *Annals of the New York Academy of Sciences*. doi: 10.1111/j.1749-6632.2011.06325.x.

Budny, B. *et al.* (2006) 'A novel X-linked recessive mental retardation syndrome comprising macrocephaly and ciliary dysfunction is allelic to oral-facial-digital type I syndrome', *Human Genetics*. doi: 10.1007/s00439-006-0210-5.

Bui, K. H. *et al.* (2012) 'Polarity and asymmetry in the arrangement of dynein and related structures in the Chlamydomonas axoneme', *Journal of Cell Biology*. doi: 10.1083/jcb.201201120.

Burghoorn, J. *et al.* (2012) 'The in vivo dissection of direct RFX-target gene promoters in C. elegans reveals a novel cis-regulatory element, the C-box', *Developmental Biology*. doi: 10.1016/j.ydbio.2012.05.033.

Burgoyne, P. S. (1987) 'The role of the mammalian Y chromosome in spermatogenesis.', *Development (Cambridge, England)*, 101 Suppl, pp. 133–41. Available at: http://www.ncbi.nlm.nih.gov/pubmed/3503711.

Bustamante-Marin, X. M. and Ostrowski, L. E. (2017) 'Cilia and mucociliary clearance', *Cold Spring Harbor Perspectives in Biology*. doi: 10.1101/cshperspect.a028241.

Button, B. *et al.* (2012) 'A periciliary brush promotes the lung health by separating the mucus layer from airway epithelia', *Science*. doi: 10.1126/science.1223012.

Canterini, S. *et al.* (2017) 'Shortened primary cilium length and dysregulated Sonic hedgehog signaling in Niemann-Pick C1 disease', *Human Molecular Genetics*. doi: 10.1093/hmg/ddx118.

Cao, J. *et al.* (2012) 'MiR-129-3p controls cilia assembly by regulating CP110 and actin dynamics', *Nature Cell Biology*. doi: 10.1038/ncb2512.

Caron, A., Xu, X. and Lin, X. (2012) 'Wnt/ -catenin signaling directly regulates Foxj1 expression and ciliogenesis in zebrafish Kupffer's vesicle', *Development*. doi: 10.1242/dev.071746.

Cartwright, J. H. E. *et al.* (2008) 'Fluid dynamics of nodal flow and left-right patterning in development', *Developmental Dynamics*. Wiley-Liss, Inc., 237(12), pp. 3477–3490. doi: 10.1002/dvdy.21672.

Cartwright, J. H. E., Piro, O. and Tuval, I. (2004) 'Fluid-dynamical basis of the embryonic development of left-right asymmetry in vertebrates.', *Proceedings of the National Academy of Sciences of the United States of America*. National Academy of Sciences, 101(19), pp. 7234–9. doi: 10.1073/pnas.0402001101.

Casey, J. P. *et al.* (2015) 'A case report of primary ciliary dyskinesia, laterality defects and developmental delay caused by the co-existence of a single

gene and chromosome disorder', *BMC Medical Genetics*. doi: 10.1186/s12881-015-0192-z.

Castleman, V. H. *et al.* (2008) 'Mutations in radial spoke head protein genes RSPH9 and RSPH4A cause primary ciliary dyskinesia with central-microtubular-pair abnormalities', *American Journal of Human Genetics*, 84(2), pp. 197–209. doi: 10.1016/j.ajhg.2009.01.011.

Cavalier-Smith, T. (2002) 'The phagotrophic origin of eukaryotes and phylogenetic classification on protozoa', *International Journal of Systematic and Evolutionary Microbiology*. doi: 10.1099/00207713-52-2-297.

Cavalier-Smith, T. and Chao, E. E. Y. (2003) 'Phylogeny of choanozoa, apusozoa, and other protozoa and early eukaryote megaevolution', *Journal of Molecular Evolution*. doi: 10.1007/s00239-002-2424-z.

Celniker, G. *et al.* (2013) 'ConSurf: Using evolutionary data to raise testable hypotheses about protein function', *Israel Journal of Chemistry*. doi: 10.1002/ijch.201200096.

Ceroni, A. *et al.* (2006) 'Disulfind: A disulfide bonding state and cysteine connectivity prediction server', *Nucleic Acids Research*. doi: 10.1093/nar/gkl266.

Chen, J. *et al.* (1998) 'Mutation of the mouse hepatocyte nuclear factor/forkhead homologue 4 gene results in an absence of cilia and random left-right asymmetry.', *The Journal of clinical investigation*. American Society for Clinical Investigation, 102(6), pp. 1077–82. doi: 10.1172/JCI4786.

Choksi, S. P. *et al.* (2014) 'Switching on cilia: transcriptional networks regulating ciliogenesis.', *Development (Cambridge, England)*, 141(7), pp. 1427–41. doi: 10.1242/dev.074666.

Christensen, S. T. *et al.* (2012) 'Primary cilia and coordination of receptor tyrosine kinase (RTK) signalling', *Journal of Pathology*. doi: 10.1002/path.3004.

Chu, J. S., Baillie, D. L. and Chen, N. (2010) 'Convergent evolution of RFX transcription factors and ciliary genes predated the origin of metazoans', *BMC Evolutionary Biology*. doi: 10.1186/1471-2148-10-130.

Chung, M. I. *et al.* (2012) 'RFX2 is broadly required for ciliogenesis during vertebrate development', *Developmental Biology*. doi: 10.1016/j.ydbio.2011.12.029.

Clevidence, D. E. *et al.* (1993) 'Identification of nine tissue-specific transcription factors of the hepatocyte nuclear factor 3/forkhead DNA-binding-domain family.', *Proceedings of the National Academy of Sciences of the United States of America*. doi: 10.1073/pnas.90.9.3948.

Clevidence, D. E. *et al.* (1994) 'Members of the HNF-3/forkhead family of transcription factors exhibit distinct cellular expression patterns in lung and regulate the surfactant protein B promoter', *Developmental Biology*. doi: 10.1006/dbio.1994.1307.

Coghill, I. D. *et al.* (2003) 'FHL3 is an actin-binding protein that regulates α-actinin-mediated actin bundling. FHL3 localizes to actin stress fibers and enhances cell spreading and stress fiber disassembly', *Journal of Biological Chemistry*. doi: 10.1074/jbc.M213259200.

Cole, D. G. *et al.* (1993) 'Novel heterotrimeric kinesin-related protein purified from sea urchin eggs', *Nature*. doi: 10.1038/366268a0.

Cole, D. G. *et al.* (1998) 'Chlamydomonas kinesin-II-dependent intraflagellar transport (IFT): IFT particles contain proteins required for ciliary assembly in Caenorhabditis elegans sensory neurons.', *The Journal of cell biology*, 141(4), pp. 993–1008. Available at: http://www.ncbi.nlm.nih.gov/pubmed/9585417 (Accessed: 20 October 2016).

Costa, M. W. *et al.* (2011) 'Complex SUMO-1 regulation of cardiac transcription factor NKX2-5', *PLoS ONE*. doi: 10.1371/journal.pone.0024812.

Courtheoux, T. *et al.* (2018) 'Aurora A kinase activity is required to maintain an active spindle assembly checkpoint during prometaphase', *Journal of*

Cell Science. doi: 10.1242/jcs.191353.

Criekinge, W. and Beyaert, R. (1999) 'Yeast two-hybrid: State of the art', *Biological Procedures Online*. doi: 10.1251/bpo16.

Cutting, G. R. (2015) 'Cystic fibrosis genetics: From molecular understanding to clinical application', *Nature Reviews Genetics*. doi: 10.1038/nrg3849.

Daniels, M. L. A. *et al.* (2013) 'Founder mutation in RSPH4A identified in patients of hispanic descent with primary ciliary dyskinesia', *Human Mutation*, 34(10), pp. 1352–1356. doi: 10.1002/humu.22371.

Davenport, J. R. *et al.* (2007) 'Disruption of Intraflagellar Transport in Adult Mice Leads to Obesity and Slow-Onset Cystic Kidney Disease', *Current Biology*. doi: 10.1016/j.cub.2007.08.034.

Davy, B. E. and Robinson, M. L. (2003) 'Congenital hydrocephalus in hy3 mice is caused by a frameshift mutation in Hydin, a large novel gene.', *Human molecular genetics*, 12(10), pp. 1163–70. Available at: http://www.ncbi.nlm.nih.gov/pubmed/12719380 (Accessed: 20 October 2016).

Deane, J. A. *et al.* (2001) 'Localization of intraflagellar transport protein IFT52 identifies basal body transitional fibers as the docking site for IFT particles', *Current Biology*. doi: 10.1016/S0960-9822(01)00484-5.

Delling, M. *et al.* (2016) 'Primary cilia are not calcium-responsive mechanosensors', *Nature*. Nature Research, 531(7596), pp. 656–660. doi: 10.1038/nature17426.

De Diego, A. S. *et al.* (2014) 'Dido3-dependent HDAC6 targeting controls cilium size', *Nature Communications*. doi: 10.1038/ncomms4500.

Dinnes, D. L. M. *et al.* (2016) 'Human macrophage cathepsin B-mediated C-terminal cleavage of apolipoprotein A-I at Ser228 severely impairs antiatherogenic capacity', *FASEB Journal*. doi: 10.1096/fj.201600508R.

Dong, F. *et al.* (2014) 'Pih1d3 is required for cytoplasmic preassembly of axonemal dynein in mouse sperm', *Journal of Cell Biology*, 204(2), pp. 203–213. doi: 10.1083/jcb.201304076.

Dosztányi, Z. *et al.* (2005) 'IUPred: web server for the prediction of intrinsically unstructured regions of proteins based on estimated energy content.', *Bioinformatics (Oxford, England)*. Oxford University Press, 21(16), pp. 3433–4. doi: 10.1093/bioinformatics/bti541.

Dosztányi, Z., Mészáros, B. and Simon, I. (2009) 'ANCHOR: web server for predicting protein binding regions in disordered proteins.', *Bioinformatics (Oxford, England)*. Oxford University Press, 25(20), pp. 2745–6. doi: 10.1093/bioinformatics/btp518.

Dougherty, G. W. *et al.* (2016) 'DNAH11 localization in the proximal region of respiratory cilia defines distinct outer dynein arm complexes', *American Journal of Respiratory Cell and Molecular Biology*. doi: 10.1165/rcmb.2015-0353OC.

Driscoll, J. A. *et al.* (2008) 'Autosomal dominant polycystic kidney disease is associated with an increased prevalence of radiographic bronchiectasis', *Chest*. doi: 10.1378/chest.07-2147.

Duriez, B. *et al.* (2007) 'A common variant in combination with a nonsense mutation in a member of the thioredoxin family causes primary ciliary dyskinesia.', *Proceedings of the National Academy of Sciences of the United States of America*, 104(9), pp. 3336–41. doi: 10.1073/pnas.0611405104.

Dykes, I. M. *et al.* (2018) 'A Requirement for Zic2 in the regulation of nodal expression underlies the establishment of left-sided identity', *Scientific Reports*. doi: 10.1038/s41598-018-28714-1.

Eddy, E. M. (2002) 'Male Germ Cell Gene Expression', *Recent Progress in Hormone Research*. doi: 10.1210/rp.57.1.103.

Eddy, E. M., Toshimori, K. and O'Brien, D. A. (2003) 'Fibrous sheath of

mammalian spermatozoa', *Microscopy Research and Technique*. doi: 10.1140/epjst/e2013-01891-2.

Edelbusch, C. *et al.* (2017) 'Mutation of serine/threonine protein kinase 36 (STK36) causes primary ciliary dyskinesia with a central pair defect', *Human Mutation*, 38(8), pp. 964–969. doi: 10.1002/humu.23261.

Efimenko, E. *et al.* (2006) 'Caenorhabditis elegans DYF-2, an orthologue of human WDR19, is a component of the intraflagellar transport machinery in sensory cilia', *Molecular biology of the cell*. doi: 10.1091/mbc.E06-04-0260.

El Khouri, E. *et al.* (2016) *Mutations in DNAJB13, Encoding an HSP40 Family Member, Cause Primary Ciliary Dyskinesia and Male Infertility*, *The American Journal of Human Genetics*. doi: 10.1016/j.ajhg.2016.06.022.

Ezzati, M. *et al.* (2014) 'Tubal transport of gametes and embryos: a review of physiology and pathophysiology', *Journal of Assisted Reproduction and Genetics*. doi: 10.1007/s10815-014-0309-x.

Fahrenkrog, B. and Aebi, U. (2003) 'The nuclear pore complex: Nucleocytoplasmic transport and beyond', *Nature Reviews Molecular Cell Biology*. doi: 10.1038/nrm1230.

Farina, F. *et al.* (2016) 'The centrosome is an actin-organizing centre', *Nature Cell Biology*. doi: 10.1038/ncb3285.

Farley, H. *et al.* (2018) 'Proceedings of the 3rd BEAT-PCD Conference and 4th PCD Training School', *BMC Proceedings*, 12(Suppl. 16), pp. 1–15.

Fassad, M. R., Shoemark, A., le Borgne, P., *et al.* (2018) 'C11orf70 Mutations Disrupting the Intraflagellar Transport-Dependent Assembly of Multiple Axonemal Dyneins Cause Primary Ciliary Dyskinesia', *American Journal of Human Genetics*. doi: 10.1016/j.ajhg.2018.03.024.

Fassad, M. R., Shoemark, A., Legendre, M., *et al.* (2018) 'Mutations in Outer Dynein Arm Heavy Chain DNAH9 Cause Motile Cilia Defects and Situs Inversus', *The American Journal of Human Genetics*. doi: 10.1016/j.ajhg.2018.10.016.

Feng, C., Xu, W. and Zuo, Z. (2009) 'Knockout of the regulatory factor X1 gene leads to early embryonic lethality', *Biochemical and Biophysical Research Communications*. doi: 10.1016/j.bbrc.2009.06.111.

Field, M. C. and Carrington, M. (2009) 'The trypanosome flagellar pocket', *Nature Reviews Microbiology*. doi: 10.1038/nrmicro2221.

Field, S. *et al.* (2011) 'Pkd1l1 establishes left-right asymmetry and physically interacts with Pkd2.', *Development (Cambridge, England)*. Oxford University Press for The Company of Biologists Limited, 138(6), pp. 1131–42. doi: 10.1242/dev.058149.

Fields, S. and Song, O. K. (1989) 'A novel genetic system to detect protein-protein interactions', *Nature*. doi: 10.1038/340245a0.

Finn, R., Evans, C. C. and Lee, L. (2014) 'Strain-dependent brain defects in mouse models of primary ciliary dyskinesia with mutations in Pcdp1 and Spef2', *Neuroscience*. doi: 10.1016/j.neuroscience.2014.07.029.

Fliegauf, M., Benzing, T. and Omran, H. (2007) 'When cilia go bad: Cilia defects and ciliopathies', *Nature Reviews Molecular Cell Biology*, pp. 880–893. doi: 10.1038/nrm2278.

Follit, J. A. (2006) 'The Intraflagellar Transport Protein IFT20 Is Associated with the Golgi Complex and Is Required for Cilia Assembly', *Molecular Biology of the Cell*. doi: 10.1091/mbc.E06-02-0133.

Follit, J. A. *et al.* (2009) 'Characterization of mouse IFT complex B', *Cell Motility and the Cytoskeleton*. doi: 10.1002/cm.20346.

Follit, J. A. *et al.* (2010) 'The cytoplasmic tail of fibrocystin contains a ciliary targeting sequence', *Journal of Cell Biology*. doi: 10.1083/jcb.200910096.

Francis, R. J. B. *et al.* (2009) 'Initiation and maturation of cilia-generated flow in newborn and postnatal mouse airway', *AJP: Lung Cellular and Molecular*

Physiology. doi: 10.1152/ajplung.00001.2009.

Francis, R. J. B. *et al.* (2012) 'Congenital heart disease and the specification of left-right asymmetry', *American Journal of Physiology-Heart and Circulatory Physiology*. doi: 10.1152/ajpheart.01118.2011.

Fu, J., Hagan, I. M. and Glover, D. M. (2015) 'The centrosome and its duplication cycle', *Cold Spring Harbor perspectives in biology*, p. a015800. doi: 10.1101/cshperspect.a015800.

Fujiwara, M., Ishihara, T. and Katsura, I. (1999) 'A novel WD40 protein, CHE-2, acts cell-autonomously in the formation of C. elegans sensory cilia.', *Development (Cambridge, England)*. doi: 10.1002/cne.901980305.

Gade, E. J. *et al.* (2014) 'Asthma affects time to pregnancy and fertility: A register-based twin study', in *European Respiratory Journal*. doi: 10.1183/09031936.00148713.

Gajiwala, K. S. *et al.* (2000) 'Structure of the winged-helix protein hRFX1 reveals a new mode of DNA binding', *Nature*. doi: 10.1038/35002634.

Ganesan, S., Comstock, A. T. and Sajjan, U. S. (2013) 'Barrier function of airway tract epithelium', *Tissue Barriers*. doi: 10.4161/tisb.24997.

Geneva, I. I., Tan, H. Y. and Calvert, P. D. (2016) 'Untangling ciliary access and enrichment of two rhodopsin-like receptors using quantitative fluorescence microscopy reveals cell-specific sorting pathways.', *Molecular biology of the cell*. doi: 10.1091/mbc.E16-07-0549.

Geng, L. (2006) 'Polycystin-2 traffics to cilia independently of polycystin-1 by using an N-terminal RVxP motif', *Journal of Cell Science*. doi: 10.1242/jcs.02818.

Gibbons, B. H. and Gibbons, I. R. (1973) 'The effect of partial extraction of dynein arms on the movement of reactivated sea-urchin sperm.', *Journal of cell science*.

Gibbons, I. (1963) 'STUDIES ON THE PROTEIN COMPONENTS OF CILIA FROM TETRAHYMENA PYRIFORMIS', *Proceedings of the National Academy of Sciences*, 50(5), pp. 1002–1010.

Girod De Bentzmann, S. *et al.* (1993) 'Distearoyl phosphatidylglycerol liposomes improve surface and transport properties of CF mucus', *European Respiratory Journal*.

Gó Mez-Orte, E. *et al.* (2013) 'Multiple functions of the noncanonical Wnt pathway', *Trends in Genetics*. doi: 10.1016/j.tig.2013.06.003.

Godinho, S. a. *et al.* (2012) 'Centriole maturation requires regulated Plk1 activity during two consecutive cell cycles', *Nature cell biology*. doi: 10.1083/jcb.201407087.

Goetz, S. C. and Anderson, K. V. (2010) 'The primary cilium: A signalling centre during vertebrate development', *Nature Reviews Genetics*. doi: 10.1038/nrg2774.

Goggolidou, P. (2014) 'Wnt and planar cell polarity signaling in cystic renal disease', *Organogenesis*. doi: 10.4161/org.26766.

Gonçalves, J. and Pelletier, L. (2017) 'The Ciliary Transition Zone: Finding the Pieces and Assembling the Gate', *Molecules and Cells*. doi: 10.14348/molcells.2017.0054.

Goodenough, U. W. and Heuser, J. E. (1982) 'Substructure of the outer dynein arm', *Journal of Cell Biology*. doi: 10.1083/jcb.95.3.798.

Goodenough, U. W. and Heuser, J. E. (1985) 'Substructure of inner dynein arms, radial spokes, and the central pair/projection complex of cilia and flagella', *Journal of Cell Biology*. doi: 10.1083/jcb.100.6.2008.

Goodson, S. G. *et al.* (2011) 'Classification of mouse sperm motility patterns using an automated multiclass support vector machines model.', *Biology of reproduction*. doi: 10.1095/biolreprod.110.088989.

Görlich, D. and Kutay, U. (1999) 'Transport between the cell nucleus and

the cytoplasm.', *Annual review of cell and developmental biology*. doi: 10.1146/annurev.cellbio.15.1.607.

Graser, S. *et al.* (2007) 'Cep164, a novel centriole appendage protein required for primary cilium formation', *Journal of Cell Biology*. doi: 10.1083/jcb.200707181.

Greenstone, M. A. *et al.* (1984) 'Hydrocephalus and Primary Ciliary Dyskinesia.', *Archives of disease in childhood*. doi: 10.1177/0883073811429856.

Grimes, Daniel T. *et al.* (2016) 'Genetic Analysis Reveals a Hierarchy of Interactions between Polycystin-Encoding Genes and Genes Controlling Cilia Function during Left-Right Determination', *PLOS Genetics*. Edited by G. S. Barsh. Public Library of Science, 12(6), p. e1006070. doi: 10.1371/journal.pgen.1006070.

Grimes, D. T. *et al.* (2016) 'Zebrafish models of idiopathic scoliosis link cerebrospinal fluid flow defects to spine curvature', *Science*. doi: 10.1126/science.aaf6419.

Grimes, D. T. and Burdine, R. D. (2017) 'Left–Right Patterning: Breaking Symmetry to Asymmetric Morphogenesis', *Trends in Genetics*. doi: 10.1016/j.tig.2017.06.004.

Gruenert, D. C., Finkbeiner, W. E. and Widdicombe, J. H. (1995) 'Culture and transformation of human airway epithelial cells.', *The American journal of physiology*.

Ha, S. *et al.* (2016) 'Mutations in Dnaaf1 and Lrrc48 Cause Hydrocephalus, Laterality Defects, and Sinusitis in Mice.', *G3 (Bethesda, Md.)*, 6(8), pp. 2479–87. doi: 10.1534/g3.116.030791.

Habermacher, G. and Sale, W. S. (1997) 'Regulation of flagellar dynein by phosphorylation of a 138-kD inner ann dynein intermediate chain', *Journal of Cell Biology*. doi: 10.1083/jcb.136.1.167.

Hackett, B. P. *et al.* (1995) 'Primary structure of hepatocyte nuclear factor/forkhead homologue 4 and characterization of gene expression in the developing respiratory and reproductive epithelium.', *Proceedings of the National Academy of Sciences of the United States of America*. doi: 10.1073/pnas.92.10.4249.

Haitchi, H. M. *et al.* (2009) 'Chronological expression of Ciliated Bronchial Epithelium 1 during pulmonary development', *European Respiratory Journal*. doi: 10.1183/09031936.00157108.

Hamed, R. and Fiegel, J. (2014) 'Synthetic tracheal mucus with native rheological and surface tension properties', *Journal of Biomedical Materials Research - Part A*. doi: 10.1002/jbm.a.34851.

Harashima, H., Dissmeyer, N. and Schnittger, A. (2013) 'Cell cycle control across the eukaryotic kingdom', *Trends in Cell Biology*. doi: 10.1016/j.tcb.2013.03.002.

Harris, P. C. and Torres, V. E. (2009) 'Polycystic Kidney Disease', *Annual Review of Medicine*. doi: 10.1146/annurev.med.60.101707.125712.

Haycraft, C. J. *et al.* (2003) 'Identification of CHE-13, a novel intraflagellar transport protein required for cilia formation', *Experimental Cell Research*. doi: 10.1016/S0014-4827(02)00089-7.

Hess, R. A. and Moore, B. J. (1993) 'Histological Methods for Evaluation of the Testis', in *Male Reproductive Toxicology*. doi: 10.1016/B978-0-12-461207-5.50008-0.

Heuser, T. *et al.* (2009) 'The dynein regulatory complex is the nexin link and a major regulatory node in cilia and flagella', *Journal of Cell Biology*. doi: 10.1083/jcb.200908067.

Hildebrandt, F. *et al.* (1997) 'A novel gene encoding an SH3 domain protein is mutated in nephronophthisis type 1', *Nature Genetics*. doi: 10.1038/ng1097-149.

Hirano, Y. *et al.* (2001) 'Relationships between sperm motility characteristics assessed by the computer-aided sperm analysis (CASA) and fertilization rates in vitro.', *Journal of assisted reproduction and genetics*. doi: 10.1023/A:1009420432234.

Hirokawa, N., Tanaka, Y. and Okada, Y. (2012) 'Cilia, KIF3 molecular motor and nodal flow', *Current Opinion in Cell Biology*, 24(1), pp. 31–39. doi: 10.1016/j.ceb.2012.01.002.

Hjeij, R. *et al.* (2013) 'ARMC4 mutations cause primary ciliary dyskinesia with randomization of left/right body asymmetry.', *American journal of human genetics*, 93(2), pp. 357–67. doi: 10.1016/j.ajhg.2013.06.009.

Hjeij, R. *et al.* (2014) 'CCDC151 mutations cause primary ciliary dyskinesia by disruption of the outer dynein arm docking complex formation', *American Journal of Human Genetics*, 95(3), pp. 257–274. doi: 10.1016/j.ajhg.2014.08.005.

Höben, I. M. *et al.* (2018) 'Mutations in C11orf70 Cause Primary Ciliary Dyskinesia with Randomization of Left/Right Body Asymmetry Due to Defects of Outer and Inner Dynein Arms', *American Journal of Human Genetics*. doi: 10.1016/j.ajhg.2018.03.025.

Horani, A. *et al.* (2012) 'Whole-exome capture and sequencing identifies HEATR2 mutation as a cause of primary ciliary dyskinesia.', *American journal of human genetics*, 91(4), pp. 685–93. doi: 10.1016/j.ajhg.2012.08.022.

Horani, A. *et al.* (2013) 'CCDC65 mutation causes primary ciliary dyskinesia with normal ultrastructure and hyperkinetic cilia.', *PloS one*, 8(8), p. e72299. doi: 10.1371/journal.pone.0072299.

Horani, A. *et al.* (2016) *Genetics and biology of primary ciliary dyskinesia*, *Paediatric Respiratory Reviews*. doi: 10.1016/j.prrv.2015.09.001.

Horani, A. and Ferkol, T. W. (2018) 'Advances in the Genetics of Primary Ciliary Dyskinesia: Clinical Implications', *Chest*. doi: 10.1016/j.chest.2018.05.007.

Van Der Horst, G., Maree, L. and Du Plessis, S. S. (2018) 'Current perspectives of CASA applications in diverse mammalian spermatozoa', *Reproduction, Fertility and Development*. doi: 10.1071/RD17468.

Horvath, G. C., Kistler, W. S. and Kistler, M. K. (2004) 'RFX2 Is a Potential Transcriptional Regulatory Factor for Histone H1t and Other Genes Expressed During the Meiotic Phase of Spermatogenesis1', *Biology of Reproduction*. doi: 10.1095/biolreprod.104.032268.

Horváth, J. *et al.* (2005) 'Identification and analysis of axonemal dynein light chain 1 in primary ciliary dyskinesia patients.', *American journal of respiratory cell and molecular biology*, 33(1), pp. 41–7. doi: 10.1165/rcmb.2004-0335OC.

Hou, Y. (2004) 'A Dynein Light Intermediate Chain, D1bLIC, Is Required for Retrograde Intraflagellar Transport', *Molecular Biology of the Cell*. doi: 10.1091/mbc.E04-05-0377.

Hsiao, Y. C., Tuz, K. and Ferland, R. J. (2012) 'Trafficking in and to the primary cilium', *Cilia*. doi: 10.1186/2046-2530-1-4.

Huang, P. and Schier, A. F. (2009) 'Dampened Hedgehog signaling but normal Wnt signaling in zebrafish without cilia', *Development*. doi: 10.1242/dev.041343.

Huangfu, D. *et al.* (2003) 'Hedgehog signalling in the mouse requires intraflagellar transport proteins', *Nature*. doi: 10.1038/nature02061.

Huangfu, D. and Anderson, K. V. (2005) 'Cilia and Hedgehog responsiveness in the mouse', *Proceedings of the National Academy of Sciences*. doi: 10.1073/pnas.0505328102.

Huizar, R. *et al.* (2017) 'A phase separated organelle at the root of motile ciliopathy', *bioRxiv*. doi: 10.1101/213793.

Huizar, R. L. *et al.* (2018) 'A liquid-like organelle at the root of motile

ciliopathy', *eLife*. doi: 10.7554/eLife.38497.

Ibañez-Tallon, I., Gorokhova, S. and Heintz, N. (2002) 'Loss of function of axonemal dynein Mdnah5 causes primary ciliary dyskinesia and hydrocephalus.', *Human molecular genetics*, 11(6), pp. 715–21. Available at: http://www.ncbi.nlm.nih.gov/pubmed/11912187 (Accessed: 20 October 2016).

IMPC (2018) *IMPC*. Available at: http://www.mousephenotype.org/ (Accessed: 7 September 2018).

Inouye, S. *et al.* (2003) 'Activation of heat shock genes is not necessary for protection by heat shock transcription factor 1 against cell death due to a single exposure to high temperatures.', *Molecular and cellular biology*. doi: 10.1128/MCB.23.16.5882.

Iomini, C. *et al.* (2001) 'Protein particles in Chlamydomonas flagella undergo a transport cycle consisting of four phases', *Journal of Cell Biology*. doi: 10.1083/jcb.153.1.13.

Iomini, C. *et al.* (2009) 'Retrograde intraflagellar transport mutants identify complex A proteins with multiple genetic interactions in Chlamydomonas reinhardtii', *Genetics*. doi: 10.1534/genetics.109.101915.

De Iongh, R. U. and Rutland, J. (1995) 'Ciliary defects in healthy subjects, bronchiectasis, and primary ciliary dyskinesia', *American Journal of Respiratory and Critical Care Medicine*. doi: 10.1164/ajrccm.151.5.7735615.

Ishikawa, H. *et al.* (2005) 'Odf2-deficient mother centrioles lack distal/subdistal appendages and the ability to generate primary cilia', *Nature Cell Biology*. doi: 10.1038/ncb1251.

Ishikawa, H. and Marshall, W. F. (2011) 'Ciliogenesis: building the cell's antenna', *Nat Rev Mol Cell Biol*, 12(4), pp. 222–234. doi: 10.1038/nrm3085.

Itsuki, Y. *et al.* (2008) 'Molecular cloning of novel Monad binding protein containing tetratricopeptide repeat domains', *FEBS Letters*. doi: 10.1016/j.febslet.2008.05.041.

Iwama, A. *et al.* (1999) 'Dimeric RFX Proteins Contribute to the Activity and Lineage Specificity of the Interleukin-5 Receptor ␣ Promoter through Activation and Repression Domains', *Molecular and cellular biology*. doi: 10.1128/MCB.19.6.3940.

Jaffe, K. M. *et al.* (2016) 'C21orf59/kurly Controls Both Cilia Motility and Polarization', *Cell Reports*, 14(8), pp. 1841–1849. doi: 10.1016/j.celrep.2016.01.069.

Janke, C. (2014) 'The tubulin code: Molecular components, readout mechanisms, functions', *Journal of Cell Biology*. doi: 10.1083/jcb.201406055.

Jeanson, L., Copin, B., Papon, J.-F., Dastot-Le Moal, F., *et al.* (2015) 'RSPH3 Mutations Cause Primary Ciliary Dyskinesia with Central-Complex Defects and a Near Absence of Radial Spokes.', *American journal of human genetics*, 97(1), pp. 153–62. doi: 10.1016/j.ajhg.2015.05.004.

Jeanson, L., Copin, B., Papon, J.-F., Dastot-Le Moal, F., *et al.* (2015) *RSPH3 Mutations Cause Primary Ciliary Dyskinesia with Central-Complex Defects and a Near Absence of Radial Spokes*, *The American Journal of Human Genetics*. doi: 10.1016/j.ajhg.2015.05.004.

Jékely, G. and Arendt, D. (2006) 'Evolution of intraflagellar transport from coated vesicles and autogenous origin of the eukaryotic cilium', *BioEssays*. doi: 10.1002/bies.20369.

Jenkins, P. M. *et al.* (2006) 'Ciliary Targeting of Olfactory CNG Channels Requires the CNGB1b Subunit and the Kinesin-2 Motor Protein, KIF17', *Current Biology*. doi: 10.1016/j.cub.2006.04.034.

Jiménez, A. J. *et al.* (2014) 'Structure and function of the ependymal barrier and diseases associated with ependyma disruption', *Tissue Barriers*. doi: 10.4161/tisb.28426.

Jin, H. *et al.* (2010) 'The conserved bardet-biedl syndrome proteins

assemble a coat that traffics membrane proteins to Cilia', *Cell*. doi: 10.1016/j.cell.2010.05.015.

Kamura, K. *et al.* (2011) 'Pkd1l1 complexes with Pkd2 on motile cilia and functions to establish the left-right axis', *Development*. Oxford University Press for The Company of Biologists Limited, 138(6), pp. 386–389. doi: 10.1242/dev.058271.

Karcher, C. *et al.* (2005) 'Lack of a laterality phenotype in Pkd1 knock-out embryos correlates with absence of polycystin-1 in nodal cilia', *Differentiation*. Elsevier, 73(8), pp. 425–432. doi: 10.1111/j.1432-0436.2005.00048.x.

Kartagener, M. (1933) 'Zur Pathogenese der Bronchiektasien', *Beiträge zur Klinik der Tuberkulose und spezifischen Tuberkulose-Forschung*. Springer-Verlag, 83(4), pp. 489–501. doi: 10.1007/BF02141468.

Kawakami, H. *et al.* (2015) 'Specific binding of eukaryotic ORC to DNA replication origins depends on highly conserved basic residues', *Scientific Reports*. doi: 10.1038/srep14929.

Kawasumi, A. *et al.* (2011) 'Left-right asymmetry in the level of active Nodal protein produced in the node is translated into left-right asymmetry in the lateral plate of mouse embryos', *Developmental Biology*. doi: 10.1016/j.ydbio.2011.03.009.

Kee, H. L. *et al.* (2012) 'A size-exclusion permeability barrier and nucleoporins characterize a ciliary pore complex that regulates transport into cilia', *Nature Cell Biology*. doi: 10.1038/ncb2450.

Kelley, L. A. *et al.* (2015) 'The Phyre2 web portal for protein modeling, prediction and analysis.', *Nature protocols*, 10(6), pp. 845–58. doi: 10.1038/nprot.2015.053.

Kim, J. *et al.* (2010) 'Functional genomic screen for modulators of ciliogenesis and cilium length', *Nature*. doi: 10.1038/nature08895.

Kim, Jongshin *et al.* (2015) 'Actin remodelling factors control ciliogenesis by regulating YAP/TAZ activity and vesicle trafficking', *Nature Communications*. doi: 10.1038/ncomms7781.

Kim, Miju *et al.* (2014) 'The MST1/2-SAV1 complex of the Hippo pathway promotes ciliogenesis', *Nature Communications*. doi: 10.1038/ncomms6370.

King, L. M., Holsberger, D. R. and Donoghue, a M. (2000) 'Correlation of CASA velocity and linearity parameters with sperm mobility phenotype in turkeys.', *Journal of andrology*. doi: 10.1002/j.1939-4640.2000.tb03277.x.

King, S. M. and Patel-King, R. S. (2015) 'The oligomeric outer dynein arm assembly factor CCDC103 is tightly integrated within the ciliary axoneme and exhibits periodic binding to microtubules', *Journal of Biological Chemistry*. doi: 10.1074/jbc.M114.616425.

Kinzel, D. *et al.* (2010) 'Pitchfork Regulates Primary Cilia Disassembly and Left-Right Asymmetry', *Developmental Cell*. doi: 10.1016/j.devcel.2010.06.005.

Knowles, M. R. *et al.* (2012) 'Mutations of DNAH11 in patients with primary ciliary dyskinesia with normal ciliary ultrastructure', *Thorax*. doi: 10.1136/thoraxjnl-2011-200301.

Knowles, M. R., Leigh, M. W., *et al.* (2013) 'Exome sequencing identifies mutations in CCDC114 as a cause of primary ciliary dyskinesia.', *American journal of human genetics*, 92(1), pp. 99–106. doi: 10.1016/j.ajhg.2012.11.003.

Knowles, M. R., Ostrowski, L. E., *et al.* (2013) 'Mutations in SPAG1 cause primary ciliary dyskinesia associated with defective outer and inner dynein arms.', *American journal of human genetics*, 93(4), pp. 711–20. doi: 10.1016/j.ajhg.2013.07.025.

Knowles, M. R. *et al.* (2014) 'Mutations in RSPH1 cause primary ciliary dyskinesia with a unique clinical and ciliary phenotype', *American Journal of Respiratory and Critical Care Medicine*, 189(6), pp. 707–717. doi:

10.1164/rccm.201311-2047OC.

Ko, H. W. *et al.* (2010) 'Broad-Minded Links Cell Cycle-Related Kinase to Cilia Assembly and Hedgehog Signal Transduction', *Developmental Cell*. doi: 10.1016/j.devcel.2009.12.014.

Kobayashi, Y. *et al.* (2002) 'Hydrocephalus, Situs Inversus, Chronic Sinusitis, and Male Infertility in DNA Polymerase -Deficient Mice: Possible Implication for the Pathogenesis of Immotile Cilia Syndrome', *Molecular and Cellular Biology*. doi: 10.1128/MCB.22.8.2769-2776.2002.

Kong, D. *et al.* (2014) 'Centriole maturation requires regulated Plk1 activity during two consecutive cell cycles', *Journal of Cell Biology*. doi: 10.1083/jcb.201407087.

Kotani, N. *et al.* (2007) 'Mechanical properties of inner-arm dynein-F (dynein I1) studied with in vitro motility assays', *Biophysical Journal*. doi: 10.1529/biophysj.106.101964.

Kott, E. *et al.* (2012) 'Loss-of-function mutations in LRRC6, a gene essential for proper axonemal assembly of inner and outer dynein arms, cause primary ciliary dyskinesia', *American Journal of Human Genetics*, 91(5), pp. 958–964. doi: 10.1016/j.ajhg.2012.10.003.

Kott, E. *et al.* (2013) 'Loss-of-function mutations in RSPH1 Cause primary ciliary dyskinesia with central-complex and radial-spoke defects', *American Journal of Human Genetics*, 93(3), pp. 561–570. doi: 10.1016/j.ajhg.2013.07.013.

Kovac, J. *et al.* (2016) 'Men with a complete absence of normal sperm morphology exhibit high rates of success without assisted reproduction', *Asian Journal of Andrology*. doi: 10.4103/1008-682X.189211.

Kozminski, K. G. *et al.* (1993) 'A motility in the eukaryotic flagellum unrelated to flagellar beating.', *Proceedings of the National Academy of Sciences of the United States of America*, 90(12), pp. 5519–23. Available at: http://www.ncbi.nlm.nih.gov/pubmed/8516294 (Accessed: 20 October 2016).

Kramer, J. M. and Erickson, R. P. (1981) 'Developmental program of PGK-1 and PGK-2 isozymes in spermatogenic cells of the mouse: Specific activities and rates of synthesis', *Developmental Biology*. doi: 10.1016/0012-1606(81)90058-0.

Kumar, N. and Singh, A. (2015) 'Trends of male factor infertility, an important cause of infertility: A review of literature', *Journal of Human Reproductive Sciences*. doi: 10.4103/0974-1208.170370.

Kunimoto, K. *et al.* (2017) 'Disruption of Core Planar Cell Polarity Signaling Regulates Renal Tubule Morphogenesis but Is Not Cystogenic', *Current Biology*. doi: 10.1016/j.cub.2017.09.011.

Laiho, A. *et al.* (2013) 'Transcriptome Profiling of the Murine Testis during the First Wave of Spermatogenesis', *PLoS ONE*. doi: 10.1371/journal.pone.0061558.

Lambe, T. *et al.* (2009) 'Identification of a Steap3 endosomal targeting motif essential for normal iron metabolism', *Blood*. doi: 10.1182/blood-2007-11-120402.

Lantinga-van Leeuwen, I. S. *et al.* (2004) 'Lowering of Pkd1 expression is sufficient to cause polycystic kidney disease', *Human Molecular Genetics*. doi: 10.1093/hmg/ddh336.

Layton, W. M. (1976) 'Random determination of a developmental process: Reversal of normal visceral asymmetry in the mouse', *Journal of Heredity*. doi: 10.1093/oxfordjournals.jhered.a108749.

Layton, W. M. *et al.* (1993) 'Expression of the IV (reversed and/or heterotaxic) phenotype in SWV mice', *Teratology*. doi: 10.1002/tera.1420470611.

Layton, W. M. and Hummel, K. (1976) 'Random determination of a developmental process Reversal of normal visceral asymmetry in the mouse', *The Journal of Heredity*, 67, pp. 336–338.

Lechtreck, K. F. *et al.* (2008) 'Mutations in Hydin impair ciliary motility in mice', *Journal of Cell Biology*, 180(3), pp. 633–643. doi: 10.1083/jcb.200710162.

Lechtreck, K. F. (2015a) 'IFT-Cargo Interactions and Protein Transport in Cilia', *Trends in Biochemical Sciences*, pp. 765–778. doi: 10.1016/j.tibs.2015.09.003.

Lechtreck, K. F. (2015b) 'IFT-Cargo Interactions and Protein Transport in Cilia', *Trends in Biochemical Sciences*. doi: 10.1016/j.tibs.2015.09.003.

Lee, J. H. *et al.* (2012) 'Evolutionarily assembled cis-regulatory module at a human ciliopathy locus', *Science*. doi: 10.1126/science.1213506.

Lee, L. *et al.* (2008) 'Primary ciliary dyskinesia in mice lacking the novel ciliary protein Pcdp1.', *Molecular and cellular biology*, 28(3), pp. 949–57. doi: 10.1128/MCB.00354-07.

Lee, L. (2013) 'Riding the wave of ependymal cilia: Genetic susceptibility to hydrocephalus in primary ciliary dyskinesia', *Journal of Neuroscience Research*. doi: 10.1002/jnr.23238.

Lee, R. T. H., Zhao, Z. and Ingham, P. W. (2016) 'Hedgehog signalling', *Development*. doi: 10.1242/dev.120154.

Li, J. B. *et al.* (2004) 'Comparative genomics identifies a flagellar and basal body proteome that includes the BBS5 human disease gene', *Cell*. doi: 10.1016/S0092-8674(04)00450-7.

Li, Y. *et al.* (2012) 'SUMOylation of the small GTPase ARL-13 promotes ciliary targeting of sensory receptors', *Journal of Cell Biology*. doi: 10.1083/jcb.201203150.

Li, Y. *et al.* (2015) 'Global genetic analysis in mice unveils central role for cilia in congenital heart disease', *Nature*, 521(7553), pp. 520–524. doi: 10.1038/nature14269.

Li, Y. *et al.* (2016) 'DNAH6 and Its Interactions with PCD Genes in Heterotaxy and Primary Ciliary Dyskinesia', *PLoS Genetics*, 12(2). doi: 10.1371/journal.pgen.1005821.

Liu, A. (2005) 'Mouse intraflagellar transport proteins regulate both the activator and repressor functions of Gli transcription factors', *Development*. doi: 10.1242/dev.01894.

Liu, Y. *et al.* (2007) 'Notch signaling controls the differentiation of transporting epithelia and multiciliated cells in the zebrafish pronephros', *Development*. doi: 10.1242/dev.02806.

Logan, M. *et al.* (1998) 'The Transcription Factor Pitx2 Mediates Situs-Specific Morphogenesis in Response to Left-Right Asymmetric Signals', *Cell*, 94(3), pp. 307–317. doi: 10.1016/S0092-8674(00)81474-9.

Loges, N. T. *et al.* (2008) 'DNAI2 Mutations Cause Primary Ciliary Dyskinesia with Defects in the Outer Dynein Arm', *American Journal of Human Genetics*, 83(5), pp. 547–558. doi: 10.1016/j.ajhg.2008.10.001.

Loges, N. T. *et al.* (2009) 'Deletions and Point Mutations of LRRC50 Cause Primary Ciliary Dyskinesia Due to Dynein Arm Defects', *American Journal of Human Genetics*, 85(6), pp. 883–889. doi: 10.1016/j.ajhg.2009.10.018.

Loges, N. T. *et al.* (2018) 'Recessive DNAH9 Loss-of-Function Mutations Cause Laterality Defects and Subtle Respiratory Ciliary-Beating Defects', *The American Journal of Human Genetics*. doi: 10.1016/j.ajhg.2018.10.020.

Lopes, S. S. *et al.* (2010) 'Notch signalling regulates left-right asymmetry through ciliary length control.', *Development (Cambridge, England)*. doi: 10.1242/dev.054452.

Lu, Q. *et al.* (2015) 'Early steps in primary cilium assembly require EHD1/EHD3-dependent ciliary vesicle formation', *Nature Cell Biology*. doi: 10.1038/ncb3109.

Lucas, J. S. *et al.* (2012) 'Static respiratory cilia associated with mutations in Dnahc11/DNAH11: a mouse model of PCD.', *Human mutation*, 33(3), pp. 495–

503. doi: 10.1002/humu.22001.

Lucas, J. S. *et al.* (2014) 'Diagnosis and management of primary ciliary dyskinesia', *Archives of Disease in Childhood*. doi: 10.1136/archdischild-2013-304831.

Lucas, J. S. *et al.* (2017) 'European Respiratory Society guidelines for the diagnosis of primary ciliary dyskinesia', *European Respiratory Journal*. doi: 10.1183/13993003.01090-2016.

Lucas, J. S. *et al.* (no date) 'European Respiratory Society guidelines for the diagnosis of primary ciliary dyskinesia'. doi: 10.1183/13993003.01090-2016.

Lyons, R. A., Saridogan, E. and Djahanbakhch, O. (2006) 'The reproductive significance of human Fallopian tube cilia', *Human Reproduction Update*. doi: 10.1093/humupd/dml012.

Ma, M. and Jiang, Y. J. (2007) 'Jagged2a-notch signaling mediates cell fate choice in the zebrafish pronephric duct', *PLoS Genetics*. doi: 10.1371/journal.pgen.0030018.

Malicki, J. J. and Johnson, C. A. (2017) 'The Cilium: Cellular Antenna and Central Processing Unit', *Trends in Cell Biology*. doi: 10.1016/j.tcb.2016.08.002.

Margulis, L. *et al.* (2006) 'The last eukaryotic common ancestor (LECA): Acquisition of cytoskeletal motility from aerotolerant spirochetes in the Proterozoic Eon', *Proceedings of the National Academy of Sciences*. doi: 10.1073/pnas.0604985103.

Marques, S. *et al.* (2004) 'The activity of the Nodal antagonist Cerl-2 in the mouse node is required for correct L/R body axis', *Genes & Development*. Cold Spring Harbor Laboratory Press, 18(19), pp. 2342–2347. doi: 10.1101/gad.306504.

Marshall, C. B. *et al.* (2016) 'P73 Is Required for Multiciliogenesis and Regulates the Foxj1-Associated Gene Network', *Cell Reports*. The Authors, 14(10), pp. 2289–2300. doi: 10.1016/j.celrep.2016.02.035.

Matsuo, M. *et al.* (2013) 'The establishment of rotational polarity in the airway and ependymal cilia: analysis with a novel cilium motility mutant mouse.', *American journal of physiology. Lung cellular and molecular physiology*, 304(11), pp. L736-45. doi: 10.1152/ajplung.00425.2012.

Matsuoka, Y. *et al.* (2008) 'Isolation and characterization of the spermatid-specific Smrp1 gene encoding a novel manchette protein', *Molecular Reproduction and Development*. doi: 10.1002/mrd.20835.

Matthews LW; Spector S;Lemm J; Potter JL; (1963) 'STUDIES ON PULMONARY SECRETIONS. I. THE OVER-ALL CHEMICAL COMPOSITION OF PULMONARY SECRETIONS FROM PATIENTS WITH CYSTIC FIBROSIS, BRONCHIECTASIS, AND LARYNGECTOMY.', *Am Rev Resp Dis*, 88, pp. 199–204.

May, S. R. *et al.* (2005) 'Loss of the retrograde motor for IFT disrupts localization of Smo to cilia and prevents the expression of both activator and repressor functions of Gli', *Developmental Biology*. doi: 10.1016/j.ydbio.2005.08.050.

Mayrose, I. *et al.* (2004) 'Comparison of site-specific rate-inference methods for protein sequences: Empirical Bayesian methods are superior', *Molecular Biology and Evolution*. doi: 10.1093/molbev/msh194.

Mazelova, J. *et al.* (2009) 'Ciliary targeting motif VxPx directs assembly of a trafficking module through Arf4', *EMBO Journal*. doi: 10.1038/emboj.2008.267.

Mazor, M. *et al.* (2011) 'Primary ciliary dyskinesia caused by homozygous mutation in DNAL1, encoding dynein light chain 1.', *American journal of human genetics*, 88(5), pp. 599–607. doi: 10.1016/j.ajhg.2011.03.018.

McClintock, T. S. *et al.* (2007) 'Tissue expression patterns identify mouse cilia genes', *Physiological Genomics*. doi: 10.1152/physiolgenomics.00128.2007.

McGrath, J. *et al.* (2003) 'Two Populations of Node Monocilia Initiate Left-

Right Asymmetry in the Mouse', *Cell*, 114(1), pp. 61–73. doi: 10.1016/S0092-8674(03)00511-7.

McIntyre, J. C. *et al.* (2015) 'SUMOylation regulates ciliary localization of olfactory signaling proteins', *Journal of Cell Science*. doi: 10.1242/jcs.164673.

McKenzie, C. W. *et al.* (2015) 'CFAP54 is required for proper ciliary motility and assembly of the central pair apparatus in mice', *Molecular Biology of the Cell*. doi: 10.1091/mbc.E15-02-0121.

Meehan, T. F. *et al.* (2017) 'Disease model discovery from 3,328 gene knockouts by the International Mouse Phenotyping Consortium', *Nature Genetics*. doi: 10.1038/ng.3901.

Meno, C. *et al.* (1998) 'lefty-1 Is Required for Left-Right Determination as a Regulator of lefty-2 and nodal', *Cell*, 94(3), pp. 287–297. doi: 10.1016/S0092-8674(00)81472-5.

Merveille, A.-C. *et al.* (2011) 'CCDC39 is required for assembly of inner dynein arms and the dynein regulatory complex and for normal ciliary motility in humans and dogs.', *Nature genetics*, 43(1), pp. 72–8. doi: 10.1038/ng.726.

Miki, K. *et al.* (2004) 'Glyceraldehyde 3-phosphate dehydrogenase-S, a sperm-specific glycolytic enzyme, is required for sperm motility and male fertility', *Proc Natl Acad Sci*. doi: 10.1073/pnas.0407708101.

Mitchell, A. L. *et al.* (2018) 'InterPro in 2019: improving coverage, classification and access to protein sequence annotations', *Nucleic Acids Research*. doi: 10.1093/nar/gky1100.

Mitchison, H. M. *et al.* (2012) 'Mutations in axonemal dynein assembly factor DNAAF3 cause primary ciliary dyskinesia', *Nature Genetics*, 44(4), pp. 381–389. doi: 10.1038/ng.1106.

Mitchison, H. M. and Valente, E. M. (2017) 'Motile and non-motile cilia in human pathology: from function to phenotypes', *Journal of Pathology*. doi: 10.1002/path.4843.

Molla-Herman, A. *et al.* (2010) 'The ciliary pocket: an endocytic membrane domain at the base of primary and motile cilia', *Journal of Cell Science*. doi: 10.1242/jcs.059519.

Mollet, G. *et al.* (2002) 'The gene mutated in juvenile nephronophthisis type 4 encodes a novel protein that interacts with nephrocystin', *Nature Genetics*. doi: 10.1038/ng996.

Moore, A. *et al.* (2006) 'RPGR is mutated in patients with a complex X linked phenotype combining primary ciliary dyskinesia and retinitis pigmentosa.', *Journal of medical genetics*, 43(4), pp. 326–33. doi: 10.1136/jmg.2005.034868.

Moore, D. J. *et al.* (2013) 'Mutations in ZMYND10, a gene essential for proper axonemal assembly of inner and outer dynein arms in humans and flies, cause primary ciliary dyskinesia.', *American journal of human genetics*, 93(2), pp. 346–56. doi: 10.1016/j.ajhg.2013.07.009.

Morgan, D. *et al.* (1998) 'Inversin, a novel gene in the vertebrate left-right axis pathway, is partially deleted in the inv mouse', *Nature Genetics*. doi: 10.1038/2450.

Morotomi-Yano, K. *et al.* (2002) 'Human regulatory factor X 4 (RFX4) is a testis-specific dimeric DNA-binding protein that cooperates with other human RFX members', *Journal of Biological Chemistry*. doi: 10.1074/jbc.M108638200.

Morris, R. L. and Scholey, J. M. (1997) 'Heterotrimeric kinesin-II is required for the assembly of motile 9+2 ciliary axonemes on sea urchin embryos', *Journal of Cell Biology*. doi: 10.1083/jcb.138.5.1009.

Mueller, J. (2005) 'The FLA3 KAP Subunit Is Required for Localization of Kinesin-2 to the Site of Flagellar Assembly and Processive Anterograde Intraflagellar Transport', *Molecular Biology of the Cell*. doi: 10.1091/mbc.E04-10-0931.

Murphy, D. B. *et al.* (1997) 'The human hepatocyte nuclear factor 3/fork

head gene FKHL13: Genomic structure and pattern of expression', *Genomics*. doi: 10.1006/geno.1996.4587.

Nachury, M. V. *et al.* (2007) 'A Core Complex of BBS Proteins Cooperates with the GTPase Rab8 to Promote Ciliary Membrane Biogenesis', *Cell*. doi: 10.1016/j.cell.2007.03.053.

Nagarkatti-Gude, D. R. *et al.* (2011) 'Spag16, an axonemal central apparatus gene, encodes a male germ cell nuclear speckle protein that regulates SPAG16 mRNA expression', *PLoS ONE*. doi: 10.1371/journal.pone.0020625.

Nagata, A. *et al.* (2012) 'Characterization of ciliary targeting sequence of rat melanin-concentrating hormone receptor 1', *General and Comparative Endocrinology*. doi: 10.1016/j.ygcen.2013.02.020.

Nakamura, K. I. *et al.* (1999) 'Rhophilin, a small GTPase Rho-binding protein, is abundantly expressed in the mouse testis and localized in the principal piece of the sperm tail', *FEBS Letters*. doi: 10.1016/S0014-5793(99)00087-3.

Nakamura, T. *et al.* (2006) 'Generation of Robust Left-Right Asymmetry in the Mouse Embryo Requires a Self-Enhancement and Lateral-Inhibition System', *Developmental Cell*. doi: 10.1016/j.devcel.2006.08.002.

Nakamura, T., Saito, D., *et al.* (2012) 'Fluid flow and interlinked feedback loops establish left–right asymmetric decay of Cerl2 mRNA', *Nature Communications*. Nature Publishing Group, 3, p. 1322. doi: 10.1038/ncomms2319.

Nakamura, T., Hamada, H., *et al.* (2012) 'Left-right patterning: conserved and divergent mechanisms.', *Development (Cambridge, England)*. Oxford University Press for The Company of Biologists Limited, 139(18), pp. 3257–62. doi: 10.1242/dev.061606.

Narita, K. and Takeda, S. (2015) 'Cilia in the choroid plexus: their roles in hydrocephalus and beyond', *Frontiers in Cellular Neuroscience*. doi: 10.3389/fncel.2015.00039.

Nauli, S. M. *et al.* (2003) 'Polycystins 1 and 2 mediate mechanosensation in the primary cilium of kidney cells', *Nature Genetics*. doi: 10.1038/ng1076.

Nebel, B. R., Amarose, A. P. and Hackett, E. M. (1961) 'Calendar of gametogenic development in the prepuberal male mouse', *Science*. doi: 10.1126/science.134.3482.832.

Nemajerova, A. *et al.* (2016) 'TAp73 is a central transcriptional regulator of airway multiciliogenesis', *Genes & Development*. Cold Spring Harbor Laboratory Press, 30(11), pp. 1300–1312. doi: 10.1101/gad.279836.116.

Neugebauer, J. M. *et al.* (2009) 'FGF signalling during embryo development regulates cilia length in diverse epithelia', *Nature*. doi: 10.1038/nature07753.

Nguyen, D. and Xu, T. (2008) 'The expanding role of mouse genetics for understanding human biology and disease', *Disease Models and Mechanisms*. doi: 10.1242/dmm.000232.

Nonaka, S. *et al.* (1998a) 'Randomization of left-right asymmetry due to loss of nodal cilia generating leftward flow of extraembryonic fluid in mice lacking KIF3B motor protein', *Cell*. doi: 10.1016/S0092-8674(00)81705-5.

Nonaka, S. *et al.* (1998b) 'Randomization of Left–Right Asymmetry due to Loss of Nodal Cilia Generating Leftward Flow of Extraembryonic Fluid in Mice Lacking KIF3B Motor Protein', *Cell*, 95(6), pp. 829–837. doi: 10.1016/S0092-8674(00)81705-5.

Nonaka, S. *et al.* (2002) 'Determination of left–right patterning of the mouse embryo by artificial nodal flow', *Nature*. Nature Publishing Group, 418(6893), pp. 96–99. doi: 10.1038/nature00849.

Norden, C. (2017) 'Pseudostratified epithelia – cell biology, diversity and roles in organ formation at a glance', *Journal of Cell Science*. doi: 10.1242/jcs.192997.

Norris, D. P. (2012) 'Cilia, calcium and the basis of left-right asymmetry.', *BMC biology*, 10, p. 102. doi: 10.1186/1741-7007-10-102.

Norris, D. P. and Grimes, D. T. (2012) 'Mouse models of ciliopathies: the state of the art', *Disease Models & Mechanisms*, 5(3), pp. 299–312. doi: 10.1242/dmm.009340.

Norris, D. P. and Robertson, E. J. (1999) 'Asymmetric and node-specific nodal expression patterns are controlled by two distinct cis-acting regulatory elements.', *Genes & development*. Cold Spring Harbor Laboratory Press, 13(12), pp. 1575–88. Available at: http://www.ncbi.nlm.nih.gov/pubmed/10385626 (Accessed: 26 August 2016).

Nozawa, Y. I. *et al.* (2013) 'Fused (Stk36) is a ciliary protein required for central pair assembly and motile cilia orientation in the mammalian oviduct', *Developmental Dynamics: An Official Publication of the American Association of Anatomists*, 242(11), pp. 1307–1319. doi: 10.1002/dvdy.24024.

O'Bryan, M. K. *et al.* (1998) 'Identification of a rat testis-specific gene encoding a potential rat outer dense fibre protein', *Molecular Reproduction and Development*. doi: 10.1002/(SICI)1098-2795(199807)50:3<313::AID-MRD7>3.0.CO;2-M.

O'Leary, N. A. *et al.* (2016) 'Reference sequence (RefSeq) database at NCBI: Current status, taxonomic expansion, and functional annotation', *Nucleic Acids Research*. doi: 10.1093/nar/gkv1189.

Ocbina, P. J. R. and Anderson, K. V (2008) 'Intraflagellar transport, cilia, and mammalian Hedgehog signaling: analysis in mouse embryonic fibroblasts.', *Developmental dynamics : an official publication of the American Association of Anatomists*. doi: 10.1002/dvdy.21551.

Ocbina, P. J. R., Tuson, M. and Anderson, K. V. (2009) 'Primary cilia are not required for normal canonical Wnt signaling in the mouse embryo', *PLoS ONE*. doi: 10.1371/journal.pone.0006839.

Ofran, Y. and Rost, B. (2007) 'ISIS: Interaction sites identified from sequence', in *Bioinformatics*. doi: 10.1093/bioinformatics/btl303.

Okada, Y. *et al.* (1999) 'Abnormal Nodal Flow Precedes Situs Inversus in iv and inv mice', *Molecular Cell*, 4(4), pp. 459–468. doi: 10.1016/S1097-2765(00)80197-5.

Olbrich, H. *et al.* (2002) 'Mutations in DNAH5 cause primary ciliary dyskinesia and randomization of left-right asymmetry.', *Nature genetics*, 30(2), pp. 143–4. doi: 10.1038/ng817.

Olbrich, H. *et al.* (2003) 'Mutations in a novel gene, NPHP3, cause adolescent nephronophthisis, tapeto-retinal degeneration and hepatic fibrosis', *Nature Genetics*. doi: 10.1038/ng1216.

Olbrich, H. *et al.* (2012) 'Recessive HYDIN mutations cause primary ciliary dyskinesia without randomization of left-right body asymmetry', *American Journal of Human Genetics*, 91(4), pp. 672–684. doi: 10.1016/j.ajhg.2012.08.016.

Olbrich, H. *et al.* (2015) 'Loss-of-Function GAS8 Mutations Cause Primary Ciliary Dyskinesia and Disrupt the Nexin-Dynein Regulatory Complex', *American Journal of Human Genetics*, 97(4), pp. 546–554. doi: 10.1016/j.ajhg.2015.08.012.

Olcese, C. *et al.* (2017) 'X-linked primary ciliary dyskinesia due to mutations in the cytoplasmic axonemal dynein assembly factor PIH1D3', *Nature Communications*. doi: 10.1038/ncomms14279.

Omori, Y. *et al.* (2008) 'Elipsa is an early determinant of ciliogenesis that links the IFT particle to membrane-associated small GTPase Rab8', *Nature Cell Biology*. doi: 10.1038/ncb1706.

Omori, Y. *et al.* (2010) 'Negative regulation of ciliary length by ciliary male germ cell-associated kinase (Mak) is required for retinal photoreceptor survival', *Proceedings of the National Academy of Sciences*. doi: 10.1073/pnas.1009437108.

Omran, H. *et al.* (2000) 'Homozygosity mapping of a gene locus for primary ciliary dyskinesia on chromosome 5p and identification of the heavy dynein chain DNAH5 as a candidate gene.', *American journal of respiratory cell and molecular biology*, 23(5), pp. 696–702. doi: 10.1165/ajrcmb.23.5.4257.

Omran, H. *et al.* (2008) 'Ktu/PF13 is required for cytoplasmic pre-assembly of axonemal dyneins.', *Nature*, 456(7222), pp. 611–6. doi: 10.1038/nature07471.

Onoufriadis, A., Shoemark, A., Munye, M. M., *et al.* (2014) 'Combined exome and whole-genome sequencing identifies mutations in ARMC4 as a cause of primary ciliary dyskinesia with defects in the outer dynein arm.', *Journal of medical genetics*, 51(1), pp. 61–7. doi: 10.1136/jmedgenet-2013-101938.

Onoufriadis, A., Shoemark, A., Schmidts, M., *et al.* (2014) 'Targeted NGS gene panel identifies mutations in RSPH1 causing primary ciliary dyskinesia and a common mechanism for ciliary central pair agenesis due to radial spoke defects', *Human Molecular Genetics*, 23(13), pp. 3362–3374. doi: 10.1093/hmg/ddu046.

Ortega, C. *et al.* (2011) 'Absolute asthenozoospermia and ICSI: What are the options?', *Human Reproduction Update*. doi: 10.1093/humupd/dmr018.

Ostrowski, L. E. *et al.* (2010) 'Conditional deletion of Dnaic1 in a murine model of primary ciliary dyskinesia causes chronic rhinosinusitis', *American Journal of Respiratory Cell and Molecular Biology*, 43(1), pp. 55–63. doi: 10.1165/rcmb.2009-0118OC.

Otto, E. *et al.* (2002) 'A gene mutated in nephronophthisis and retinitis pigmentosa encodes a novel protein, nephroretinin, conserved in evolution.', *American journal of human genetics*. doi: 10.1086/344395.

Otto, E. A. *et al.* (2003) 'Mutations in INVS encoding inversin cause nephronophthisis type 2, linking renal cystic disease to the function of primary cilia and left-right axis determination', *Nature Genetics*. doi: 10.1038/ng1217.

Paff, T. *et al.* (2017) 'Mutations in PIH1D3 Cause X-Linked Primary Ciliary Dyskinesia with Outer and Inner Dynein Arm Defects', *American Journal of Human Genetics*. doi: 10.1016/j.ajhg.2016.11.019.

Palermo, G. *et al.* (1992) 'Pregnancies after intracytoplasmic injection of single spermatozoon into an oocyte', *The Lancet*. doi: 10.1016/0140-6736(92)92425-F.

Panizzi, J. R. *et al.* (2012) 'CCDC103 mutations cause primary ciliary dyskinesia by disrupting assembly of ciliary dynein arms.', *Nature genetics*, 44(6), pp. 714–9. doi: 10.1038/ng.2277.

Pazour, G. J. *et al.* (2000) 'Chlamydomonas IFT88 and its mouse homologue, polycystic kidney disease gene Tg737, are required for assembly of cilia and flagella', *Journal of Cell Biology*. doi: 10.1083/jcb.151.3.709.

Pazour, G J, Dickert, B. L. and Witman, G. B. (1999) 'The DHC1b (DHC2) isoform of cytoplasmic dynein is required for flagellar assembly.', *The Journal of cell biology*, 144(3), pp. 473–81. Available at: http://www.ncbi.nlm.nih.gov/pubmed/9971742 (Accessed: 20 October 2016).

Pazour, Gregory J., Dickert, B. L. and Witman, G. B. (1999) 'The DHC1b (DHC2) isoform of cytoplasmic dynein is required for flagellar assembly', *Journal of Cell Biology*. doi: 10.1083/jcb.144.3.473.

Pazour, G. J., Wilkerson, C. G. and Witman, G. B. (1998) 'A dynein light chain is essential for the retrograde particle movement of intraflagellar transport (IFT).', *The Journal of cell biology*, 141(4), pp. 979–92. Available at: http://www.ncbi.nlm.nih.gov/pubmed/9585416 (Accessed: 20 October 2016).

Pazour, G. J. and Witman, G. B. (2003) 'The vertebrate primary cilium is a sensory organelle', *Current Opinion in Cell Biology*. doi: 10.1016/S0955-0674(02)00012-1.

Pennekamp, P. *et al.* (2002) *The Ion Channel Polycystin-2 Is Required for*

Left-Right Axis Determination in Mice, *Current Biology*. Elsevier. doi: 10.1016/S0960-9822(02)00869-2.

Pintado, P. *et al.* (2017) 'Dynamics of cilia length in left–right development', *Royal Society Open Science*. doi: 10.1098/rsos.161102.

Piovesan, D. *et al.* (2018) 'MobiDB 3.0: More annotations for intrinsic disorder, conformational diversity and interactions in proteins', *Nucleic Acids Research*. doi: 10.1093/nar/gkx1071.

Piperno, G. *et al.* (1994) 'Mutations in the "dynein regulatory complex" alter the ATP-insensitive binding sites for inner arm dyneins in Chlamydomonas axonemes', *Journal of Cell Biology*. doi: 10.1083/jcb.125.5.1109.

Piperno, G. and Mead, K. (1997) 'Transport of a novel complex in the cytoplasmic matrix of Chlamydomonas flagella.', *Proceedings of the National Academy of Sciences of the United States of America*, 94(9), pp. 4457–62. Available at: http://www.ncbi.nlm.nih.gov/pubmed/9114011 (Accessed: 20 October 2016).

Pitaval, A. *et al.* (2010) 'Cell shape and contractility regulate ciliogenesis in cell cycle-arrested cells', *Journal of Cell Biology*. doi: 10.1083/jcb.201004003.

Porter, M. E. *et al.* (1999) 'Cytoplasmic dynein heavy chain 1b is required for flagellar assembly in Chlamydomonas.', *Molecular biology of the cell*, 10(3), pp. 693–712. Available at: http://www.ncbi.nlm.nih.gov/pubmed/10069812 (Accessed: 20 October 2016).

Potenza, E. *et al.* (2015) 'MobiDB 2.0: An improved database of intrinsically disordered and mobile proteins', *Nucleic Acids Research*. doi: 10.1093/nar/gku982.

Prevo, B., Scholey, J. M. and Peterman, E. J. G. (2017) 'Intraflagellar transport: mechanisms of motor action, cooperation, and cargo delivery', *FEBS Journal*. doi: 10.1111/febs.14068.

Prevost, B. *et al.* (2014) 'Genotype-phenotype correlations in patients with primary ciliary dyskinesia with central complex defects related to RSPH1, RSPH4A or RSPH9 mutations', *European Respiratory Journal*.

Pugacheva, E. N. *et al.* (2007) 'HEF1-Dependent Aurora A Activation Induces Disassembly of the Primary Cilium', *Cell*. doi: 10.1016/j.cell.2007.04.035.

Pupko, T. *et al.* (2002) 'Rate4Site: An algorithmic tool for the identification of functional regions in proteins by surface mapping of evolutionary determinants within their homologues', in *Bioinformatics*. doi: 10.1093/bioinformatics/18.suppl_1.S71.

Qin, H. *et al.* (2007) 'Intraflagellar transport protein 27 is a small G protein involved in cell-cycle control', *Curr Biol*. doi: 10.1016/j.cub.2006.12.040.

Raidt, J. *et al.* (2014) 'Ciliary beat pattern and frequency in genetic variants of primary ciliary dyskinesia', *European Respiratory Journal*, 44(6), pp. 1579–1588. doi: 10.1183/09031936.00052014.

Randell, S. H. and Boucher, R. C. (2006) 'Effective mucus clearance is essential for respiratory health', *American Journal of Respiratory Cell and Molecular Biology*. doi: 10.1165/rcmb.2006-0082SF.

Rattner, J. B. *et al.* (2010) 'Primary cilia in fibroblast-like type B synoviocytes lie within a cilium pit: A site of endocytosis', *Histology and Histopathology*. doi: 10.14670/HH-25.865.

Reiter, J. F., Blacque, O. E. and Leroux, M. R. (2012) 'The base of the cilium: roles for transition fibres and the transition zone in ciliary formation, maintenance and compartmentalization', *EMBO reports*, 13(7), pp. 608–618. doi: 10.1038/embor.2012.73.

Reiter, J. F. and Leroux, M. R. (2017) 'Genes and molecular pathways underpinning ciliopathies', *Nature Reviews Molecular Cell Biology*. doi: 10.1038/nrm.2017.60.

Rogers, T. D. *et al.* (2018) 'Mucociliary Clearance in Mice Measured by

Tracking Trans-tracheal Fluorescence of Nasally Aerosolized Beads', *Scientific Reports*. doi: 10.1038/s41598-018-33053-2.

Rohatgi, R. and Snell, W. J. (2010) 'The ciliary membrane', *Current Opinion in Cell Biology*. doi: 10.1016/j.ceb.2010.03.010.

Rokicki, W. *et al.* (2016) 'The role and importance of club cells (Clara cells) in the pathogenesis of some respiratory diseases', *Kardiochirurgia i Torakochirurgia Polska*. doi: 10.5114/kitp.2016.58961.

Rubbo, B. and Lucas, J. S. (2017) 'Clinical care for primary ciliary dyskinesia: current challenges and future directions.', *European respiratory review : an official journal of the European Respiratory Society*, 26(145), p. 170023. doi: 10.1183/16000617.0023-2017.

Ruiz-Binder, N. E., Geimer, S. and Melkonian, M. (2002) 'Regulation of flagellar dynein by the axonemal central apparatus', *Cell Motility and the Cytoskeleton*. doi: 10.1002/cm.10031.

Sakka, L., Coll, G. and Chazal, J. (2011) 'Anatomy and physiology of cerebrospinal fluid.', *European annals of otorhinolaryngology, head and neck diseases*. doi: 10.1016/j.anorl.2011.03.002.

Salathe, M. (2007) 'Regulation of Mammalian Ciliary Beating', *Annual Review of Physiology*. doi: 10.1146/annurev.physiol.69.040705.141253.

Sale, W. S. and Satir, P. (1977) 'Direction of active sliding of microtubules in Tetrahymena cilia.', *Proceedings of the National Academy of Sciences of the United States of America*. doi: 10.1073/pnas.74.5.2045.

Sánchez, I. and Dynlacht, B. D. (2016) 'Cilium assembly and disassembly'. doi: 10.1038/ncb3370.

Sanderson, M. J. and Sleigh, M. A. (1981) 'CILIARY ACTIVITY OF CULTURED RABBIT TRACHEAL EPITHELIUM: BEAT PATTERN AND METACHRONY', *J. Cell Sci*.

Satir, P. (1968) 'Studies on cilia. 3. Further studies on the cilium tip and a "sliding filament" model of ciliary motility.', *The Journal of cell biology*. doi: 10.1083/jcb.39.1.77.

Satir, P. and Christensen, S. T. (2007) 'Overview of Structure and Function of Mammalian Cilia', *Annual Review of Physiology*. doi: 10.1146/annurev.physiol.69.040705.141236.

Satir, P., Heuser, T. and Sale, W. S. (2014) 'A structural basis for how motile cilia beat', *BioScience*. doi: 10.1093/biosci/biu180.

Saund, R. S. *et al.* (2012) 'Gut endoderm is involved in the transfer of left-right asymmetry from the node to the lateral plate mesoderm in the mouse embryo.', *Development (Cambridge, England)*. Oxford University Press for The Company of Biologists Limited, 139(13), pp. 2426–35. doi: 10.1242/dev.079921.

Saunier, S. *et al.* (1997) 'A novel gene that encodes a protein with a putative src homology 3 domain is a candidate gene for familial juvenile nephronophthisis.', *Human molecular genetics*. doi: dda294 [pii].

Schlessinger, A. *et al.* (2009) 'Improved disorder prediction by combination of orthogonal approaches', *PLoS ONE*. doi: 10.1371/journal.pone.0004433.

Schlessinger, A., Liu, J. and Rost, B. (2007) 'Natively unstructured loops differ from other loops', *PLoS Computational Biology*. doi: 10.1371/journal.pcbi.0030140.

Schlessinger, A., Punta, M. and Rost, B. (2007) 'Natively unstructured regions in proteins identified from contact predictions', *Bioinformatics*. doi: 10.1093/bioinformatics/btm349.

Schneider, C. A., Rasband, W. S. and Eliceiri, K. W. (2012) 'NIH Image to ImageJ: 25 years of image analysis', *Nature Methods*. doi: 10.1038/nmeth.2089.

Schofield, L. M., Duff, A. and Brennan, C. (2018) 'Airway Clearance Techniques for Primary Ciliary Dyskinesia; is the Cystic Fibrosis literature

portable?', *Paediatric Respiratory Reviews*. doi: 10.1016/j.prrv.2017.03.011.

Schwabe, G. C. *et al.* (2008) 'Primary ciliary dyskinesia associated with normal axoneme ultrastructure is caused by DNAH11 mutations.', *Human mutation*, 29(2), pp. 289–98. doi: 10.1002/humu.20656.

Schweickert, A. *et al.* (2000) 'Pitx2 isoforms: Involvement of Pitx2c but not Pitx2a or Pitx2b in vertebrate left-right asymmetry', *Mechanisms of Development*. doi: 10.1016/S0925-4773(99)00227-0.

Sears, P. R., Yin, W.-N. and Ostrowski, L. E. (2015) 'Continuous mucociliary transport by primary human airway epithelial cells in vitro', *American Journal of Physiology - Lung Cellular and Molecular Physiology*. doi: 10.1152/ajplung.00024.2015.

Seeger-Nukpezah, T. *et al.* (2012) 'The centrosomal kinase Plk1 localizes to the transition zone of primary cilia and induces phosphorylation of nephrocystin-1', *PLoS ONE*. doi: 10.1371/journal.pone.0038838.

Shapiro, A. J. *et al.* (2014) 'Laterality defects other than situs inversus totalis in primary ciliary dyskinesia: Insights into situs ambiguus and heterotaxy', *Chest*, 146(5), pp. 1176–1186. doi: 10.1378/chest.13-1704.

Shima, J. E. *et al.* (2004) 'The Murine Testicular Transcriptome: Characterizing Gene Expression in the Testis During the Progression of Spermatogenesis1', *Biology of Reproduction*. doi: 10.1095/biolreprod.103.026880.

Shinohara, K. *et al.* (2012) 'Two rotating cilia in the node cavity are sufficient to break left–right symmetry in the mouse embryo', *Nature Communications*. Nature Publishing Group, 3, p. 622. doi: 10.1038/ncomms1624.

Shiratori, H. and Hamada, H. (2014) 'TGFβ signaling in establishing left-right asymmetry', *Seminars in Cell and Developmental Biology*. doi: 10.1016/j.semcdb.2014.03.029.

Shoemark, A. *et al.* (2017) 'High prevalence of *CCDC103* p.His154Pro mutation causing primary ciliary dyskinesia disrupts protein oligomerisation and is associated with normal diagnostic investigations', *Thorax*, p. thoraxjnl-2017-209999. doi: 10.1136/thoraxjnl-2017-209999.

Shoemark, A., Moya, E., *et al.* (2018) 'High prevalence of CCDC103 p.His154Pro mutation causing primary ciliary dyskinesia disrupts protein oligomerisation and is associated with normal diagnostic investigations', *Thorax*. doi: 10.1136/thoraxjnl-2017-209999.

Shoemark, A., Burgoyne, T., *et al.* (2018) 'Primary ciliary dyskinesia with normal ultrastructure: three-dimensional tomography detects absence of DNAH11', *European Respiratory Journal*. doi: 10.1183/13993003.01809-2017.

Shukla, A. *et al.* (2015) 'Plk1 relieves centriole block to reduplication by promoting daughter centriole maturation', *Nature Communications*. doi: 10.1038/ncomms9077.

Signor, D. *et al.* (1999) 'Role of a class DHC1b dynein in retrograde transport of IFT motors and IFT raft particles along cilia, but not dendrites, in chemosensory neurons of living Caenorhabditis elegans.', *The Journal of cell biology*, 147(3), pp. 519–30. Available at: http://www.ncbi.nlm.nih.gov/pubmed/10545497 (Accessed: 20 October 2016).

Singla, V. and Reiter, J. F. (2006) 'The primary cilium as the cell's antenna: Signaling at a sensory organelle', *Science*. doi: 10.1126/science.1124534.

Sironen, A. *et al.* (2011) 'Loss of SPEF2 Function in Mice Results in Spermatogenesis Defects and Primary Ciliary Dyskinesia1', *Biology of Reproduction*. doi: 10.1095/biolreprod.111.091132.

Sivaramakrishnan, H., Cottee, A. and Coon, C. (2015) 'Successful pregnancies for five women with primary ciliary dyskinesia (PCD)', *Respirology*. doi: 10.1111/resp.12495.

Sleigh, M. A., Blake, J. R. and Liron, N. (1988) 'The Propulsion of Mucus by Cilia', *American Review of Respiratory Disease*. doi: 10.1164/ajrccm/137.3.726.

Solomon, G. M. *et al.* (2017) 'Assessment of ciliary phenotype in primary ciliary dyskinesia by micro-optical coherence tomography', *JCI Insight*. doi: 10.1172/jci.insight.91702.

Steimle, V. *et al.* (1995) 'A novel DNA-binding regulatory factor is mutated in primary MHC class II deficiency (bare lymphocyte syndrome)', *Genes and Development*. doi: 10.1101/gad.9.9.1021.

Stepanek, L. *et al.* (2016) 'Microtubule doublets are double-track railways for intraflagellar transport trains.', *Science (New York, N.Y.)*. doi: 10.1126/science.aaf4594.

Stewart, M. (2007) 'Molecular mechanism of the nuclear protein import cycle', *Nature Reviews Molecular Cell Biology*. doi: 10.1038/nrm2114.

Stubbs, J. L. *et al.* (2012) 'Multicilin promotes centriole assembly and ciliogenesis during multiciliate cell differentiation', *Nature Cell Biology*. doi: 10.1038/ncb2406.

Suarez, S. S., Varosi, S. M. and Dai, X. (1993) *Intracellular calcium increases with hyperactivation in intact, moving hamster sperm and oscillates with the flagellar beat cycle (indo-1)*, *Proc. Natl. Acad. Sci. USA*. doi: 10.1073/pnas.90.10.4660.

Sun, Z. (2004) 'A genetic screen in zebrafish identifies cilia genes as a principal cause of cystic kidney', *Development*. doi: 10.1242/dev.01240.

Sundberg, J. and Collins, R. (1993) *THE SITUS INVERSUS IV MUTATION*, *JAX Notes*. Available at: https://www.jax.org/news-and-insights/1993/january/the-situs-inversus-iv-mutation (Accessed: 25 February 2019).

Sung, Y. H. *et al.* (2010) 'Pierce1, a novel p53 target gene contributing to the ultraviolet-induced DNA damage response', *Cancer Res*, 70(24), pp. 10454–10463. doi: 10.1158/0008-5472.CAN-10-0031.

Sung, Y. H. *et al.* (2016) 'PIERCE1 is critical for specification of left-right asymmetry in mice.', *Scientific reports*, 6, p. 27932. doi: 10.1038/srep27932.

Supp, D. M. *et al.* (1997) 'Mutation of an axonemal dynein affects left|[ndash]|right asymmetry in inversus viscerum mice', *Nature*. Nature Publishing Group, 389(6654), pp. 963–966. doi: 10.1038/40140.

Swoboda, P., Adler, H. T. and Thomas, J. H. (2000) 'The RFX-type transcription factor DAF-19 regulates sensory neuron cilium formation in C. Elegans', *Molecular Cell*. doi: 10.1016/S1097-2765(00)80436-0.

Szklarczyk, D. *et al.* (2015) 'STRING v10: protein-protein interaction networks, integrated over the tree of life.', *Nucleic acids research*, 43(Database issue), pp. D447-52. doi: 10.1093/nar/gku1003.

Takaki, E. *et al.* (2006) 'Maintenance of olfactory neurogenesis requires HSF1, a major heat shock transcription factor in mice', *Journal of Biological Chemistry*. doi: 10.1074/jbc.M506911200.

Takaki, E. *et al.* (2007) 'Heat shock transcription factor 1 is required for maintenance of ciliary beating in mice.', *The Journal of biological chemistry*. doi: 10.1074/jbc.M704562200.

Takao, D. *et al.* (2014) 'An assay for clogging the ciliary pore complex distinguishes mechanisms of cytosolic and membrane protein entry', *Current Biology*. doi: 10.1016/j.cub.2014.08.012.

Takeda, S. *et al.* (1999) 'Left-right asymmetry and kinesin superfamily protein KIF3A: new insights in determination of laterality and mesoderm induction by kif3A-/- mice analysis.', *The Journal of cell biology*. Rockefeller University Press, 145(4), pp. 825–36. doi: 10.1083/jcb.145.4.825.

Tam, L. W., Wilson, N. F. and Lefebvre, P. A. (2007) 'A CDK-related

kinase regulates the length and assembly of flagella in Chlamydomonas', *Journal of Cell Biology*. doi: 10.1083/jcb.200610022.

Tamplin, O. J., Cox, B. J. and Rossant, J. (2011) 'Integrated microarray and ChIP analysis identifies multiple Foxa2 dependent target genes in the notochord', *Developmental Biology*. doi: 10.1016/j.ydbio.2011.10.002.

Tanaka, C. *et al.* (2007) 'Long-range action of Nodal requires interaction with GDF1', *Genes and Development*. doi: 10.1101/gad.1623907.

Tanaka, Y., Okada, Y. and Hirokawa, N. (2005) 'FGF-induced vesicular release of Sonic hedgehog and retinoic acid in leftward nodal flow is critical for left–right determination', *Nature*. Nature Publishing Group, 435(7039), pp. 172–177. doi: 10.1038/nature03494.

Tanos, B. E. *et al.* (2013) 'Centriole distal appendages promote membrane docking, leading to cilia initiation', *Genes and Development*. doi: 10.1101/gad.207043.112.

Tao, B. *et al.* (2009) 'Cystin Localizes to Primary Cilia via Membrane Microdomains and a Targeting Motif', *Journal of the American Society of Nephrology*. doi: 10.1681/ASN.2009020188.

Tarkar, A. *et al.* (2013) 'DYX1C1 is required for axonemal dynein assembly and ciliary motility.', *Nature genetics*, 45(9), pp. 995–1003. doi: 10.1038/ng.2707.

Tarran, R. *et al.* (2005) 'Normal and cystic fibrosis airway surface liquid homeostasis: The effects of phasic shear stress and viral infections', *Journal of Biological Chemistry*. doi: 10.1074/jbc.M505832200.

Terré, B. *et al.* (2016) 'GEMC1 is a critical regulator of multiciliated cell differentiation.', *The EMBO journal*. doi: 10.15252/embj.201592821.

Thielicke, W. and Buma (2014) *The Flapping Flight of Birds (Analysis and Application)*, *Experiments in fluids*. doi: http://irs.ub.rug.nl/ppn/382783069.

Thielicke, W. and Stamhuis, E. J. (2014) 'PIVlab – Towards User-friendly, Affordable and Accurate Digital Particle Image Velocimetry in MATLAB', *Journal of Open Research Software*. doi: 10.5334/jors.bl.

Thisse, B. *et al.* (2001) *Expression of the zebrafish genome during embryogenesis*, *ZFIN Direct Data Submission (http://zfin.org)*. doi: cb646.

Thorpe, S. D. *et al.* (2017) 'Reduced primary cilia length and altered Arl13b expression are associated with deregulated chondrocyte Hedgehog signaling in alkaptonuria', *Journal of Cellular Physiology*. doi: 10.1002/jcp.25839.

Tichelaar, J. W. *et al.* (1999) 'HNF-3/forkhead homologue-4 (HFH-4) is expressed in ciliated epithelial cells in the developing mouse lung', *Journal of Histochemistry and Cytochemistry*. doi: 10.1177/002215549904700612.

Tran, P. V. *et al.* (2008) 'THM1 negatively modulates mouse sonic hedgehog signal transduction and affects retrograde intraflagellar transport in cilia', *Nature Genetics*. doi: 10.1038/ng.105.

Tsao, C.-C. and Gorovsky, M. a (2008) 'Tetrahymena IFT122A is not essential for cilia assembly but plays a role in returning IFT proteins from the ciliary tip to the cell body.', *Journal of cell science*. doi: 10.1242/jcs.015826.

Turner, R. M. (2006) 'Moving to the beat: A review of mammalian sperm motility regulation', *Reproduction, Fertility and Development*. doi: 10.1071/RD05120.

'UniProt: a worldwide hub of protein knowledge' (2019) *Nucleic acids research*. doi: 10.1093/nar/gky1049.

Vetrini, F. *et al.* (2016) 'Bi-allelic Mutations in PKD1L1 Are Associated with Laterality Defects in Humans', *American Journal of Human Genetics*. doi: 10.1016/j.ajhg.2016.07.011.

Vieira, J. P., Lopes, P. and Silva, R. (2012) 'Primary ciliary dyskinesia and hydrocephalus with aqueductal stenosis', *Journal of Child Neurology*. doi: 10.1177/0883073811429856.

Viotti, M. *et al.* (2012) 'Role of the Gut Endoderm in Relaying Left-Right Patterning in Mice', *PLoS Biology*. Edited by B. L. M. Hogan. Public Library of Science, 10(3), p. e1001276. doi: 10.1371/journal.pbio.1001276.

Vladar, E. K. *et al.* (2015) 'Observing planar cell polarity in multiciliated mouse airway epithelial cells', *Methods in Cell Biology*. doi: 10.1016/bs.mcb.2015.01.016.

Vladar, E. K. and Brody, S. L. (2013) 'Chapter Fourteen – Analysis of Ciliogenesis in Primary Culture Mouse Tracheal Epithelial Cells', in *Methods in Enzymology*. doi: 10.1016/B978-0-12-397944-5.00014-6.

Vogel, P. *et al.* (2010) 'Situs Inversus in Dpcd/Poll-/-, Nme7-/- , and Pkd1l1-/- Mice', *Veterinary Pathology*. SAGE Publications, 47(1), pp. 120–131. doi: 10.1177/0300985809353553.

Vogel, P. *et al.* (2012) 'Congenital hydrocephalus in genetically engineered mice', *Veterinary Pathology*. doi: 10.1177/0300985811415708.

Walentek, P. *et al.* (2012) 'ATP4a Is Required for Wnt-Dependent Foxj1 Expression and Leftward Flow in Xenopus Left-Right Development', *Cell Reports*. doi: 10.1016/j.celrep.2012.03.005.

Wallmeier, J. (2014) 'Mutations in CCNO result in congenital mucociliary clearance disorder with reduced generation of multiple motile cilia', *Nature Genet.*, 46, pp. 646–651. Available at: http://dx.doi.org/10.1038/ng.2961.

Wallmeier, J. *et al.* (2016) 'TTC25 Deficiency Results in Defects of the Outer Dynein Arm Docking Machinery and Primary Ciliary Dyskinesia with Left-Right Body Asymmetry Randomization.', *American journal of human genetics*, 99(2), pp. 460–9. doi: 10.1016/j.ajhg.2016.06.014.

Wang, J. and Sauer, M. V. (2006) 'In vitro fertilization (IVF): A review of 3 decades of clinical innovation and technological advancement', *Therapeutics and Clinical Risk Management*. doi: 10.2147/tcrm.2006.2.4.355.

Wanner, A., Salathe, M. and O'Riordan, T. G. (1996) 'Mucociliary clearance in the airways', *American Journal of Respiratory and Critical Care Medicine*. doi: 10.1164/ajrccm.154.6.8970383.

Warde-Farley, D. *et al.* (2010) 'The GeneMANIA prediction server: biological network integration for gene prioritization and predicting gene function.', *Nucleic acids research*, 38(Web Server issue), pp. W214-20. doi: 10.1093/nar/gkq537.

Warner, F. D. and Satir, P. (1974) 'The structural basis of ciliary bend formation: Radial spoke positional changes accompanying microtubule sliding', *Journal of Cell Biology*. doi: 10.1083/jcb.63.1.35.

Waterhouse, A. M. *et al.* (2009) 'Jalview Version 2-A multiple sequence alignment editor and analysis workbench', *Bioinformatics*. doi: 10.1093/bioinformatics/btp033.

Waters, A. M. and Beales, P. L. (2011) 'Ciliopathies: An expanding disease spectrum', *Pediatric Nephrology*. doi: 10.1007/s00467-010-1731-7.

Watson, C. M. *et al.* (2014) 'Robust diagnostic genetic testing using solution capture enrichment and a novel variant-filtering interface.', *Human mutation*, 35(4), pp. 434–41. doi: 10.1002/humu.22490.

Wemmer, K. A. and Marshall, W. F. (2007) 'Flagellar Length Control in Chlamydomonas-A Paradigm for Organelle Size Regulation', *International Review of Cytology*. doi: 10.1016/S0074-7696(06)60004-1.

Werner, M. E. *et al.* (2011) 'Actin and microtubules drive differential aspects of planar cell polarity in multiciliated cells', *Journal of Cell Biology*. doi: 10.1083/jcb.201106110.

Wheway, G. *et al.* (2013) 'Aberrant Wnt signalling and cellular over-proliferation in a novel mouse model of Meckel-Gruber syndrome', *Developmental Biology*. doi: 10.1016/j.ydbio.2013.02.015.

Wheway, G., Nazlamova, L. and Hancock, J. T. (2018) 'Signaling through

the Primary Cilium', *Frontiers in Cell and Developmental Biology*. doi: 10.3389/fcell.2018.00008.

Whitsett, J. A., Wert, S. E. and Weaver, T. E. (2010) 'Alveolar Surfactant Homeostasis and the Pathogenesis of Pulmonary Disease', *Annual Review of Medicine*. doi: 10.1146/annurev.med.60.041807.123500.

Wiese, M., Kuhn, D. and Grünfelder, C. G. (2003) 'Protein kinase involved in flagellar-length control', *Eukaryotic Cell*. doi: 10.1128/EC.2.4.769-777.2003.

Wilke, M. *et al.* (2011) 'Mouse models of cystic fibrosis: Phenotypic analysis and research applications', *Journal of Cystic Fibrosis*. doi: 10.1016/S1569-1993(11)60020-9.

Williams, C. L. *et al.* (2011) 'MKS and NPHP modules cooperate to establish basal body/transition zone membrane associations and ciliary gate function during ciliogenesis', *Journal of Cell Biology*. doi: 10.1083/jcb.201012116.

Williams, O. W. *et al.* (2006) 'Airway mucus: From production to secretion', *American Journal of Respiratory Cell and Molecular Biology*. doi: 10.1165/rcmb.2005-0436SF.

Wilson, N. F. and Lefebvre, P. A. (2004) 'Regulation of flagellar assembly by glycogen synthase kinase 3 in Chlamydomonas reinhardtii', *Eukaryotic Cell*. doi: 10.1128/EC.3.5.1307-1319.2004.

Wirschell, M. *et al.* (2011) 'Regulation of ciliary motility: Conserved protein kinases and phosphatases are targeted and anchored in the ciliary axoneme', *Archives of Biochemistry and Biophysics*. doi: 10.1016/j.abb.2011.04.003.

Wirschell, M. *et al.* (2013) 'The nexin-dynein regulatory complex subunit DRC1 is essential for motile cilia function in algae and humans.', *Nature genetics*, 45(3), pp. 262–8. doi: 10.1038/ng.2533.

Witman, G. B. and Hou, Y. (2017) 'Dynein and intraflagellar transport', in *Dyneins: The Biology of Dynein Motors: Second Edition*. doi: 10.1016/B978-0-12-809471-6.00013-9.

Witman, G. B., Plummer, J. and Sander, G. (1978) 'Chlamydomonas flagellar mutants lacking radial spokes and central tubules. Structure, composition, and function of specific axonemal components.', *The Journal of cell biology*. doi: 10.1083/jcb.76.3.729.

Wolfe, S. A. *et al.* (2004) 'Regulatory factor X2 (RFX2) binds to the H1t/TE1 promoter element and activates transcription of the testis-specific histone H1t gene', *Journal of Cellular Biochemistry*. doi: 10.1002/jcb.10748.

Wu, C. T., Chen, H. Y. and Tang, T. K. (2018) 'Myosin-Va is required for preciliary vesicle transportation to the mother centriole during ciliogenesis', *Nature Cell Biology*. doi: 10.1038/s41556-017-0018-7.

Wu, G. *et al.* (2000) 'Cardiac defects and renal failure in mice with targeted mutations in Pkd2.', *Nature genetics*. doi: 10.1038/71724.

Yachdav, G. *et al.* (2014a) 'PredictProtein--an open resource for online prediction of protein structural and functional features.', *Nucleic acids research*, 42(Web Server issue), pp. W337-43. doi: 10.1093/nar/gku366.

Yachdav, G. *et al.* (2014b) 'PredictProtein - An open resource for online prediction of protein structural and functional features', *Nucleic Acids Research*. doi: 10.1093/nar/gku366.

Yang, A. and McKeon, F. (2000) 'P63 and P73: P53 mimics, menaces and more', *Nature reviews. Molecular cell biology*, 1(3), pp. 199–207. doi: 10.1038/35043127.

Yoder, B. K., Hou, X. and Guay-Woodford, L. M. (2002) 'The polycystic kidney disease proteins, polycystin-1, polycystin-2, polaris, and cystin, are co-localized in renal cilia', *Journal of the American Society of Nephrology*. doi: 10.1097/01.ASN.0000029587.47950.25.

Yokoyama, T. *et al.* (1993) 'Reversal of left-right asymmetry: a situs inversus mutation.', *Science (New York, N.Y.)*. American Association for the

Advancement of Science, 260(5108), pp. 679–82. doi: 10.1126/science.8480178.

Yoshiba, S. *et al.* (2012) 'Cilia at the node of mouse embryos sense fluid flow for left-right determination via Pkd2.', *Science (New York, N.Y.)*. American Association for the Advancement of Science, 338(6104), pp. 226–31. doi: 10.1126/science.1222538.

Yoshimura, S. I. *et al.* (2007) 'Functional dissection of Rab GTPases involved in primary cilium formation', *Journal of Cell Biology*. doi: 10.1083/jcb.200703047.

Yoshioka, H. *et al.* (1998) 'Pitx2, a Bicoid-Type Homeobox Gene, Is Involved in a Lefty-Signaling Pathway in Determination of Left-Right Asymmetry', *Cell*, 94(3), pp. 299–305. doi: 10.1016/S0092-8674(00)81473-7.

Yu, F. *et al.* (2017) 'Aurora-A promotes the establishment of spindle assembly checkpoint by priming the Haspin-Aurora-B feedback loop in late G2 phase', *Cell Discovery*. doi: 10.1038/celldisc.2016.49.

Yu, X. *et al.* (2001) 'Differential expression and functional analysis of Pitx2 isoforms in regulation of heart looping in the chick.', *Development (Cambridge, England)*.

Yu, X. *et al.* (2008) 'Foxj1 transcription factors are master regulators of the motile ciliogenic program', *Nature Genetics*. Nature Publishing Group, 40(12), pp. 1445–1453. doi: 10.1038/ng.263.

Yuan, S. *et al.* (2015) 'Intraciliary calcium oscillations initiate vertebrate left-right asymmetry', *Curr Biol*, 25(5), pp. 556–567. doi: 10.1016/j.cub.2014.12.051.

Zanconato, F. *et al.* (2015) 'Genome-wide association between YAP/TAZ/TEAD and AP-1 at enhancers drives oncogenic growth', *Nature Cell Biology*. doi: 10.1038/ncb3216.

Zariwala, M. *et al.* (2004) 'Investigation of the possible role of a novel gene, DPCD, in primary ciliary dyskinesia', *American Journal of Respiratory Cell and Molecular Biology*. doi: 10.1165/rcmb.2003-0338RC.

Zariwala, M. A. *et al.* (2006) 'Mutations of DNAI1 in primary ciliary dyskinesia: evidence of founder effect in a common mutation.', *American journal of respiratory and critical care medicine*, 174(8), pp. 858–66. doi: 10.1164/rccm.200603-370OC.

Zariwala, M. A. *et al.* (2013) 'ZMYND10 is mutated in primary ciliary dyskinesia and interacts with LRRC6', *American Journal of Human Genetics*, 93(2), pp. 336–345. doi: 10.1016/j.ajhg.2013.06.007.

Zariwala, M. A., Knowles, M. R. and Omran, H. (2007) 'Genetic Defects in Ciliary Structure and Function', *Annual Review of Physiology*. doi: 10.1146/annurev.physiol.69.040705.141301.

El Zein, L. *et al.* (2009) 'RFX3 governs growth and beating efficiency of motile cilia in mouse and controls the expression of genes involved in human ciliopathies', *Journal of Cell Science*. doi: 10.1242/jcs.048348.

Zhang, D. *et al.* (2006) 'Identification of potential target genes for RFX4_v3, a transcription factor critical for brain development', *Journal of Neurochemistry*. doi: 10.1111/j.1471-4159.2006.03930.x.

Zhang, Y. *et al.* (2008) 'Mice Lacking Histone Deacetylase 6 Have Hyperacetylated Tubulin but Are Viable and Develop Normally', *Molecular and Cellular Biology*. doi: 10.1128/MCB.01154-06.

Zhang, Z. *et al.* (2002) 'A sperm-associated WD repeat protein orthologous to Chlamydomonas PF20 associates with Spag6, the mammalian orthologue of Chlamydomonas PF16', *Society*. doi: 10.1128/MCB.22.22.7993.

Zhang, Z. *et al.* (2004) 'Haploinsufficiency for the murine orthologue of Chlamydomonas PF20 disrupts spermatogenesis.', *Proceedings of the National Academy of Sciences of the United States of America*. doi: 10.1073/pnas.0404280101.

Zhang, Z. *et al.* (2006) 'Deficiency of SPAG16L Causes Male Infertility Associated with Impaired Sperm Motility1', *Biology of Reproduction*. doi: 10.1095/biolreprod.105.049254.

Zhou, F. *et al.* (2015) 'Gmnc Is a Master Regulator of the Multiciliated Cell Differentiation Program', *Current Biology*. doi: 10.1016/j.cub.2015.10.062.

Zhou, J. (2009) 'Polycystins and Primary Cilia: Primers for Cell Cycle Progression', *Annual Review of Physiology*. doi: 10.1146/annurev.physiol.70.113006.100621.

Zhou, J. *et al.* (2012) 'MNS1 is essential for spermiogenesis and motile ciliary functions in mice', *PLoS Genetics*. doi: 10.1371/journal.pgen.1002516.